

7. SITE 892¹

Shipboard Scientific Party²

HOLE 892A

Date occupied: 6 November 1992
Date departed: 9 November 1992
Time on hole: 2 days, 14 hr
Position: 44°40.451'N, 125°7.139'W
Bottom felt (rig floor; m, drill-pipe measurement): 685.5
Distance between rig floor and sea level (m): 11.0
Water depth (drill-pipe measurement from sea level; m): 674.5
Total depth (rig floor; m): 862.0
Penetration (m): 176.5
Number of cores (including cores with no recovery): 21
Total length of cored section (m): 176.5
Total core recovered (m): 62.82
Core recovery (%): 35
Oldest sediment cored:
 Depth (mbsf): 100.0
 Nature: silt
 Earliest age: early(?) Pliocene
Comments: *N.B.:* The oldest sediment is not the deepest.

HOLE 892B

Date occupied: 9 November 1992
Date departed: 15 November 1992
Time on hole: 3 days, 19 hr
Position: 44°40.537'N, 125°7.086'W
Bottom felt (rig floor; m, drill-pipe measurement): 685.5
Distance between rig floor and sea level (m): 11.1
Water depth (drill-pipe measurement from sea level; m): 674.4
Total depth (rig floor; m): 864.0
Penetration (m): 178.5
Number of cores (including cores with no recovery): 0
Comments: CORK borehole seal installed

HOLE 892C

Date occupied: 11 November 1992
Date departed: 12 November 1992
Time on hole: 1 day, 12 hr
Position: 44°40.44'N, 125°7.13'W

Bottom felt (rig floor; m, drill-pipe measurement): 685.5
Distance between rig floor and sea level (m): 11.1
Water depth (drill-pipe measurement from sea level; m): 674.4
Total depth (rig floor; m): 862.0
Penetration (m): 176.5
Number of cores (including cores with no recovery): 1
Total length of cored section (m): 176.5
Total core recovered (m): 7.35
Core recovery (%): 4

HOLE 892D

Date occupied: 15 November 1992
Date departed: 16 November 1992
Time on hole: 1 day, 7 hr
Position: 44°40.447'N, 125°7.154'W
Bottom felt (rig floor; m, drill-pipe measurement): 681.5
Distance between rig floor and sea level (m): 11.2
Water depth (drill-pipe measurement from sea level; m): 670.3
Total depth (rig floor; m): 848.0
Penetration (m): 166.5
Number of cores (including cores with no recovery): 16
Total length of cored section (m): 143.5
Total core recovered (m): 76.17
Core recovery (%): 53
Oldest sediment cored:
 Depth (mbsf): 100.0
 Nature: silt
 Earliest age: early(?) Pliocene
Comments: *N.B.:* The oldest sediment is not the deepest.

HOLE 892E

Date occupied: 16 November 1992
Date departed: 17 November 1992
Time on hole: 1 day, 2 hr
Position: 44°40.446'N, 125°7.144'W
Bottom felt (rig floor; m, drill-pipe measurement): 685.5
Distance between rig floor and sea level (m): 11.2
Water depth (drill-pipe measurement from sea level; m): 674.3
Total depth (rig floor; m): 747.5
Penetration (m): 62.0
Number of cores (including cores with no recovery): 5
Total length of cored section (m): 33.01

¹ Westbrook, G.K., Carson, B., Musgrave, R.J., et al., 1994. *Proc. ODP, Init. Repts.*, 146 (Pt. 1): College Station, TX (Ocean Drilling Program).

² Shipboard Scientific Party is as given in the list of participants preceding the contents.

Total core recovered (m): 15.36

Core recovery (%): 46

Oldest sediment cored:

Depth (mbsf): 47.0

Nature: silt

Earliest age: late Pliocene

Drill below core (m): 7.0

Comments: *N.B.:* The oldest sediment is not the deepest.

Principal results: Ocean Drilling Program (ODP) Site 892 lies on the Oregon continental slope at 674 m below sea level (mbsl). The site was positioned on the western flank of the second ridge within the accretionary wedge to intersect both the bottom-simulating reflector (BSR) at 73 m below seafloor (mbsf) and a hydrologically active, landward-dipping fault (105 mbsf). Site 892 was drilled to delineate the hydrogeology and fluid chemistry of a Pliocene portion of the accretionary wedge, to assess the importance of the fault zone as an active aquifer, to determine the history of flow along this fault and its effect on the temperature regime, to analyze the structures developed around active and relict fault zones, and to investigate the effect of focused fluid advection on the occurrence of gas hydrates and the BSR.

Coring extended to a depth of 176.5 mbsf at Hole 892A. Hole 892B was drilled to a depth of 178.5 mbsf; a packer test was conducted in the hole and a borehole seal (CORK) was deployed to provide for long-term observation of the thermal, chemical, and hydrogeological conditions at the fault zone. Hole 892C was logged to a depth of 139 mbsf with the seismic stratigraphic tool string, lithodensity tool, and Formation MicroScanner (FMS), and a vertical seismic profile (VSP) was run. Holes 892D (0–166.5 mbsf) and 892E (0–62.0 mbsf) provided cores and temperature determinations additional to those collected at Hole 892A, in selected intervals.

The section cored at Hole 892A is divided on the basis of structural characteristics into three domains. Domain I (0–52 mbsf) consists of moderately dipping (<35°) beds of silt and fine sand with fractured intervals in some silts. A fault zone is inferred at 52 mbsf (Domain I/II boundary) from an abrupt reduction in the dip of bedding to 10°–20° and from fractures observed in the FMS log. The abundance of fractured intervals, scaly fabric, and veins increases downhole in Domain II to culminate in a strongly developed fault-zone fabric in Domain III (106–175 mbsf). The interval between 116 and 147 mbsf exhibits a pervasively sheared, consolidated mélange fabric.

Hole 892D differs in some respects structurally from Hole 892A. The Domain I/II boundary fault is not recognized. The interval from 33 to 77 mbsf consists of extensively stratally disrupted, un lithified sediments. Shear fabrics indicative of a mature fault zone including mélange, scaly fabric, and cemented, cataclastized fault gorge are present from 100 to 166.5 mbsf and at 70–75 mbsf.

Radiolarian-based biostratigraphy of the Pliocene section confirms the positions of the fault zones. Two stratigraphic inversions are apparent in Hole 892A, between 45 and 50 mbsf and between 107 and 117 mbsf. In addition, the biostratigraphy defines a hiatus at 23–30 mbsf. In Hole 892D, the hiatus occurs between 32 and 43 mbsf, and only one stratigraphic reversal is recorded, between 76 and 110 mbsf.

The sediments at Site 892 consist dominantly of terrigenous silty clay and clayey silts with sporadic sand layers. Lithostratigraphic Subunit IA (0–68 mbsf) is richer in sand than the deeper section of the hole. Most of the sand layers consist of authigenic glaucony pellets. Grain size decreases downward through the subunit, whereas the proportion of biogenic silica increases near its base. Subunit IB contains fewer sand layers, less glaucony and biogenic silica, and an irregular distribution of grain sizes. Most distinctively, however, Subunit IB exhibits the fracturing and stratal disruption previously described in structural Domains II and III. The sediments at Site 892 appear to be Pliocene abyssal plain deposits, similar to the lowermost sediments recovered at Deep Sea Drilling Project (DSDP) Site 174 in the Cascadia Basin.

The physical properties at Site 892 display marked discontinuities in their respective distributions. Abrupt dislocations in bulk density and porosity occur at 17, 68, 116, 144, and 164 mbsf. The discontinuity at 17

mbsf is clearly a function of the gas hydrates observed between 2 and 19 mbsf, the sublimation of which disrupted the near-surface sediment and yielded an abnormally high porosity (>67%). Beneath the visible hydrates, porosity declines normally to about 55% at 68 mbsf (top of lithostratigraphic Subunit IB), and then becomes variable (42%–62%), with little evidence for further general consolidation. Compaction appears to be localized about the faulted intervals, where strain hardening has occurred. These same intervals are adjacent to porous, fractured zones, at 68 and 116 mbsf, that may serve as active fluid-flow conduits.

Active flow at Site 892 is indicated by the geochemical anomalies in the pore waters, by a packer test that measured superhydrostatic fluid pressures, and by local temperature excursions above an otherwise linear increase in temperature with depth. Furthermore, the unusual occurrence of gas hydrates and elevated levels of hydrogen sulfide as shallow as 2–19 mbsf may be an indirect consequence of the underlying flow regime.

Bacterial methanogenesis occurs at shallow depths (possibly within the upper 2 mbsf) at Site 892. Although biogenic methane probably persists to the base of the hole, it is diluted by the higher hydrocarbon gases below 68 mbsf. These thermogenic hydrocarbons (C₂–C₆) must be derived from deeper within the prism (1–4 km), as the maturity of the local kerogen is insufficient to produce them. The gases also include ethene, an unstable olefin, the presence of which implies advection of petroliferous pore waters, although gas migration might occur independently. The distribution of higher hydrocarbons suggests the movement of fluids through the section at 68, 107, and 125 mbsf.

Gas hydrates occur as macroscopic crystals, pellets, and aggregations distributed in the upper 19 m of sediment and probably as disseminated deposits to 73 mbsf. Temperature measurements and heat-budget calculations in the interval 2–19 mbsf suggest that gas hydrate occupies <10% of the pore volume; no massive hydrate was encountered. The disseminated hydrates below 19 mbsf have a patchy distribution as indicated by the variable dilution of Cl⁻. Gases derived from the hydrate zone include methane, ethane, hydrogen sulfide, and carbon disulfide. The hydrates may contain all of these species.

The occurrence of high concentrations (up to 10,000 ppmv) of H₂S in near-surface sediments and its presence to 60 mbsf may indicate that it is formed bacterially but its usual removal as monosulfides and/or pyrite is inhibited, or that H₂S is allochthonous to these near-surface sediments and has a hydrothermal source. The close association of H₂S with the gas hydrate zone suggests that free sulfide may be stored as clathrate in situ.

The geophysical logs in Hole 892C (located 100 m southeast of Hole 892A) are sensitive, though somewhat inconsistent, indicators of the fault zones inferred from the cores. Between 61 and 68 mbsf and between 83 and 90 mbsf, measurements of high density, high velocity, and high resistivity from the logs define fault zones that are apparently strain hardened. The same intervals show temperature and ethane anomalies, and the upper interval exhibits a pronounced discontinuity in density/porosity. By contrast, a fault zone inferred to occur at 106 mbsf (ethane anomaly, fracturing in core) is represented by low resistivity and bulk density and high neutron porosity.

Logging unequivocally indicates that the BSR is caused by the presence of free gas below 72 mbsf. Below this level sonic velocity drops to a uniform value of 1.5 km/s, indicative of borehole fluid, which implies that velocity in the sediment surrounding the borehole is even lower. The low sonic velocities are attributed to free gas in the formation below the BSR and are confirmed by the VSP (<1.4 km/s).

A sensitive indicator of advective flow is temperature change. In-situ temperature measurements at Site 892 define a linear temperature gradient of 51°C/km, which implies conductive heat transfer. Superimposed on this gradient, however, are two anomalous points at 67.5 and 87.5 mbsf, which have temperatures 1.6°C and 2.5°C higher than predicted by the regression line, respectively. These points are attributed to local advection of warm fluids along fault zones defined by the logs. The limited vertical extent of the anomalies, however, indicates small spatial diffusion of the temperature signal and requires recent fluid flow.

The temperature distribution also constrains the hydrate stability field at Site 892. The linear temperature gradient predicts the base for the stability field of pure methane–pure water at 120 ± 4 mbsf. The BSR, which is

commonly interpreted to indicate the base of the hydrate zone, is situated at 73 mbsf. The disparity between the measured temperature and predicted temperature at the BSR (1.9°), suggests that the experimentally derived phase boundary for pure methane–pure water is not directly applicable to the gas hydrate system on this margin. Application of the theoretical pure methane–pure water hydrate stability zone to the temperature anomalies noted in Hole 892A would imply two or more layers of hydrate stability. Resolution of the apparent disparity between the theoretical gas hydrate stability field and the position of the base of that field observed at Site 892 must await determination of the gas composition of the hydrates and may require experimental determination of an appropriate gas hydrate–seawater stability field.

The drill string packer experiment determined that the pressure of the fluid in the formation at Hole 892B is 0.25–0.30 MPa above hydrostatic pressure. Because the hole was open for more than 12 hr before the test, however, the apparent formation pressure does not represent an equilibrium condition. A post-cruise record of pressure (and temperature) recovery at Hole 892B will come from the CORK borehole seal deployed in this hole.

BACKGROUND AND OBJECTIVES

Site 892 (prospectus Site OM-7) is located near the crest of the second ridge east of the base of the Oregon continental slope (Fig. 1), at a depth of 674 m below sea level (mbsl). The site lies on the western flank of the ridge, just east of the trace of a landward-dipping thrust fault that strikes $N15^{\circ}E$. In this position, Site 892 lies topographically and structurally above Site 891, but because the deformation front has migrated westward with time, the sedimentary section is older than that sampled at Site 891. Sediments comprising the second ridge are apparently Pliocene in age (Kulm et al., 1986).

Seismic reflectors beneath the second ridge are poorly defined, but the few reflectors that can be identified indicate landward-dipping horizons, which crop out on the western flank of the ridge (Fig. 2).

Some of these reflectors are thrust faults, and Site 892 is positioned down-dip of the trace of one of these thrusts (Fig. 2). The site is located about 350 m east of a prominent bioherm that is associated with the surface trace of the thrust fault. The occurrence of clams, bacterial mats, methane bubbles, and massive diagenetic carbonate deposits at the bioherm indicate active fluid venting from the fault zone (Moore et al., in press), and a flow rate of $1765 \text{ L/m}^2/\text{d}$ was recorded within the bioherm (Linke et al., in press). Analysis of *GLORIA* data in this area indicates that anomalously high-amplitude backscattering encompasses the bioherm and extends 22 km along strike on the eastern flank of the second ridge (Carson et al., 1991). These high-reflectance zones have been interpreted to be areas of surface and subsurface diagenetic carbonate deposition, and therefore positive indicators of fluid discharge (Ritger et al., 1987). If correct, this interpretation and the apparent volume of material deposited suggest that the fault intersected at Site 892 has been a long-lived, significant fluid conduit.

A well-defined BSR lies beneath Site 892. The BSR is deflected toward the surface along the fault zone, presumably by the movement of warm fluids from depth, which perturbs the position of the base of the hydrate stability field. Moore et al. (in press) calculated the temperature gradient by assuming the temperature at the base of the BSR from an empirically calibrated methane stability field (Hyndman et al., 1992). The results suggest a temperature gradient beneath the bioherm that is more than twice as large as the regional gradient.

Site 892 provided an opportunity to sample an active fluid pathway at shallow depths; based on the seismic reflection data, the BSR occurs at about 73 mbsf and the imaged fault zone at 107–113 mbsf. Drilling at Site 892 was undertaken to determine the hydrogeology and fluid chemistry of the Pliocene portion of the accretionary wedge, to assess the role of a thrust fault as an active aquifer, to determine the history of venting along this fault, and to investigate the effect of focused fluid advection on the development of gas hydrates. The proposed sampling program incorporated coring, logging, and down-

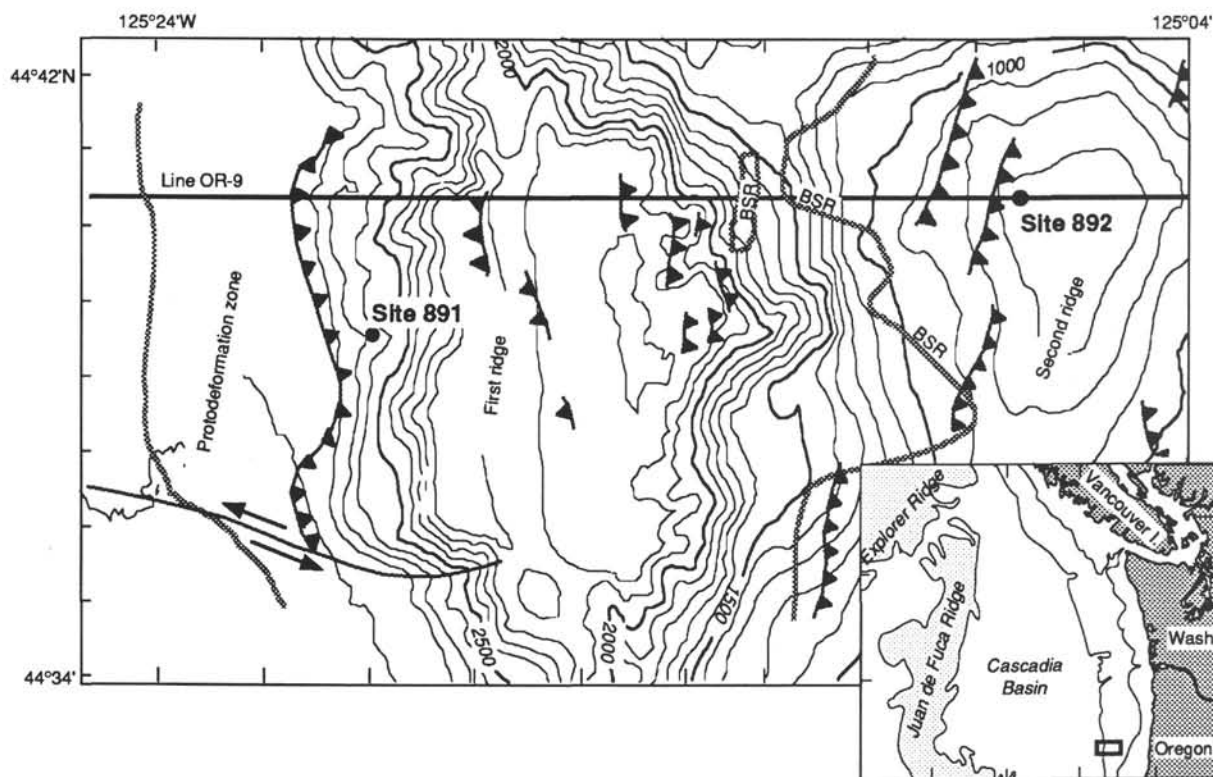


Figure 1. Position of Site 892 and seismic-reflection line OR-9 (Fig. 2) adjacent bathymetry. Relative to positions or faults are indicated by black lines; triangles point down-dip along thrust faults. After MacKay et al. (1992).

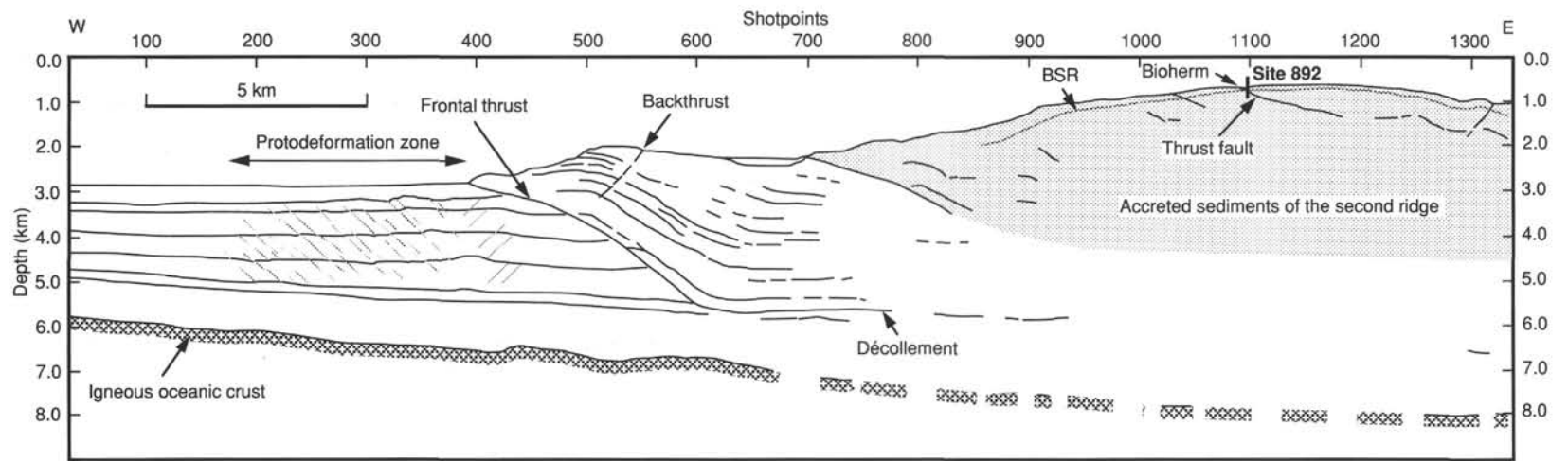


Figure 2. Interpreted, generalized depth section across the Oregon Margin along seismic-reflection line OR-9. The position of Site 892, the fault it penetrates, and the bioherm associated with the fault are plotted.

hole experiments (in-situ temperature, lateral stress tools) to characterize the flow regime associated with the fault zone. A CORK borehole seal was deployed to monitor temperature and pressure and to provide access to collect fluid samples and conduct hydrogeologic tests after the completion of Leg 146.

SEISMIC STRATIGRAPHY

The second ridge of the Oregon accretionary prism is underlain by landward-dipping reflectors; the reflectors appear to be folded and faulted locally (Fig. 3). Accumulations of slope deposits are not apparent on the crest or the on seaward slope of the second ridge; however, slope basins occur both seaward and landward of the ridge. The second ridge is cut by faults striking N15°E, approximately parallel to the bathymetric trend of the ridge (Fig. 1). Surface offsets, and the association of the faults with currently growing folds, indicate that some of the faults are active (Fig. 3). All surface offsets are thrusts, which along with the presence of compressional folds, suggests the second ridge is currently undergoing shortening. These faults and folds indicate a continuing and distributed deformation process, which contrasts with the more localized major displacement and imbrication along the frontal thrust.

A well-developed BSR crosses the crest of the second ridge, extends partially down the seaward flank, and continues landward up the slope (Fig. 1). The depth of the BSR decreases locally beneath active faults and folds; of the two faults apparent on the seismic line in Figure 3, the one adjacent to Site 892 shows both a surface offset and an upward deflection of the BSR.

OPERATIONS

Site 892

Site 891 had been intended as the location of a reentry/borehole seal (CORK) hole, but the inability to plug Hole 891B and thus isolate it hydraulically from the planned reentry hole forced a change of plans. Operations for reentry and installation of the CORK therefore

were relocated to Site 892 (prospectus Site OM-7), about 10 nmi to the east of Site 891. Ultimately, five holes were drilled at this site; the positions of the holes are diagrammed in Figure 4.

Hole 892A

Operations at Site 892 began when a positioning beacon was dropped at 2115 hr Universal Time Coordinated (UTC), 6 November 1992. In preparation for the CORK installation, a jetting test was conducted first. Firm sediment was encountered, and despite several attempts, maximum jet-in was to only 19 mbsf. Because of the degree of consolidation of the sediment, it was not considered advisable to spud Hole 892A with the advanced piston corer (APC), so the first core was cut with the extended core barrel (XCB) (Table 1). The depth of the seafloor (674.5 mbsl) was determined by a tag while the vibration-isolated television (VIT) was still at the bottom.

Arrival of Core 146-892A-1X on deck was accompanied by a strong odor of hydrogen sulfide. A hand-held monitor was used to check the gas level as the core was removed from the inner barrel, and readings in excess of 100 ppm near the core were registered. The core also contained a considerable amount of gas hydrate, which was readily recognizable as millimeter- to centimeter-sized, white, effervescing lumps. A hydrogen sulfide alert was declared and core handlers were outfitted with breathing apparatus. The H₂S concentration was exceptionally high, extremely hazardous, and completely unexpected. Core 146-892A-2X also produced high H₂S readings, but Core 146-892A-3X had only traces of H₂S and no further hydrogen sulfide was detected in subsequent cores.

Hole conditions were good until the faults were crossed, and then 1–4 m of fill accumulated on connections despite mud sweeps. The fill did not affect coring operations but hampered deployments of the water-sampling temperature probe (WSTP) in the lower portion of the hole.

Pressure core sampler (PCS) cores were attempted at 38 and 77 mbsf; both runs recovered water under hydrostatic pressure but no core. In total, ten WSTP runs were made.

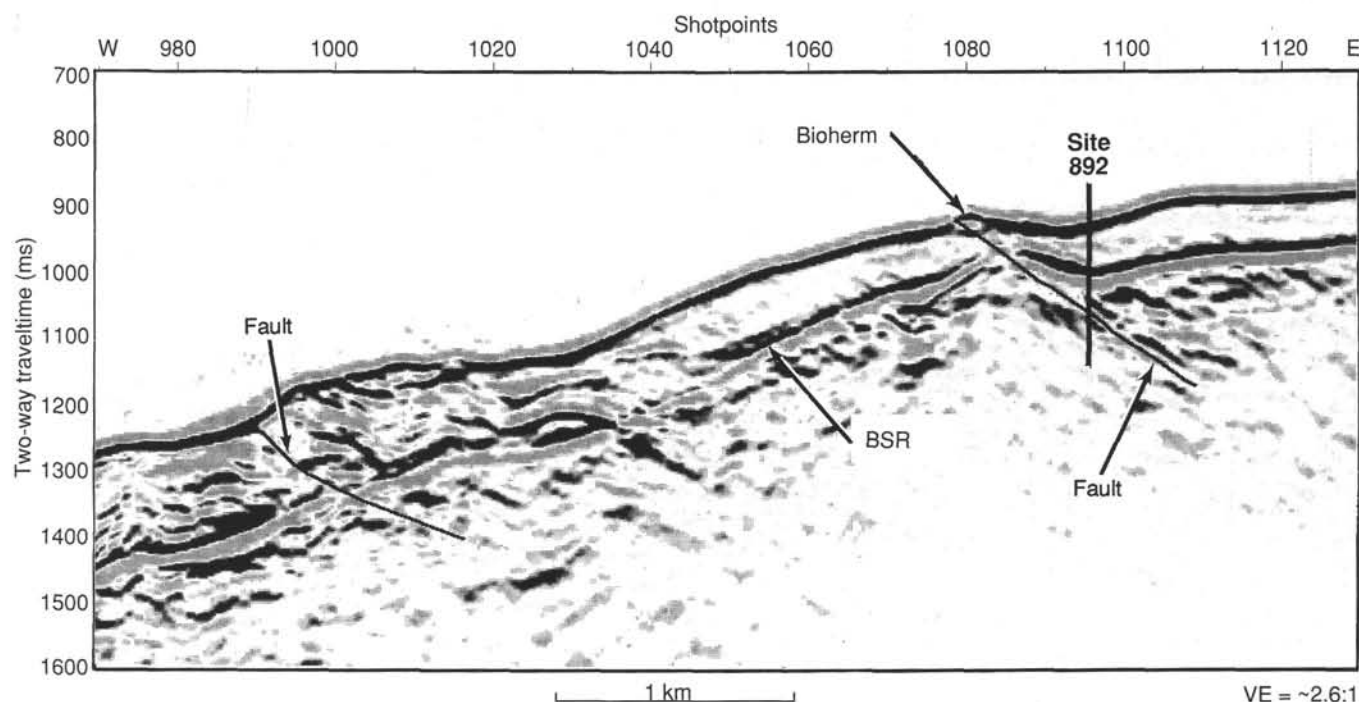


Figure 3. Seismic line OR-9 near Site 892. Note that the fault (solid line, dipping east) penetrated by the drill hole at depth shows surface offset and an upward deflection in the BSR, indicating recent displacement and fluid flow. In contrast, the fault (solid line) to the west (Fig. 2) shows no clear surface offset nor disturbance of the BSR.

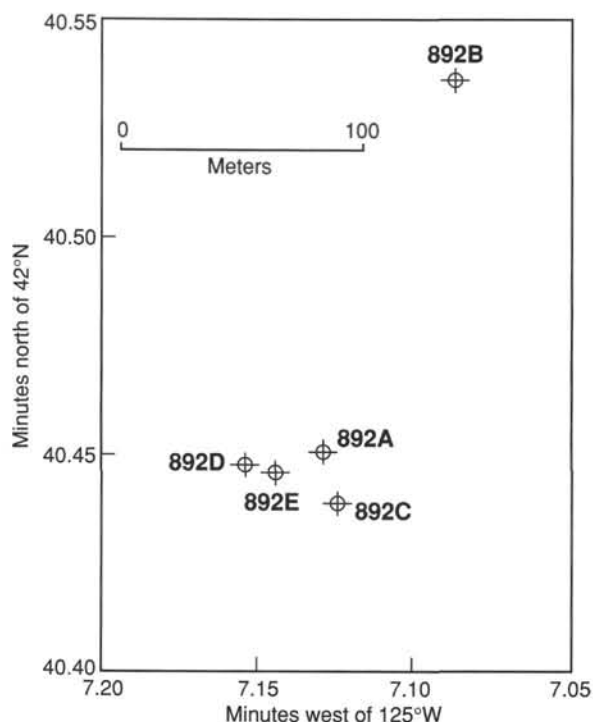


Figure 4. Positions of holes drilled at Site 892.

Coring was discontinued at 176.5 mbsf when cores and gas samples indicated that the hole had penetrated well into the footwall of the major thrust fault. Weighted drilling mud was displaced into the lower portion of the hole before the bit was pulled to 67.5 mbsf for a cement plug. The drill string was then recovered while the vessel was offset 200 m north to the reentry location.

Hole 892B

Because the thrust fault planes had been penetrated at a shallow depth, only a relatively short surface-casing string was required. It was considered that an extra-short 19- to 20-m conductor could support the weight of the surface casing and that the planned reentry-cone installation could proceed.

Jetting was slow as it apparently was necessary to "melt" the gas hydrates in the sediments to advance the casing. Progress slowed at 13–14 mbsf but did not stop until the shoe was at 21 mbsf, close to the depth calculated to put the "mud skirt" of the cone at the seafloor. The 1 3/4-in. hole for the surface casing was then drilled to 105 mbsf, and a short string of seven joints of 1 3/4-in. casing was installed and cemented.

Hole 892C

To ensure the mechanical and pressure integrity of the casing cementation, it was necessary to allow about 36 hr for the cement to cure. As logging and downhole instrumentation had high priority at the site, a dedicated logging hole was drilled during the interruption of operations at Hole 892B.

The 10 1/8-in. hole was drilled to 176.5 mbsf in 11 hr. After the hole had been swept with mud and the inner barrel retrieved, the bit was pulled to 65 mbsf. No overpull was experienced, so a wiper trip was considered unnecessary. The top drive was rigged down and preparations were made for logging.

Because the hole was shallow, the long geophysical tool string was divided into seismic stratigraphic (sonic-induction-gamma ray) and lithoporosity (density-neutron-gamma ray) sections. The seismic stratigraphic string was run first and failed to pass tight hole at about

Table 1. Coring summary, Site 892.

Core no.	Date (November 1992)	Time (UTC)	Depth (mbsf)	Cored (m)	Recovered (m)	Recovery (%)
146-892A-						
1X	7	1245	0.0–9.5	9.5	4.32	45.5
2X	7	1440	9.5–19.0	9.5	3.95	41.6
3X	7	1630	19.0–28.5	9.5	4.16	43.8
4X	7	1745	28.5–38.0	9.5	1.81	19.0
5P	7	1900	38.0–39.0	1.0	0.00	0.0
6X	7	2155	39.0–48.5	9.5	6.69	70.4
7X	7	2320	48.5–58.0	9.5	9.76	103.0
8X	8	0100	58.0–67.5	9.5	6.69	70.4
9X	8	0340	67.5–77.0	9.5	1.12	11.8
10P	8	0425	77.0–78.0	1.0	0.00	0.0
11X	8	0615	78.0–87.5	9.5	3.28	34.5
12X	8	0900	87.5–97.0	9.5	1.11	11.7
13X	8	1140	97.0–106.5	9.5	9.12	96.0
14X	8	1500	106.5–116.0	9.5	0.51	5.4
15X	8	1750	116.0–125.5	9.5	1.36	14.3
16X	8	2015	125.5–135.0	9.5	0.75	7.9
17X	9	0000	135.0–144.5	9.5	1.77	18.6
18X	9	0400	144.5–154.0	9.5	2.37	24.9
19X	9	0525	154.0–163.5	9.5	0.00	0.0
20X	9	0655	163.5–173.0	9.5	3.93	41.3
21X	9	0800	173.0–176.5	3.5	0.12	3.4
Coring totals				176.5	62.82	35.6
146-892C-						
1W	12	0800	0.0–176.5	176.5	7.35	(wash core)
Coring totals				0.0	0.00	
Washing totals				176.5	7.35	
Combined totals					176.50	4.2
146-892D-						
1X	15	2030	0.0–8.5	8.5	0.12	1.4
2X	15	2120	8.5–18.0	9.5	3.24	34.1
3X	15	2235	18.0–27.5	9.5	2.20	23.1
4X	15	2330	27.5–37.0	9.5	4.38	46.1
5X	16	0050	37.0–46.5	9.5	6.12	64.4
6X	16	0205	46.5–54.0	7.5	7.02	93.6
7X	16	0405	54.0–61.7	7.7	7.60	98.7
8X	16	0510	61.7–69.3	7.6	5.11	67.2
9X	16	0640	69.3–77.0	7.7	6.73	87.4
10X	16	1050	100.0–109.5	9.5	10.69	112.5
11X	16	1310	109.5–119.0	9.5	3.60	37.9
12X	16	1440	119.0–128.5	9.5	5.79	60.9
13X	16	1650	128.5–138.0	9.5	0.26	2.7
14X	16	1800	138.0–147.5	9.5	2.08	21.9
15X	16	2015	147.5–157.0	9.5	5.03	52.9
16X	16	2150	157.0–166.5	9.5	7.47	78.6
Coring totals				143.5	77.44	54.0
146-892E-						
1X	17	0205	0.0–13.0	13.0	3.18	24.5
2P	17	0300	13.0–14.0	1.0	0.00	0.0
3H	17	0805	33.0–42.5	9.5	7.90	83.1
4H	17	0920	42.5–52.0	9.5	4.28	45.0
5M	17	1230	55.0–55.0	0.0	0.00	0.0
Coring totals				33.0	15.36	46.5

130 mbsf. A log was recorded up to the bit, which was raised an additional 30 m.

The drill string then was run back into the hole in an attempt to remove the obstruction. Pipe was raised to 49 mbsf and lithoporosity logs were run in this short open-hole interval. Resistance was met at 147 mbsf but the bit was circulated to total depth using the circulating head; top-drive rotation was not required. After a mud sweep, the bit was pulled back to 65 mbsf with no resistance.

The lithoporosity string then was lowered to 125 mbsf before it was stopped by an obstruction. As the cores and seismic records showed the interval from 120 to 150 mbsf to be a zone of major faulting, no further effort was made to open the hole for logging. The next tool into the hole was the FMS, which reached 120 mbsf and also recorded a useful log.

The Schlumberger well seismic tool (WST) had been deployed for a check-shot vertical seismic profile (VSP) when equipment problems forced withdrawal of the tool. After repair, the VSP experiment con-

tinued. The results were degraded by washed-out hole and the inability to clamp the tool in some intervals. The allotted time for down-hole work expired after 2.5 hr and the VSP was terminated.

When the seismic guns and logging tools had been rigged down, the bit was run back into the hole for plugging. Heavy mud was emplaced to fill the hole to about 65 mbsf, and cement was spotted from that depth to about 49 mbsf. The drill string was recovered while the ship was offset back to Hole 892B.

Return to Hole 892B

A 9 $\frac{7}{8}$ -in. tricone drill bit and drilling bottom-hole assembly (BHA) were installed for the final phase of drilling Hole 892B. The cement plug and shoe were drilled out, and 73 m of new hole was drilled to total depth (TD) of 178.5 mbsf. Five joints of 5-in. perforated pipe and one joint of unperforated pipe were made up, reentered, and run into the open hole.

The Texas A&M straddle packer (TSP) was then assembled in the dual-element configuration. Two stands of drill collars were run above the packer and the assembly was reentered.

When the BHA had been lowered completely into the casing, a pressure test of the surface equipment was conducted before the packer go-devil was dropped. The go-devil was pumped into place and the packer set easily. High permeability was indicated and three pulse tests were followed by three constant-rate injection tests.

Weather/motion conditions were excellent and the go-devil was retrieved while the packer remained set. While the downhole instrument data were read to determine whether further tests were needed, the sinker bars were lowered into the perforated liner to check for fill. About 5.5 m of fill was found in the liner.

The downhole pressure recorders were attached to a second go-devil for deployment to the packer. Upon landing of the go-devil, the TSP could not be set, with the failure apparently caused by either a leaking element or leaking go-devil seals. The second go-devil was recovered and the recorders were switched to the first-run go-devil (with its original seals). A good set then was obtained and further constant-rate injection tests were conducted for 4 hr. After the packer had been deflated and the go-devil recovered, it was discovered that the electronic downhole recorder had malfunctioned and no usable data had been collected on the second run.

Before the drill string was tripped, a deviation survey of the hole was conducted. The survey determined that the maximum hole deviation was 2° from vertical, and also found that hole fill had increased to 9.5 m during the 7 hr since the earlier sounding.

Two stands of drill collars were used as a BHA for the CORK installation, and the assembly was run to reentry depth. After a smooth reentry, the string was spaced out with the CORK a few meters above the cone.

More than 4 hr were required to deploy the thermistor string, which had been doubled and redoubled to shorten it to 122 m in length (Fig. 5). The thermistor string and data logger were run into place with the coring line, the data logger was latched into the CORK, and the overshot tool was sheared off and retrieved. When the CORK had been landed on the casing hanger, a ball was pumped down the drill string to blank off the bore and set the CORK latch hydraulically. An overpull of 20,000-lb verified latch-in. The landing platform for the remotely operated vehicle was bolted around the drill string and launched through the moon pool to free-fall to the cone.

Hole 892D

Hole 892D was spudded after "feeling for bottom" and noting a reaction of the weight indicator at 670.3 mbsl. Core 146-892D-1X recovered only 12 cm of sediment. Average recovery for Cores 146-892D-2X to -4X was 34% and all cores contained gas hydrates and gave high H₂S readings. Core recovery improved in Cores 146-892D-6X to -9X with no more H₂S but considerable quantities of hydrocarbon gas as in Hole 892A. The WSTP runs were made at 54 and 77

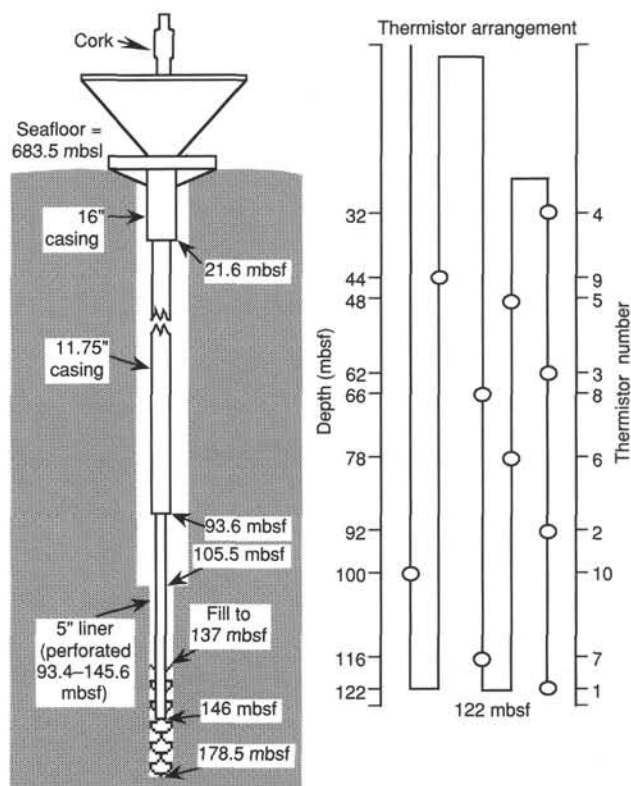


Figure 5. Schematic diagram of CORK deployment and thermistor-string configuration in Hole 892B.

mbsf. The interval from 77 to 100 mbsf was drilled without coring. Continuous XCB coring then proceeded to TD at 166.5 mbsf with interruptions for WSTP runs at 109.5, 128.5, and 147.5 mbsf.

The hole was displaced with mud and plugged with cement in a manner identical to that at Hole 892A. The bit then was pulled clear of the seafloor and the rig was offset 6 m east.

Hole 892E

Weight indication during the spud of Hole 892E was not noted until 674.3 mbsl (the same as for Hole 892A). As spacing was awkward, the core was "overdrilled" to 13 mbsf before it was recovered and the blocks were kept low to avoid pulling the bit above the seafloor during recovery. Core recovery in Core 146-892E-1X was 3.2 m and the core catcher contained gas hydrates.

With the presence of hydrates confirmed, the PCS was run next in an attempt to recover hydrates under in-situ pressure. Hydrogen sulfide precautions remained in effect as the PCS was brought on deck, but again only water under pressure was recovered.

The hole was then drilled to 33 mbsf with a WSTP run at 30 mbsf. Two consecutive APC cores then were attempted, primarily for the purpose of temperature measurements with the ADARA shoe. Though stroke was incomplete, surprisingly good penetration was made into the stiff sediment and 12.2 m of gassy sediment was recovered in the two cores. Liner failures occurred on both cores, with the second seriously affecting the condition of the core. Following another WSTP run and 3-m drilled interval, the APC-deployed lateral stress tool (LAST-I) was deployed. The LAST-I was "fired" from a depth of 55 mbsf into quite firm sediment. Data were recorded for about 1.5 hr before the drill string was raised to pull the LAST-I from the sediment. No overpull was noted. Upon recovery, no core was recovered and the data reflected only bottom-hole conditions, indicating that no penetration had been achieved.

After the hole had been drilled ahead to 62 mbsf, a final WSTP run was made. The hole was pumped full of 12 lb/gal mud and the bit was pulled above the seafloor.

The VIT then was deployed for a final visual check of the seafloor and the Geoprops probe was run to the bit for in-pipe function testing. When the successful Geoprops tests had been concluded, the ship was maneuvered for a brief look at Hole 892E with the VIT, which verified that there was no fluid flow out of the hole.

With the allotted operating time running out, the drill string was recovered. The *JOIDES Resolution* departed Hole 892E at 2400 UTC, 17 November.

Sites 892–893, Santa Barbara Channel

The vessel ran a single, short tie-in seismic line over Hole 892B; the gear was retrieved and the ship turned south and increased speed to 11 kt.

Favorable weather conditions prevailed during the transit down the Oregon and California coasts to the operations area for Site 893 in the Santa Barbara Channel. Operations at Site 893 began at 1930 hr, 20 November.

LITHOSTRATIGRAPHY

Introduction

At Site 892 five holes were drilled, but only Hole 892A was cored fully (mainly by XCB), with penetration extending to 176.5 mbsf. Hole 892D penetrated 166.5 m with good recovery in the intervals not well recovered in Hole 892A. Hole 892E penetrated 62 mbsf and provided some additional data for the top part of the lithostratigraphic sequence. Considering the data from all the holes together, recovery of the entire stratigraphic section was good. Because the lithologic character of the sediments in the recovered interval is uniform, only one lithostratigraphic unit was identified (see master chart, Fig. 81). However, because of observed and inferred structural complexities, there are some differences in the lithologies recovered from the same depth below the seafloor in the adjacent Holes 892A and 892D. This complexity precludes a definitive summary of the stratigraphy at the site.

Unit I is a sequence of dark gray to very dark greenish gray fine-grained sediments, which are mainly terrigenous and hemipelagic clayey silt and silty clay. Most of the recovered sediments are firm and slightly fissile. In the lower part of the hole the sediment is weakly to heavily fractured. Original sedimentary structures are rare. Scattered bedding can be recognized from slight changes in grain size or color in the sediment, and is mostly subhorizontal to low dip (0° – 30°).

Unit I was divided in two subunits on the basis of the visual core descriptions, smear slide descriptions, grain-size analyses, and X-ray-diffraction (XRD) analyses. The variable recovery was better at the top of the hole, so that the character of Subunit IA is better defined than that of the underlying Subunit IB. In Hole 892A, the boundary between the two subunits falls at Section 146-892A-9X-1, 25 cm (67.75 mbsf), at the base of a cemented sandy layer, and corresponds with marked changes in the physical properties of the sediments (see "Physical Properties" section, this chapter). In Hole 892D, the boundary between the two subunits was placed between Cores 146-892D-8X and -9X (69.3 mbsf), where the characteristic sand layer was also found (see Hole 892A in Fig. 6).

Subunit IA contains a higher concentration of thin, terrigenous, and glauconitic sand layers and shows a downward increase of the mean grain size (from very fine silt to fine silt) toward the subunit boundary with Subunit IB. The lower interval of the subunit (Cores 146-892A-6X to -8X; 48.5–66.8 mbsf) is also characterized by a higher concentration of biogenic silica. The sediments of Subunit IA are slightly disturbed by fracturing and gas cracking.

Subunit IB shows a scattered and irregular distribution of mean grain size and contains fewer sandy layers, substantially less glaucony, and less biogenic silica. Subunit IB is intensely disturbed by fracturing and stratal disruption at several intervals.

Lithostratigraphic Units

Subunit IA

Intervals: Hole 892A, Core 146-892A-1X to Section -9X-1, 25 cm; Hole 892D, Cores 146-892D-1X to -8X; Hole 892E, Cores 146-892E-1X to -4H

Depth: Hole 892A, 0–67.75 mbsf; Hole 892D, 0–69.3 mbsf; Hole 892E, 0–52.0 mbsf

Age: early (?) to late Pliocene

Lithostratigraphic Subunit IA consists of very dark greenish gray to dark gray clayey silt (7.3GY 3.1/1.3 to 2.0GY 3.1/1.3) interbedded with rare layers of fine sand and coarse silt. The dominant grain size in the clayey silts is fine to very fine silt (Fig. 7; see also "Grain Size" summary, this section). Thin (1- to 2-cm-thick), greenish black (7.9GY 2.4/1.5) layers of glaucony sand are found at a number of intervals. Scattered layers and dispersed patches of quartzofeldspathic sand are also present, but they do not form a significant proportion of the sediment.

The major components of the clayey silts, which form the bulk of the subunit, are clay minerals, quartz, and feldspar. The biogenic component (mainly siliceous microfossils) mainly ranges between 5% and 15% (rarely 30%–40%; Fig. 8). In the silts near the base of Subunit IA, most of the silt fraction consists of biogenic silica (diatoms, sponge spicules, and radiolarians; Fig. 9). The clayey silt displays bedding on a 1- to 10-cm scale, defined by slight color changes and by the occurrence of centimeter-size sandy layers or patches. At the top of the subunit (Cores 146-892A-1X through -3X; 0–23.2 mbsf), the sediments are silty clays with subordinate clayey silts. In Section 146-892A-1X-1 (0–1.5 mbsf), the silty clays host up to 20% glaucony pellets and grains.

The XRD studies show that quartz, feldspar, and clay minerals are present throughout the subunit. The main clay minerals present are chlorite, illite/mica, and mixed-layer clays, with a minor amount of kaolinite. A change in the clay mineralogy occurs with depth toward more mixed-layer clays and a lesser proportion of well-crystallized phases (chlorite and illite/mica) at the base of the subunit (Fig. 10). This change is accompanied by fluctuations in the amount and types of feldspars, and the amount of quartz relative to clay minerals. These latter changes may be a product of the different grain sizes of the samples that were analyzed.

Patches of olive gray carbonate-rich silt are present throughout the subunit (Sections 146-892A-1X-1, 18–20 cm; -6X-CC, 10–24 cm; and -7X-3, 10–13 cm, 25 cm, 39–42 cm, and 143 cm; Fig. 11). Smear slide observations show that these silts are of three types. Clayey silts with 20%–60% crystalline carbonate (small granules, needles, or laths) are present in Samples 146-892A-2X-1, 16 cm; -3X-1, 119 cm; -6X-1, 65 cm; -6X-3, 42 cm; -8X-5, 14 cm; and 146-892D-4X-1, 145 cm. Pure carbonate silt occurs in a 2-cm-thick layer at Section 146-892A-7X-3, 55–57 cm (53.6 mbsf) and in a 1-cm layer at Section 146-892D-6X-3, 87 cm (50.8 mbsf). The third type of calcareous sediment is nannofossil ooze, consisting of up to 60% nannofossil tests in a matrix of clayey silt. Carbonate ooze layers are present in Sections 146-892A-8X-1, 25–26 cm and 87–88 cm. Less concentrated layers of nannofossil silt were found in Cores 146-892D-4X to -7X (27.5–61.6 mbsf). It is possible that at least some of the granular carbonate-rich silts were originally deposited as a biogenic ooze component in the sediment and have been recrystallized by diagenesis.

Many of the sands in Subunit IA are glauconitic. The glaucony sand occurs either as 1- to 3-cm-thick layers (Sections 146-892A-1X-1, -3X-1, -6X-2 to -4, and -7X-4 to -CC, and abundant in Cores 146-892D-3X to -7X) or as patches approximately 1 cm in size (Fig. 12). Otherwise, glaucony grains are dispersed apparently homogeneously in the clayey silt. The glaucony pellets are dark green and of fine- to medium-sand size, commonly with a rim of pale green clay and pyrite (Fig. 13). The paragenesis of the glaucony is similar to that observed at Site 889. The type of glaucony determined from XRD is also similar

(a mixed chlorite-smectite; Fig. 10D). In view of its abundance and paragenesis, at least some of the glaucony is thought to have formed in situ in the sediment, whereas the remainder, if transported, is not considered to be far-traveled.

Sands consisting of quartz, feldspar, and lithic fragments, rather than mainly of glaucony grains and clay pellets, are present throughout the subunit, but are thin and poorly defined (the bedding is diffuse). Where sand occurs in Subunit IA, it is always mixed with clay and silt and has a high proportion of quartz and feldspar, with an appreciable amount of mica, clear volcanic glass (Fig. 14), and carbonate. Layers of typical silty sand and sand-silt-clay are found at Sections 146-892D-4X-1, 84 cm (28.3 mbsf), 146-892A-7X-7, 18 cm (57.6 mbsf), and 146-892D-8X-2, 132 cm (64.5 mbsf). Other components in the sands are altered rock fragments (typically 4%–10% of the sediment), pyroxene (1%–5%), and amphiboles (1%–10%). Heavy minerals, and accessory minerals such as epidote and garnet, are present in amounts up to 2%. Opaque grains are common in sands and also in silts. On the basis of the XRD analyses, the opaque component is thought to consist mainly of pyrite.

A thick layer of quartzose sand is found at the base of the unit in Section 146-892A-9X-1, 3–20 cm. It is 10–15 cm thick, with a disturbed upper part and a sharp base. At the same depth in Hole 892D (at the base of Section 146-892D-8X-CC; 69.3 mbsf), where recovery was more complete, a corresponding sand layer was recovered. The sand in this interval is micaceous (white mica and brown biotite form 7%–15% of the sediments in the four smear slides taken).

Layers of silt rich in colorless volcanic glass, which are interpreted as ash layers, are present in Cores 146-892D-5X and -6X (37.0–54.0 mbsf).

Carbonate cementation (Figs. 15–16), occurring as irregular and rounded lumps up to 4 cm across, is common in Cores 146-892A-3X to -9X (19.0–68.6 mbsf) and 146-892D-4X to -8X (27.5–69.3 mbsf). These cemented lumps are thought to be in-situ occurrences (cemented layers and concretions) as they enclose sediment grains similar to the surrounding host material. The concretions are developed preferentially in intervals rich in sand and pelletal glaucony. In addition to these in-situ occurrences, carbonate-cemented sediments are also found as fragments. These are either true sedimentary clasts or are reworked from drilling. The latter interpretation is favored, as the fragments are more common at the top of cores (e.g., Core 146-892A-7X), and so are most likely to be fill from hole caving. In the interval 60.1–67.5 mbsf (best recovered in Core 146-892D-8X), carbonate cementation particularly affects sandy lithologies.

Gas hydrates were observed in the core catchers of Cores 146-892A-1X and -2X and at the top and bottom of Sections 146-892A-1X-4 to -2X-3 as they were cut on the catwalk. In Cores 146-892A-1X to -3X (0–28.5 mbsf), the sediments are generally soft, “soupy,” or “mousse-like” in texture. Hydrates were also directly observed from the adjacent holes in Cores 146-892D-2X to -3X and 146-892E-2X to -4X. Soupy intervals, presumably related to the sublimation of the hydrates from the sediment (see “Lithostratigraphy” section, “Sites 889/890” chapter, this volume) are present in Subunit IA from Cores 146-892A-1X to -8X (0–66.8 mbsf), 146-892D-4X (27.5–31.9 mbsf), and 146-892E-1X (0–3.2 mbsf) (Fig. 17). The distribution of soupy layers in the sediment, and the relationship with the occurrence of gas hydrates, is discussed subsequently.

The firm sediment that occurs from Section 146-892A-4X-1 downward is fragmented in millimeter- or centimeter-sized angular pieces. Subhorizontal cracks, thought to be gas expansion fractures, are common in the firmer sediments. The rare indicators of bedding suggest generally shallow dips (subhorizontal to 30°).

The lower boundary of Subunit IA is defined as the base of a thick zone of stratal disturbance, at a depth of about 68.0 mbsf. In Section 146-892A-9X-1, this zone lies at 67.75 mbsf, immediately below a 25-cm-thick indurated sand layer (Fig. 18). In Hole 892D the boundary of the disrupted interval is less clearly defined, and the base of Subunit IA was picked at the base of Section 146-892D-8X-CC (69.3

mbsf). Below this interval, the mean grain size of the sediment decreases and the visual estimates of biogenic silica and carbonate contents decrease (Figs. 7–8 and 16). The content of glaucony in the sediment is also generally lower in Subunit IB (Fig. 19). A discontinuity in the bulk density and porosity profile falls at this boundary (see “Physical Properties” section, this chapter).

Subunit IB

Interval: Hole 892A, Section 146-892A-9X-1, 25 cm, to Core 146-892A-21X; Hole 892D, Cores 146-892D-9X to -16X

Depth: Hole 892A, 67.75–176.5 mbsf; Hole 892D, 69.3–166.5 mbsf

Age: early (?) to late Pliocene

Lithostratigraphic Subunit IB is composed of clayey silt with scattered silty clay and very fine sand. Colors range from very dark greenish grays and olive grays to dark grays (about 8.0GY 4.0/1.5 to about 2.0GY 2.6/1.2). The sediment is mostly firm, fissile, and fractured, without sedimentary structures.

For the most part, the recovered sediment is fragmented into millimeter- to centimeter-size angular pieces, making recognition of original sedimentary structures difficult. Load-cast structures were observed in Section 146-892A-9X-1, 50 cm, where a 15-cm-thick silty layer overlies very fine calcareous silt (Section 146-892A-9X-1, 30–51 cm; Fig. 20). Scouring, sag structures, load casts, and small mud clasts at the base of a hemipelagic layer have been observed in Section 146-892A-9X-1, 46–65 cm (Fig. 21). Sporadic bedding laminations, defined by subtle grain-size and color differences, were observed in Cores 146-892A-14X and -15X (106.8–125.0 mbsf).

The major components in the sediments of Subunit IB are clay minerals, quartz, and feldspar. Volcanic glass is common in silts and sands, ranging from 2% to >14% in Core 146-892D-14X (138.0–147.5 mbsf). Opaque grains, mostly sulfides in cubic and framboidal forms, are common in sediments of all grain sizes. The presence of pyrite is confirmed by XRD studies. In the rare sands present, quartz and feldspar are accompanied by mica, both white and brown varieties, pyroxenes, green amphibole and volcanic glass. Other accessory minerals are rare garnet, epidote, rutile, and zircon.

Glaucony is present in Cores 146-892A-11X and -13X and in Cores 146-892D-10X and -15X either as diffused black sandy patches or dispersed in the clayey silt. The glaucony in Subunit IB is in general softer and less mature in appearance than that found in Subunit IA.

The biogenic component (foraminifers, nannofossils, diatoms, radiolarians, and sponge spicules) ranges from 5% to 20%. Several small intervals occur in which the sediment is composed primarily of clays and diatoms, with little terrigenous silt (e.g., Samples 146-892A-18X-1, 95 cm; -20X-1, 20 cm; and -20X-2, 135 cm; Fig. 8). One layer of clay with 20% nannofossil content occurs in Subunit IB (Section 146-892A-12X-1, 19 cm; 87.7 mbsf).

The sediments are, in general, too fine grained to possibly identify all the mineral components in the smear slides. However, considering only the sands and coarse silts, no consistent changes in sediment composition with depth can be identified. The XRD studies show that quartz, feldspar, and clay minerals (chlorite, illite/mica, and mixed-layer clays, with a minor amount of kaolinite; Fig. 22) are present throughout the subunit, but the relative proportions change quite markedly. Most of these changes can be related to the different grain sizes of the samples, and no clear change occurs in the background clay mineralogy with depth.

Layers of olive gray silt composed of microgranular carbonate are present in Sections 146-892A-9X-1, 51–53 cm (70 mbsf) and -17X-2, 65 cm (137.2 mbsf) and in Sections 146-892D-10X-5, 100 cm (108.5 mbsf), -12X-1, 15 cm (119.2 mbsf), and -12X-3, 87 cm (123.4 mbsf). Carbonate silt is found as patches, rather than continuous layers as elsewhere in the subunit, throughout Cores 146-892A-11X to -13X (78.0–106.5 mbsf) and -19X (154.0–163.5 mbsf) and as disrupted layers in Sections 146-892A-15X-1, 38 cm (116.38 mbsf; Fig. 23), -18X-1, 59–62 cm (145.1 mbsf), and -16X-4, 17 cm (163.2 mbsf). In

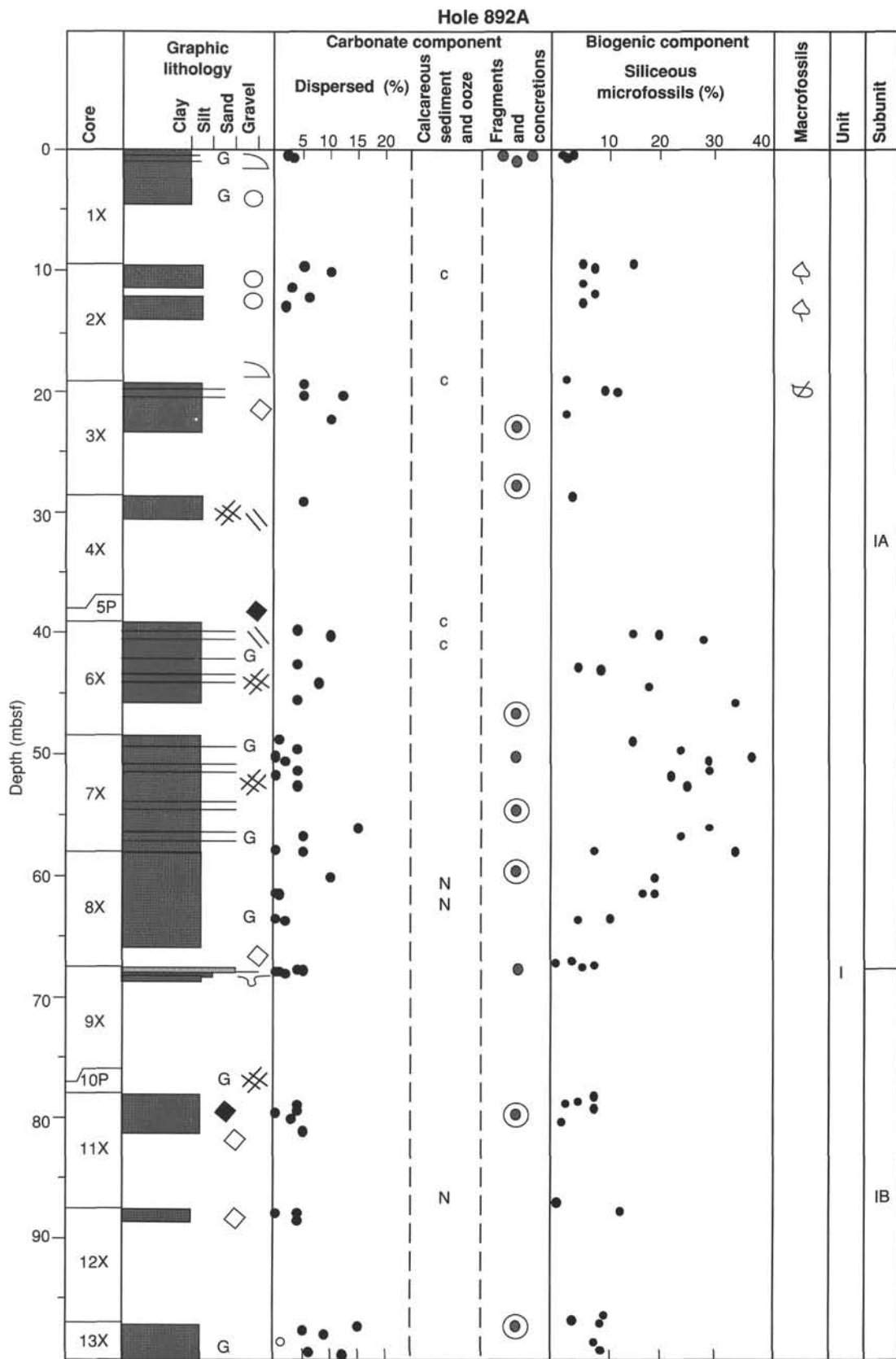


Figure 6. Graphic lithologic representation of Holes 892A and 892D. The distribution of the carbonate and biogenic components is shown to emphasize the difference between lithostratigraphic Subunits IA and IB.

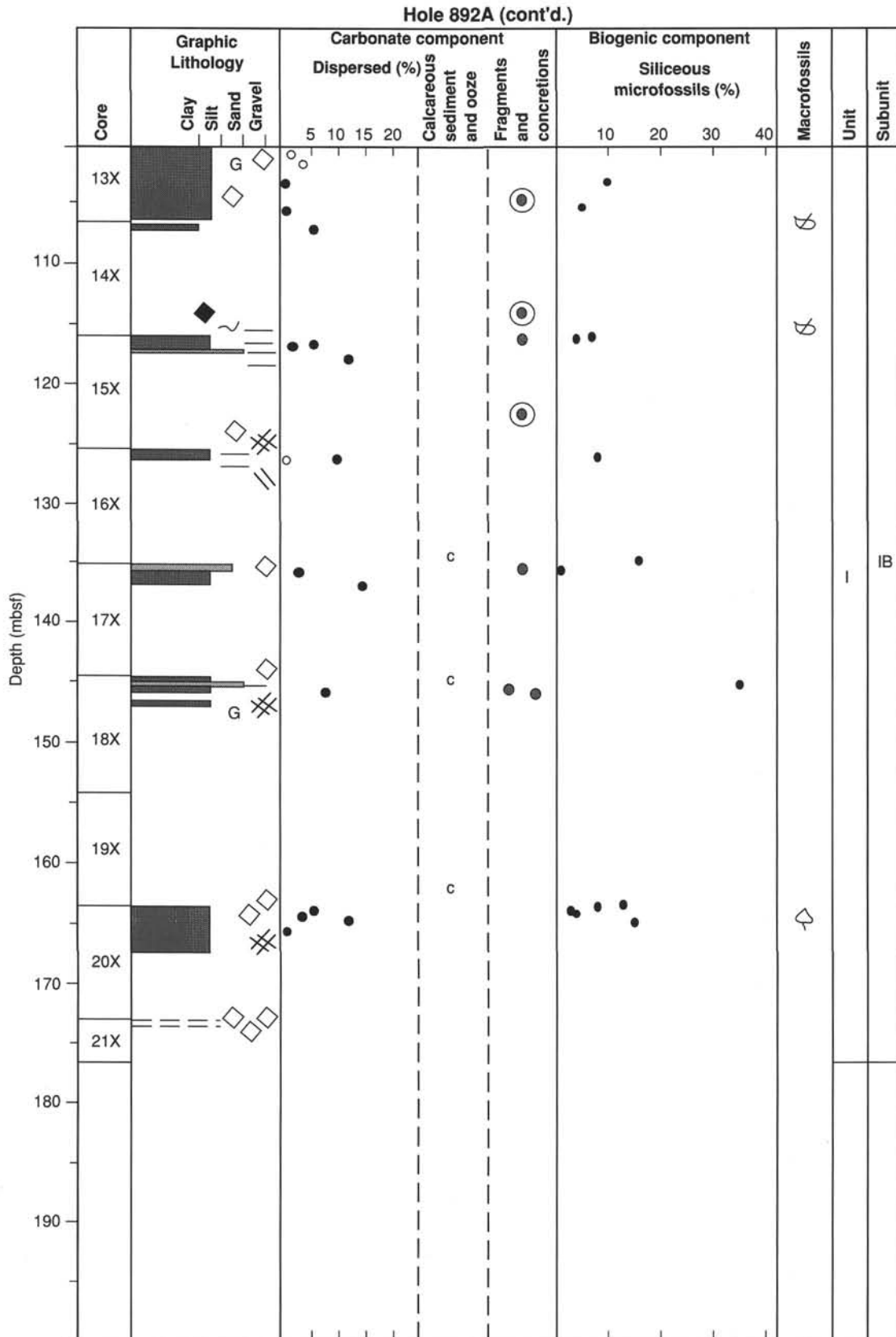


Figure 6 (continued).

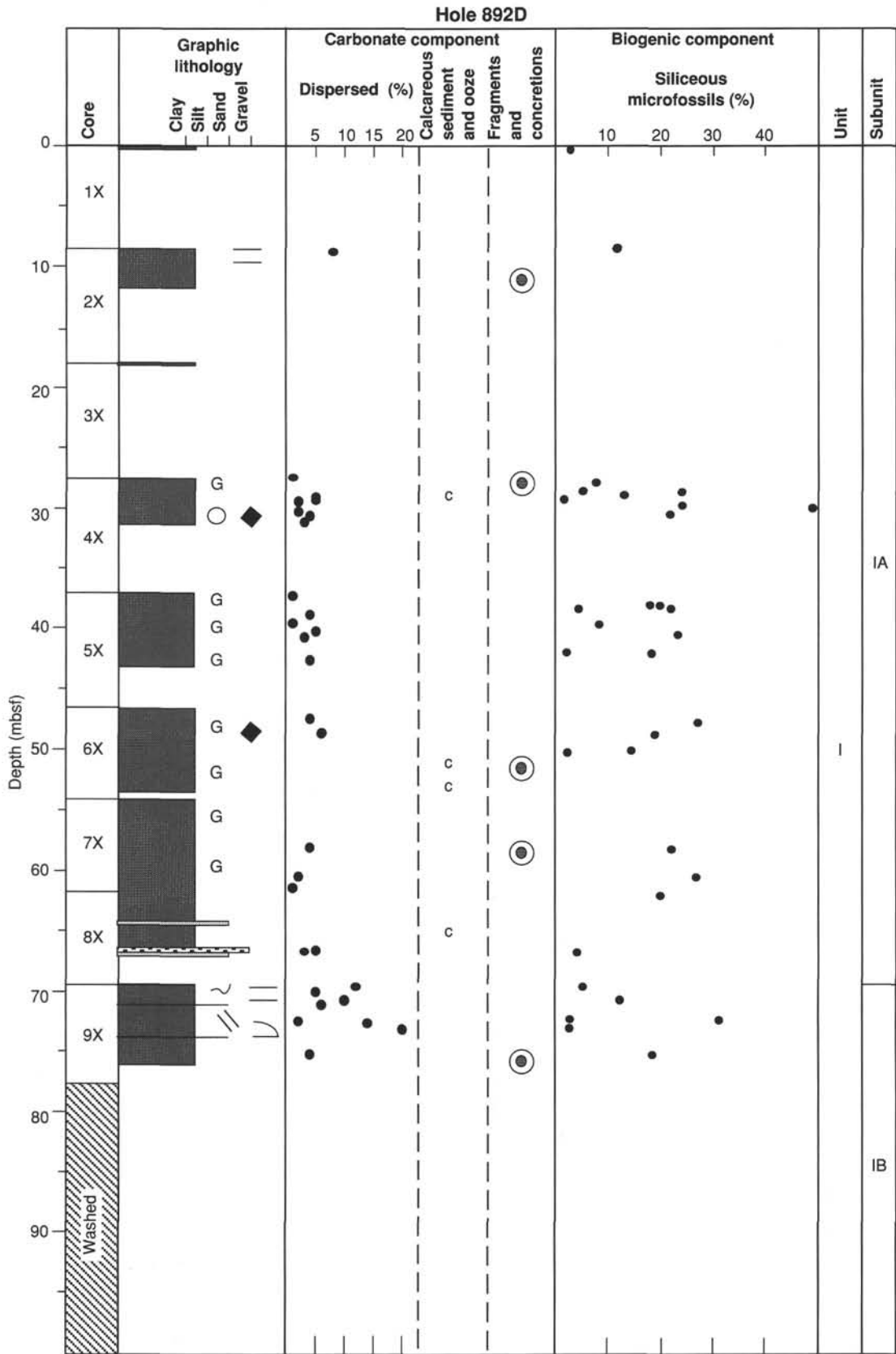


Figure 6 (continued).

Hole 892D (cont'd.)

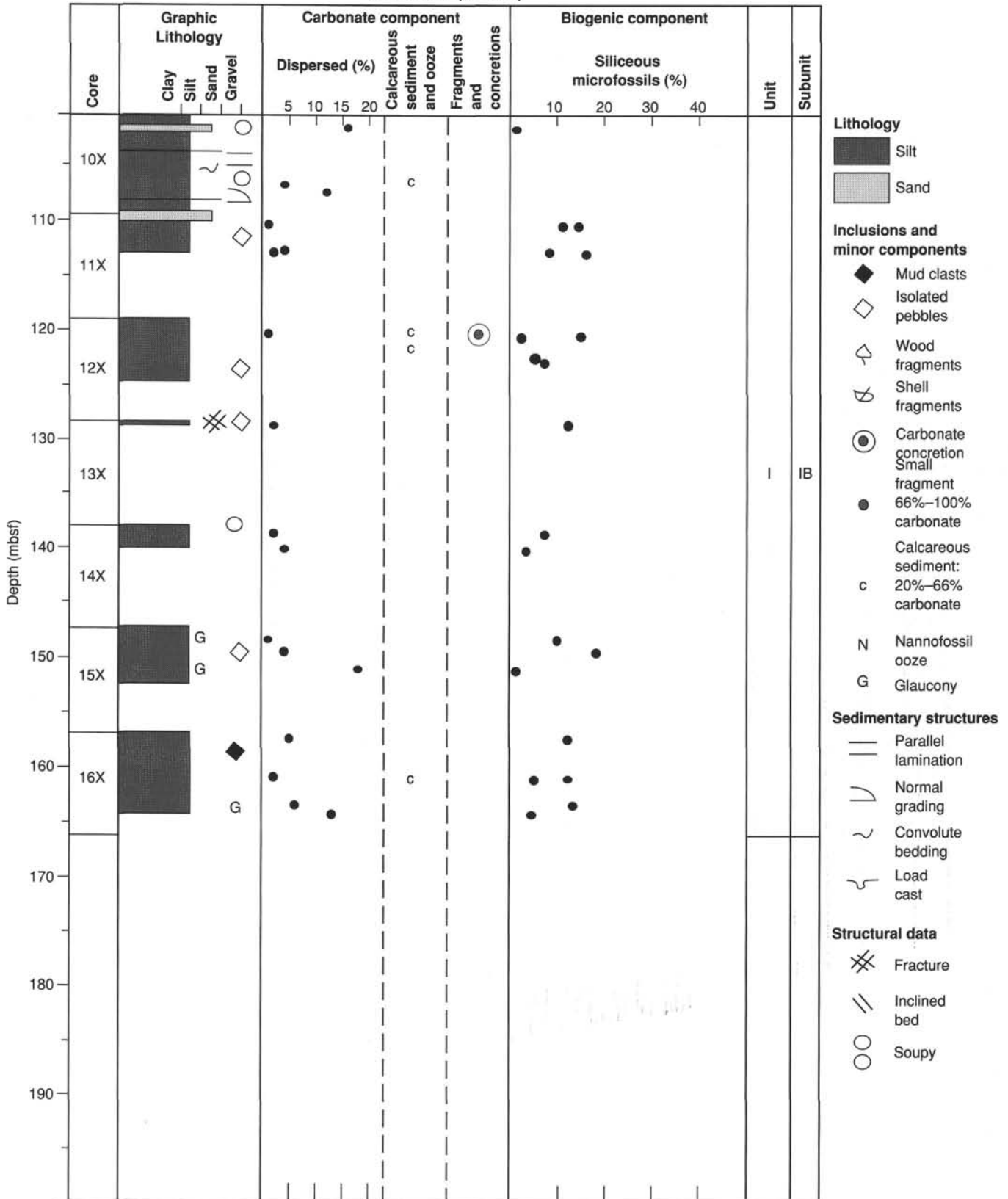


Figure 6 (continued).

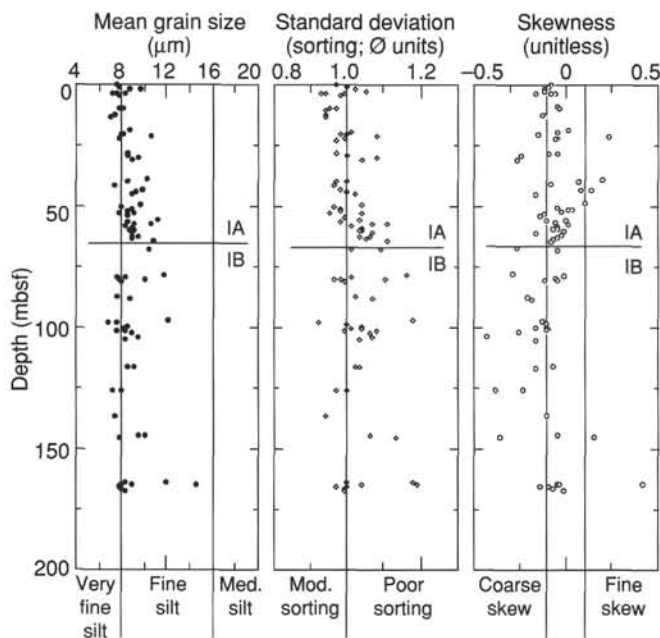


Figure 7. Results of shipboard grain-size analysis on the fine fraction of the sediment. Mean size, sorting, and skewness indicate a different grain population between Subunits IA and IB.

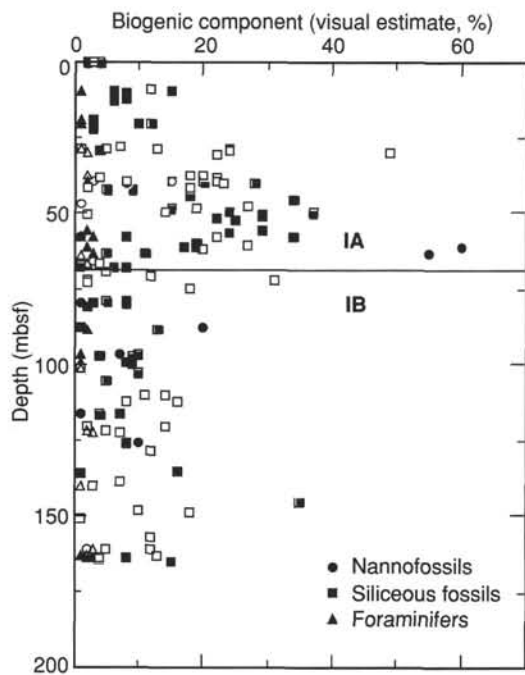


Figure 8. Distribution of the biogenic components with depth in Holes 892A and 892D (determined from smear slides). Filled symbols = Hole 892A, and open symbols = Hole 892D.

Hole 892D, carbonate-cemented silt occurs in thin layers, streaked patches, and as subrounded concretions throughout the recovered part of Subunit IB and as thin layers (up to 8 mm thick) in Cores 146-892D-9X, -10X, -12X, and -15X.

A heavy mineral silt layer, consisting mainly of opaque grains (probably the spinel group with pyrite) is present at Section 146-892D-10X-2, 50 cm (102.0 mbsf).

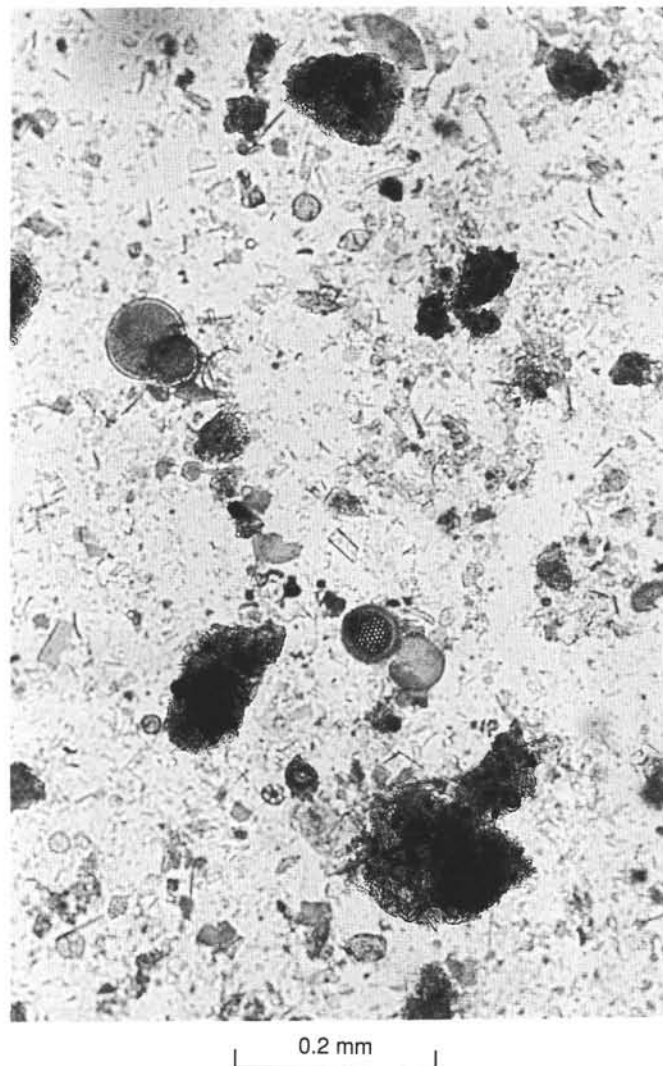


Figure 9. Photomicrograph of siliceous microfossils: diatoms, radiolarians, and sponge spicules in a pelletal clayey silt (Sample 146-892A-7X-1, 145 cm).

Centimeter-size fragments of dolomite-cemented silt and carbonate concretions are present in Cores 146-892A-11X to -15X (78.0–97.0 mbsf), -18X (144.5–154.0 mbsf), -20X (163.5–173.0 mbsf), and -21X (173.0–176.0 mbsf). Similar concretions and carbonate-cemented silt fragments are present in Cores 146-892D-4X, -6X, -7X, -9X, -10X, and -12X (27.5–128.5 mbsf). The sediment disruption makes the identification of in-situ concretions difficult, but two cemented sediment layers are present in Core 146-892A-18X, in which host sediment grains, including glaucony, are included by the concretion. The tops of Cores 146-892A-9X, -14X, -18X, -20X, and -21X contain hole fill composed of rounded carbonate concretions and pebbles of firm, partially cemented sediment.

The percentage of carbonate grains and cement in the sediments fluctuates throughout Subunit IB but shows no trend with depth. Carbonate contents generally range up to 15%, rarely exceeding 40%. The proportion of carbonate estimated in both subunits from smear slides correlates well with that determined by chemical analysis. However, fluctuations in carbonate content could not be detected by XRD studies: no calcite was recognized, and a weak reflection from dolomite was produced by almost all samples. This discrepancy is possibly a result of peak masking by feldspars, which have reflections in the same range as calcite.

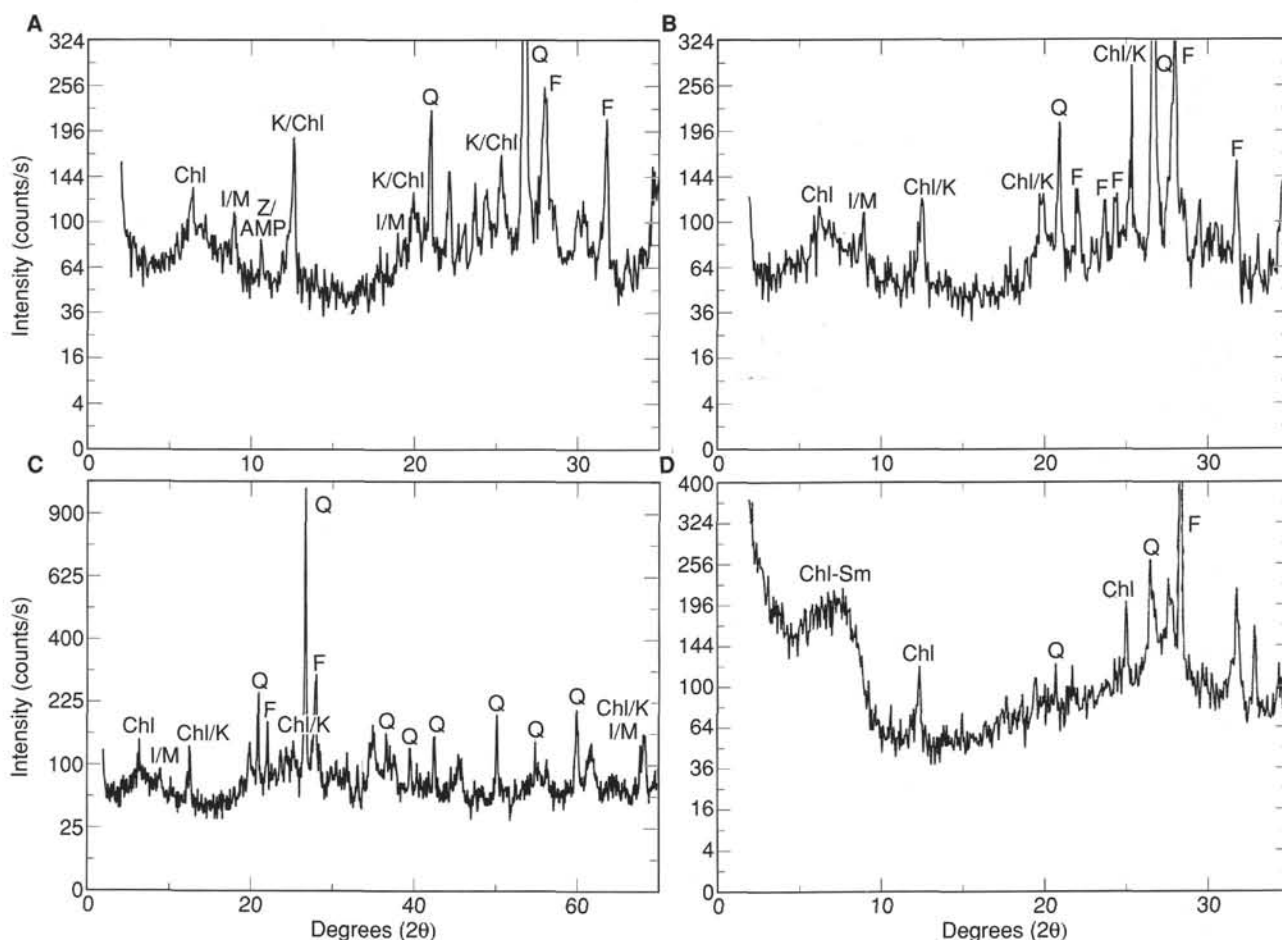


Figure 10. Results from XRD measurements. **A.** Typical clay from the upper part of Subunit IA (Sample 146-892A-1X-1, 109–110 cm). The main minerals present are quartz and feldspars, with highly crystalline chlorite and illite/mica in the clay assemblage. **B.** Typical clay from the middle part of Subunit IA (Sample 146-892A-4X-1, 73–74 cm). The main minerals present are quartz and feldspars, with chlorite and illite/mica, and lesser amounts of kaolinite and mixed-layer minerals in the clay assemblage. **C.** Typical clay from the basal part of Subunit IA (Sample 146-892A-7X-6, 8–9 cm). The main minerals present are quartz and feldspars, with mixed-layer clays, a little chlorite, and a trace of illite/mica in the clay assemblage. **D.** Typical glaucony-rich clayey silt (Sample 146-892A-6X-1, 59–60 cm). Chl = chlorite, I/M = illite/mica, K = kaolinite, Q = quartz, F = feldspar, Z/amp = zeolite/amorphous phase, and Sm = smectite.

At the top of Subunit IB, in Core 146-892A-9X, the sediment is firm, unfractured, and disturbed only slightly (probably by gas expansion). In Cores 146-892A-11X and -13X (78.0–106.5 mbsf), the sediment is composed of an alternation of layers (from 20 cm to about 1 m thick) of firm and soft clayey silt. The boundaries between layers are outlined by slight color changes. The few indications of bedding suggest generally shallow dips (subhorizontal to 20°). Below this level the sediment is consistently firm but more heavily fractured, and intervals of intense disruption are present. In Cores 146-892A-15X (116.0–125.5 mbsf) and -18X (144.5–154.0 mbsf) slickenlines, polished surfaces, and shear zones indicate intense deformation attributed to drilling enhancement of original tectonic disturbance (see “Structural Geology” section, this chapter). In Hole 892D, the sediments generally show the same pattern of deformation, but with more intense development. This is in part because coring was targeted at fault zones in this hole. Nevertheless, the interval of intense disruption at the top of Subunit IB is thicker in Hole 892D, extending at least down to the base of Core 146-892D-9X (77.0 mbsf).

Grain Size

The result of 85 grain-size analyses performed on the fine sediment fraction visually identified in cores from Hole 892A provides additional support for the subdivision of Unit I into two subunits. The

distribution with depth of the mean grain size (Fig. 7A) shows an increase of the mean size, from about 7 μm at the top of the hole to about 10 μm at the base of Subunit IA, which matches the occurrence of thin layers and patches of glaucony sand in Cores 146-892A-6X, -7X, and -8X. The standard deviation (a measure of the sorting; Fig. 7B) also shows a general decrease from moderate to poor sorting with increasing depth in Subunit IA. Scattered values, leaning toward poor sorting, are characteristic of Subunit IB. Skewness (Fig. 7C) clearly indicates symmetric distribution, or fine skewing, in Subunit IA and coarse skewing in Subunit IB.

A difference in grain-size populations corresponding to the two subunits is indicated by the distribution of the silt grain-size classes (Fig. 24). In particular, very fine silt and medium silt identify a major break at the boundary between the two subunits.

Sedimentological Evidence of Gas Hydrates

At Site 892 hydrates were recovered in Cores 146-892A-1X and -2X, and we had the opportunity to observe and describe the disturbance induced in the sediment texture by the dissociation of the gas hydrates. The observations of the sediments of this site support the inferences drawn at Site 889, where no direct observation was available of the gas hydrates in the sediments (see “Lithostratigraphy” section, “Sites 889/890” chapter, this volume).

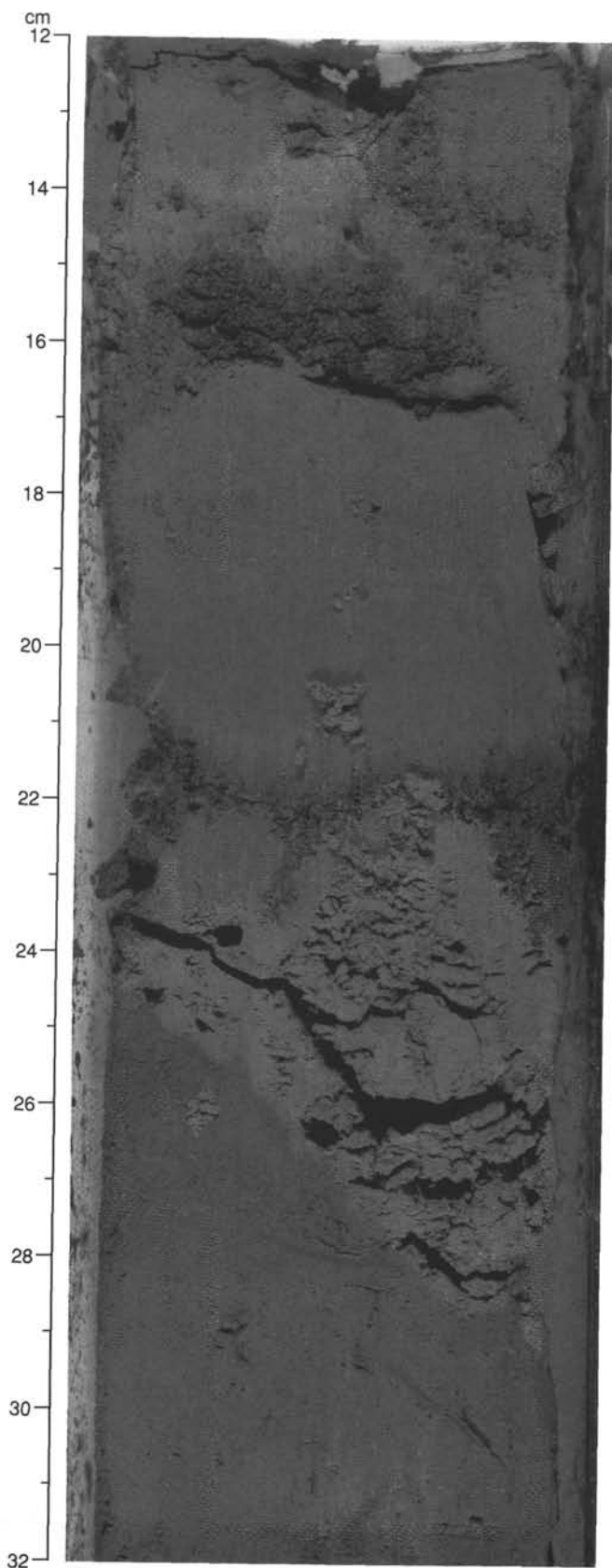


Figure 11. Undisturbed sediments containing clayey silt interbedded with glaucony sand (darker layer) and olive gray, calcareous silt (lighter layer) in Section 146-892A-1X-1, 12–32 cm.

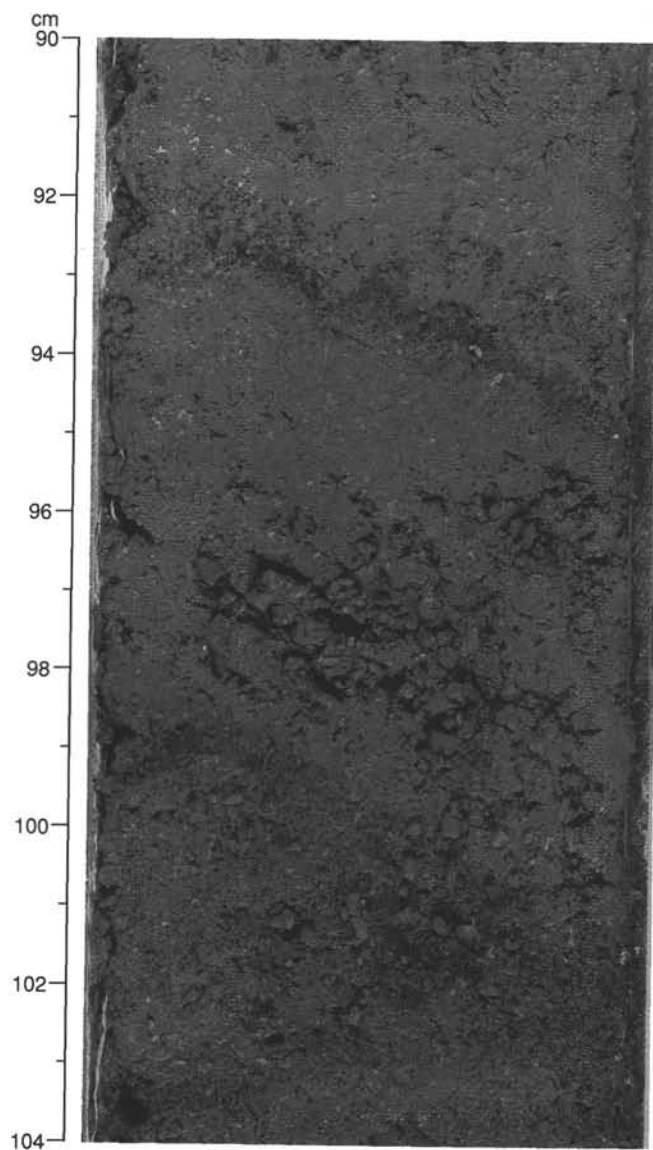


Figure 12. Inclined layers of glaucony sand in fractured clayey silt in Section 146-892-6X-2, 90–104 cm.

Sediments in Cores 146-892A-1X and -2X are characterized by sediment disturbance that we distinguish in two prevalent types, called soupy and mousse-like disturbed textures (Fig. 25).

Soupy sediments are watery homogeneous sediments with uniform color; many are completely fluidized. They are usually associated with core voids because they can easily flow away from their original position during core recovery (Fig. 26).

Mousse-like sediments are homogeneous, soft, cohesive sediments, easily deformable with the slight pressure of one finger, and commonly contain gas vesicles. The stiffer mousse-like sediments show a characteristic apparently foliated texture produced by the core-cutter wire during core splitting. Mousse-like sediments are also associated with gas expansion fractures.

Soupy and mousse-like sediments were found not only in the uppermost two cores, where the hydrates were observed, but also in deeper cores down to about 60 mbsf (Core 146-892A-8X; Fig. 17). Although this is still several tens of meters above the projected depth of the base of the stability field of a pure water–pure methane hydrate (approximately 120 mbsf; see “WSTP and ADARA Temperature Measurements” section, this chapter), it is close to the depth of the



Figure 13. Photomicrograph of a patch of glaucony sand, with pyrite alteration on glaucony pellets (Sample 146-892A-6X-1, 55 cm).

BSR (73 mbsf; see “Downhole Logging” section, this chapter). The thickness of the disturbed layers (as at Site 889) is typically less than 1 m (less than 0.6 m at Site 892). The composition of the sediments above and below these layers does not show any particular characteristics that can be related to their preferential fluidization, and ship-board grain-size analyses indicate that no correlation exists between soupy or mousse-like intervals and intervals of coarse sediment size. Contamination by drilling mud can be ruled out because pumping of mud began only in Core 146-892A-14X (106.5 mbsf).

The correlation between the soupy and mousse-like sediments and the gas hydrate is further supported (analogously to Site 889) by the chemical composition of the interstitial water, which indicates dilution by fresh water possibly derived from the dissociation of the hydrates during core retrieval.

The occurrence of carbonate concretions at Site 892 does not relate to the position of the soupy and mousse-like intervals (Fig. 17). Post-cruise carbon- and oxygen-isotopic analyses will help to determine whether any relationship exists between the formation of concretions and the presence of gas hydrates in the sediments.

Sedimentary Structures and Environment of Deposition

Most of the sediments at Site 892 are fine grained. The bedding and grading patterns, where preserved, display the general characteristics

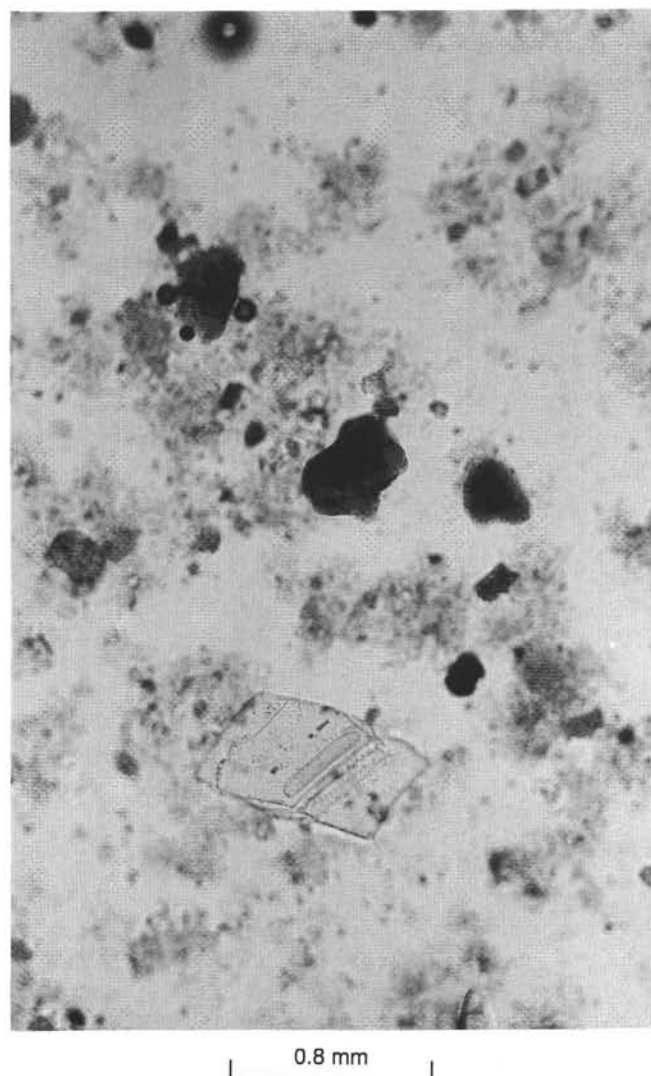


Figure 14. Photomicrograph of a large volcanic glass fragment in poorly sorted, medium-grained silty sand (Sample 146-892A-7X-7, 18 cm).

of deposition by dilute turbidity currents, interspersed with background hemipelagic sedimentation (the T_{ode} intervals of the classification of Bouma, 1962). This interpretation is supported by the composition of the sediments, which indicates relatively little terrigenous material and a high proportion of biogenic material.

Some of the layers considered to be of hemipelagic origin reach 10–12 cm in thickness. This is comparable to the thickness of the adjacent intervals considered to be turbidites. Alternatively, the sediment may have been transported by a combination of traction and saltation in bottom currents, rather than by turbidity currents. This combination of mechanisms could explain both the relatively large thickness of the hemipelagic layer (10–12 cm) and the presence of load cast structures at the base of the hemipelagic layers (Fig. 21).

Load casts are found at the top of Subunit IB (Section 146-892A-9X-1, 50 cm), where they mark a clear boundary between calcareous very fine silt (interpreted as a hemipelagic facies, possibly an altered nannofossil ooze) and terrigenous silt (interpreted as a distal turbidite facies). Some sag structures can be identified by thin black laminae, composed of microframboids of pyrite (Fig. 21).

Both load casts and sag structures are indicative of postdepositional liquidization of sediments. This process may have been responsible for the destruction of the soft, water-saturated, thin hemipelagic layers.

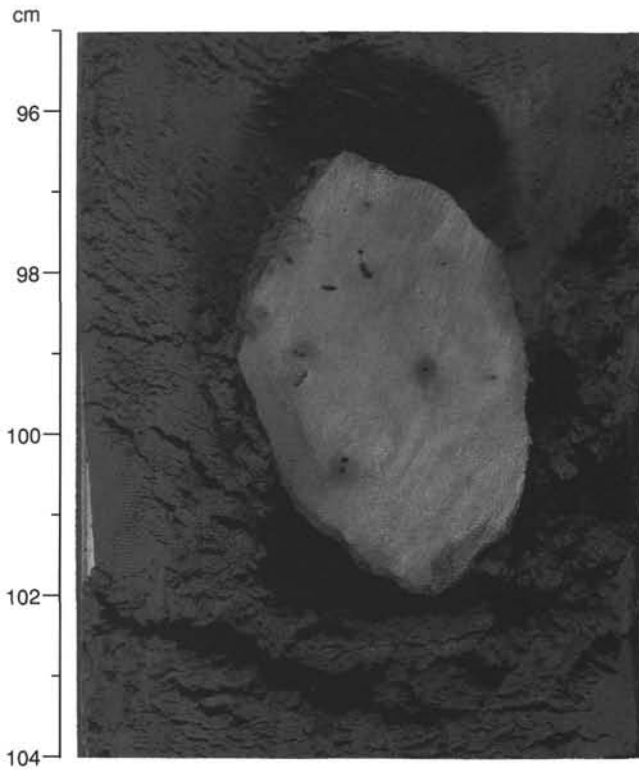


Figure 15. Carbonate concretions in Section 146-892A-3X-2, 95–104 cm.

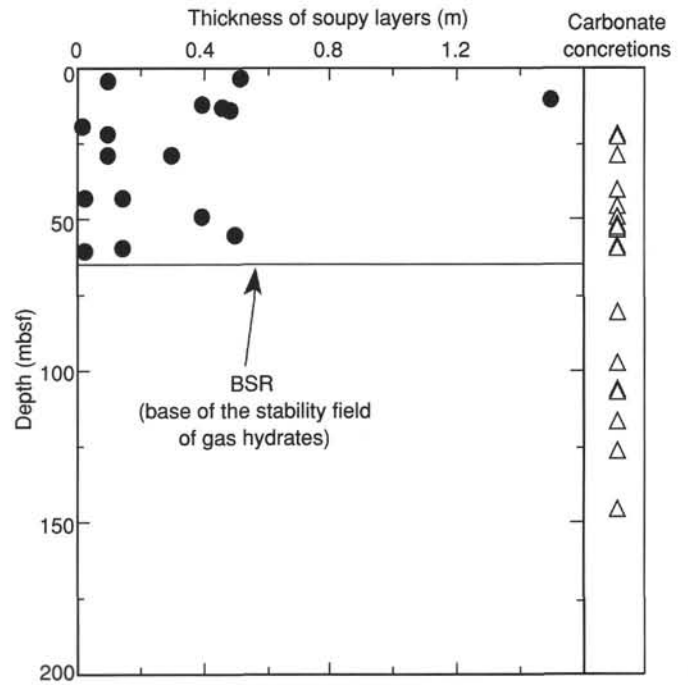


Figure 17. Distribution of soupy and mousse-like layers (circles) and carbonate concretions (triangles) with depth, based on the visual core description. Soupy and mousse-like layers do not occur below the depth of the BSR (73 mbsf). Carbonate concretions were also found below the hydrate stability field.

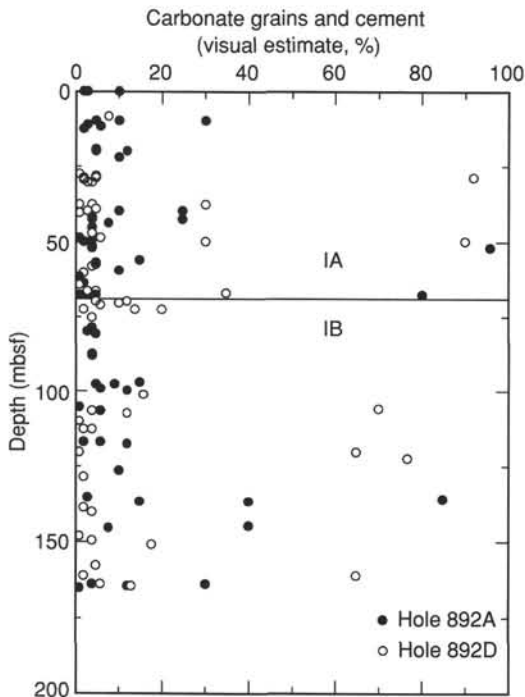


Figure 16. Distribution of carbonate grains and cement with depth in Holes 892A and 892D (determined from smear slides).

Highly deformed layers and patches of diffuse hemipelagic material (the olive gray sediments observed) may reflect this destruction.

Two different styles of sedimentation may have been operating to produce the sediments observed at Site 892. A background of hemipelagic sedimentation produced diatomaceous clays and silty clays,

with a small proportion of nanofossil ooze, against which influxes of terrigenous material occurred: mainly fine silts, but with rare sands. These were probably deposited by weak turbidity currents. One can speculate that the inflows were distal turbidity currents, which implies that the site lay far away from any slope, channel, or other source of terrigenous sediment.

No accumulation rates can be constrained for Site 892 using the available biostratigraphic data (see “Biostratigraphy” section, this chapter). The nature of the sediment, and the high proportion of biogenic material, including oozes, is typical of a low-sedimentation-rate environment. The presence of in-situ glaucony is also an indication of low sedimentation rate. Formation of the observed type of glaucony (immature mixed-layer chlorite/smectite) is thought to require thousands of years residence at the sediment/water interface (Odin, 1985).

Comparison with DSDP Site 174

At DSDP Site 174 (Leg 18), located on the Astoria Fan about 80 km to the east of Site 892 (Kulm, von Huene, et al., 1973), lithostratigraphic Unit 2 consists of thin beds of compacted, fissile silty clay with a thin basal silt or, rarely, a very fine sand interval. Individual beds range in thickness from 2 to 60 cm, but are generally 10–20 cm thick. The silty clay is commonly calcareous (calcareous mudstone) and the sands are carbonate cemented. Sedimentary structures identified were parallel- and cross-laminations, mud clasts, load casts, and bioturbated sediments. Unit 2 at Site 174 was correlated with the pre-Astoria Fan (Pliocene to late Pleistocene) seismostratigraphic unit and was interpreted as produced by fine-grained, abyssal-plain sedimentation (von Huene and Kulm, 1973) with accumulation rates ranging between 140 and 220 m/m.y.

The lithofacies recovered at Site 892 are similar in terms of grain size, bulk composition, and sedimentary structure to those recorded in Unit 2 at Site 174. The sedimentation rate at Site 892 cannot be well constrained because of the probable presence of hiatuses and faults in the sequence (see “Biostratigraphy” section, this chapter), but it is thought to be on the same order as Site 174, and the depositional

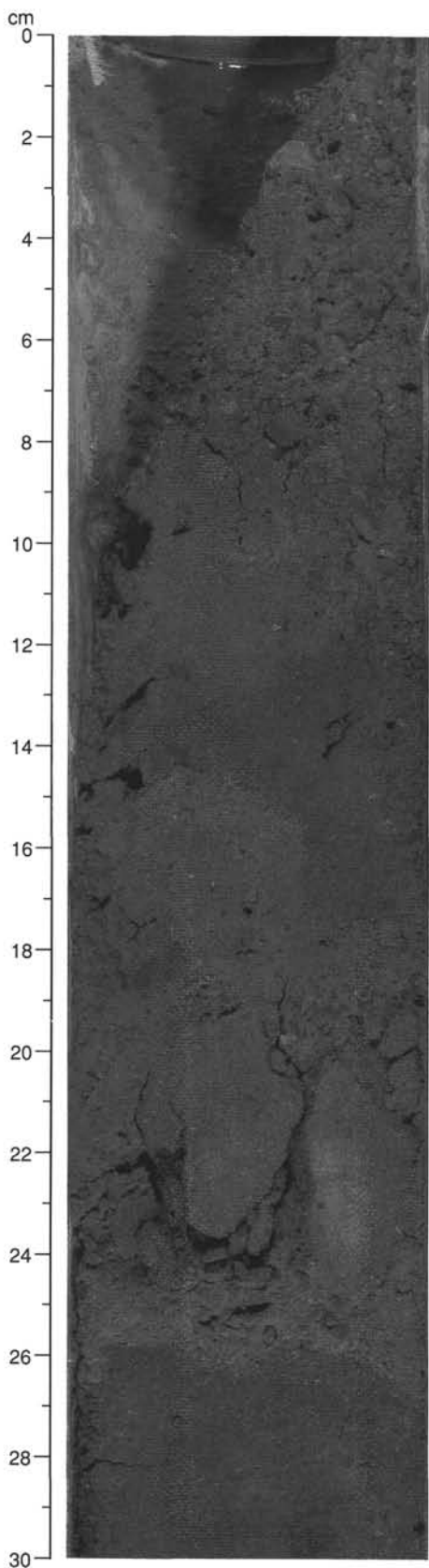


Figure 18. Sand layer in Section 146-892A-9X-1, 0–30 cm. The base of this sand layer was picked as the Subunit IA/IB boundary (67.75 mbsf).

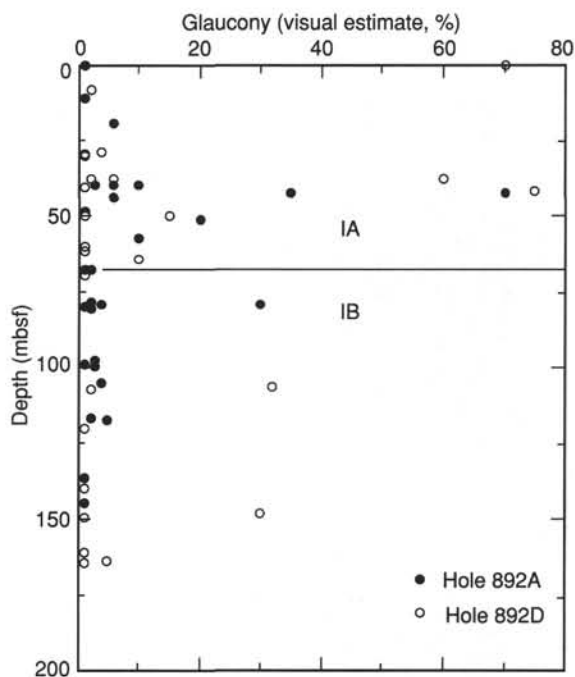


Figure 19. Distribution of glaucony with depth in Holes 892A and 892D (determined from smear slides).

environment of the Pliocene fauna is lower bathyal (see “Biostratigraphy” section, this chapter).

From these preliminary observations, lithostratigraphic Unit I recovered at Site 892 can be correlated with the basal portion of lithostratigraphic Unit 2 of Site 174. The sediments recovered at Site 892 appear to be Pliocene abyssal plain silts that were uplifted and thrust on the Oregon accretionary complex to the present location, some 15 km landward of the deformation front.

BIOSTRATIGRAPHY

A discontinuous sequence of upper Pliocene sediments was cored at Site 892. Poorly to moderately preserved planktonic foraminifers and poorly to well-preserved benthic foraminifers and radiolarians are rare to common at this site (Tables 2–4). Diatoms are common to abundant in radiolarian-bearing samples. A lower bathyal environment is interpreted for Site 892. The planktonic foraminifers suggest cool-temperate surface waters.

On the basis of both radiolarians and foraminifers, the sediments from Site 892 are considered to be mainly late Pliocene in age (*Lamprocyrtis heteroporos* radiolarian Zone and CD13–15 coiling zones); however, radiolarians indicate that sediments of early Pliocene to late Miocene age are also present in the section.

A hiatus that separates upper Pliocene sediments of the *L. heteroporos* Zone from sediments which may be from the lower Pliocene *Stichocorys peregrina* Zone is inferred between 23.2 and 30.3 mbsf in Hole 892A. Additional hiatuses or intervals of missing section are inferred in the interval from 30 to 67 mbsf in Hole 892A; however, additional work is needed to evaluate the position of these gaps.

Two stratigraphic inversions are present in Hole 892A. One inversion occurs between 45.7 and 50.1 mbsf and separates possible lower Pliocene sediments (*S. peregrina* Zone) above from upper Pliocene sediments (at the base of the *L. heteroporos* Zone) below. The second inversion is recognized in the interval between 106.1 and 164.4 mbsf by the occurrence of sediments from the top of the *L. heteroporos* Zone in a position below sediments from the base of the *L. heteroporos* Zone. The depth of this inversion may be from 106.1 to 117.4

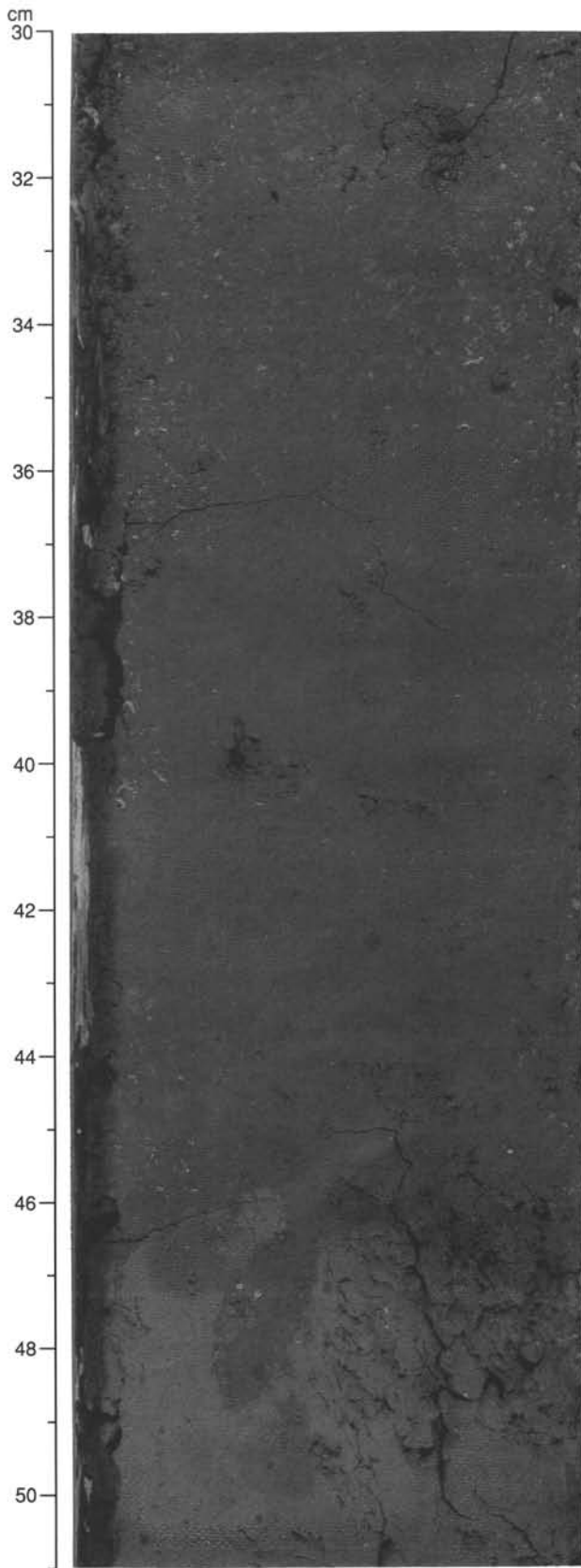


Figure 20. Calcareous silt layers with load marks in Section 146-892A-9X-1, 30-51 cm.

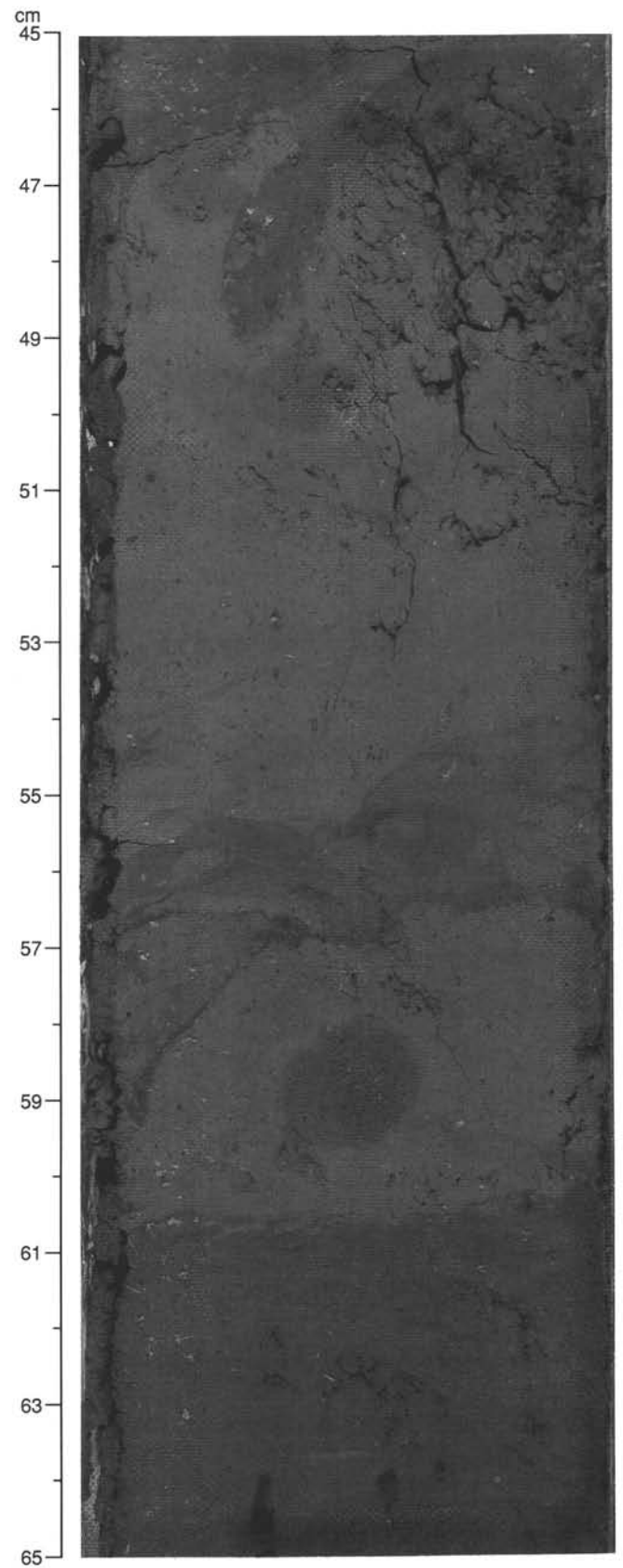


Figure 21. Scouring, sag structures, load casts, and small mud clasts at the base of a hemipelagic layer in Section 146-892A-9X-1, 45-65 cm.

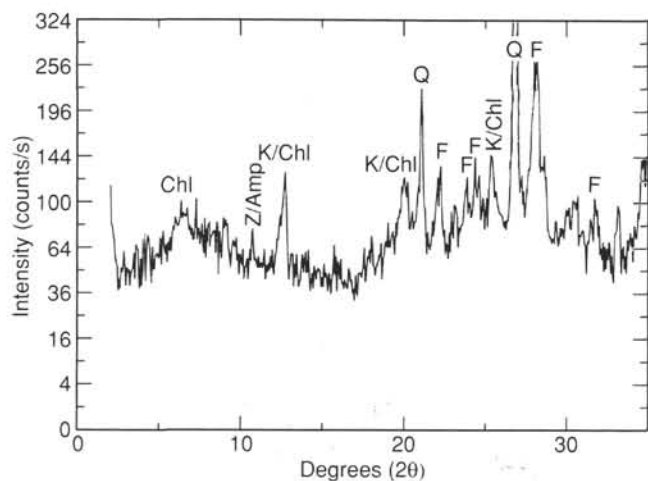


Figure 22. XRD measurement of typical clays from the upper part of Subunit IB. The main minerals present are quartz and feldspars, with mixed-layer clays, a little chlorite, and a trace of illite/mica in the clay assemblage (Sample 146-892A-11X-3, 20–21 cm). Abbreviations as in Figure 10.

mbsf on the basis of the mixed dextral and sinistral assemblage of *Neogloboquadrina pachyderma* in Sample 146-892A-15X-CC (117.4 mbsf), which is assigned to the CD13 coiling zone. This lower stratigraphic inversion is consistent with the major fault zone inferred at this site (see "Structural Geology" section, this chapter).

The radiolarians and foraminifers found in Hole 892D are similar in abundance and preservation to those found at Hole 892A. A hiatus is inferred between 31.9 and 43.1 mbsf separating upper Pliocene sediments from sediments of a possible early Pliocene age.

A stratigraphic inversion is inferred between 76.0 and 110.7 mbsf in Hole 892D, which places sediments of possible early Pliocene age above sediments of the late Pliocene *L. heteroporos* Zone. The upper stratigraphic inversion found in Hole 892A was not observed at Hole 892D, however. Additional detailed shore-based analyses are needed to correlate these two holes, to constrain the biostratigraphy, and to determine the origin, position, and amounts of time and/or sediments missing from these two sections.

Hole 892A

Radiolarians

All core-catcher samples from Hole 892A were examined for radiolarians. Some extra samples were processed for observation.

Samples 146-892A-1X-CC through -3X-CC (4.3–23.2 mbsf) contain well-preserved assemblages. The occurrence of *Cycladophora davisiana*, *Lamprocyrtis neoheteroporos*, *Eucyrtidium calvertense*, and *Sphaeropyle langii* and the absence of *Eucyrtidium matuyamai* place this interval in the base of the late Pliocene *Lamprocyrtis heteroporos* Zone (1.9–2.9 Ma). Radiolarian species indicative of upwelling environments, such as *Pterocanium auritum*, *Pterocanium grandiporus*, *Phormostichoartus crustula*, and *Phormostichoartus schneideri* (Nigrini and Caulet, 1992), were found in all samples from this interval.

The abundant occurrence of *Stichocorys peregrina* in Sample 146-892A-4X-CC (30.3 mbsf) is suggestive of the early to late Pliocene *Sphaeropyle langii* Zone. However, the absence of other stratigraphic markers, particularly *Lamprocyrtis heteroporos* and *S. langii*, could be indicative of an older age, although no assignment to a precise zone can be suggested. Below this sample, the radiolarian assemblage observed in Samples 146-892A-4X-CC (30.3 mbsf) and -6X-CC (45.7 mbsf) is characterized by species indicative of the late Miocene to early Pliocene *S. peregrina* Zone, such as *Cyrtocapsella japonica*, *Dictyophimus splendens*, *Phormostichoartus fistula*, and *S. peregrina*. The occurrence of these species suggests many stratigraphic hiatuses

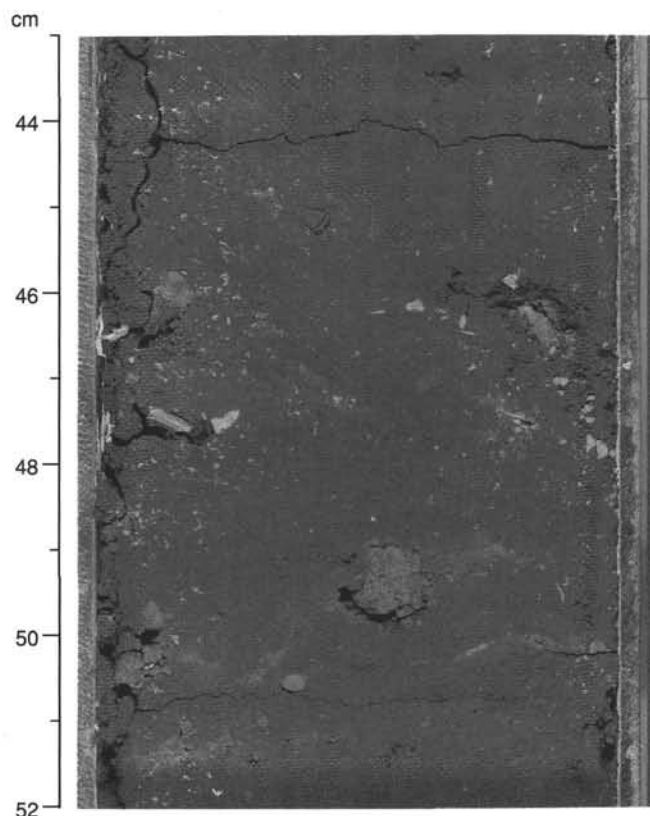


Figure 23. Stratally disrupted calcareous mudstone layers typical of Section 146-892A-15X-1, 43–52 cm.

or intervals of missing section in Core 146-892A-6X and part of Core 146-892A-7X, but further shore-based analyses are required to determine the precise location, number, and duration of these hiatuses.

The occurrence of many representatives of *L. neoheteroporos* and *Phormostichoartus caryoforma*, together with the absence of *C. davisiana* and *S. peregrina*, places Sample 146-892A-7X-2, 10–15 cm (50.1 mbsf), in the base of the *L. heteroporos* Zone (2.8–3.0 Ma), suggesting a stratigraphic inversion between 45.7 and 50.1 mbsf.

Samples 146-892A-8X-CC and -9X-CC (64.7 and 68.6 mbsf) are assigned to an older age (*S. peregrina* Zone), based on the occurrence of *Botryostrobus bramlettei*, *Dictyophimus splendens*, and *S. peregrina*. Further shore-based analyses are required to determine the precise location, number, and duration of the inferred stratigraphic hiatuses between 58.2 and 68.6 mbsf.

Samples 146-892A-11X-CC through -13X-CC (81.3–106.1 mbsf) contain very rare specimens of *Stauroxiphos communis* (?) and *S. peregrina*, which is indicative of a Miocene to early Pliocene age. No precise age determination can be proposed.

Very rare recrystallized debris of radiolarians not identifiable to the species level were found in Samples 146-892A-14X-CC through -17X-CC (107.0–136.8 mbsf).

Samples 146-892A-18X-CC (146.8 mbsf) and -20X-CC (167.4 mbsf) contain rare, moderately preserved radiolarians of Pliocene age. Sample 146-892A-20X-1, 87–92 cm (164.4 mbsf), contains well-preserved radiolarians. The occurrence of many representatives of *C. davisiana* and the absence of *L. nigrinae*, *L. neoheteroporos*, and *Eucyrtidium matuyamai* suggest a Pleistocene to late Pliocene age for this sample. The co-occurrence of many representatives of the foraminifer *Neogloboquadrina asanoi* in Samples 146-892A-20X-1, 87–92 cm, and -20X-CC assigns a late Pliocene age (1.9–2.8 Ma) to the interval between 164.4 and 167.4 mbsf. A possible stratigraphic inversion (separating upper Miocene through lower Pliocene sediments

Table 2. Distribution and zonation of planktonic foraminifers and radiolarians in core-catcher samples and two additional samples from Hole 892A.

Core, section, interval (cm)	Depth (mbsf)	Planktonic foraminifers											Radiolarians					Epoch					
		Abundance	Preservation	<i>Globigerina bulloides</i>	<i>Globigerina umbilicata</i>	<i>Globigerinita glutinata</i>	<i>Globigerinoides ruber</i>	<i>Globorotalia inflata</i> (primitive form)	<i>Globorotalia scitula</i>	<i>Neogloboquadrina asanoi</i>	<i>Neogloboquadrina pachyderma</i> (d)	<i>Neogloboquadrina pachyderma</i> (s)	<i>Turborotalia quinqueloba</i>	Planktonic spp.	Paleotemperature	Coiling dominance zone	Paleobathymetry		Abundance	Preservation	<i>Cycladophora davisiana</i>	<i>Lamprocyrtis neoheteroporos</i>	<i>Stichocorys peregrina</i>
146-892A-1X-CC	4.3	F	M	R			R		R	F	R						C	G	A	C		L. het.	
2X-CC	13.5	C	M	F	R		R		R	F	R						C	G	C	C		L. het.	late Pliocene
3X-CC	23.2	C	M	R			R		R	F					CD15		F	G	C	C			
4X-CC	30.3	R	M	R					R								F	G	C	C			
6X-CC	45.7	R	M	R		R			R								F	G	C	C			
7X-2, 10-15	50.1	R	M	R					R								F	M	M		A	?	?
7X-CC	58.3	F	M	F		R			R	F	R	R	R		CD15		F	G	G	A		L. het.	late Pliocene
8X-CC	64.7	R	P						R	R							F	G	G		A		
9X-CC	68.6	R	P	R					R	R	R						F	P	P			S. peregrina (?)	
11X-CC	81.3	R	M	R									R				F	P	P				?
12X-CC	88.6	B															F	B	B				?
13X-CC	106.1	B															F	B	B	P		C	
14X-CC	107.0	R	P						R	R	R						F	B	B				
15X-CC	117.4	F	M						R	F	F						F	B	B				
16X-CC	126.3	F	M	R					R	F	F						F	B	B				
17X-CC	136.8	B															F	B	B				
18X-CC	146.9	F	P	R						R	R						F	B	B	P			
20X-1, 87-92	164.4	F	M	R					F	F	F				CD13		F	R	M	R		L. heter.	late Pliocene
20X-CC	167.4	C	M						R	F	F						F	R	P				
21X-CC	173.1	R	M							R	F						F	R	P				

----- Hiatus
 ~~~~~ Stratigraphic inversion  
 ?\* = early Pliocene (?)

Note: Table also includes paleobathymetry and surface-water paleotemperatures. Abundance is represented by A = abundant, C = common, F = few, and R = rare. Preservation is represented by G = good, M = moderate, and P = poor. See "Explanatory Notes" chapter (this volume) for explanation of categories.

above from upper Pliocene sediments below) is, thus, inferred between 106.1 and 164.4 mbsf. Although the depth level of this inversion cannot be exactly defined owing to the lack of well-preserved fauna between 107 and 136.8 mbsf, its occurrence within this interval is consistent with the position of the major fault zone inferred at this site (see "Structural Geology" section, this chapter).

Rare recrystallized radiolarians not identifiable to the species level were found in Sample 146-892A-21X-CC (173.1 mbsf).

**Planktonic Foraminifers**

Fifteen core-catcher samples from Hole 892A contain poorly to moderately preserved planktonic foraminifers. Three core-catcher samples are barren of planktonic foraminifers.

Most of the samples have an assemblage consisting of rare to few *Globigerina bulloides*, *Neogloboquadrina asanoi*, and *N. pachyderma* (dextral and sinistral). *Globorotalia inflata* (primitive form) is rare in Samples 146-892A-1X-CC (4.3 mbsf) and 146-892A-2X-CC (13.5 mbsf) and is frequent in Sample 146-892A-7X-CC (58.3 mbsf). The other planktonic foraminifers found at this site are shown in Table 2.

Within the interval from 4.3 to 68.6 mbsf, samples with assemblages containing mainly dextral populations of *N. pachyderma*, *N.*

*asanoi*, and *G. inflata* (see Table 2) are assigned to the upper part of the CD15 coiling zone. With the exception of Samples 146-892A-15X-CC (117.4 mbsf), -16X-CC (126.5 mbsf), -18X-CC (146.9 mbsf), -20X-1, 87-92 cm (164.4 mbsf), and -20X-CC (173.0 mbsf), samples below 68.6 mbsf are either barren or contain rare, poorly to moderately preserved assemblages that are not age diagnostic. Samples 146-892A-15X-CC (117.4 mbsf) through -16X-CC (126.5 mbsf), -20X-1, 87-92 cm (164.4), and -20X-CC (167.4 mbsf) are assigned to the CD13 coiling zone based on the occurrence of *N. asanoi* with both dextral and sinistral *N. pachyderma*.

**Benthic Foraminifers**

All core-catcher samples from Hole 892A contain rare to common, poorly to well-preserved benthic foraminifers. A preliminary list of benthic foraminifers present in Hole 892A is provided in Table 3.

The benthic assemblages, which typically contain *Bulimina subacuminata*, *Cibicidoides wuellerstorfi*, *Fissurina lucida*, *Martinotiella communis*, *Melonis barleeanum*, *Melonis pompilioides*, *Pullenia bulloides*, *Sphaeroidina bulloides*, and *Uvigerina senticosa*, indicate deposition in a lower bathyal environment with some faunas transported from a middle bathyal environment. Sample 146-892A-4X-CC (30.3

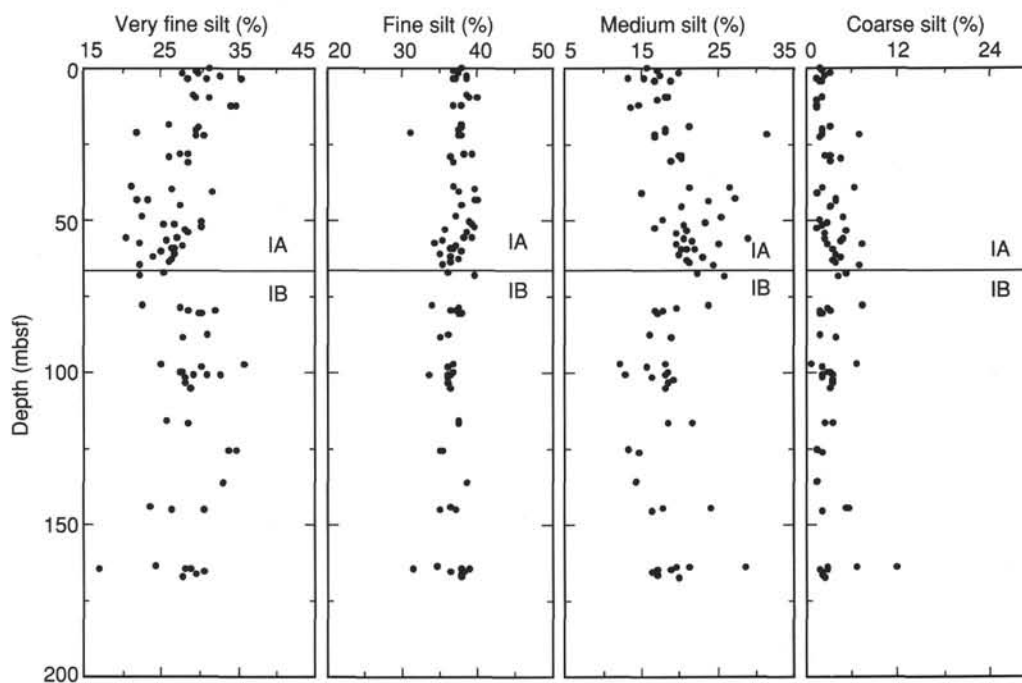


Figure 24. Distribution of silt grain-size classes in Hole 892A. The very fine silt and medium silt classes outline a difference in grain-size distribution between Subunits IA and IB.

mbsf), which has common, well-preserved *Buccella tenerrima*, is the only sample that contains downslope-transported neritic taxa.

### Hole 892D

#### Radiolarians

Radiolarians are rare to abundant in all core catchers from Hole 892D (Table 4). In the interval from Sample 146-892D-1X-CC (0.1 mbsf) to -4X-CC (31.9 mbsf), the radiolarian assemblage contains *C. davisiana*, *L. neoheteroporos*, and *S. langii*; it is indicative of the late Pliocene *L. heteroporos* Zone. The occurrence of some specimens of the old form of *C. davisiana* in Sample 146-892D-4X-CC (31.9 mbsf) places the base of this interval in the early *L. heteroporos* Zone.

Radiolarians are rare and moderately preserved in Samples 146-892D-5X-CC through -9X-CC (43.1–76 mbsf). Rare representatives of *S. peregrina*, *B. bramlettei*, *Lamprocyclus hannai*, and *Phormostichoartus fistula* may place this interval in the early Pliocene. Many stratigraphic markers in this interval are missing so a precise age determination cannot be made.

A few specimens of *C. davisiana* (old form) and *Eucyrtidium calvertense* (old form) assign an early late Pliocene age (base of *L. heteroporos* Zone) to Sample 146-892D-10X-CC (110.7 mbsf). This early late Pliocene age suggests a stratigraphic inversion between 76.0 and 110.7 mbsf.

Samples 146-892D-11X-CC through -16X-CC (113.1–164.5 mbsf) contain very rare recrystallized radiolarians of uncertain age.

#### Planktonic Foraminifers

Nine of 16 core-catcher samples contained rare to common, poorly to well-preserved planktonic foraminifers. In the interval from 0.1 to 31.9 mbsf, the planktonic assemblages consist of *G. bulloides*, *N. asanoi*, and *N. pachyderma* (dextral and sinistral), which, like the equivalent interval in Hole 892A, is indicative of the upper part of late Pliocene CD15 coiling zone. This assemblage also indicates cool-temperate surface waters.

The interval from 43.1 through 110.7 mbsf is barren of planktonic foraminifers, with the exception of Sample 146-892D-9X-CC (76

mbsf), which contains one poorly preserved planktonic foraminifer. Between 113.1 and 152.0 mbsf, rare to few planktonic foraminifers are present, but no age assignment can be made. Sample 146-892D-16X-CC is barren of planktonic foraminifers.

#### Benthic Foraminifers

Benthic foraminifers are rare to common in Hole 892D. Two samples are barren of benthic foraminifers. Table 3 includes the benthic foraminifers identified from Hole 892D.

Benthic assemblages at Hole 892D are similar to those found at Hole 892A and represent deposition in a lower bathyal environment. The rare occurrence of taxa such as *Uvigerina peregrina*, *Epistominella pacifica*, and *Globobulimina pacifica* indicates some transport from middle bathyal environments. Neritic taxa are not present in the core-catcher samples.

### PALEOMAGNETISM

Shipboard paleomagnetic measurements from both split cores and discrete samples taken from Holes 892A and 892D did not successfully yield stable results for the purpose of defining a magnetostratigraphy at this site. Two primary reasons for this lack of success were (1) the alternating-field (AF) demagnetizer coils in the 2G magnetometer were unable to generate fields greater than 7 mT, which was insufficient to isolate a stable remanence direction in the split-core samples; and (2) the low (<2 mA/m) remanence intensity in the sediments, coupled with the presence of AF-resistant magnetic sulfides, yielded remanence data from the discrete samples that are highly scattered in direction. The whole-core susceptibility data are also highly scattered and are not included in this report. The split-core results for both Holes 892A and 892D after 7-mT AF demagnetization are shown in Figure 27; note the highly scattered declinations and inclinations. The discrete sample data for Hole 892A after 5-mT AF demagnetization are displayed in Figure 28. The directions obtained from 20 samples that were AF-demagnetized at higher (up to 60 mT) fields are similarly scattered, so further AF-demagnetization treatments were abandoned in favor of shore-based thermal demagnetization treatment.

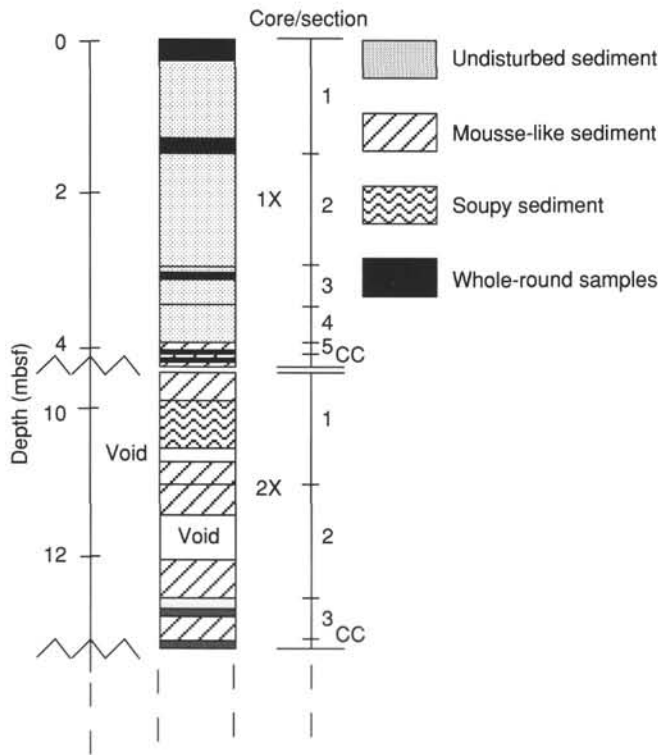


Figure 25. Distribution of undisturbed, soupy, and mousse-like sediments in Cores 146-892A-1X and -2X, where gas hydrates were recovered.

Detailed examination of typical demagnetization results indicates behavior (little decrease in remanence intensity, erratic directional behavior during AF demagnetization) similar to that observed for remanence carried by magnetic sulfides in samples from other sites (Site 889 and a few samples from Site 891) of Leg 146 (Fig. 29A). The vast majority of these results represents a remagnetized remanence carried in magnetic sulfides and cannot be used, therefore, in the definition of a magnetostratigraphy at this site. An exceptional sample (146-892A-18X-1, 17–19 cm) displayed stable demagnetization behavior, with a well-defined steeply inclined downward (normal polarity) direction isolated by AF demagnetization (Fig. 29B).

**STRUCTURAL GEOLOGY**

**Introduction**

Site 892 contains a range of structural features, from little-deformed, unlithified sediments, to the most mature structural fabrics recovered on Leg 146, which are indicative of a major fault zone (Fig. 30). Site 892 exhibits generally shallow dips of both bedding and structural fabrics (Fig. 31 and Table 5); however, intervals of steeper dips in Hole 892D suggest folding. The most prominent structural feature is a zone of stratal disruption and mélangé, varying in thickness from tens of meters to >100 m. Structural fabrics vary significantly in character and thickness from Hole 892A to Hole 892D, which are 20 m apart in a strike-perpendicular direction on the seismically imaged thrust fault (see Fig. 3). We were able to measure the core-reference-frame attitudes of many features, presented in Table 5. Paleomagnetic reorientation was not possible during Leg 146 because of the poor quality of the remanence data (see “Paleomagnetism” section, this chapter), but these studies will be conducted on selected samples post-cruise. As almost all coring was done with the XCB technique, multishot tool orientations were not obtained.

One of the most interesting features of Site 892 proved to be the significant lateral heterogeneity between Holes 892A and 892D, sum-

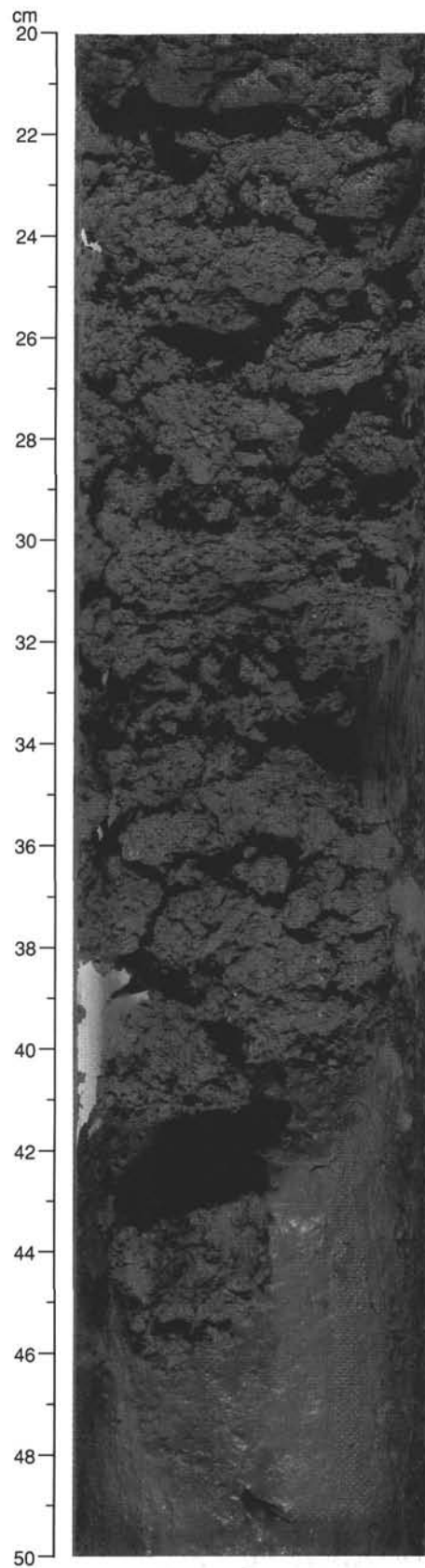


Figure 26. Mousse-like (Section 146-892A-2X-1, 20–40 cm) and soupy (Section 146-892A-2X-1, 40–50 cm) layers, thought to be produced by the dissociation of gas hydrate during core recovery.

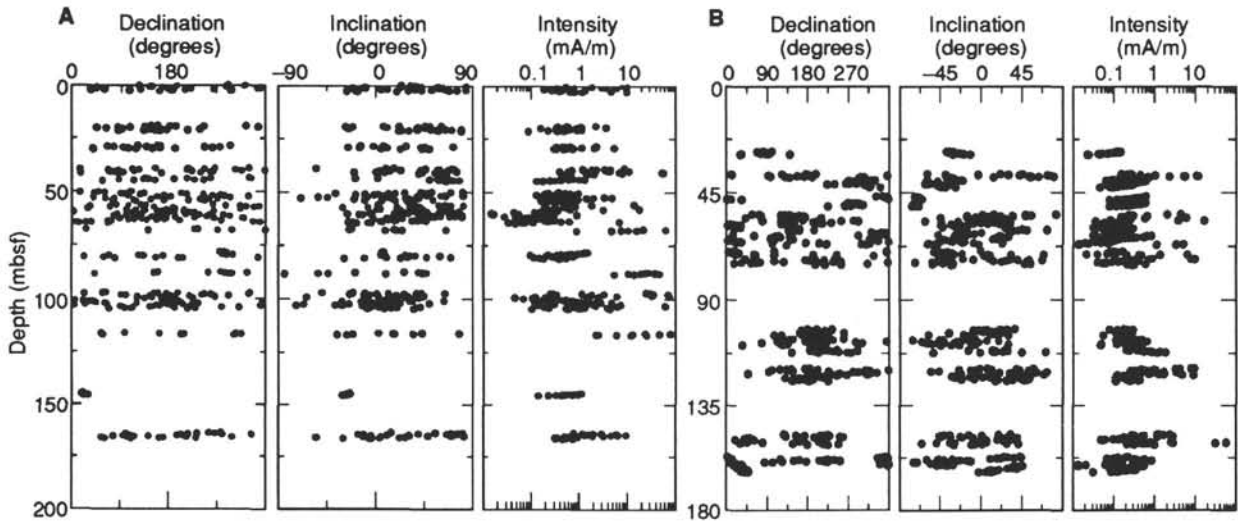


Figure 27. Declination, inclination, and intensity plots of split-core remanence from Hole 892A (A) and Hole 892D (B) after 7-mT AF demagnetization in the 2G magnetometer.

**Table 3. Preliminary list of benthic foraminifers recovered at Site 892.**

---

|                                    |
|------------------------------------|
| <i>Bolivinita quadrilatera</i>     |
| <i>Buccella tenerrima</i>          |
| <i>Bulimina fossa</i>              |
| <i>Bulimina subacuminata</i>       |
| <i>Buliminella exilis</i>          |
| <i>Buliminella subfusiformis</i>   |
| <i>Cassidulina</i> spp.            |
| <i>Cassidulina translucens</i>     |
| <i>Cassidulinoides bradyi</i>      |
| <i>Cibicides</i> spp.              |
| <i>Cibicidoides mckannai</i>       |
| <i>Cibicidoides wuellerstorfi</i>  |
| <i>Dentalina soluta</i>            |
| <i>Dentalina</i> spp.              |
| <i>Eggerella bradyi</i>            |
| <i>Elphidium</i> spp.              |
| <i>Epistominella pacifica</i>      |
| <i>Eponides</i> sp.                |
| <i>Fissurina lucida</i>            |
| <i>Glandulina</i> sp.              |
| <i>Globobulimina pacifica</i>      |
| <i>Globobulimina</i> sp.           |
| <i>Globocassidulina subglobosa</i> |
| <i>Gyroidina multilocula</i>       |
| <i>Gyroidina soldanii</i>          |
| <i>Gyroidina</i> sp.               |
| <i>Lagena</i> spp.                 |
| <i>Lagena striata</i>              |
| <i>Laticarinina pauperata</i>      |
| <i>Lenticulina</i> sp.             |
| <i>Martinotiella communis</i>      |
| <i>Melonis barleanum</i>           |
| <i>Melonis pompilioides</i>        |
| <i>Nodosaria</i> spp.              |
| <i>Nodosaria tornata</i>           |
| <i>Nnonella miocenica</i>          |
| <i>Nonionellina labradorica</i>    |
| <i>Oridorsalis umbonatus</i>       |
| <i>Plectofrondicularia advena</i>  |
| <i>Plectofrondicularia</i> spp.    |
| <i>Pullenia bulloides</i>          |
| <i>Pyrgo</i> spp.                  |
| <i>Quinqueloculina</i> spp.        |
| <i>Sphaeroidina bulloides</i>      |
| <i>Stilostomella advena</i>        |
| <i>Triloculina</i> sp.             |
| <i>Uvigerina dirupta</i>           |
| <i>Uvigerina hispida</i>           |
| <i>Uvigerina peregrina</i>         |
| <i>Uvigerina senticosa</i>         |
| <i>Valvulineria</i> sp.            |

---

marized in Figure 30. Because coring of Holes 892D and 892E was very late in the leg, structural domain divisions discussed in this section are based on Hole 892A, with differences in the other two holes noted in the text.

We divide the cored interval at Hole 892A into three structural domains for the purposes of description, based on the dip of bedding and the development of shear-induced fabrics. The three domains are discussed in separate sections in the following. The boundaries between Domains I and II proved to be less distinct in the cores from Hole 892D, but the overall structural trends are largely the same. Differences between the microstructures in the holes at this site illustrate the lateral heterogeneity possible in a region of this structural complexity.

#### Domain I (0–52 mbsf in Hole 892A)

The first structural domain exhibits moderately dipping bedding and weak fracturing of the silty unlithified sediments. Cores 146-892A-1X and -2X (0–19 mbsf) were extremely disturbed by the pres-

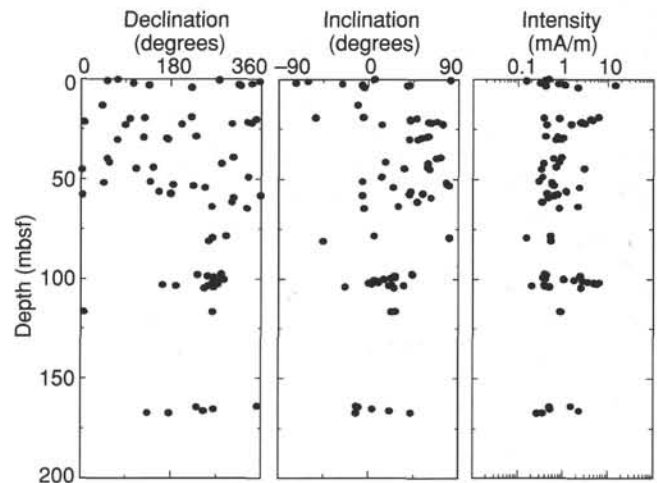


Figure 28. Declination, inclination, and intensity plots of discrete sample results from Hole 892A after 5-mT AF demagnetization on the GSD-1 demagnetizer.



Table 5. Structural data collected at Site 892.

| Core, section, interval (cm) | Depth (mbsf) | Identifier                | Core face orientation (degrees) |           | Second orientation (degrees) |           | Corrected core reference frame |     |           | Comments                                                      |
|------------------------------|--------------|---------------------------|---------------------------------|-----------|------------------------------|-----------|--------------------------------|-----|-----------|---------------------------------------------------------------|
|                              |              |                           | Apparent dip                    | Direction | Apparent dip                 | Direction | Strike                         | Dip | Direction |                                                               |
| 146-892A-                    |              |                           |                                 |           |                              |           |                                |     |           |                                                               |
| 4X-1, 72-74                  | 29           | Fault? bed?               | 31                              | 90        | 15                           | 180       | 24                             | 33  | E         | Contact between fractured siltstone below silts.              |
| 6X-1, 71-73                  | 40           | Bed                       | 14                              | 270       | 15                           | 180       | 133                            | 20  | S         |                                                               |
| 6X-2, 90-93                  | 41           | Bed                       | 23                              | 90        | 6                            | 0         | 346                            | 24  | E         |                                                               |
| 7X-3, 0-3                    | 51           | Bed                       | 27                              | 90        | 18                           | 180       | 33                             | 31  | E         |                                                               |
| 7X-3, 62-65                  | 52           | Bed                       | 33                              | 270       | 14                           | 0         | 201                            | 35  | W         |                                                               |
| 7X-2, 120                    | 51           | Color boundary (bed?)     | 2                               | 90        | 10                           | 180       | 79                             | 10  | S         |                                                               |
| 7X-4, 86-87                  | 53           | Bed                       | 10                              | 270       | 16                           | 180       | 122                            | 19  | S         |                                                               |
| 7X-6, 22                     | 57           | Bed                       | 1                               | 90        | 5                            | 180       | 79                             | 5   | S         |                                                               |
| 8X-4, 91-92                  | 63.5         | Color change (bed?)       | 3.5                             | 90        | 11                           | 180       | 73                             | 12  | S         |                                                               |
| 8X-4, 141-143                | 64           | Vein                      | 26                              | 90        | 9                            | 180       | 18                             | 27  | E         |                                                               |
| 8X-4, 135-136                | 64           | Stratal disruption        | 14                              | 90        | 30                           | 0         | 293                            | 32  | N         |                                                               |
| 9X-1, 60-61                  | 68           | Bed                       | 6                               | 270       | 8                            | 180       | 127                            | 10  | S         |                                                               |
| 9X-1, 23                     | 67.5         | Vein                      |                                 |           |                              |           |                                |     |           | Bedding-parallel, subhorizontal.                              |
| 9X-1, 26                     | 67.5         | Bed                       | 4                               | 90        | 17                           | 180       | 77                             | 17  | S         |                                                               |
| 11X-1, 74-77                 | 79           | Fracture                  | 36                              | 90        | 14                           | 0         | 341                            | 38  | E         | Two fractures representing two sets of parallel systems.      |
| 11X-1, 73-81                 | 79           | Fracture                  | 58                              | 270       | 30                           | 0         | 200                            | 60  | W         |                                                               |
| 11X-2, 72-78                 | 80           | Vein                      |                                 |           |                              |           |                                |     |           | Not in original orientation.                                  |
| 13X-1, 16-17                 | 97           | Bed                       | 8                               | 90        | 20                           | 0         | 291                            | 21  | N         |                                                               |
| 13X-2, 13-15                 | 97.5         | Fracture                  | 62                              | 90        | 21                           | 0         | 348                            | 62  | E         |                                                               |
| 13X-3, 50-52                 | 98           | Fracture                  | 54                              | 90        | 19                           | 180       | 14                             | 55  | E         |                                                               |
| 14X-1                        | 106.5        | Angular scaly fragments   |                                 |           |                              |           |                                |     |           | Disaggregated core of scaly fragments.                        |
| 15X-1, 63                    | 116.5        | Stratal disruption fabric | 3                               | 270       | 3                            | 0         | 225                            | 4   | W         | Core 15X has strong stratal disruption fabric.                |
| 15X-1, 51-52                 | 116.5        | Mudstone stringer         | 6                               | 270       | 27                           | 180       | 102                            | 27  | S         | With bounding of calcareous mudstone.                         |
| 17X-1, 40-50                 | 135.5        | Stratal disruption        |                                 |           |                              |           |                                |     |           | Disturbed.                                                    |
| 17X-2, 63-80                 | 136          | Scaly fabric              |                                 |           |                              |           |                                |     |           | Best developed fabric anywhere on Leg 146.                    |
| 18X-1, 85-86                 | 145.5        | Mélange fabric            | 12                              | 90        | 0                            | 0         | 0                              | 12  | E         | Shear bands in proto-mélange.                                 |
| 18X-1, 71-72                 | 145.5        | Mélange fabric            | 10                              | 90        | 0                            | 0         | 0                              | 10  | E         | Shear bands in proto-mélange.                                 |
| 20X-1, 94-95                 | 164.5        | Bed                       | 6                               | 270       | 16                           | 0         | 250                            | 17  | N         |                                                               |
| 146-892D-                    |              |                           |                                 |           |                              |           |                                |     |           |                                                               |
| 4X-1, 119-120                |              | Bedding                   | 6                               | 90        | Unknown                      |           |                                |     |           | Sandy layer bedding plane.                                    |
| 4X-1, 133-134                |              | Bedding                   | 3                               | 270       | 3                            | 180       | 135                            | 4   | W         | Sandy layer bedding plane.                                    |
| 4X-1, 137-137                |              | Bedding                   | 3                               | 270       | 1                            | 0         | 198                            | 3   | W         | Sandy layer bedding plane.                                    |
| 5X-1, 85                     |              | Bedding                   | 0                               | 90        | 0.5                          | 180       | 90                             | 1   | S         | Glaucconitic sand layer.                                      |
| 5X-2, 78                     |              | Bedding/dark bands        | 1                               | 270       | 2                            | 180       | 117                            | 2   | S         | On calcareous mud layer—disrupted by bedding. Parallel shear? |
| 5X-4, 2-4                    |              | Fold axial plane          |                                 |           |                              |           |                                |     |           | Trend: 120, plunge: 6.                                        |
| 5X-4, 16-20                  |              | Stratal disruption        |                                 |           |                              |           |                                |     |           | Variable but subhorizontal fabric.                            |
| 6X-1, 100-102                |              | Bedding                   | 14                              | 270       | 20                           | 180       | 124                            | 24  | S         | In bedded glauconitic layers.                                 |
| 6X-1, 124-126                |              | Bedding                   | 17                              | 270       | 8                            | 0         | 205                            | 15  | W         |                                                               |
| 6X-1, 142-143                |              | Bedding                   | 5                               | 90        | 2                            | 0         | 338                            | 5   | E         |                                                               |
| 6X-3, 20-30                  |              | Contorted beds            |                                 |           |                              |           |                                |     |           | Recumbent tight fold.                                         |
| 6X-4, 80-81                  |              | Bedding                   | 20                              | 90        | 25                           | 180       | 52                             | 31  | S         | In less fractured interval.                                   |
| 7X-1, 38-40                  |              | Bedding                   | 30                              | 270       |                              |           |                                |     |           |                                                               |
| 7X-4, 40-44                  |              | Fold                      |                                 |           |                              |           |                                |     |           | Subhorizontal axial plane; limb width of 3 cm.                |
| 8X-2, 135                    |              | Bedding                   | 0                               | 270       | 7                            | 0         | 270                            | 7   | N         | Layer of sand in silty clay.                                  |
| 8X-CC                        |              | Veins                     |                                 |           |                              |           |                                |     |           | Many broken calcitic veins.                                   |
| 9X-1, 44-48                  |              | Bedding                   | 31                              | 270       | 21                           | 0         | 213                            | 35  | W         | Color change boundary.                                        |
| 9X-1, 97-103                 |              | Bedding                   | 39                              | 270       | 23                           | 0         | 208                            | 42  | W         | Top of soupy layer.                                           |
| 10X-3, 95-99                 |              | Mud stringer              | 38                              | 90        | 8                            | 180       | 10                             | 38  | E         | In shear fabric.                                              |
| 10X-3, 121-124               |              | Mud stringer              | 19                              | 90        | 19                           | 180       | 45                             | 26  | E         |                                                               |
| 10X-3, 77-80                 |              | Mud stringer              | 25                              | 270       | 15                           | 0         | 210                            | 28  | W         |                                                               |
| 10X-4, 44-47                 |              | Mélange fabric            | 32                              | 270       | 22                           | 180       | 147                            | 37  | W         | Grain of mélange zone dark bands.                             |
| 10X-4, 38-41                 |              | Mélange fabric            | 33                              | 270       | 19                           | 180       | 148                            | 37  | W         |                                                               |
| 10X-4, 71-76                 |              | Veins                     | 40                              | 90        | 21                           | 0         | 335                            | 43  | E         | Extensional veins in concretion block in mélange.             |
| 10X-4, 145-147               |              | Mud stringer              | 23                              | 90        | 14                           | 180       | 30                             | 26  | E         | Stringers coming off tan calcareous mud block.                |
| 10X-5, 14-17                 |              | Mélange fabric            | 35                              | 270       |                              |           |                                |     |           | Second orientation not measurable.                            |
| 146-892D- (cont.)            |              |                           |                                 |           |                              |           |                                |     |           |                                                               |
| 10X-5, 60-62                 |              | Mélange fabric            | 19                              | 90        | 11                           | 0         | 331                            | 22  | E         |                                                               |
| 10X-6, 125-132               |              | Mélange fabric            | 54                              | 90        | 20                           | 0         | 345                            | 55  | E         |                                                               |
| 11X-1, 44-45                 |              | Mélange fabric            | 40                              | 270       |                              |           |                                |     |           | Second measurement not possible.                              |
| 11X-1                        |              | Mud stringer              | 27                              | 270       | 5                            | 180       | 170                            | 27  | W         | In mélange matrix.                                            |
| 11X-3, 9-13                  |              | Fold                      |                                 |           |                              |           |                                |     |           | Recumbent "s" fold.                                           |
| 15X-3, 60-63                 |              | Bedding                   | 28                              | 270       | 43                           | 180       | 120                            | 47  | S         | Low confidence.                                               |
| 146-892E-                    |              |                           |                                 |           |                              |           |                                |     |           |                                                               |
| 3H-4, 64-65                  |              | Bedding                   | 3                               | 270       | 34                           | 0         | 266                            | 34  | N         | Layers of clayey silt with different composition.             |
| 3H-4, 67-72                  |              | Bedding                   | 22                              | 270       | 34                           | 0         | 239                            | 38  | N         |                                                               |
| 3H-4, 74-77                  |              | Bedding                   | 25                              | 270       | 28                           | 0         | 229                            | 35  | N         | Core also has stratal disruption in Section 4.                |
| 3H-4, 78-81                  |              | Bedding                   | 33                              | 270       | 52                           | 0         | 243                            | 55  | N         |                                                               |
| 3H-4, 94-96                  |              | Bedding                   | 11                              | 270       | 3                            | 0         | 195                            | 11  | W         |                                                               |
| 3H-4, 138-141                |              | Bedding                   | 19                              | 270       | 25                           | 0         | 234                            | 30  | N         |                                                               |

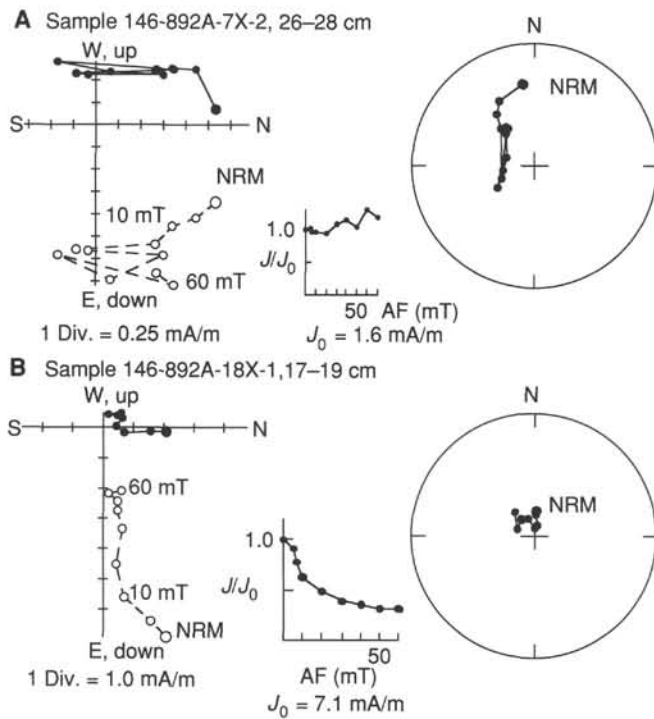


Figure 29. Demagnetization behavior of a typical (A) and an exceptional (B) sample from Hole 892A. Filled symbols on the Zijderveld plot are results projected on the horizontal plane, open symbols are projections on the vertical plane. Filled symbols on the stereonet plot are lower hemisphere directions, and open symbols are upper hemisphere directions.

Section 146-892A-9X-1, 23 cm (67.5 mbsf), is subhorizontal and bedding parallel. No other in-place veins were observed in Domain II.

Cores 146-892A-11X to -13X (78–105 mbsf) show no evidence for faulting. They exhibit alternations of fractured and unfractured layers, averaging about 50 cm thick; the latter exhibit hackly parting and have a dry, friable texture. The fractured intervals do show some down-hole increase in polish and the development of slickenlines of variable orientation on fracture surfaces. One submillimeter-size vein was observed in this interval, in a calcareous concretion in Core 146-892A-11X (80 mbsf). No apparent macroscopic structural features are visible at 90 mbsf, where logging data and temperature measurements suggest a fault zone; however, recovery of this interval was poor.

The interval coincident with Domain II in Hole 892D exhibits extensive development of stratal disruption throughout, producing broken formation. Stratal disruption is a subtle feature in the un lithified sediments at this site. We found that scraping the split-core face with a razor blade was necessary to remove the smear layer produced by splitting of the core in order to expose the fabric.

Stratal disruption, illustrated in Figure 32, occurs in layers of un lithified clayey silt and calcareous mud. Individual blocks of disrupted bedding are bounded by shallowly inclined dark fine-grained bands, interpreted as shear zones, pervasive on a millimeter-to-centimeter scale. This fabric is exhibited in Holes 892D and 892E as shallowly as 33 mbsf and persists to 77 mbsf (the top of the uncoring interval in Hole 892D), and sporadically in the deeper fault zone interval (100–166 mbsf).

### Domain III (106.5–176.5 mbsf in Hole 892A)

Core 146-892A-14X, at 106.5 mbsf, marks the onset of an interval dominated by intense shear zone fabrics, defining the top of Domain III. This core, in which the amount of recovered material was small, comprises angular polished chips of siltstone, which are completely

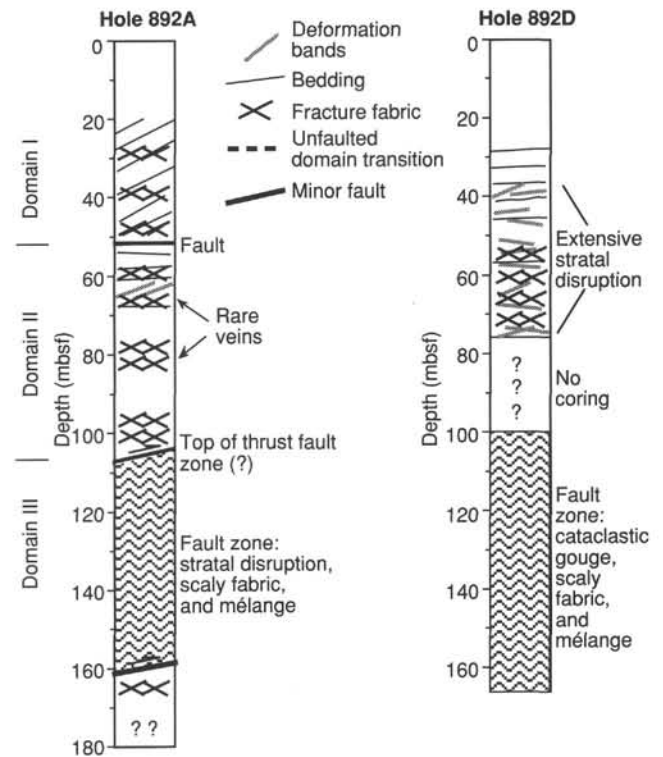


Figure 30. Summary diagram illustrating structural features identified in Holes 892A and 892D. Hole 892D was located about 20 m west of Hole 892A, perpendicular to strike and up-dip along the seismically imaged thrust fault. Differences between the recovered structures are discussed in the text.

disaggregated. The chips are fine, 1–5 mm in long dimension, and are more indurated than the material recovered above. The next core (146-892A-15X; 116–125.5 mbsf) recovered an interval of strongly developed stratal disruption, as defined by Lundberg and Moore (1986). The fabric is made visible by the presence of calcareous mudstone layers, which have been extensively disrupted and exhibit stringers of mud extending from intact blocks (Fig. 23). The fabric in this core is subhorizontal, dipping up to 10°, although one relatively intact mudstone block has a measured inclination of 27°. The matrix of the core exhibits numerous anastomosing shear zone deformation bands, also strongly aligned in a subhorizontal direction. Core 146-892A-16X (125.5–135.0 mbsf) was poorly recovered and highly disturbed, but intact intervals exhibit strong stratal disruption. Disturbed intervals in this core contain scaly chips, which may be the product of an open fracture system in the subsurface.

Core 146-892A-17X (135.0–144.5 mbsf) also exhibits stratal disruption, although below the first section it is almost monolithic, and disrupted bedded layers were not observed. This core has a well-developed true scaly fabric, with dark, highly polished parting surfaces. The fabric is much more strongly developed here than any observed at Sites 889 or 891. Core 146-892A-18X (144.5–154.0 mbsf) has a similar pervasive shear fabric, with highly polished parting surfaces. This core contains a significant amount of fine sand, which rendered the fabric discernible on a freshly scraped core-face surface. This fabric is composed of an anastomosing network of submillimeter to 1-mm-wide dark shear zones surrounding lenses of fine sand (Fig. 33) and is best described as an early stage of development of a Type I mélangé (Cowan, 1985). This fabric is shallowly inclined to subhorizontal, dipping no more than 12°. In Section 146-892A-18X-1, 59–62 cm, a dolomite (?) concretion was recovered, which is apparently in place relative to the surrounding sediment, as it fills the core liner and is not associated with any adjacent coarse-grained material (see "Litho-

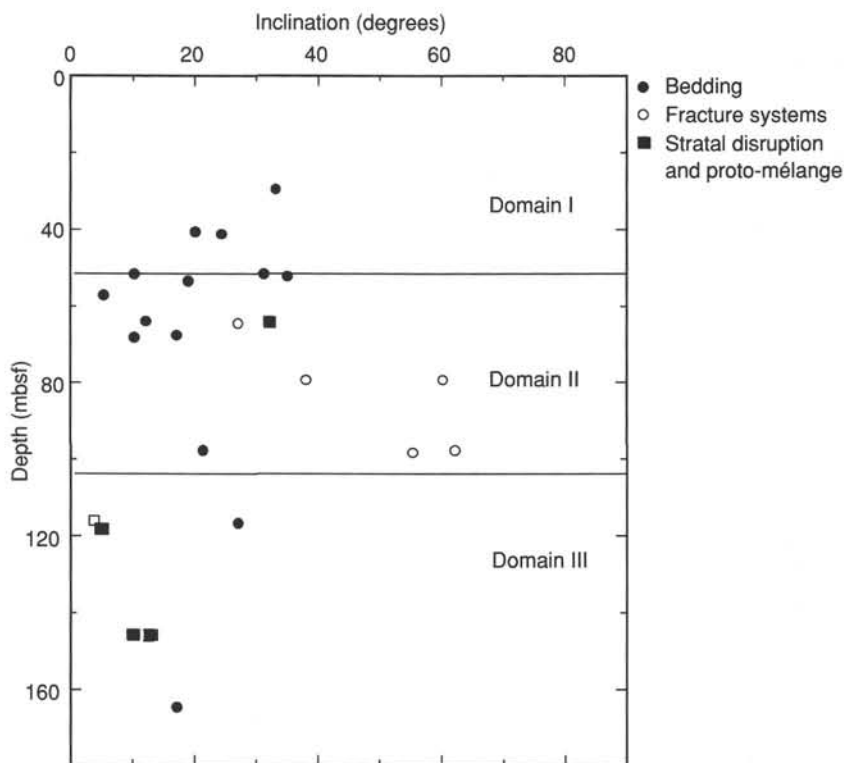


Figure 31. True dip inclination vs. depth of various structures from Hole 892A.

stratigraphy” section, this chapter). The concretion exhibits brecciation and extensive crosscutting veins (Fig. 34), indicating that it formed progressively during a period of shearing, probably associated with the development of the *mélange* fabric. Associated with this fabric is an interval from 45 to 56 cm of black, gravelly, angular fragments with a strong petroliferous odor.

Taken together, Cores 146-892A-15X through -18X appear to represent a 31-m-thick interval that is pervasively sheared to an apparent relatively high strain. The recovered material in this interval does not exhibit open fractures along which drilling disaggregation has occurred, unlike many of the fracture fabrics observed on Leg 146. The cores are coherent and, although recovery is only partial, the material is quite intact. These observations may reflect the high degree of strain and associated shear consolidation (see “Physical Properties” section, this chapter) experienced by these sediments, or they may reflect rheological changes resulting from partial cementation during progressive deformation. By contrast, the fractures in Core 146-892A-14X (106.5–116.0 mbsf) were apparently open, because they were disaggregated by XCB coring. We speculate that Core 146-892A-14X may represent the active fault zone, and the deeper cores may be fabrics formed earlier. The fabric of Core 146-892A-14X is clearly different from that of the subjacent interval and is more reminiscent of the fabrics recovered around the 375-mbsf fault zone at Site 891 (see “Structural Geology” section, “Site 891” chapter, this volume), suggesting that it is typical of a young fault zone. Other intervals of apparent open scaly fractures in Cores 146-892A-16X and -18X may represent additional active zones of discrete shear.

The calculated depth to the fault imaged in the multichannel seismic (MCS) line is about 107 to 113 mbsf, coinciding approximately with the depth to the scaly fracture fabric in Core 146-892A-14X (see “Seismic Stratigraphy” section, this chapter). This may be indicative of a thrust with a history of progressive strain hardening, which causes the plane of active faulting to move upward from the older, deeper locus to a present position at about 106 mbsf, consistent with the observation of progressively more strained and higher density (see

“Physical Properties” section, this chapter) material downhole from Cores 146-892A-14X to -18X.

Below this fault zone interval, only Core 146-892A-20X (163.5–168.0 mbsf) was recovered intact. This core exhibits the slightly polished fractures and unfractured intervals typical of the cores just above the fault zone (i.e., Cores 146-892A-11X to -13X); it appears to represent a return to the structural regime of Domain II. This core is probably from below the fault zone, but it may be a block of less deformed material within the *mélange*. With the poor recovery and the termination of drilling at Core 146-892A-21X, it is impossible to differentiate between these possibilities.

In Hole 892D, the core-scale expression of the fault zone was somewhat different. Because the interval from 77 to 100 mbsf was not cored, the top of the fault zone was not identified. Some fabric similar to that of the fault zone below 100 mbsf was recovered at 69.5 and 76 mbsf, suggesting that a strand of the fault zone may occur more shallowly at Hole 892D.

Four different fault fabrics are exhibited by the cores of Hole 892D (Fig. 35): (1) stratal disruption of interbedded silt and calcareous mud layers (Fig. 35A); (2) zones exhibiting broken and dispersed fragments of cemented sediment in a fine-grained matrix macroscopically resembling cataclastic fault gouge (Fig. 35B); (3) “*mélange* fabric” of pervasive anastomosing dark shear zones surrounding lenticular to round blocks of fine-sand-sized, partially cemented sediment (see Fig. 33); and (4) intervals of scaly fabric, with open fractures and polished and slickenlined fragment surfaces, which were commonly disaggregated by drilling (Fig. 35C). Stratal disruption and *mélange* fabric begin in Core 146-892D-5X (37.0–46.5 mbsf) and continue downhole throughout the deformed interval. Intercalated with these fabrics are discrete intervals of gouge fabric, the first in Section 146-892D-9X-1 (69.5 mbsf), extending for about 1 m.

Core 146-892D-10X (100.0–109.5 mbsf) contains interlayered intervals of gouge and *mélange*. The *mélange* fabric is semiplanar, dips 37°, and includes an apparently in-place calcareous concretion with extensional calcite veins oriented perpendicular to the *mélange* matrix

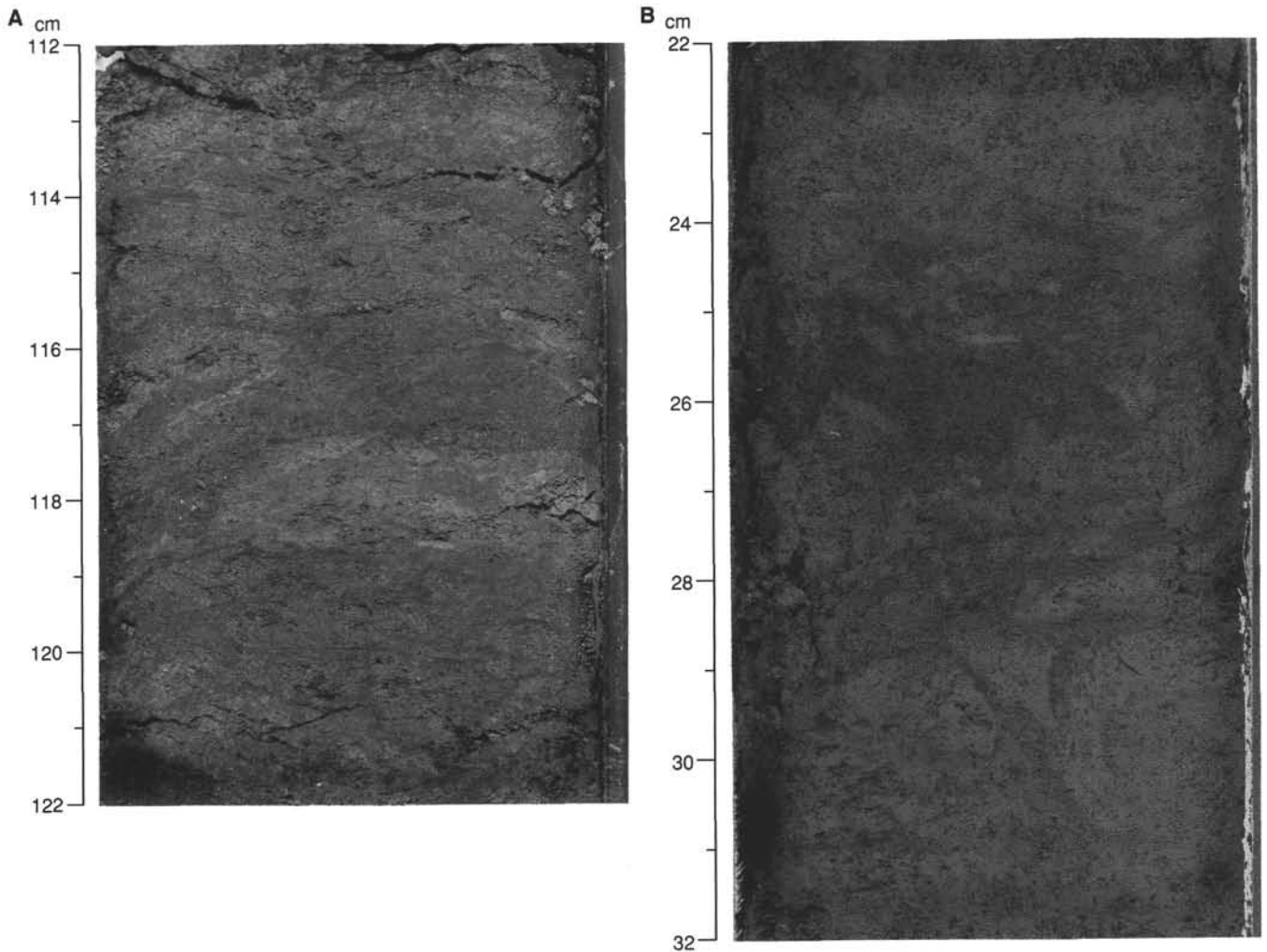


Figure 32. Examples of stratal disruption of beds of clayey silt and calcareous silt recovered from shallow depths (as little as 33 mbsf). **A.** Subhorizontal stratal disruption from Section 146-892E-3H-4, 112–122 cm. The subtle darker gray bands are a pervasive network of millimeter-scale shear zones surrounding lenses of disrupted bedding. This photo is from an APC core; thus, it contains no rotational drill-induced deformation. **B.** An example of more heterogeneous disruption, exhibiting shear zones and folded bedding (Section 146-892D-6X-3, 22–32 cm).

fabric (Fig. 35D). The rest of Core 146-892D-10X, in which recovery was excellent, exhibits alternations of *mélange* and gouge fabric, with quite variable dips. It is possible that recumbent folding of the fabric on a scale of tens of centimeters is present; alternatively the fabric may have been subjected to artificial differential rotation by XCB biscuiting, although biscuit surfaces are not clearly present. Some intervals contain angular calcareous mudstone blocks that have asymmetric stringers of mud extending from their top and bottom surfaces and parallel to the local shear fabric (Fig. 35A).

The *mélange* fabric persists into Section 146-892D-11X (110 mbsf) and is succeeded downhole by an interval of open scaly fractures. This fabric dominates through Cores 146-892D-11X to -16X (110–166 mbsf). The fragments have generally been partially disaggregated by drilling, and they exhibit polished and commonly slickenlined surfaces. Orientation was not well preserved, except in a few locations where fractures are pervasive and highly variable. Interspersed throughout all of these cores are intervals of a few to a few tens of centimeters that are intact and unfractured. These intact intervals invariably exhibit stratal disruption or *mélange* fabric. Unlike Hole 892A, less deformed material, interpreted as below the fault, was not recovered, lending support to the argument that Core 146-892A-20X is a block in the *mélange*, rather than true footwall material.

## Summary and Conclusions

Site 892 exhibits a high degree of variability among several holes separated by only tens of meters. Hole 892A penetrated an upper structural domain from 0 to 52 mbsf that exhibits moderately dipping bedding, probably emplaced in fault contact above a more shallowly dipping fractured interval (Fig. 30). This second domain, which exhibits evidence for some shear deformation, extends down to about 106 mbsf. From at least 116 mbsf (and possibly from 106 mbsf) to at least 147 mbsf, a highly sheared zone of subhorizontal stratal disruption, scaly fabric, and incipient *mélange* was recovered, which is interpreted as a mature fault zone. The downhole variation in fault-fabric development lends support to the interpretation that an active fault strand may be located at the top of the fault-fabric interval, in the fractured sediments at about 106 mbsf (Core 146-892A-14X), although others may be present. Further support for this interpretation comes from Hole 892D, where the most intensely deformed zone recovered is at 100–110 mbsf.

Hole 892D recovered stratially disrupted material and a *mélange* fabric from about 38 mbsf to the total depth of 166.5 mbsf. From 110 to 166.5 mbsf, the fabrics are intercalated with intervals of open scaly fractures. Evidence is present for microscale to mesoscale folding of

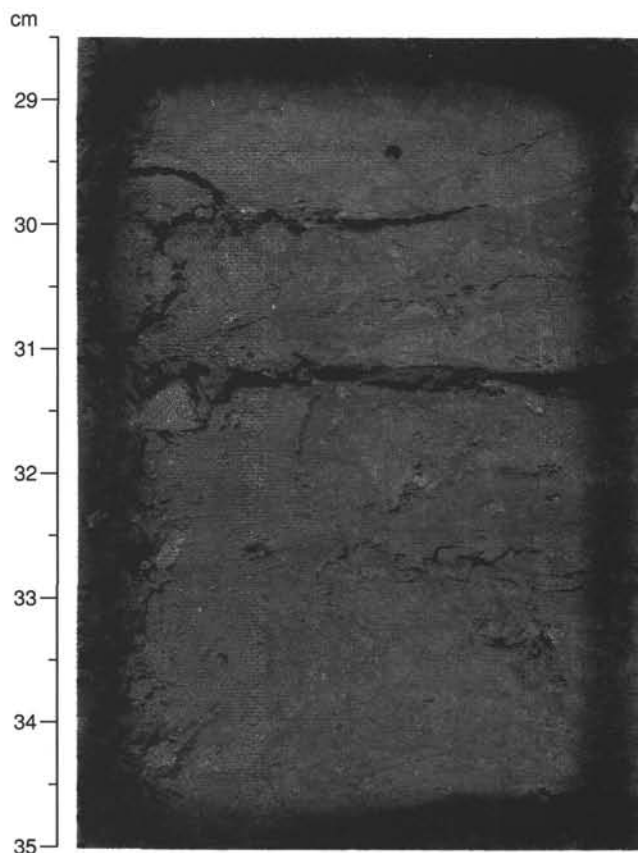


Figure 33. Disrupted sand layers of Section 146-892A-18X-1. The sand lenses are bounded by subhorizontal, anastomosing dark shear zones, forming an incipient mélangé. Shear zones exhibit polished curvilinear scaly surfaces when broken open.

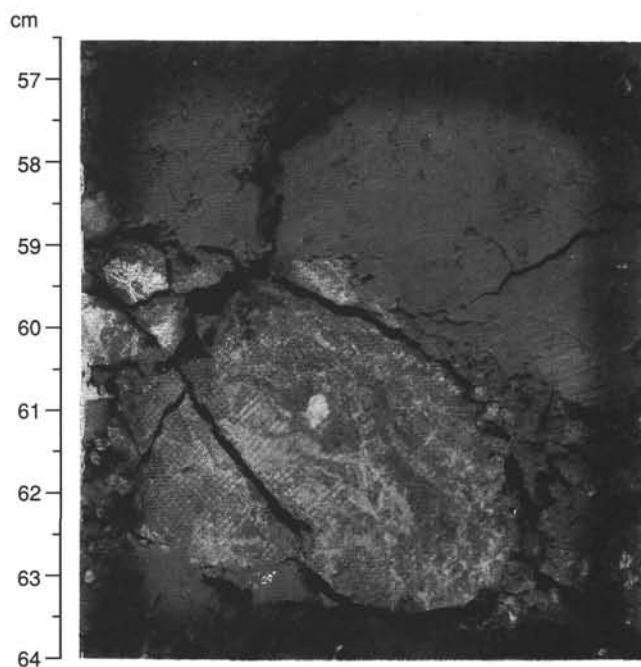


Figure 34. Brecciated and veined dolomitic (?) concretion included in incipient mélangé of Section 146-892A-18X-1, 56.5–64 cm.

the shear fabric at about 104 mbsf and for microscale folding of the bedding in several locations throughout the interval from 38 to 166.5 mbsf.

Synthesizing the results from all three cored holes at Site 892 is difficult because of the large lateral variation in fabrics from hole to hole. Taken together, the cores indicate a complexly deformed zone throughout most of the cored interval from about 30 to 170 mbsf. The major thrust common to both Holes 892A and 892D is the thick sequence of shear-induced fabrics recovered from about 100 to at least 165 mbsf that suggest a major thrust fault zone. In addition, the sediments structurally above this zone have been extensively and heterogeneously subjected to stratal disruption, producing broken formation and proto-mélangé from as shallow as 38 mbsf to the top of the thrust. This fabric suggests extensive distributed shear strain in the hanging wall of the thrust.

The material recovered between 100 and 170 mbsf displays a wide range of distinct structural fabrics that appear macroscopically to be different responses to thrust shearing depending on lithologic characteristics such as induration, grain size, and especially degree of cementation. Detailed information regarding factors controlling the formation of these fabrics and the internal structure of the fault zone requires post-cruise microstructural studies.

## ORGANIC GEOCHEMISTRY

### Overview

The sediments encountered during drilling of Site 892 consist mainly of accreted hemipelagic clays and fine-grained (silt) turbidites. Organic carbon varies between 0.94 and 1.92 wt% in Hole 892A. Sediments surprisingly rich in  $H_2S$  (more than 10,000 ppmv in expansion void gases) were encountered at only 3.6 mbsf, but the concentration declined to zero at 80 mbsf. The sediments between 2 and 9 mbsf also contained pieces of gas hydrate up to 2 cm in length. Most of the gas hydrate was, however, distributed in the sediment matrix as white pellets, about 0.5 cm in diameter. Methane and higher order hydrocarbons of mixed biogenic and thermogenic origin are found above 67.5 mbsf. Below this depth thermogenic hydrocarbons are abundant. Their distribution suggests active migration at 67.5 and 107 mbsf.

### Introduction

Shipboard organic geochemical analyses of sediments from Hole 892A included volatile hydrocarbon and nonhydrocarbon gases; total carbon, organic carbon, nitrogen, and sulfur; fluorescence intensity; hexane-soluble lipid/bitumen analysis; and Rock-Eval/Geofina analysis. The instrumentation, operating conditions, and procedures are summarized in the "Explanatory Notes" chapter (this volume).

Shipboard organic geochemical analyses of sediments from Holes 892D and 892E were limited to volatile hydrocarbon and nonhydrocarbon gases because of lack of time at the end of the leg. The data for Holes 892D and 892E are included here, but are only discussed preliminarily.

### Organic Carbon

In Subunit IA (Hole 892A, 0–67.75 mbsf),  $C_{org}$  fluctuates between 0.94 and 1.84 wt% (Fig. 36). In Subunit IB,  $C_{org}$  is generally greater than 1.4 wt%, with the exception of a minimum value of 0.96 wt% at 116.9 mbsf. The highest value (1.92 wt%) was found at 145.8 mbsf (Table 6 and Fig. 36).

### Total Nitrogen

Total nitrogen ( $N_{tot}$ ) generally varies sympathetically with the organic carbon contents at Hole 892A (Table 6 and Fig. 36). The total nitrogen concentrations range from 0.09 wt% at 12.5 mbsf to 0.18 wt% at several sample depths in Hole 892A.

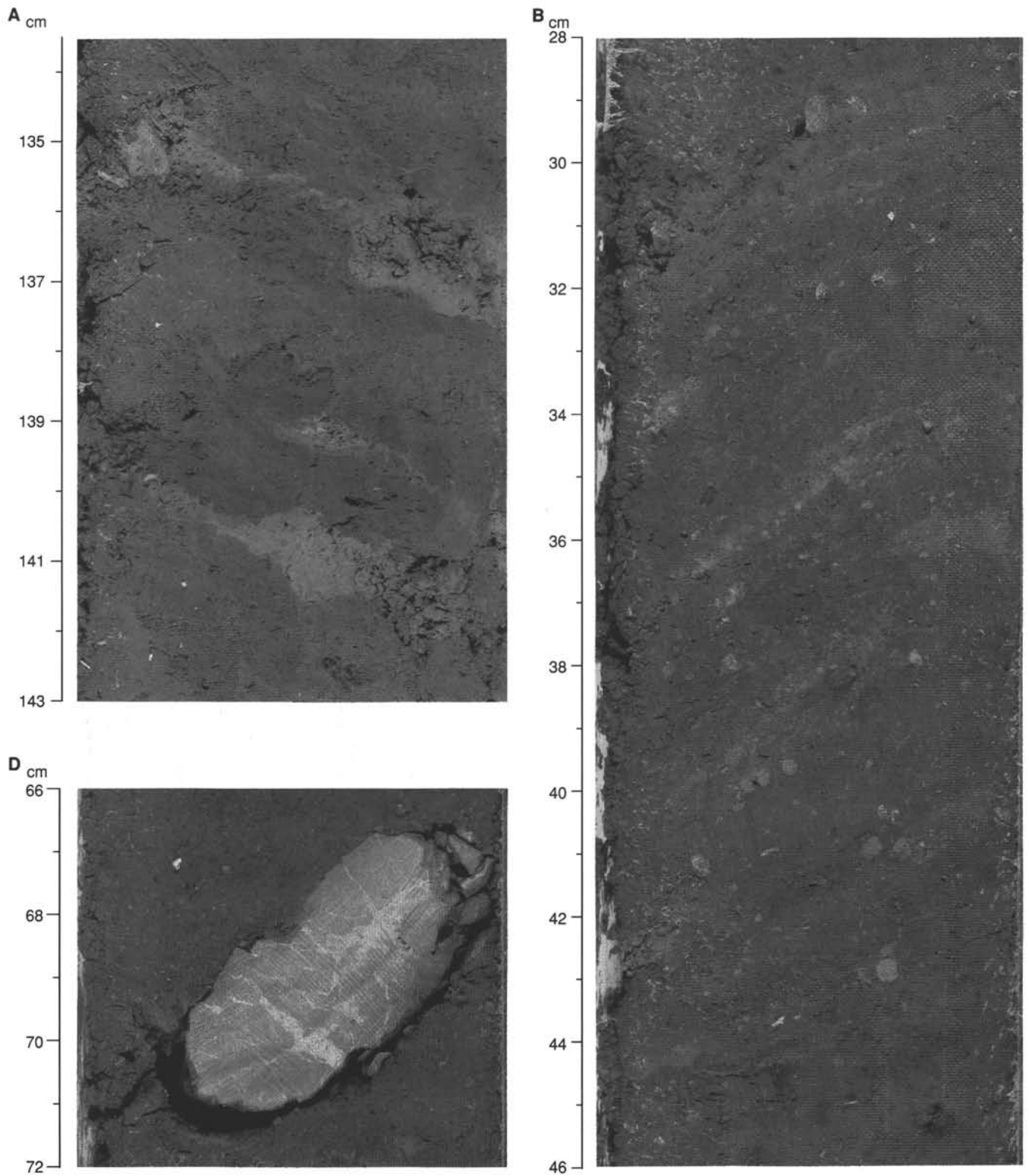


Figure 35. **A.** Disruption of blocks of calcareous mudstone in the consolidated fault zone fabric (Section 146-892D-10X-4, 133.5–143 cm). Asymmetric stringers of mud extend from the margins of the blocks. **B.** Example of interval of shear fabric macroscopically resembling gouge from 106 mbsf with dispersed broken grains of carbonate cement and small block of cemented siltstone (Section 146-892D-10X-4, 28–46 cm). The fabric is planar on the core scale, and dips from right to left in the photo. **C.** Example of disaggregated angular fragments typical of scaly fabric in fault zone intervals with apparently open fractures (Section 146-892D-12X-1, 38–56 cm [120 mbsf]). **D.** Close-up of a block-in-matrix concretion recovered with the fault zone at 106 mbsf (Section 146-892D-10X-4, 66–72 mbsf). Extensional calcite veins in the block are dominantly perpendicular to the shear fabric, whereas the long axis of the concretion is parallel to the fabric.

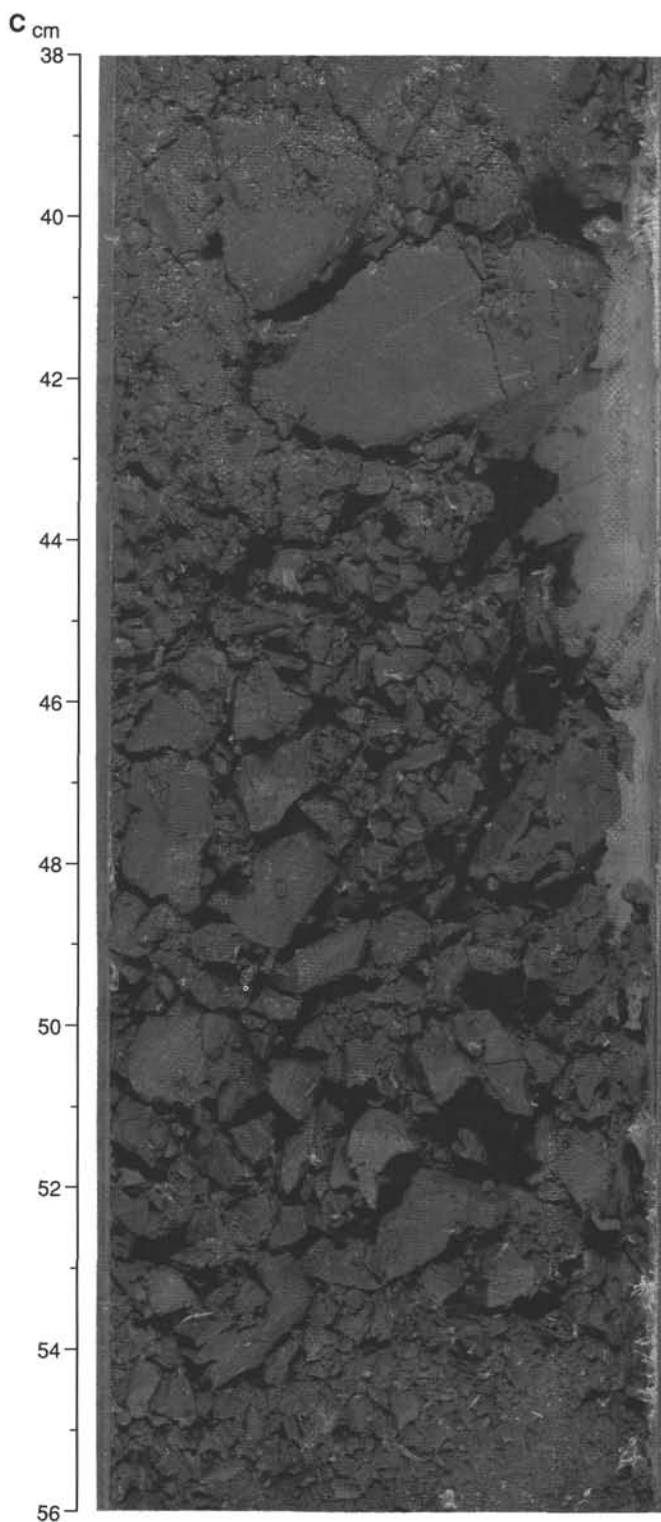


Figure 35 (continued).

Regression of  $C_{org}$  with  $N_{tot}$  gives a C/N ratio of 10:1, which is indicative of a mixed source of marine and terrigenous organic matter (Fig. 37).

#### Total Sulfur

Total sulfur ( $S_{tot}$ ) in Hole 892A varies between 1.47 wt% at 40.5 mbsf and 0.65 wt% at 116.9 mbsf (Table 6 and Fig. 36). The sulfur in the sediments is probably derived from the reduction of  $SO_4^{2-}$ . The

Table 6. Carbon, nitrogen, and sulfur data from Hole 892A.

| Core, section, interval (cm) | Depth (mbsf) | Inorganic carbon (wt%) | CaCO <sub>3</sub> (wt%) | Total carbon (wt%) | Organic carbon (wt%) | Total nitrogen (wt%) | Total sulfur (wt%) |
|------------------------------|--------------|------------------------|-------------------------|--------------------|----------------------|----------------------|--------------------|
| 146-892A-                    |              |                        |                         |                    |                      |                      |                    |
| 1X-5, 10-13                  | 3.8          | 0.15                   | 1.25                    | 1.33               | 1.18                 | 0.11                 | 0.8                |
| 2X-3, 0-11                   | 12.5         | 0.17                   | 1.42                    | 1.11               | 0.94                 | 0.09                 | 1.2                |
| 3X-2, 0-10                   | 20.5         | 0.11                   | 0.92                    | 1.66               | 1.55                 | 0.17                 | 1.3                |
| 3X-3, 0-10                   | 21.8         | 0.41                   | 3.42                    | 1.63               | 1.22                 | 0.13                 | 0.9                |
| 4X-2, 0-10                   | 29.5         | 0.54                   | 4.50                    | 2.38               | 1.84                 | 0.18                 | 1.0                |
| 6X-2, 0-10                   | 40.5         | 0.68                   | 5.66                    | 2.37               | 1.69                 | 0.15                 | 1.5                |
| 7X-5, 140-150                | 55.9         | 0.16                   | 1.33                    | 1.72               | 1.56                 | 0.17                 | 0.8                |
| 8X-3, 0-10                   | 61.0         | 1.53                   | 12.70                   | 3.04               | 1.51                 | 0.15                 | 0.9                |
| 9X-1, 69-74                  | 68.2         | 0.08                   | 0.67                    | 1.34               | 1.26                 | 0.15                 | 1.4                |
| 11X-2, 0-10                  | 79.5         | 0.27                   | 2.25                    | 1.83               | 1.56                 | 0.18                 | 0.8                |
| 12X-1, 0-7                   | 87.5         | 1.51                   | 12.60                   | 3.15               | 1.64                 | 0.18                 | 0.9                |
| 13X-6, 69-82                 | 101.6        | 0.22                   | 1.83                    | 1.73               | 1.51                 | 0.18                 | 1.1                |
| 14X-1, 35-38                 | 106.9        | 0.30                   | 2.50                    | 1.83               | 1.53                 | 0.16                 | 1.1                |
| 15X-1, 88-100                | 116.9        | 0.32                   | 2.67                    | 1.28               | 0.96                 | 0.14                 | 0.7                |
| 16X-1, 34-43                 | 125.8        | 0.69                   | 5.75                    | 2.12               | 1.43                 | 0.17                 | 0.8                |
| 17X-2, 3-13                  | 135.6        | 0.20                   | 1.67                    | 1.76               | 1.56                 | 0.18                 | 1.1                |
| 18X-1, 140-150               | 145.9        | 0.21                   | 1.75                    | 2.13               | 1.92                 | 0.18                 | 1.3                |
| 20X-2, 0-10                  | 165.0        | 0.66                   | 5.50                    | 2.04               | 1.38                 | 0.16                 | 0.8                |
| 20X-3, 0-10                  | 166.5        | 0.14                   | 1.17                    | 1.50               | 1.36                 | 0.16                 | 0.8                |

two highest values, 1.47 and 1.44 wt%, occur at 40.5 and 68 mbsf, respectively. The latter value corresponds with the depth of a sharp rise in thermogenic hydrocarbons.

#### Hydrogen Sulfide

Sediments containing white pieces of gas hydrate and a surprisingly high content of  $H_2S$  were encountered at only 1.8 mbsf. The level of  $H_2S$  declined to zero at about 80 mbsf. Whereas headspace gases only gave trace amounts of  $H_2S$ , extremely high values were found in the expansion void gases (Tables 7-8 and Fig. 38). Shipboard determination of the absolute  $H_2S$  concentration in the expansion void gases proved difficult because of the lack of suitable high-concentration  $H_2S$  standards. The concentrations provided here were roughly determined (Table 8 and Fig. 38) by linear extrapolation. This uncertainty should be borne in mind in the following.

The highest  $H_2S$  concentrations (10,716 and 7,538 ppmv) were found in the first core, at 1.78 and 3.55 mbsf, respectively. The  $H_2S$  concentration in the second core was 6,513 ppmv (at 15.15 mbsf). At 21.71 mbsf concentrations were lower by a factor of about 1000. Below 81 mbsf no trace of  $H_2S$  was detected, either in the expansion void gases or in headspace gases.

Hydrogen sulfide was also found in Holes 892D and 892E in high concentrations (Table 8). The highest concentrations (19,539 ppmv) occurred at 10.55 mbsf in Hole 892D. However, no hydrogen sulfide occurred below 28.34 mbsf in Hole 892D.

#### Visible Gas Hydrates

The sediments sampled in the two first cores, between 3.6 and about 18 mbsf, contained white pieces of gas hydrate up to 2 cm in length. Most of the gas hydrate was, however, distributed in the sediment matrix as white pellets, about 0.5 cm in diameter.

The headspace (HS) and expansion void gas (EVG) analyses show that the gases released from these sediments consist mainly of methane (132,767 ppmv at 3.67 mbsf) with minor amounts of carbon dioxide (578 ppmv at 3.67 mbsf) and ethane (77 ppmv at 3.67 mbsf) (see Table 7 and Fig. 39). In addition, a gas species previously not recorded on this leg, carbon disulfide ( $CS_2$ ), was identified in the EVG gases, but only from the gas hydrate zone.

Visible gas hydrates were also present at Hole 892D and 892E in the upper two cores.

#### Headspace Gases

Beside  $H_2S$ , the other volatile gases (hydrocarbons,  $CO_2$ ,  $N_2$ , and  $O_2$ ) released by the sediments recovered at Site 892 were measured

Table 7. Molecular composition of headspace gases at Site 892.

| Core, section, interval (cm) | Method | Depth (mbsf) | O <sub>2</sub> | N <sub>2</sub> | C <sub>1</sub> | CO <sub>2</sub> | C <sub>2=</sub> | C <sub>2</sub> | H <sub>2</sub> S | C <sub>3</sub> | iC <sub>4</sub> | nC <sub>4</sub> | iC <sub>5</sub> | nC <sub>5</sub> | iC <sub>6</sub> | nC <sub>6</sub> | ΣC <sub>2+</sub> | C <sub>1</sub> /C <sub>2</sub> | C <sub>1</sub> /C <sub>2+</sub> |
|------------------------------|--------|--------------|----------------|----------------|----------------|-----------------|-----------------|----------------|------------------|----------------|-----------------|-----------------|-----------------|-----------------|-----------------|-----------------|------------------|--------------------------------|---------------------------------|
| 146-892A-                    |        |              |                |                |                |                 |                 |                |                  |                |                 |                 |                 |                 |                 |                 |                  |                                |                                 |
| 1X-2, 0-2                    | HS     | 1.51         | 161918         | 692267         | 80252          | 1713            |                 | 32             | Tr               |                |                 |                 | 1.4             |                 |                 | 3.9             | 37               | 2541                           | 2172                            |
| 1X-4, 13-15                  | HS     | 3.67         | 154836         | 740766         | 132767         | 578             |                 | 77             |                  |                |                 |                 |                 |                 |                 |                 | 77.3             | 1718                           | 1718                            |
| 2X-3, 0-5                    | HS     | 12.53        | 151045         | 687839         | 129760         | 393             |                 | 53             | Tr               |                |                 |                 |                 |                 |                 |                 | 53               | 2442                           | 2442                            |
| 3X-1, 0-5                    | HS     | 19.03        | 188098         | 757871         | 39861          | 5701            |                 | 10             |                  |                |                 |                 |                 |                 |                 |                 | 10               | 3908                           | 3908                            |
| 3X-3, 0-5                    | HS     | 22.03        | 176566         | 783687         | 33947          | 1684            |                 | 16             |                  |                |                 |                 |                 |                 |                 |                 | 16               | 2095                           | 2095                            |
| 4X-1, 95-100                 | HS     | 29.48        | 179080         | 762634         | 50447          | 3533            |                 | 34             |                  |                |                 |                 |                 |                 |                 |                 | 34               | 1497                           | 1497                            |
| 6X-1, 145-150                | HS     | 40.48        | 153340         | 667552         | 38213          | 2601            | Tr              | 31             |                  | 0.8            | Tr              | 1.8             | 2.4             | Tr              |                 |                 | 36               | 1234                           | 1063                            |
| 7X-6, 0-5                    | HS     | 56.03        | 127472         | 698926         | 58799          | 9700            |                 | 43             |                  | 1.9            | 4.5             |                 | 6.7             |                 | 2.3             | 0.9             | 59               | 1364                           | 990                             |
| 8X-3, 145-150                | HS     | 62.48        | 103641         | 719730         | 60327          | 5420            | 1.0             | 41             |                  | 6.8            | 5.1             | 3.4             | 3.2             | 1.5             | 6.5             |                 | 68               | 1475                           | 884                             |
| 9X-1, 0-5                    | HS     | 67.53        | 162469         | 645999         | 61564          | 5420            |                 | 281            |                  | 39.4           | 32.6            | 31.4            | 45.9            | 16.2            | 10.7            | 9.2             | 467              | 219                            | 132                             |
| 9X-1, 64-69                  | HS     | 68.17        | 114746         | 710498         | 10015          | 5420            | 0.9             | 339            |                  | 17.0           | 15.8            | 15.4            | 58.9            | 3.6             | 6.7             | 4.1             | 461              | 29.5                           | 22                              |
| 11X-2, 10-15                 | HS     | 79.63        | 143192         | 704554         | 35800          | 334             |                 | 264            |                  | 35.8           | 38.3            |                 | 8.2             |                 | 1.9             |                 | 348              | 136                            | 103                             |
| 12X-1, 60-65                 | HS     | 88.13        | 167365         | 781741         | 25299          | 6451            | Tr              | 167            |                  | 29.4           | 20.4            | 2.6             | 17.7            | 1.8             |                 |                 | 239              | 152                            | 106                             |
| 13X-3, 96-101                | HS     | 100.99       | 176890         | 1028848        | 20081          | 4741            | Tr              | 121            |                  | 23.1           | 28.5            | Tr              | 12.6            |                 | 2.2             |                 | 188              | 166                            | 107                             |
| 13X-8, 0-5                   | HS     | 103.45       | 162343         | 1055523        | 61304          | 4849            | Tr              | 186            |                  | 29.4           | 31.5            | 3.9             | 28.5            |                 | 2.5             | 2.7             | 285              | 329                            | 215                             |
| 14X-1, 6-11                  | HS     | 106.59       | 173101         | 718681         | 32385          | 1147            | Tr              | 249            |                  | 58.8           | 47.1            | 20.5            | 22.6            | 5.5             | 1.6             | 0.3             | 406              | 130                            | 80                              |
| 14X-1, 20-25                 | HS     | 106.73       | 147248         | 781741         | 12530          | 2941            | Tr              | 327            |                  | 116.2          | 45.1            | 31.3            | 43.6            | 9.3             | 4.6             | 4.4             | 581              | 38.3                           | 22                              |
| 15X-1, 98-100                | HS     | 116.99       | 146993         | 686294         | 47617          | 11138           | Tr              | 354            |                  | 102.8          | 50.2            | 5.0             | 28.3            |                 | 4.3             |                 | 544              | 135                            | 87                              |
| 16X-1, 41-43                 | HS     | 125.92       | 191269         | 925261         | 19513          | 4060            | Tr              | 525            |                  | 267.5          | 109.5           | 52.8            | 123.4           | 9.7             | 14.6            | 2.5             | 1105             | 37.2                           | 18                              |
| 17X-2, 0-3                   | HS     | 135.61       | 207599         | 808947         | 61211          | 3056            | Tr              | 302            |                  | 33.9           | 10.2            | 2.6             | 8.3             | 2.4             | 2.7             |                 | 362              | 203                            | 169                             |
| 18X-2, 0-5                   | HS     | 146.03       |                |                | 11856          | 3056            |                 | 188            |                  | 50.4           |                 |                 |                 |                 |                 |                 | 238              | 63.2                           | 50                              |
| 20X-CC, 0-5                  | HS     | 167.07       | 147042         | 734007         | 18868          | 2680            |                 | 51             |                  | 18.1           | 19.7            | 8.3             | 12.9            | 8.7             | 4.4             | 3.9             | 127              | 367                            | 148                             |
| 20X-2, 145-150               | HS     | 166.48       | 116652         | 725586         | 28625          | 846             |                 | 106            |                  | 33.1           | 35.2            | 8.5             | 24.5            | 3.7             | 3.9             | 1.6             | 217              | 269                            | 132                             |
| 21X-1, 7-12                  | HS     | 173.10       | 201518         | 788412         | 95309          | 906             |                 | 176            |                  | 25.6           | 22.9            | 18.9            | 19.7            | 16.4            | 5.3             | 6.0             | 291              | 541                            | 327                             |
| 146-892D-                    |        |              |                |                |                |                 |                 |                |                  |                |                 |                 |                 |                 |                 |                 |                  |                                |                                 |
| 1X-1, 5-7                    | HS     | 0.06         | 145672         | 638348         | 517            | 543             |                 | 5              |                  | 0.4            |                 |                 |                 |                 |                 |                 | 5.5              | 102                            | 94                              |
| 2X-1, 0-5                    | HS     | 8.53         | 184162         | 711913         | 5893           | 407             |                 | 1              |                  | 0.1            |                 |                 |                 |                 |                 |                 | 1.4              | 4397                           | 4092                            |
| 2X-2, 0-5                    | HS     | 10.03        | 121472         | 697491         | 70147          | 932             |                 | 22             |                  |                |                 |                 |                 |                 |                 |                 | 22               | 3248                           | 3248                            |
| 2X-2, 145-150                | HS     | 11.48        | 144870         | 673071         | 10062          | 571             |                 | 16             |                  | 5.7            | 2.2             | 1.9             | 3.9             | 3.3             |                 |                 | 33               | 647                            | 309                             |
| 3X-1, 0-5                    | HS     | 18.03        | 187573         | 758607         | 36104          | 1934            |                 | 15             |                  | 0.1            |                 |                 |                 |                 |                 |                 | 15               | 2423                           | 2407                            |
| 3X-2, 0-5                    | HS     | 19.53        | 123895         | 596837         | 18222          | 2353            |                 | 8              |                  | 0.1            |                 |                 |                 |                 |                 |                 | 8.4              | 2185                           | 2159                            |
| 4X-2, 0-4                    | HS     | 29.02        | 197011         | 774283         | 14399          | 3716            |                 | 31             |                  | 0.6            |                 |                 |                 |                 |                 |                 | 32               | 458                            | 449                             |
| 4X-3, 30-35                  | HS     | 30.83        | 117260         | 565663         | 9509           | 8475            |                 | 6              |                  | Tr.            |                 |                 |                 |                 |                 |                 | 5.6              | 1704                           | 1704                            |
| 4X-3, 95-100                 | HS     | 31.48        | 194465         | 781034         | 8306           | 4097            |                 | 14             |                  | 0.4            | 2.5             |                 |                 |                 |                 |                 | 17               | 596                            | 493                             |
| 5X-2, 0-5                    | HS     | 38.53        | 203576         | 787825         | 46883          | 4492            |                 | 23             |                  | 0.6            |                 |                 |                 |                 |                 |                 | 23               | 2047                           | 1998                            |
| 5X-3, 0-5                    | HS     | 40.03        | 120194         | 544113         | 36492          | 3598            |                 | 39             |                  | 0.8            |                 |                 |                 |                 | 4.6             | 2.9             | 47               | 948                            | 781                             |
| 6X-4, 135-140                | HS     | 52.38        | 160326         | 666856         | 24069          | 4070            | Tr              | 29             |                  | 1.2            |                 |                 |                 |                 |                 |                 | 30               | 845                            | 811                             |
| 7X-4, 145-150                | HS     | 59.98        | 161842         | 687668         | 31143          | 4335            |                 | 29             |                  | 3.3            | 1.8             |                 |                 |                 | 2.0             |                 | 36               | 1089                           | 874                             |
| 8X-3, 10-15                  | HS     | 64.83        | 163236         | 790548         | 10078          | 1975            | Tr              | 17             |                  | 5.8            | 9.0             | 1.2             |                 |                 |                 |                 | 33               | 583                            | 302                             |
| 9X-4, 15-20                  | HS     | 73.98        | 125804         | 634234         | 38891          | 4546            |                 | 237            |                  | 31.3           | 41.0            | 5.1             | 27.3            |                 |                 |                 | 342              | 164                            | 114                             |
| 10X-4, 15-20                 | HS     | 104.68       | 2575           | 4779           | 54819          | 620             |                 | 385            |                  | 629.9          | 158.0           | 185.7           | 86.0            | 47.8            | 22.8            | 5.0             | 1520             | 142                            | 36                              |
| 10X-6, 0-5                   | HS     | 107.53       | 60632          | 260612         | 43753          | 125             |                 | 613            |                  | 576.0          | 191.3           | 400.0           | 142.9           | 77.6            | 14.2            | 0.8             | 2016             | 71.3                           | 22                              |
| 11X-1, 125-130               | HS     | 110.78       | 54405          | 249574         | 54511          | 3233            |                 | 621            |                  | 101.0          | 10.9            | 3.0             | 29.8            | 3.0             |                 | 769             | 87.8             | 71                             | 3                               |
| 12X-4, 0-5                   | HS     | 123.53       | 153879         | 696886         | 55436          | 2893            |                 | 408            |                  | 76.6           | 36.7            | 2.7             | 42.4            |                 | 4.4             |                 | 570              | 136                            | 97                              |
| 14X-2, 0-5                   | HS     | 139.53       | 206460         | 851797         | 42269          | 3531            |                 | 109            |                  | 15.2           | 11.9            |                 | 4.9             |                 |                 |                 | 141              | 389                            | 300                             |
| 15X-3, 0-5                   | HS     | 150.53       | 135574         | 638314         | 65074          | 963             | Tr              | 269            |                  | 48.3           | 8.4             |                 | 7.6             |                 | 2.2             |                 | 335              | 242                            | 194                             |
| 16X-3, 0-5                   | HS     | 160.03       | 142266         | 614633         | 106913         | 5155            | Tr              | 247            |                  | 30.8           | 19.2            | 3.1             | 9.6             |                 |                 |                 | 310              | 433                            | 345                             |
| 146-892E-                    |        |              |                |                |                |                 |                 |                |                  |                |                 |                 |                 |                 |                 |                 |                  |                                |                                 |
| 1X-1, 0-5                    | HS     | 0.03         | 42504          | 249592         | 730754         | 3397            | Tr              | 593            |                  | 0.3            | 0.9             |                 |                 |                 |                 |                 | 594              | 1233                           | 1230                            |
| 1X-1, 128-132                | HS     | 1.30         | 99929          | 703422         | 43950          | 7116            | Tr              | 31             |                  | 0.6            |                 | 0.5             |                 |                 |                 |                 | 32               | 1432                           | 1384                            |
| 1X-2, 125-130                | HS     | 2.78         | 80713          | 381245         | 542390         | 4257            | Tr              | 448            |                  | 0.3            | 2.9             |                 |                 |                 |                 |                 | 451              | 1211                           | 1202                            |
| 3H-5, 125-130                | HS     | 40.28        | 136336         | 261470         | 57984          | 866             | Tr              | 50             |                  | 0.3            | 3.3             |                 |                 |                 |                 |                 | 54               | 1150                           | 1074                            |
| 146-892A-                    |        |              |                |                |                |                 |                 |                |                  |                |                 |                 |                 |                 |                 |                 |                  |                                |                                 |
| 1X-4, 13-15                  | HH     | 3.67         | 178369         | 872556         | 66408          | 504             |                 | 30             | 11733            | 1.4            | 21.2            |                 |                 |                 |                 | 4.0             | 56               | 2244                           | 1182                            |
| 1X-4, 13-15                  | HH     | 3.67         | 152440         | 598181         | 10210          | 711             |                 | 8              | 12280            | 1.5            | 3.1             | 28.4            |                 |                 |                 |                 | 41               | 1207                           | 246                             |
| 1X-4, 13-15                  | HH     | 3.67         | 209043         | 890491         | 36026          | 274             |                 | 12             |                  |                |                 |                 |                 |                 |                 |                 | 12               | 3116                           | 3116                            |
| 1X-4, 13-15                  | HH     | 3.67         | 165080         | 747892         | 46085          | 731             |                 | 22             | 12408            | 1.5            |                 | 31.0            |                 |                 |                 |                 | 55               | 2056                           | 840                             |

Note: HS = headspace method, and HH = headspace gases from hydrate in syringes. C<sub>n</sub> = n-alkanes, iC<sub>n</sub> = iso-alkanes, nC<sub>n</sub> = normal alkanes, C<sub>2=</sub> = unsaturated alkanes, and ΣC<sub>2+</sub> = (C<sub>2</sub> + C<sub>3</sub> + ... + C<sub>6</sub>), U/D = C<sub>1</sub>/C<sub>2</sub> > 10<sup>6</sup>. Values for O<sub>2</sub> and N<sub>2</sub> are uncorrected for volume and represent relative measures only. Tr = trace.

Table 8. Molecular composition of expansion void gases at Site 892.

| Core, section, interval (cm) | Depth (mbsf) | O <sub>2</sub> | N <sub>2</sub> | C <sub>1</sub> | CO <sub>2</sub> | C <sub>2=</sub> | C <sub>2</sub> | H <sub>2</sub> S | C <sub>3</sub> | iC <sub>4</sub> | nC <sub>4</sub> | iC <sub>5</sub> | nC <sub>5</sub> | iC <sub>6</sub> | nC <sub>6</sub> | ΣC <sub>2+</sub> | C <sub>1</sub> /C <sub>2</sub> | C <sub>1</sub> /C <sub>2+</sub> |
|------------------------------|--------------|----------------|----------------|----------------|-----------------|-----------------|----------------|------------------|----------------|-----------------|-----------------|-----------------|-----------------|-----------------|-----------------|------------------|--------------------------------|---------------------------------|
| 146-892A-                    |              |                |                |                |                 |                 |                |                  |                |                 |                 |                 |                 |                 |                 |                  |                                |                                 |
| 1X-2, 27-28                  | 1.78         | 45756          | 194880         | 802197         | 717             |                 | 808            | 10716            |                |                 |                 |                 |                 |                 |                 | 807.9            | 993                            | 993                             |
| 1X-3, 54-55                  | 3.55         | 26591          | 115715         | 805749         | 1342            |                 | 819            | 7538             |                |                 |                 |                 |                 |                 |                 | 818.5            | 984                            | 984                             |
| 2X-4, 114-115                | 15.15        | 69990          | 295237         | 724806         | 508             |                 | 596            | 6513             |                |                 |                 |                 |                 | 0.9             | 0.8             | 597.2            | 1217                           | 1214                            |
| 3X-2, 120-121                | 21.71        | 37946          | 225897         | 919909         | 1217            |                 | 359            | 10               | 1.0            |                 |                 |                 |                 |                 |                 | 360.0            | 2562                           | 2555                            |
| 4X-2, 11-12                  | 30.12        | 133002         | 519833         | 455003         | 2155            |                 | 678            | 21               | 0.6            |                 |                 |                 |                 |                 |                 | 678.2            | 671                            | 671                             |
| 6X-2, 74-74                  | 41.24        | 50542          | 211185         | 360704         | 333             |                 | 446            | 1                | 2.7            |                 |                 |                 |                 |                 |                 | 448.7            | 809                            | 804                             |
| 6X-3, 148-148                | 43.48        | 21718          | 98855          | 851695         | 4570            |                 | 994            | 10               | 6.1            |                 |                 |                 |                 |                 |                 | 999.8            | 857                            | 852                             |
| 7X-7, 22-22                  | 57.72        | 30449          | 128382         | 854304         | 2965            | 77              | 2070           | 16               | 11.1           | 7.3             | 7.1             | 5.8             |                 | 1.1             | 1.8             | 2181.2           | 413                            | 392                             |
| 8X-4, 135-135                | 63.85        | 33932          | 155427         | 848342         | 8094            | 64              | 1155           | 24               | 32.6           | 9.9             | 4.3             | 4.3             |                 |                 | 1.6             | 1272.0           | 734                            | 667                             |
| 11X-3, 26-26                 | 81.26        | 31388          | 164599         | 931873         | 3039            |                 | 6322           | 0                | 273.0          | 121.0           | 1.9             | 10.4            |                 |                 |                 | 6728.3           | 147                            | 139                             |
| 13X-4, 66-67                 | 102.17       | 7133           | 63835          | 949757         | 2715            |                 | 5311           |                  | 205.3          | 61.9            | 2.0             | 8.9             |                 |                 |                 | 6589.0           | 179                            | 170                             |
| 13X-7, 17-18                 | 106.18       | 200333         | 757084         | 266039         | 777             |                 | 763            |                  | 39.0           | 16.3            | 8.0             | 5.4             |                 |                 |                 | 832.7            | 349                            | 319                             |
| 15X-1, 83-84                 | 116.84       | 84613          | 368405         | 648209         | 4823            |                 | 7137           |                  | 3473.0         | 346.0           | 16.1            | 74.2            | 1.5             | 4.6             | 3.5             | 11055.9          | 91                             | 59                              |
| 17X-2, 63-63                 | 137.13       | 46483          | 198426         | 811411         | 27698           | 3               | 6201           |                  | 332.2          | 65.7            | 26.6            | 23.2            | 3.0             | 2.0             | 2.3             | 6659.5           | 131                            | 122                             |
| 18X-2, 6-7                   | 146.07       | 208803         | 799594         | 139571         | 533             |                 | 353            |                  | 29.4           | 9.7             | 14.7            | 17.3            | 14.0            | 6.0             | 10.2            | 454.2            | 395                            | 307                             |
| 20X-1, 147-148               | 164.98       | 158255         | 606386         | 390854         | 2060            |                 | 1007           |                  | 102.0          | 33.4            | 8.5             | 12.2            | 3.0             | 3.8             | 5.4             | 1175.3           | 388                            | 333                             |
| 20X-2, 81-82                 | 165.82       | 196486         | 737379         | 29449          |                 | 420             |                | 26               |                | 2.8             | 6.1             | 15.3            | 4.7             | 4.4             | 3.0             | 6.4              | 68.6                           | 1137                            |
| 146-892D-                    |              |                |                |                |                 |                 |                |                  |                |                 |                 |                 |                 |                 |                 |                  |                                |                                 |
| 2X-1, 50-51                  | 9.01         | 88704          | 364433         | 925696         | 8760            |                 | 827            | 8760             | 0.4            |                 |                 |                 |                 |                 |                 | 827.2            | 1120                           | 1119                            |
| 2X-2, 54-55                  | 10.55        | 55830          | 233463         | 922205         | 375             |                 | 833            | 19539            | 4.2            |                 |                 |                 |                 |                 |                 | 837.1            | 1107                           | 1102                            |
| 3X-3, 87-88                  | 21.88        | 54814          | 228730         | 837820         | 902             |                 | 586            | 7517             | 0.0            |                 |                 |                 |                 |                 |                 | 586.2            | 1429                           | 1429                            |
| 4X-1, 83-84                  | 28.34        | 53350          | 232569         | 834469         | 4670            |                 | 575            | 0                | 1.0            |                 |                 |                 |                 |                 |                 | 576.4            | 1450                           | 1448                            |
| 4X-2, 87-88                  | 29.88        | 61319          | 257959         | 843122         | 1605            |                 | 335            |                  | 1.1            |                 |                 |                 |                 |                 |                 | 335.8            | 2519                           | 2511                            |
| 5X-2, 10-11                  | 38.61        | 95             | 956            | 368856         | 0               |                 | 381            |                  | 17.6           | 8.0             |                 |                 |                 |                 |                 | 406.9            | 967                            | 906                             |
| 6X-3, 95-96                  | 50.46        | 131398         | 511620         | 745476         | 3139            |                 | 1683           |                  | 7.6            | 1.7             |                 |                 |                 |                 |                 | 1692.3           | 443                            | 441                             |
| 7X-5, 113-114                | 61.14        | 53106          | 222535         | 888714         | 5705            |                 | 2916           |                  | 16.6           | 5.0             |                 |                 |                 |                 |                 | 2937.6           | 305                            | 303                             |
| 8X-2, 120-121                | 64.41        | 39956          | 167732         | 927827         | 1624            |                 | 2944           |                  | 12.9           | 7.2             |                 |                 |                 |                 |                 | 2964.0           | 315                            | 313                             |
| 9X-5, 25-26                  | 75.56        | 45952          | 200096         | 967572         | 3667            |                 | 7722           |                  | 212.4          | 41.0            |                 |                 |                 |                 |                 | 7975.4           | 125                            | 121                             |
| 9X-6, 15-16                  | 76.96        | 35654          | 149383         | 835427         | 267             |                 | 7568           |                  | 190.8          | 101.5           |                 |                 |                 |                 |                 | 7860.3           | 110                            | 106                             |
| 10X-8, 67-68                 | 111.18       | 1947           | 1596           | 735459         | 690             |                 | 4715           |                  | 691.4          | 175.3           |                 |                 |                 |                 |                 | 5581.7           | 156                            | 132                             |
| 1X-2, 20-21                  | 111.21       | 75             | 765            | 945242         | 393             |                 | 7348           |                  | 405.6          | 10.1            |                 |                 |                 |                 |                 | 7763.7           | 129                            | 122                             |
| 12X-4, 20-21                 | 123.71       | 128165         | 501763         | 807070         | 2343            |                 | 6799           |                  | 515.4          | 71.9            |                 |                 |                 |                 |                 | 7386.3           | 119                            | 109                             |
| 14X-2, 4-5                   | 139.55       | 6125           | 255373         | 778173         | 1727            |                 | 5404           |                  | 270.4          | 83.4            |                 |                 |                 |                 |                 | 5757.8           | 144                            | 135                             |
| 15X-1, 25-25                 | 147.75       | 75159          | 303508         | 947389         | 4580            | Tr              | 5596           |                  | 383.8          | 83.9            |                 |                 |                 |                 |                 | 6063.7           | 169                            | 156                             |
| 16X-2, 25-25                 | 168.25       | 39717          | 172937         | 921328         | 4032            | Tr              | 4365           |                  | 219.4          | 63.5            |                 |                 |                 |                 |                 | 4647.9           | 211                            | 198                             |
| 16X-4, 25-25                 | 171.25       | 25334          | 112160         | 973887         | 4573            | Tr              | 4798           |                  | 271.6          | 2.0             |                 |                 |                 |                 |                 | 5071.6           | 203                            | 192                             |
| 146-892E-                    |              |                |                |                |                 |                 |                |                  |                |                 |                 |                 |                 |                 |                 |                  |                                |                                 |
| 1X-1, 25-25                  | 0.25         | 135449         | 466972         | 95             | 1424            |                 |                | 4272             |                | 1.8             |                 |                 |                 |                 |                 | 1.8              | U/D                            | 53                              |
| 3H-3, 0-1                    | 36.01        | 59449          | 246834         | 833169         | 6498            |                 | 2704           | 0                | 1.4            | 5.0             |                 |                 |                 |                 |                 | 2709.9           | 308                            | 307                             |

Note: C<sub>x</sub> = n-alkanes, iC<sub>x</sub> = iso-alkanes, nC<sub>x</sub> = normal alkanes, C<sub>2=</sub> = unsaturated alkanes, ΣC<sub>2+</sub> = (C<sub>2</sub> + C<sub>3</sub> + ... + C<sub>6</sub>), and U/D = C<sub>1</sub>/C<sub>2</sub> > 10<sup>6</sup>. Values for O<sub>2</sub> and N<sub>2</sub> are uncorrected for volume and represent relative measures only. Tr = trace.

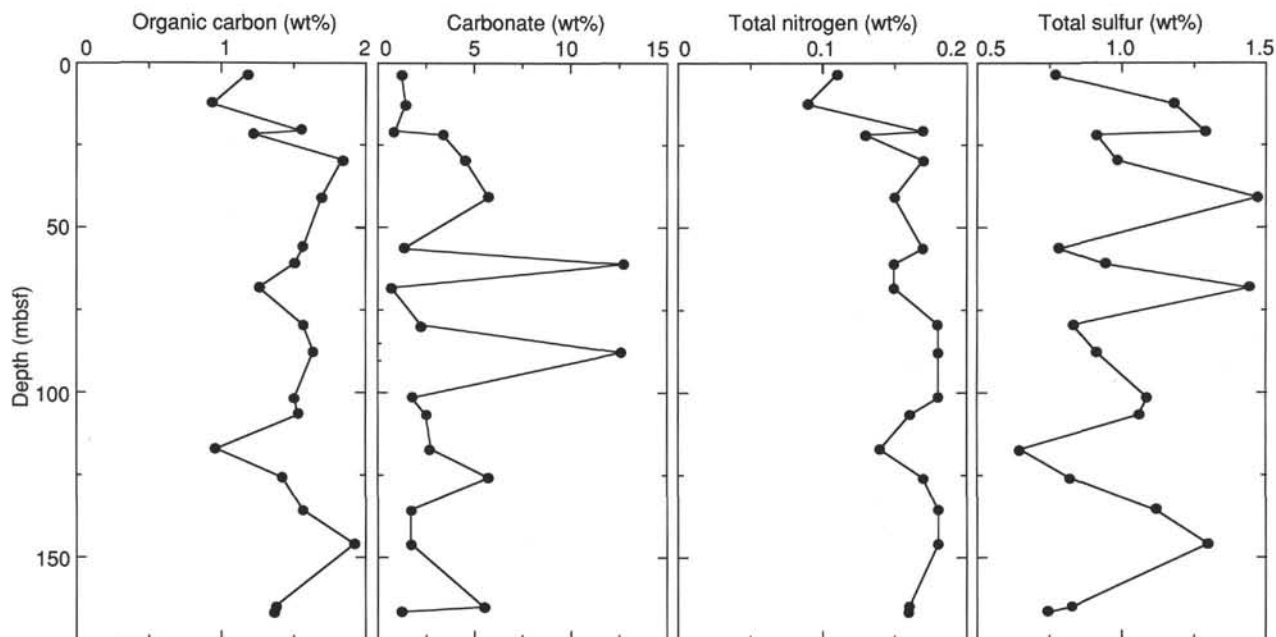


Figure 36. Depth distribution of organic carbon, total carbonate, total nitrogen, and total sulfur in Hole 892A.

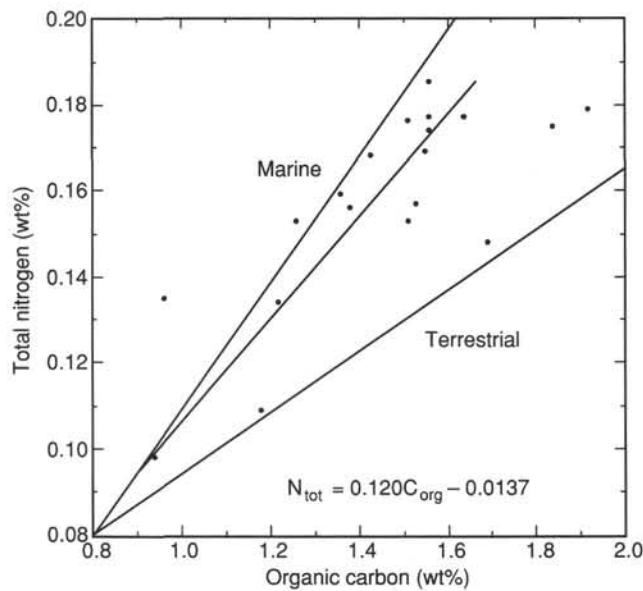


Figure 37. Cross plot of  $C_{org}$  and  $N_{tot}$  showing a relatively dominant marine hemipelagic influence at Hole 892A. Typical marine and terrestrial C/N relationships are drawn for reference.

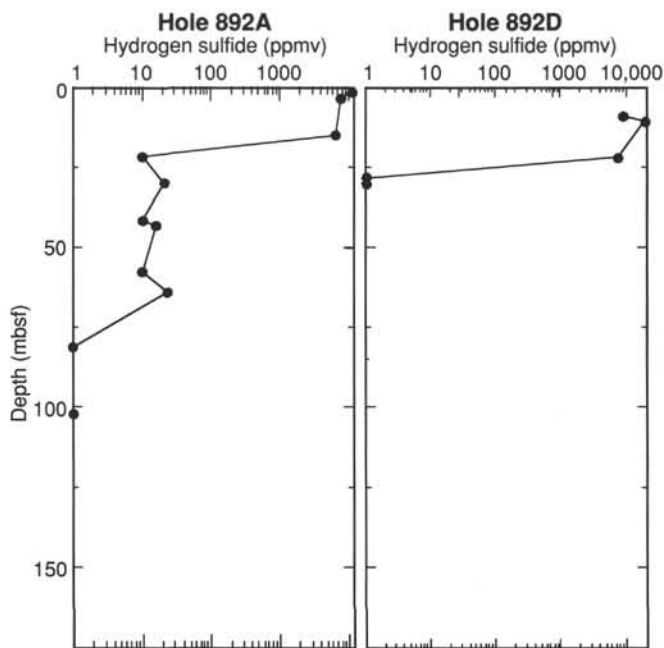


Figure 38. Depth distribution of expansion void hydrogen sulfide at Holes 892A and 892D. Note log concentration scale.

by gas chromatography. The results are listed in Table 7 and some are illustrated in Figures 39 and 40.

In Hole 892A, HS methane concentrations range between 10,015 and 132,767 ppmv (Fig. 39). Immediately below the seafloor, methane increases rapidly from 80,252 ppm at 1.51 mbsf to 132,767 ppmv at 3.67 mbsf. At 68.17 mbsf, HS methane has a minimum value of 10,015 ppmv; a second local minimum of 12,530 ppmv occurs at 106.73 mbsf.

Ethane and higher hydrocarbons up to  $C_7$  (heptane) were also detected in Holes 892A and 892D. The downhole profiles for headspace ethane, propane, *i*-butane, *i*-pentane, and hexanes for Hole

892A are shown in Figures 39 and 40, respectively. Three significant peaks in headspace ethane were found in Hole 892A: in the gas hydrate zone at 3.67 mbsf (77 ppmv), at 68.17 mbsf (339 ppmv), and at 125.92 mbsf (525 ppmv). The highest headspace propane and *i*-butane values were found at 125.92 mbsf (267.5 and 109.5 ppmv, respectively). Headspace *i*-pentane and *i*-hexane in Hole 892A also peaked sympathetically at the same depths (68.17 and 125.92 mbsf).

The  $C_1/C_{2+}$  ratio profile for HS gases in Hole 892A is shown in Figure 39. Extremely low  $C_1/C_{2+}$  values were measured at all depths below 67.5 mbsf. A second sharp inflection in the  $C_1/C_{2+}$  ratio profile occurs at 106.7 mbsf. Here the headspace gas chromatogram was almost identical to that found at 67.5 mbsf.

In Hole 892A, the HS carbon dioxide concentration generally varies between 1000 and 7000 ppmv (Fig. 39). Low headspace carbon dioxide values (393 ppmv at 12.53 mbsf) were observed in the near-surface gas hydrate zone and also immediately below the first suspected thermogenic hydrocarbon conduit (334 ppmv at 79.63 mbsf). The two highest  $CO_2$  peaks were found at 56.03 and at 116.99 mbsf (9,700 and 11,138 ppmv, respectively).

No HS nitrogen was found in Holes 892A, 892D, or 892E other than what could be accounted for by air contamination during HS sampling.

The HS gas and  $C_1/C_{2+}$  distribution with depth for Hole 892D is shown in Figures 41 and 42. The most notable differences between Holes 892A and 892D are (1) the methane-charged sediment layer near the surface is thinner in Hole 892D than in Hole 892A; (2) only one main higher hydrocarbon peak occurs in Hole 892D, against two main peaks in Hole 892A; and (3) the deepest  $C_2-C_6$  peaks in Hole 892D occur at about 106 mbsf, whereas they occur at about 126 mbsf in Hole 892A.

### Expansion Void Gases

In Holes 892A, 892D, and 892E gas expansion voids were observed in the core liners for all cores of medium to good recovery. These gases were sampled as explained in the "Explanatory Notes" chapter (this volume). Besides  $H_2S$ , as previously described, the EVG samples contain hydrocarbons in the  $C_1$  to  $C_7$  range. The EVG results from Holes 892A, 892D, and 892E are listed in Table 8.

The EVG hydrocarbon and nonhydrocarbon profiles (apart from the  $H_2S$  profile) in Hole 892A generally show similar vertical trends to the HS gases. The EVG  $C_1/C_{2+}$  profile in Hole 892A also follows the same trends as the equivalent HS profile.

Apart from the EVG carbon dioxide distribution in Hole 892D, the EVG values show similar trends with depth as those of the HS gases (Table 8). In the HS carbon dioxide for Hole 892D, the highest concentration (about 8,500 ppmv) occurs at approximately 31 mbsf (Table 7), whereas no peaks of this significance were seen in the EVG carbon dioxide data for Hole 892D.

### Fluorescence Analysis

Extracts from 11 sediment samples, prepared as described in the "Explanatory Notes" chapter (this volume), were observed under ultraviolet light.

For the first time on Leg 146, fluorescing material was found (Fig. 40). The fluorescence ranged from no fluorescence, to dull (at 62.5, 106.6, 125.9, and 166.5 mbsf), to strong white fluorescence (at 29.5 mbsf). White fluorescence of moderate strength occurred at 22.0, 88.3, and 146.0 mbsf. The fluorescence suggests thermally generated aromatic compounds.

### Kerogen Analysis

Eleven samples from Hole 892A were analyzed for kerogen by Geofina hydrocarbon meter pyrolysis. They gave relatively high  $S_1$  and  $S_2$  counts (Table 9) reflecting the presence of the fluorescing organic matter, which has a source dominated by a marine input.

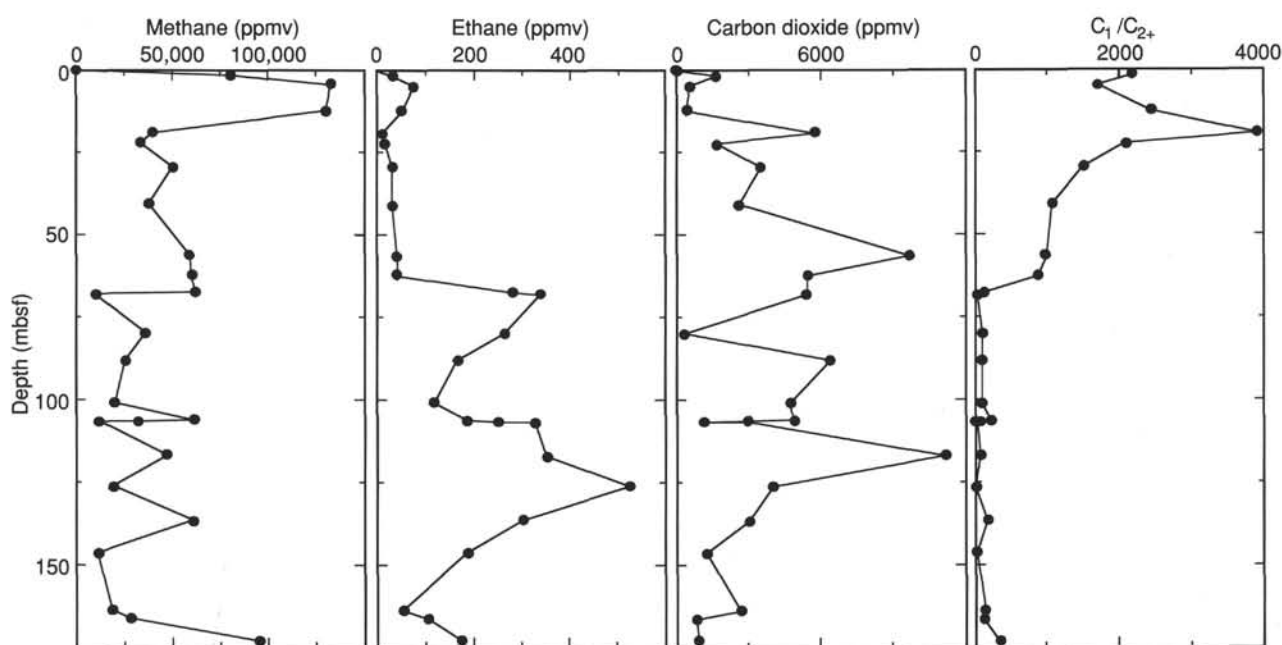


Figure 39. Depth distribution of headspace methane, ethane, carbon dioxide, and  $C_1/C_{2+}$  at Hole 892A.

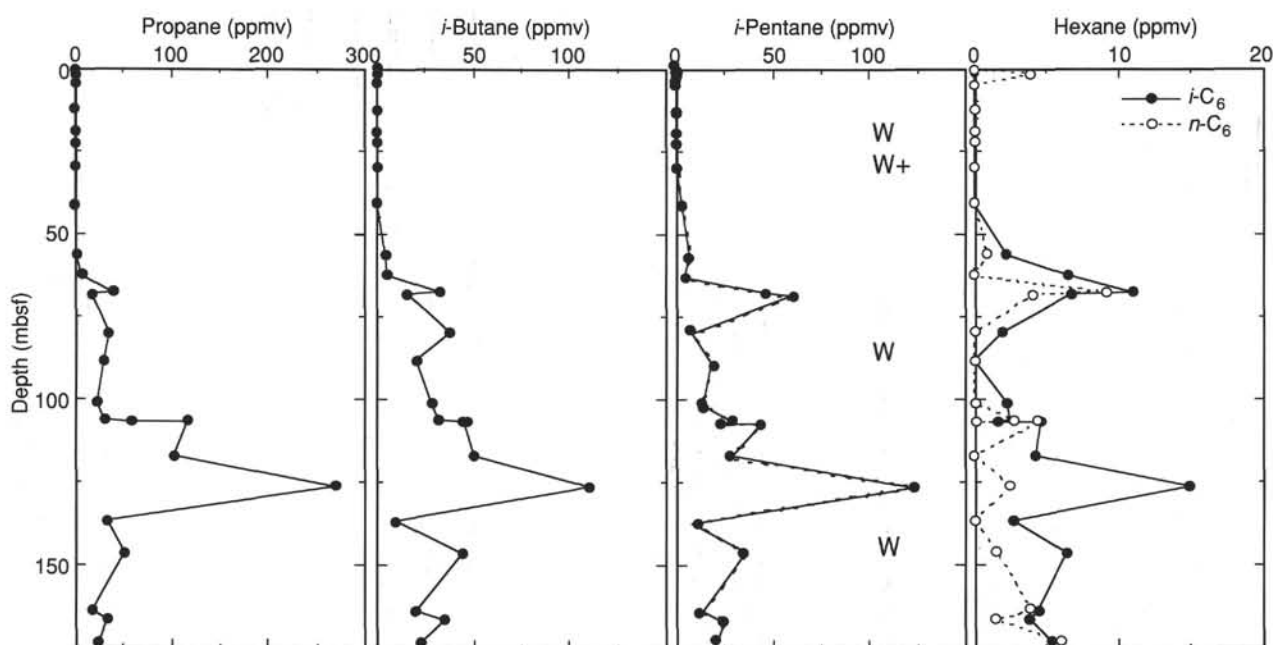


Figure 40. Depth distribution of headspace propane, *i*-butane, *i*-pentane and occurrence of white fluorescence (W and W+ illustrating observations of moderate and strong fluorescence, respectively) in sediment extracts, and hexane at Hole 892A.

Examples of pyrolysis runs (Fig. 43) show that the calculated  $T_{max}$  varies between 395° and 418°C.

### Bitumen Analysis

In contrast to Site 891, the high-resolution  $C_{11}$ – $C_{40}$  gas chromatography of the hexane-soluble fraction at Site 892 shows that some of the original labile hydrocarbons in the organic matter occur as *n*-alkanes and isoprenes (Fig. 44). Some of the most prominent peaks

correspond to common alkanes and can readily be identified. Some of the residual bitumen clearly contains lipids from methanogenesis.

Examples of typical  $C_{11}$ – $C_{40}$  gas chromatograms in Figure 44 illustrate the high degree of variability of the hydrocarbons in the extracts in Hole 892A. The most striking feature of the bitumen analysis at Site 892 is the low grade biodegradation of the higher hydrocarbons compared to other sites of this leg. This observation suggests that higher hydrocarbons may have migrated to the cored sediments recently. The  $C_{37}$ – $C_{40}$  alkenones were not detected in Hole 892A.

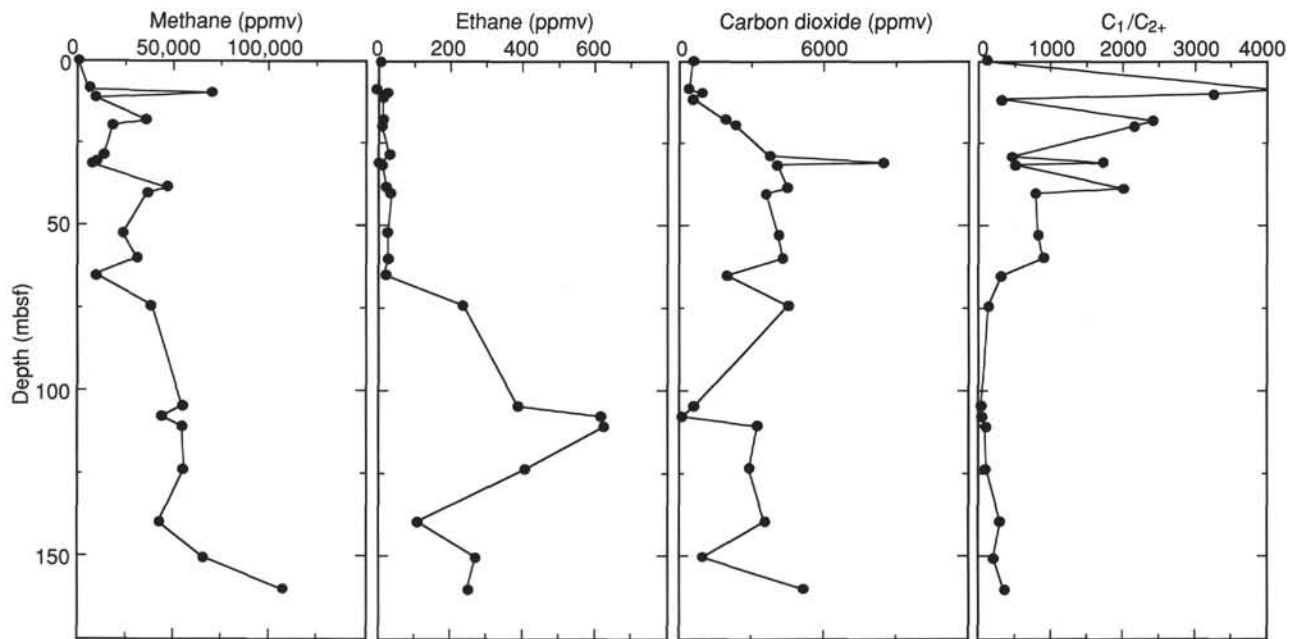


Figure 41. Depth distribution of headspace methane, ethane, carbon dioxide, and C<sub>1</sub>/C<sub>2+</sub> at Hole 892D.

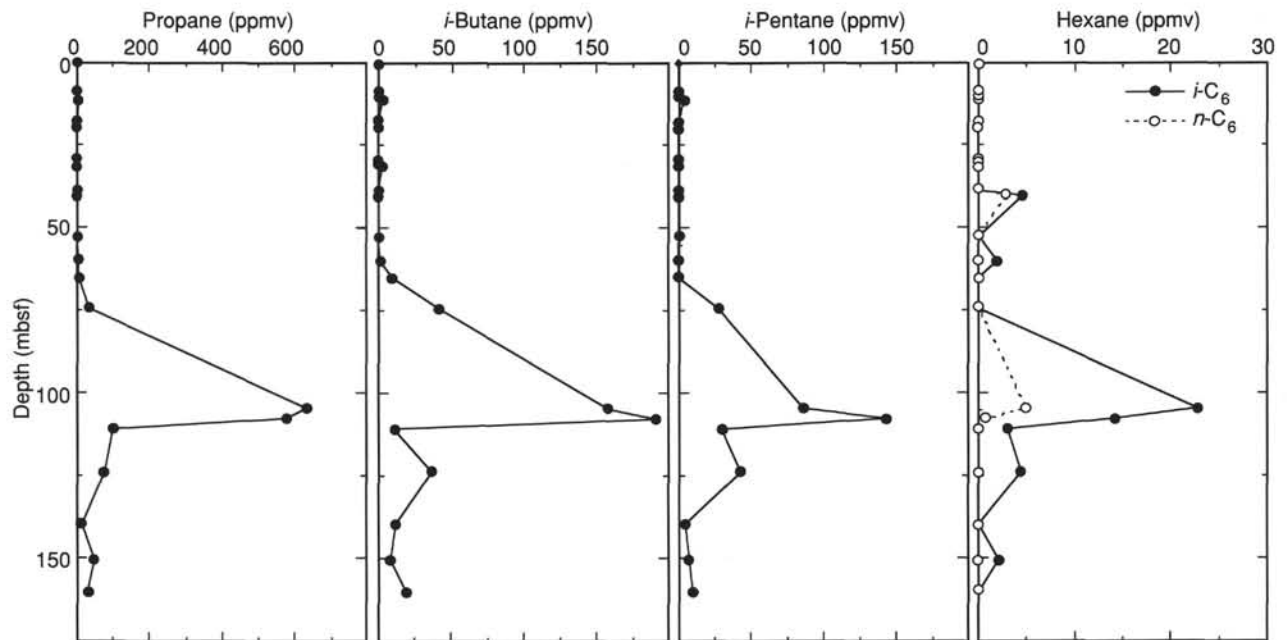


Figure 42. Depth distribution of headspace propane, *i*-butane, *i*-pentane, and hexane at Hole 892D.

### Preliminary Interpretation

Before drilling at Site 892, hydrocarbons of thermogenic origin were anticipated at the depth (133 mbsf) corresponding to the fault imaged on MCS line OR-9. The upwarped BSR seen on the seismic section, furthermore, suggested abundant gas hydrates in the near-surface sediments.

Thermogenic hydrocarbons were found as predicted. However, recovered gas hydrates were documented to occur only above about 19 mbsf, rather than extending down to the depth of the BSR (73 mbsf) at the site. Furthermore, prolific amounts of hydrogen sulfide gas were not anticipated in these same near-surface deposits.

Site 892 represents a dynamic geochemical situation. The gas composition data indicate the presence of both bacterial and thermogenic hydrocarbons. In addition, H<sub>2</sub>S is found at high concentrations in the uppermost 19 m in Hole 892A, but also occurs at lower concentrations, at least to 65 mbsf. Although the relationship between these and the other geochemical and geologic parameters needs further analytical work and refinement, the following is an initial interpretation.

#### Bacterial Methane

In contrast to Site 891, the organic carbon contents at Site 892 are significantly higher (0.2–0.8 wt% at Site 891 vs. 1.0–1.9 wt% at

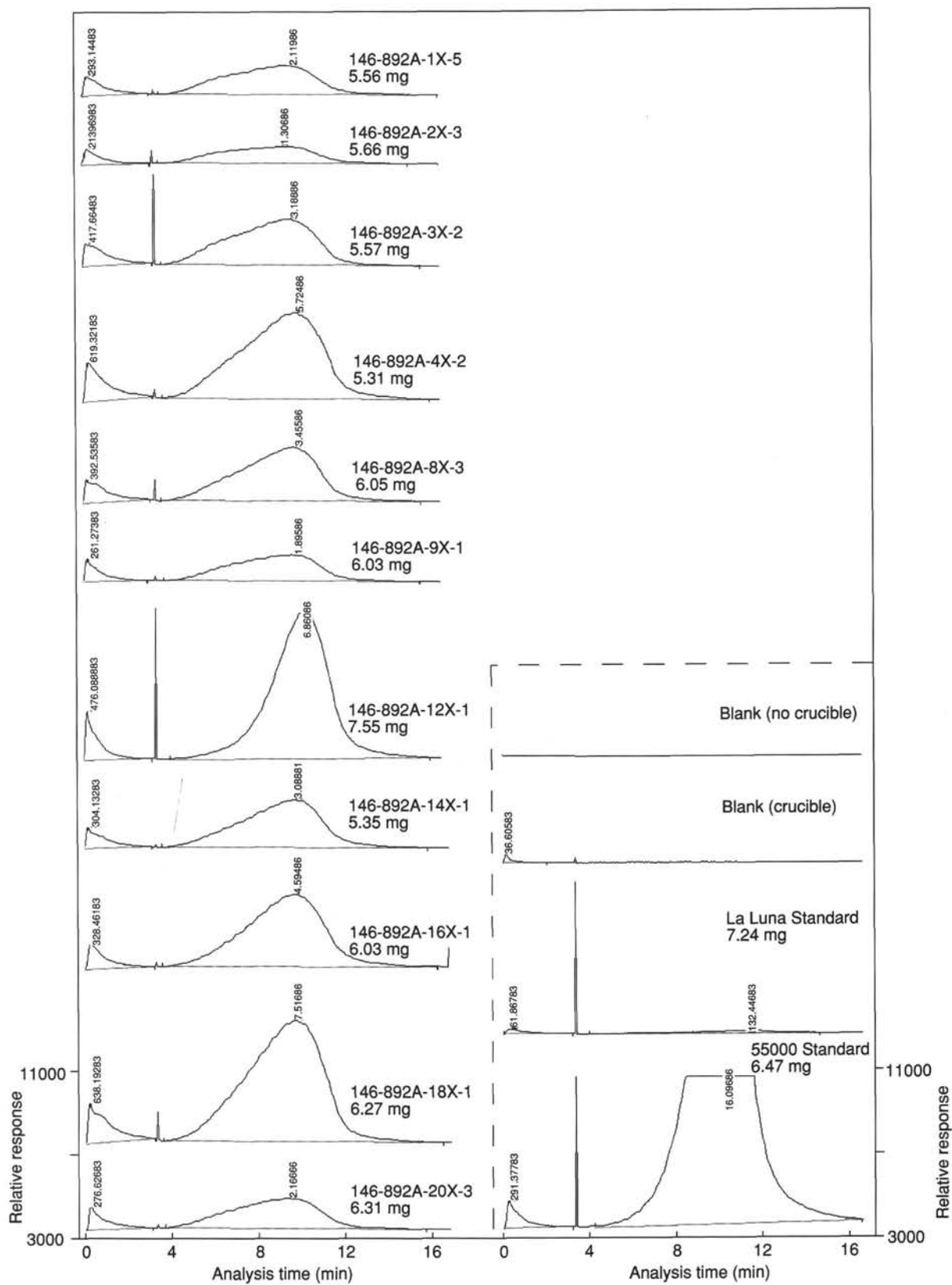


Figure 43. Example of Geofina hydrocarbon meter pyrograms at Hole 892A.

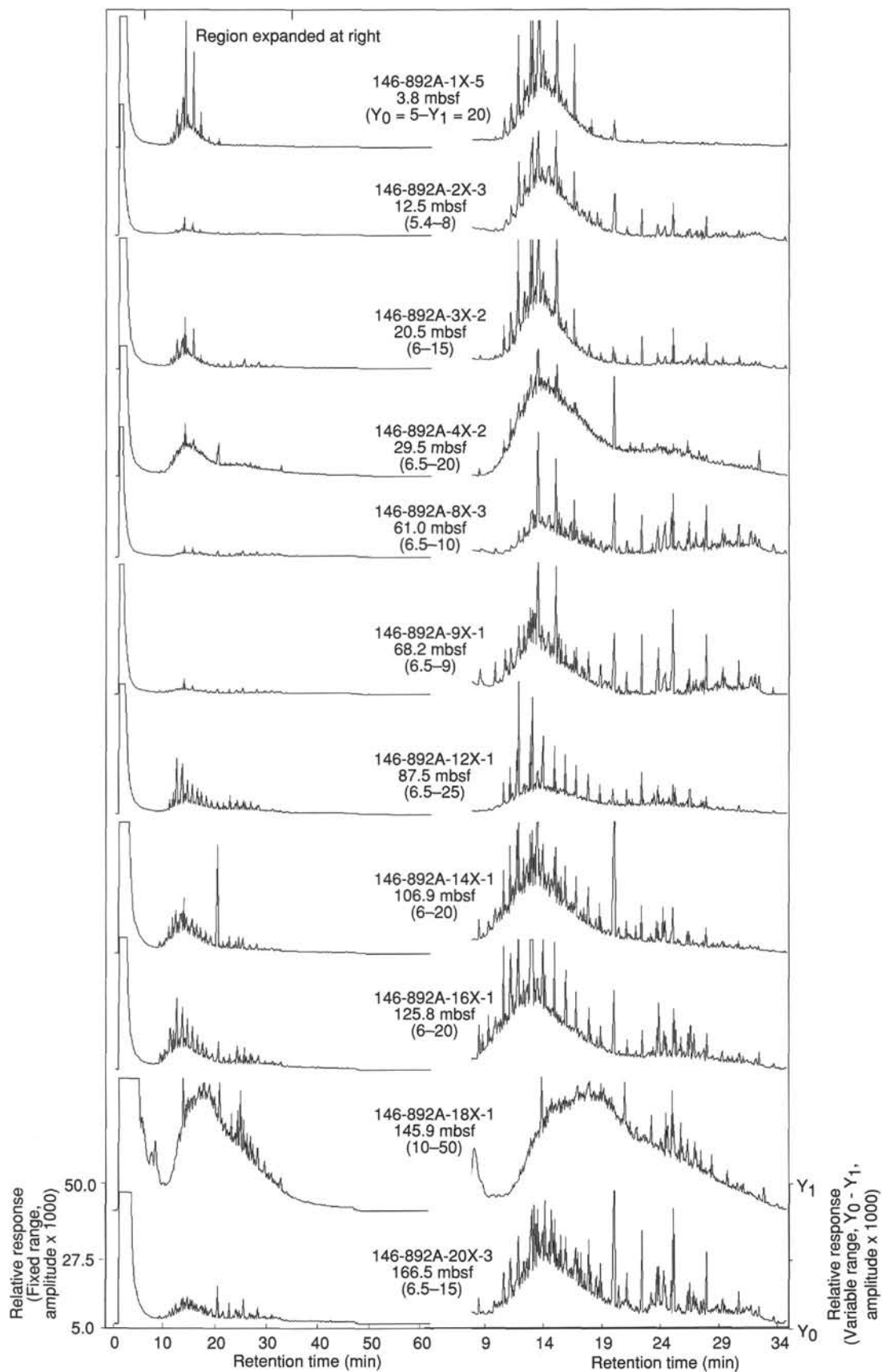


Figure 44. Examples of typical  $C_{11}$ - $C_{40}$  gas chromatograms at Hole 892A. Figures in parentheses show the range in retention time on the expanded section on the right.

**Table 9. Results of Geofina hydrocarbon meter pyrolysis at Hole 892A.**

| Sample name | S <sub>1</sub><br>(mg C/g) | S <sub>2</sub><br>(mg C/g) | Calculated               | Measured                 |
|-------------|----------------------------|----------------------------|--------------------------|--------------------------|
|             |                            |                            | T <sub>max</sub><br>(°C) | T <sub>max</sub><br>(°C) |
| 146-892A-   |                            |                            |                          |                          |
| 1X-5        | 0.23                       | 1.43                       | 403                      | 483                      |
| 2X-3        | 0.16                       | 0.87                       | 395                      | 474                      |
| 3X-2        | 0.34                       | 2.15                       | 404                      | 484                      |
| 4X-2        | 0.53                       | 4.05                       | 410                      | 492                      |
| 8X-3        | 0.29                       | 2.15                       | 408                      | 489                      |
| 9X-1        | 0.19                       | 1.18                       | 406                      | 487                      |
| 12X-1       | 0.28                       | 3.41                       | 418                      | 501                      |
| 14X-1       | 0.25                       | 2.17                       | 409                      | 490                      |
| 16X-1       | 0.24                       | 2.86                       | 408                      | 489                      |
| 18X-1       | 0.46                       | 4.50                       | 407                      | 488                      |
| 20X-3       | 0.19                       | 1.29                       | 398                      | 477                      |

Site 892). As a consequence, the rates of remineralization of organic matter are higher and dissolved sulfate is rapidly removed. The onset of methanogenesis occurs at much shallower depths at Site 892 than at Site 891, possibly within the uppermost 2 m. Methanogenesis clearly persists down to 67.5 mbsf, as indicated by the higher amounts of methane in this interval, and by the C<sub>1</sub>/C<sub>2</sub> ratio greater than 103. Bacterial methane is also likely to be present in the deeper section of Hole 892A, but as discussed subsequently, there is a strong influence of thermogenic hydrocarbons below 67.5 mbsf that masks the bacterial molecular signature. Stable carbon isotopes in combination with the molecular information are required to ascertain the degree of bacterial/thermogenic gas mixing at Site 892.

#### Thermogenic Hydrocarbons

In several samples, notably at 68.2 and 126 mbsf in Hole 892A, the suites of higher hydrocarbon gases (C<sub>2</sub>–C<sub>6</sub>, inclusive) that were detected are typical of thermogenic hydrocarbons. Indigenous organic matter is precluded as the source for these higher hydrocarbons, because of the maturity of the kerogen. Although the strongest indications of thermogenic hydrocarbons in Hole 892A are at 68.2 and 126 mbsf, they are recorded in significant amounts throughout the section below 67.5 mbsf and in minor amounts at shallower depths.

The thermogenic hydrocarbons are also associated with minor amounts of the olefin ethene. This unsaturated hydrocarbon is not stable over geologic periods, and its presence indicates a relatively recent generation event for the thermogenic hydrocarbons, which in turn implies advective transport and hydrothermal activity. The qualitative observation of a petroliferous odor in the cores occurred in concert with the appearance of ethene. This odor was similarly noticeable in the sections of Site 891 influenced by thermogenic hydrocarbons.

Minor staining, seen by its fluorescence, is evidence that bitumens have also moved from depth into the sediments. The intensity of the fluorescence, however, does not correspond to the location of the current higher hydrocarbon maxima. This disparity suggests that the bitumens extracted from the sediment may have come in independently of the gases, possibly with advecting fluids.

The high-resolution C<sub>11</sub>–C<sub>40</sub> gas chromatography of the hexane-soluble fraction shows a surprisingly low degree of biodegradation in the higher hydrocarbons. This observation suggests that thermogenic gas may migrate relatively rapidly from a deeper source. The occurrence of higher hydrocarbons in some layers and their absence in others may have resulted from the relative permeability of the sediment layers or fault zones to the migrating gases.

One of the primary organic geochemical differences between Holes 892A and 892D is the number and depth position of peaks in the HS hydrocarbons C<sub>2</sub>–C<sub>6</sub> (inclusive). This difference suggests that only one main thermogenic hydrocarbon incursion is present at Hole 892D, as

opposed to two at Hole 892A. Furthermore, the depth to the suspected thermogenic hydrocarbon conduit at Hole 892D is about 20 m shallower than at its equivalent (the deeper incursion) at Hole 892A. However, according to the composition of the C<sub>2</sub>–C<sub>6</sub> gases the thermogenic hydrocarbons recorded in the two holes have the same source.

#### Hydrogen Sulfide

The unexpected accumulation of reduced sulfur gases, in particular H<sub>2</sub>S, near the surface is a geochemical novelty, but the persistence of H<sub>2</sub>S to 65 mbsf complicates the interpretation. As noted earlier, oxidized sulfur species (dissolved SO<sub>4</sub><sup>2-</sup>) are exhausted by 20 mbsf in Hole 892D. Generally, the reactive nature of sulfide leads to its rapid removal in unconsolidated sediments as monosulfides, and then to the formation of minerals such as pyrite. The occurrence of H<sub>2</sub>S in sediments at 65 mbsf indicates that either (1) the H<sub>2</sub>S sulfide was formed bacterially, but its removal was prohibited; or (2) the sulfide is not diagenetic/autochthonous and has moved into the sediments.

The first case requires that either insufficient elemental iron, or similar species, was present to react with the sulfide and remove it from the pore fluids, which is unlikely, or that somehow monosulfide reactions were inhibited. The spatial connection between the depth of hydrate stability and the occurrence of free sulfide suggests a causal relationship. If the free sulfide were taken up in the hydrate crystal lattice, then upon retrieval of the cores and subsequent dissociation of the hydrate, the "stored" and hence unreacted sulfide either would be released into the pore fluid or would ebulliate as free sulfur gas. Support for this hypothesis comes from the higher H<sub>2</sub>S contents in the 2–19 mbsf depth interval (Sections 146-892B-1X-4 and -2X-3). Here, larger hydrate pieces were recovered in the cores (see below), whereas only disseminated hydrate is thought to be present in deeper cores to 65.7 mbsf, which therefore have a lower H<sub>2</sub>S-retentive capacity. This scenario demands that the sulfide was taken up by the hydrate relatively soon after sulfide formation. Thus, either the sulfide-bearing hydrates were formed near the surface in the sulfate-reducing zone (i.e., 0–20 mbsf) and were then buried, or the sulfide was transported into the 0–65 mbsf section and hydrate formation occurred after burial (i.e., more recently than the depositional age of the sediments).

In the second case (allochthonous sulfide), the sulfide is derived not only from the reduction of seawater-derived sulfate by sulfate-reducing bacteria, but also at least some sulfide is generated hydrothermally, possibly by higher temperature reactions with organic matter at greater depth. The H<sub>2</sub>S has then been transported, or has migrated, into the sediments of Site 892. Strong evidence exists for the movement of thermogenic hydrocarbons at Site 892, but the clearest expressions of the thermogenic hydrocarbon incursions are beneath the level of observed sulfide or hydrate.

## GAS HYDRATE STUDIES

### Gas Hydrate Occurrence and Sampling

Gas hydrates were recovered unexpectedly in a restricted zone between about 2–5 and <19 mbsf in Holes 892A, 892D, and 892E. They seem to be similar to those known from shallow sediments in the Gulf of Mexico (Brooks et al., 1989), among other places. The hydrates occur as (1) individual, dispersed, platy to prismatic 1- to 1.5-cm-long white crystals; (2) intergrown 3- to 5-cm clusters of these crystals; (3) massive, thin (0.3–0.5 cm) layers and veinlets, parallel and oblique to bedding, respectively; and (4) pockets of sediment cemented by hydrates. A 2- to 3-cm-thick massive hydrate layer was recovered from Core 146-892D-3X, and frozen in liquid N<sub>2</sub>. In Cores 146-892E-1X through -3H, the distribution of the gas hydrate was rather patchy. Upon recovery, the cores had an unusually strong H<sub>2</sub>S smell, significantly stronger than expected from a zone of intense bacterial sulfate reduction.

## Core Temperature Measurements

Gas hydrate dissociation is an endothermic process that produces substantial cooling of the surrounding sediment (see "Core Temperature Measurement" section, "Sites 889/890" chapter, this volume). To detect the low temperatures that possibly indicate the dissociation of gas hydrates in the cores, sediment temperatures were systematically measured in the shallowest cores recovered from Holes 892A, 892D, and 892E (Table 10). Measurements were made less than 5 min after the cores had been brought to the catwalk. They were generally taken at between 5 and 10 points at the bases of the cores and/or at ends of cut sections, with a portable digital thermometer that has a precision of 0.1°C.

### Hole 892A

Low temperatures of  $-1.2^{\circ}$  and  $-1.7^{\circ}\text{C}$  in Cores 146-892A-1X and -2X, respectively, were observed in close proximity to small pieces (<1 cm long) of gas hydrates. Temperatures significantly higher,  $1.5^{\circ}\text{C}$  for Core 146-892A-1X and  $3.5^{\circ}$  to  $4.2^{\circ}\text{C}$  for Core 146-892A-2X, were observed in intervals (extending over a few centimeters) between the pieces of hydrates. Distinctly higher temperatures, between  $6.6^{\circ}$  and  $11.6^{\circ}\text{C}$ , were measured in all the other cores, with no apparent trend with depth. However, temperatures between  $6.6^{\circ}$  and  $7.6^{\circ}\text{C}$  measured in Core 146-892A-9X are lower, by about  $2^{\circ}\text{C}$ , than in the surrounding cores.

### Hole 892D

A low temperature of  $-0.8^{\circ}\text{C}$  was measured at three different points at the base of Core 146-892D-2X. Temperatures between  $6.8^{\circ}$  and  $7.0^{\circ}\text{C}$  were measured in the upper part of this core. Low temperatures between  $2.2^{\circ}$  and  $3.5^{\circ}\text{C}$  were observed in the first section of Core 146-892D-3X. A markedly low temperature of  $-1.8^{\circ}\text{C}$  was observed in the second section of this core in close proximity to a layer of massive hydrate about 2 cm thick. A fairly uniform temperature between  $7^{\circ}$  and  $8^{\circ}\text{C}$  was observed in Core 146-892D-4X, with the exception, in the second section, of a few-centimeters-long interval at  $0.9^{\circ}\text{C}$ . The other cores showed normal temperatures between  $6.8^{\circ}$  and  $10^{\circ}\text{C}$ .

### Hole 892E

A temperature of  $-1.5^{\circ}\text{C}$  was measured at the base of Core 146-892E-1X in proximity to small pieces (<1 cm long) of hydrates. Temperatures of  $7^{\circ}$  to  $8^{\circ}\text{C}$  were observed in the rest of the core. Similar normal temperatures between  $6.5^{\circ}$  and  $10^{\circ}\text{C}$  were measured in Core 146-892E-3H.

### Implications

As in the case of Core 146-889B-3R (see "Gas Hydrate Studies" section, "Sites 889 and 890" chapter, this volume), hydrate dissociation is the proposed explanation for the low temperatures measured in the shallow cores recovered at Site 892. Clearly anomalous low temperatures were confined to the upper 30 m of sediment, which probably corresponds to the layer in which most hydrate is present. Within this layer, the variations in the measured temperatures reflect the patchy distribution of the hydrates. The lowest temperatures of  $-1.2^{\circ}$  and  $-1.7^{\circ}\text{C}$  in Cores 146-892A-1X and -2X, respectively;  $-1.8^{\circ}\text{C}$  in Core 146-892D-3X; and  $-1.5^{\circ}\text{C}$  in Core 146-892E-1X were all observed in proximity to pieces of hydrates that had not yet completely dissociated. They are attributed to the conductive cooling associated with the dissociation of the observed pieces of hydrates. Temperatures significantly higher ( $1.5^{\circ}\text{C}$  in Core 146-892A-1X,  $3.5^{\circ}$ – $4.2^{\circ}\text{C}$  in Core 146-892A-2X,  $2.2^{\circ}$ – $3.5^{\circ}\text{C}$  in Core 146-892D-3X, and  $0.9^{\circ}\text{C}$  in Core 146-892D-4X) were observed in intervals in which hydrates were apparently not present. Hydrates were present, how-

Table 10. Summary of core temperatures measured on catwalk.

| Core, section, interval (cm) | Depth (mbsf) | Core length (m) | Minimum temperature ( $^{\circ}\text{C}$ ) | Maximum temperature ( $^{\circ}\text{C}$ ) | Comments                    |
|------------------------------|--------------|-----------------|--------------------------------------------|--------------------------------------------|-----------------------------|
| 146-892A-                    |              |                 |                                            |                                            |                             |
| 1X                           | 0            | 4.32            | $-1.2$                                     | 1.5                                        | Measured at core base only. |
| 2X                           | 9.5          | 3.90            | $-1.7$                                     | 4.2                                        | Measured at core base only. |
| 3X                           | 19.0         | 4.16            | 7.6                                        |                                            | Measured at core base only. |
| 4X                           | 28.5         | 1.81            | 8.6                                        |                                            | Measured at core base only. |
| 6X                           | 39.0         | 6.89            | 8.3                                        | 9.2                                        |                             |
| 7X                           | 48.5         | 9.76            | 7.2                                        | 9.6                                        |                             |
| 8X                           | 58.0         | 6.69            | 9.2                                        | 10.2                                       |                             |
| 9X                           | 67.5         | 1.12            | 6.6                                        | 7.6                                        |                             |
| 11X                          | 78.0         | 3.23            | 8.6                                        | 11.6                                       |                             |
| 12X                          | 87.5         | 1.12            | 8.0                                        | 9.0                                        |                             |
| 13X                          | 97.0         | 9.27            | 7.3                                        | 9.2                                        |                             |
| 146-892D-                    |              |                 |                                            |                                            |                             |
| 2X                           | 8.5          | 3.24            | $-0.8$                                     | 7.0                                        |                             |
| 3X                           | 18.0         | 2.20            | $-1.8$                                     | 3.5                                        |                             |
| 4X                           | 27.5         | 4.38            | 0.9                                        | 8.0                                        |                             |
| 5X                           | 37.0         | 6.12            | 8.2                                        | 9.0                                        |                             |
| 7X                           | 54.0         | 7.60            | 7.5                                        | 9.4                                        |                             |
| 8X                           | 61.7         | 5.11            | 7.2                                        | 7.7                                        |                             |
| 9X                           | 69.3         | 6.73            | 6.8                                        | 10.0                                       |                             |
| 146-892E-                    |              |                 |                                            |                                            |                             |
| 1X                           | 0            | 3.18            | $-1.5$                                     | 8.0                                        |                             |
| 3H                           | 33.0         | 7.90            | 6.5                                        | 10.0                                       |                             |

Note: Depth represents depth to the top of the core.

ever, at a short distance away (a few centimeters) in the case of Core 146-892A-1X. These temperatures are compatible with interpretations that assume either the conductive propagation of cooling from pieces of hydrates located a few centimeters from the temperature measurements or the presence in the cores of small amounts (a few percent) of disseminated hydrates that would have dissociated by the time the cores were inspected on the catwalk.

## Organic Geochemistry of the Gas Hydrates

The suite of gases (methane, ethane, and hydrogen sulfide) found in EVG and HS samples taken between 0 and 18 mbsf at Site 892 suggests that the hydrates may contain all of these species (Hitchon, 1974). Significant amounts (up to 3665 counts on the natural gas analyzer) of carbon disulfide were recorded in expansion void gases in Holes 892D and 892E only from the gas hydrate zone. This suggests that carbon disulfide also exists as a guest molecule in the gas hydrates at Site 892.

Shore-based isotopic analysis of both occluded and sorbed gases will provide more information on the character of the gases in the hydrates.

## Gas Hydrates and Hydrogen Sulfide

The occurrence of methane hydrate in a zone of extremely high hydrogen sulfide concentration near the sediment/water interface was geochemically most surprising. Preliminary analyses indicate  $\text{H}_2\text{S}$  concentrations in this zone over 10,000 ppmv (see "Organic Geochemistry" section, this chapter). How is such a high concentration of sulfide produced and such an enormous concentration gradient maintained close to the water/sediment interface? Bacterial reduction of dissolved sulfate was complete almost at the sediment interface (Tables 11–12). Sulfate reduction is accompanied by sulfide production, and if detrital material is present, as in these sediments, the sulfide is expected to react rapidly with the reduced Fe to form mono- and disulfides, such as pyrite, greigite, mackinawite, or pyrrhotite. Clearly, most of the sulfide produced or introduced has not been removed by sulfide mineralization. Normally, if not enough detrital Fe is available, some of the sulfide produced combines with organic matter and most of it diffuses into the overlying seawater. The sulfur

Table 11. Interstitial-water geochemical data, Hole 892A.

| Core, section,<br>interval (cm) | Depth<br>(mbsf) | Water<br>(mL) | pH  | Alkalinity<br>(mM) | Salinity<br>(g/kg) | Cl <sup>-</sup><br>(mM) | Mg <sup>2+</sup><br>(mM) | Ca <sup>2+</sup><br>(mM) | Mg/Ca | SO <sub>4</sub> <sup>2-</sup><br>(mM) | NH <sub>4</sub> <sup>+</sup><br>(μM) | SiO <sub>2</sub><br>(μM) | K <sup>+</sup><br>(mM) | Na <sup>+</sup><br>(mM) | Na/Cl |
|---------------------------------|-----------------|---------------|-----|--------------------|--------------------|-------------------------|--------------------------|--------------------------|-------|---------------------------------------|--------------------------------------|--------------------------|------------------------|-------------------------|-------|
| 146-892A-                       |                 |               |     |                    |                    |                         |                          |                          |       |                                       |                                      |                          |                        |                         |       |
| 1X-5, 10-13                     | 6.10            | 25            | 8.5 | 20.48              | 28.5               | 483                     | 36.14                    | 3.27                     | 11.1  | 0.62                                  | 957                                  | 959                      | 10.28                  | 415                     | 0.86  |
| 2X-3, 0-11                      | 12.60           | 30            | 8.6 | 15.63              | 28.5               | 468                     | 35.28                    | 4.13                     | 8.5   | 5.57                                  | 3160                                 | 1376                     | 9.62                   | 403                     | 0.86  |
| 3X-2, 0-10                      | 20.60           | 35            | 7.7 | 19.45              | 32.0               | 557                     | 34.97                    | 5.40                     | 6.5   | 0.16                                  | 4476                                 | 952                      | 9.92                   | 482                     | 0.87  |
| 3X-3, 0-10                      | 22.10           | 25            | 7.8 | 16.88              | 32.0               | 552                     | 34.01                    | 4.60                     | 7.4   | 0.63                                  | 4422                                 | 933                      | 8.80                   | 476                     | 0.86  |
| 4X-2, 0-10                      | 30.10           | 35            | 7.6 | 17.75              | 30.5               | 523                     | 32.06                    | 5.30                     | 6.0   | 0.15                                  | 4725                                 | 988                      | 8.80                   | 452                     | 0.86  |
| 6X-2, 0-10                      | 40.60           | 22            | 7.5 | 17.33              | 30.5               | 544                     | 32.80                    | 5.54                     | 5.9   | 0.13                                  | 5488                                 | 1010                     | 8.80                   | 471                     | 0.87  |
| 6X-2, 10-30                     | 40.70           | 38            |     |                    | 32.0               | 545                     | 33.01                    | 5.89                     | 5.6   | 0.13                                  | 5316                                 | 1098                     | 8.65                   | 471                     | 0.86  |
| 7X-5, 140-150                   | 55.92           | 26            | 7.6 | 16.09              | 29.0               | 507                     | 27.76                    | 6.04                     | 4.6   | 0                                     | 6047                                 | 965                      | 7.62                   | 444                     | 0.88  |
| 8X-3, 0-10                      | 61.00           | 38            | 7.5 | 15.73              | 30.0               | 534                     | 28.38                    | 6.38                     | 4.4   | 0                                     | 6438                                 | 924                      |                        | 470                     | 0.88  |
| 9X-1, 69-74                     | 68.19           | 8             |     |                    | 27.5               | 480                     | 22.52                    | 6.16                     | 3.7   | 0.13                                  | 6379                                 | 880                      | 6.75                   | 431                     | 0.90  |
| 11X-2, 0-10                     | 79.60           | 18            | 7.8 | 14.71              | 29.5               | 517                     | 24.50                    | 6.77                     | 3.6   | 0.12                                  | 6930                                 | 902                      | 6.75                   | 465                     | 0.90  |
| 11X-2, 70-95                    | 80.30           | 48            |     |                    | 29.5               | 516                     | 24.07                    | 7.12                     | 3.4   | 0.12                                  | 6744                                 | 956                      | 6.65                   | 461                     | 0.89  |
| 12X-1, 0-7                      | 87.50           | 3             |     |                    | 28.0               | 489                     | 23.37                    | 7.50                     | 3.1   | 0.69                                  | 5273                                 |                          | 5.01                   | 438                     | 0.90  |
| 13X-4, 0-25                     | 101.60          | 28            |     |                    | 29.5               | 504                     | 21.74                    | 6.99                     | 3.1   | 0.50                                  | 7063                                 | 852                      | 6.24                   | 454                     | 0.90  |
| 13X-6, 69-82                    | 105.30          | 25            | 7.7 | 12.82              | 29.0               | 501                     | 22.04                    | 6.75                     | 3.3   | 1.31                                  | 7005                                 | 948                      | 6.45                   | 452                     | 0.90  |
| 14X-1, 35-38                    | 106.90          | 5             |     |                    | 27.0               | 491                     | 21.93                    | 7.74                     | 2.8   | 0.93                                  | 4917                                 | 1193                     | 6.14                   | 442                     | 0.90  |
| 15X-1, 88-100                   | 116.90          | 22            | 7.8 | 14.08              | 29.0               | 497                     | 20.95                    | 6.92                     | 3.0   | 0.72                                  | 6936                                 | 882                      | 6.14                   | 450                     | 0.91  |
| 16X-1, 34-43                    | 125.84          | 9             |     |                    | 28.0               | 493                     | 20.51                    | 7.09                     | 2.9   | 0.29                                  | 6479                                 | 962                      | 5.99                   | 448                     | 0.91  |
| 17X-2, 3-13                     | 136.60          | 29            | 7.6 | 12.96              | 28.0               | 481                     | 21.56                    | 6.78                     | 3.2   | 1.60                                  | 6700                                 | 950                      | 5.68                   | 432                     | 0.90  |
| 18X-1, 115-140                  | 145.80          | 49            |     |                    | 27.0               | 487                     | 22.12                    | 6.89                     | 3.2   | 0.13                                  | 5546                                 | 996                      | 5.42                   | 440                     | 0.90  |
| 18X-1, 140-150                  | 146.00          | 14            | 7.9 | 15.64              | 27.5               | 487                     | 21.96                    | 6.87                     | 3.2   | 0.14                                  | 5960                                 | 965                      | 5.68                   | 441                     | 0.91  |
| 20X-2, 0-10                     | 165.10          | 12            | 7.9 | 15.93              | 30.0               | 489                     | 21.07                    | 6.80                     | 3.1   | 0.13                                  | 6019                                 | 898                      | 6.19                   | 444                     | 0.91  |
| 20X-3, 0-10                     | 166.50          | 4             |     |                    | 31.5               | 496                     | 20.11                    | 6.73                     | 3.0   | 0.14                                  | 5696                                 | 972                      | 5.83                   | 455                     | 0.92  |

Table 12. Interstitial-water geochemical data, Hole 892D.

| Core, section,<br>interval (cm) | Depth<br>(mbsf) | Water<br>(mL) | pH  | Alkalinity<br>(mM) | Salinity<br>(g/kg) | Cl <sup>-</sup><br>(mM) | SO <sub>4</sub> <sup>2-</sup><br>(mM) | NH <sub>4</sub> <sup>+</sup><br>(μM) | SiO <sub>2</sub><br>(μM) |
|---------------------------------|-----------------|---------------|-----|--------------------|--------------------|-------------------------|---------------------------------------|--------------------------------------|--------------------------|
| 146-892D-                       |                 |               |     |                    |                    |                         |                                       |                                      |                          |
| 1X-1, 9-12                      | 0.09            | 18            | 7.8 | 3.30               | 34.0               | 547                     | 27.65                                 | 522                                  | 475                      |
| 2X-1, 145-150                   | 9.95            | 39            | 8.4 | 20.20              | 31.0               | 539                     | 0.38                                  | 706                                  | 834                      |
| 2X-2, 140-150                   | 11.40           | 48            | 8.5 | 17.74              | 25.0               | 447                     | 0.78                                  | 921                                  | 729                      |
| 3X-1, 40-45                     | 18.40           | 23            | 8.5 | 12.95              | 25.0               | 433                     | 5.52                                  | 626                                  | 797                      |
| 4X-2, 4-11                      | 29.04           | 10            |     |                    | 32.5               | 575                     | 0.03                                  | 4704                                 | 738                      |
| 4X-2, 21-30                     | 29.21           | 32            | 7.7 | 14.11              | 30.5               | 505                     | 3.71                                  | 4094                                 | 851                      |
| 4X-3, 80-88                     | 30.82           | 26            | 7.8 | 18.18              | 33.0               | 570                     | 0.39                                  | 4619                                 |                          |
| 5X-2, 140-150                   | 39.90           | 47            | 7.7 | 16.89              | 32.0               | 560                     | 0.05                                  | 5202                                 | 1024                     |
| 6X-4, 140-150                   | 52.40           | 28            | 7.6 | 15.44              | 31.0               | 550                     | 0.03                                  | 5536                                 | 1001                     |
| 7X-3, 142-150                   | 58.18           | 27            | 7.5 | 15.49              | 32.0               | 551                     | 0.11                                  | 5942                                 | 976                      |
| 8X-3, 0-10                      | 64.70           | 30            | 7.6 | 15.21              | 31.0               | 541                     | 0.03                                  | 6135                                 | 828                      |
| 9X-4, 0-15                      | 73.80           | 30            | 7.7 | 12.08              | 29.0               | 500                     | 0.26                                  | 6265                                 | 772                      |
| 10X-4, 0-15                     | 104.50          | 4             |     |                    | 27.5               | 496                     | 0.03                                  | 5444                                 |                          |
| 11X-1, 130-150                  | 110.90          | 15            | 7.9 | 12.41              | 28.5               | 505                     | 0.02                                  | 6265                                 | 761                      |
| 12X-3, 130-150                  | 123.40          | 20            | 7.6 | 14.28              | 28.5               | 488                     | 0.04                                  | 6102                                 | 909                      |
| 13X-CC, 22-24                   | 128.50          | 3             |     |                    | 28.5               | 484                     | 0.06                                  | 5566                                 |                          |
| 14X-1, 115-130                  | 139.15          | 13            | 7.7 | 14.50              | 28.5               | 490                     | 0.08                                  | 5753                                 | 841                      |
| 15X-2, 110-135                  | 148.60          | 30            |     |                    | 28.0               | 489                     | 0.02                                  | 5474                                 | 802                      |
| 15X-2, 135-150                  | 148.90          | 19            | 7.7 | 16.24              | 28.0               | 492                     |                                       | 5784                                 | 856                      |
| 16X-3, 135-150                  | 161.40          | 27            | 7.7 | 15.83              | 27.8               | 484                     | 0.02                                  | 5816                                 | 1038                     |
| 16X-5, 135-150                  | 164.40          | 22            | 7.8 | 15.32              | 27.5               | 485                     | 0.08                                  | 5784                                 | 936                      |

isotopes of dissolved sulfate in seawater are controlled mainly by the diffusion of sulfide from surface sediments. No diffusion barrier has been encountered at this site. Therefore, unless the sulfide has been or is being actively transported into this horizon, these unusually high sulfide concentrations near the sediment-water interface could be maintained through "storage" within the gas hydrate. Upon retrieval of the cores and the partial dissociation of the gas hydrate, some of the "stored" sulfide must have been released and produced the unusually high concentrations measured.

At this site, the sulfide is most probably stored in methane hydrate, which must be forming at and close to the seafloor, near the base of the narrow sulfate reduction zone. Theoretically, Site 892 lies within the methane gas-hydrate stability field from the sediment/water interface to about 110 mbsf (although the occurrence of free gas below 72 mbsf [see "Downhole Logging" section, this chapter] indicates that the actual hydrate stability field is limited to lesser depths). Methane gas hydrate can accommodate the H<sub>2</sub>S molecule, which at this site is probably being produced close to the seafloor. Continuous rapid removal of the produced H<sub>2</sub>S into the hydrate (before reactions with reduced

Fe) would maintain an active sulfate reduction and sulfide production zone within the stability field of both methane and H<sub>2</sub>S hydrates.

Because no elevated sulfide concentrations were measured at the major fault zone at this site, the possibility that the carrier of the sulfide is an advecting hydrothermal sulfide-rich fluid seems unlikely. The bacterial vs. thermal origin of the H<sub>2</sub>S and CH<sub>4</sub> associated with the gas hydrate at this site will be resolved by shore-based isotopic analyses.

## INORGANIC GEOCHEMISTRY

### Introduction and Operation

The pore-water geochemistry objectives at Site 892 were (1) to determine the fluid chemistry, fluid sources, and solute fluxes in this older (Pliocene) portion of the central Oregon accretionary complex, at a site where a prominent BSR is intersected by a fault; and (2) to ascertain the geochemical relationships between the BSR and the calculated base of the CH<sub>4</sub>-H<sub>2</sub>O gas hydrate stability field.

The in-situ pore fluid sampling program was largely unsuccessful because of design problems with the two available in-situ sampling

**Table 13. Interstitial-water chemical data recovered with the water sampler temperature probe, Hole 892A.**

| Sample        | Depth (mbsf) | Salinity (g/kg) | Cl <sup>-</sup> (mM) | Cl <sub>cor</sub> <sup>-</sup> (mM) | Mg <sup>2+</sup> (mM) | Mg <sub>cor</sub> <sup>2+</sup> (mM) | Ca <sup>2+</sup> (mM) | Ca <sub>cor</sub> <sup>2+</sup> (mM) | SO <sub>4</sub> <sup>2-</sup> (mM) | Correction for drilling fluid contamination (%) | Correction for drilling fluid contamination |                                      |                       |                          |
|---------------|--------------|-----------------|----------------------|-------------------------------------|-----------------------|--------------------------------------|-----------------------|--------------------------------------|------------------------------------|-------------------------------------------------|---------------------------------------------|--------------------------------------|-----------------------|--------------------------|
|               |              |                 |                      |                                     |                       |                                      |                       |                                      |                                    |                                                 | NH <sub>4</sub> <sup>+</sup> (μM)           | NH <sub>4cor</sub> <sup>+</sup> (μM) | SiO <sub>2</sub> (μM) | SiO <sub>2cor</sub> (μM) |
| 146-892A-3X-1 | 20.1         | 33.0            | 546                  | 547                                 | 40.99                 | 40.77                                | 6.67                  | 6.59                                 | 0.64                               | 2.5                                             | —                                           | —                                    | 477                   | 489                      |
| 6X-1          | 40.1         | 2.0             | 523                  | 528                                 | 42.13                 | 36.14                                | 7.93                  | 6.40                                 | 11.28                              | 43.4                                            | —                                           | —                                    | 459                   | 811                      |
| 12X-1         | 87.5         | 32.2            | 505                  | 476                                 | 41.17                 | 19.97                                | 9.21                  | 7.44                                 | 18.37                              | 70.7                                            | 2918                                        | 4127                                 | 160                   | 226                      |
| 13X-1         | 97.5         | 33.5            | 506                  | 338                                 | 42.37                 | 14.37                                | 8.81                  | 4.65                                 | 20.44                              | 78.7                                            | 3549                                        | 4510                                 | 196                   | 249                      |

tools, the pressure core sampler (PCS) and the water-sampling temperature probe (WSTP). Although the PCS retained pressure on deck approximately equal to the in-situ hydrostatic pressure, it recovered only drilling water; no sediment was recovered in three deployments. In two of the PCS runs, small amounts of gas, which will be analyzed on shore, were recovered.

The WSTP was deployed four times in Hole 892A and once in Hole 892E, for in-situ pore fluid samples. In each of the Hole 892A deployments, the Ti coil was only partially filled with water upon recovery (3–6 cm<sup>3</sup>; Table 13), and except for the fourth deepest deployment the stainless steel coil was empty. The volumes of overflow water were small, approximately equal to the sum of the volumes of the two coils, and the water consisted mainly of the expelled nanopure water. In Hole 892E, the Ti coil was almost filled with water (8 cm<sup>3</sup>), but the stainless steel coil contained only 4 cm<sup>3</sup> of water, and the overflow was very large, more than 1 L. In Hole 892A, the majority of the original nanopure water within the coils must have been displaced by gas, most probably evolved upon pressure release and temperature increase. The 2.5 cm<sup>3</sup> of water recovered from the shallowest WSTP deployment in Hole 892A, at 20 mbsf, following Section 146-892A-3X-1, consisted largely (97.5%) of in-situ formation water. Because both the formation water from the depth at which the samples were taken and the nanopure water contain no sulfate, the sulfate concentration could be used for calculations of percent contamination with drilling water. The SO<sub>4</sub><sup>2-</sup> corrected chemical data for the four WSTP samples from Hole 892A are given in Table 13. The percentage of correction increases systematically with sub-bottom depths, to more than 70% drilling water in the third and fourth WSTP pore-fluid samples from Hole 892A. The WSTP sample from Hole 892E contained about 85% drilling water.

The chemical data corrected for sulfate indicate that the in-situ formation waters recovered in the two shallowest WSTP samples from Hole 892A have higher Ca<sup>2+</sup> and Mg<sup>2+</sup> and lower silica and ammonia concentrations than pore fluids squeezed from the adjacent whole-round samples. Not enough water was available for alkalinity analyses; however, the in-situ formation waters are expected to have higher alkalinities than those measured in the fluids squeezed from cores. At high alkalinities (>10 to 15 mM), some carbonate may precipitate upon pressure release during drilling and core recovery. This will lower the Ca<sup>2+</sup> and Mg<sup>2+</sup> concentrations of the squeezed pore fluids relative to the in-situ concentrations, as is observed. Upon warming of the cores during recovery and handling, the dissolved silica rapidly reequilibrates with the host sediment, because solubilities of all silicates are strongly positively temperature dependent. The silica concentrations of the squeezed pore fluids are higher than the in-situ concentrations obtained with the WSTP as expected, because shipboard temperatures are higher than those at which the in-situ samples were taken. The chemistry of the two deeper WSTP water samples (following Sections 146-892A-2X-1, at 89 mbsf, and -13X-1, at 98 mbsf) indicate mixing of three end-member fluids: primarily surface seawater (about 71% and 79% in WSTP Runs 3 and 4, respectively), formation water, and some unexpelled nanopure water.

As at the previous sites, the whole-round (5–10 cm length), squeezed pore fluids of Hole 892A were analyzed for salinity, Cl<sup>-</sup>,

Ca<sup>2+</sup>, Mg<sup>2+</sup>, K<sup>+</sup>, silica, ammonia, phosphate, sulfate, pH, and alkalinity. The pore fluids of Hole 892D were only analyzed for salinity, Cl<sup>-</sup>, silica, sulfate, pH, and alkalinity because of the short time remaining in the cruise. The corrections for drilling-water contamination involved the same considerations and calculations discussed in the "Inorganic Geochemistry" section of chapter on Sites 889 and 890. The corrected data are presented in Tables 11 and 12.

## Results

### Overall Trends in the Chemical Profiles

The low and variable concentrations of Cl<sup>-</sup>, Ca<sup>2+</sup>, Na<sup>+</sup>, and alkalinity observed at <20 mbsf are artifacts of dissociation of the (inferred) sulfide-methane gas hydrates present in the first two cores. The pore-fluid chemistry of this depth interval will not be discussed further in this chapter, because the interpretations depend on shore-based analyses of the gas hydrate composition.

Significant decreases in the Cl<sup>-</sup>, Na<sup>+</sup>, and Mg<sup>2+</sup> concentrations and in alkalinity and increases in Ca<sup>2+</sup> concentrations from the base of the (macroscopically observable) gas hydrate zone at about 20 mbsf to the distinct concentration minima at 125–135 mbsf (Figs. 45–46) suggest that fluid is advecting through fractures in this depth interval. Assuming that the vertical chemical profiles are controlled by diffusional communication with fluid flowing along the primary fault zone and discharging at its surface trace (J.C. Moore, pers. comm., 1992), establishing a diffusion path length of 130 m would require about 10<sup>5</sup> yr, assuming diffusion coefficients of 2–5 × 10<sup>-6</sup> cm<sup>2</sup>/s.

In the uppermost 20–110 m (and most distinctly in the first 20–70 m) of the sediment section, superimposed on the general concentration gradients, are closely spaced concentration reversals rarely observed in marine sediment pore-fluid chemical concentration profiles. Below about 70 m, the gradients are less variable. The origin of the observed deepest geochemical discontinuities in Cl<sup>-</sup>, Na<sup>+</sup>, Mg<sup>2+</sup>, K<sup>+</sup>, ammonia, and silica at about 160 mbsf in Hole 892A is difficult to evaluate on the basis of only two data points per component. Furthermore, this feature was not observed in the Hole 892D profiles (see Cl<sup>-</sup> profile, Fig. 46).

Potassium concentrations also decrease with depth (Fig. 45), but the gradient decreases beneath the depth of the seismic BSR (73 mbsf). A distinct potassium minimum is present at about 88 mbsf, which is also the depth of one of the prominent Cl<sup>-</sup> minima discussed below; but potassium concentrations show no response in the vicinity of the primary fault zone (116–147 mbsf) (see Fig. 45). In contrast, ammonia concentrations (Fig. 45) increase downhole to about 70 mbsf, and from 70 to 140 mbsf the concentrations remain high, and generally constant, except for minima at 88 and 107 mbsf. The distribution suggests either diffuse lateral fluid transport across a broadly faulted interval or focused flow modified by reactions.

In Holes 892A and 892D, silica concentrations reach 900 to >1000 μM from 20 to 40 mbsf; these pore fluids are saturated with respect to opal-A. Below approximately 50 mbsf, except for a distinct maximum at 107 m in Hole 892A, silica concentrations remain generally constant with depth at about 900 μM, suggesting little silica diagenesis beyond biogenic opal-A dissolution (Figs. 45–46).

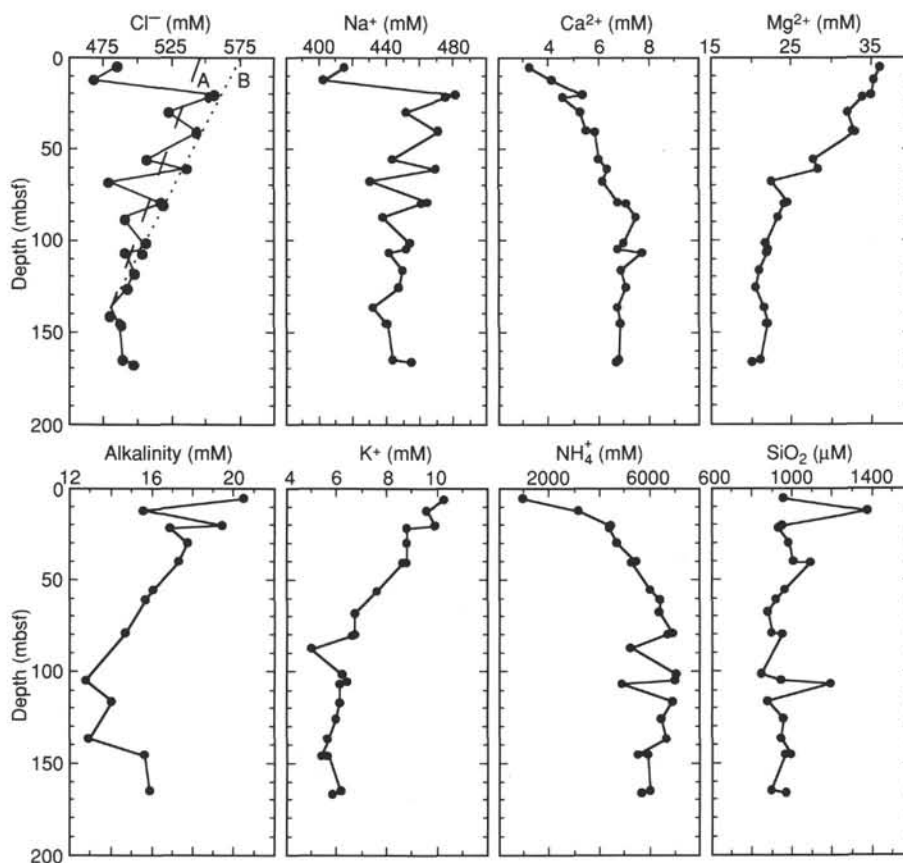


Figure 45. Concentration vs. depth profiles for chloride, sodium, calcium, magnesium, alkalinity, potassium, ammonium, and silica, Hole 892A. In the chloride profile, dashed line A connects the  $\text{Cl}^-$  minimum within the major fault zone with modern bottom-water  $\text{Cl}^-$  concentrations, and dotted line B connects the  $\text{Cl}^-$  minimum within the major fault zone with the  $\text{Cl}^-$  maxima points.

### The Chlorinity Profiles

Closely spaced strong concentration reversals characterize the  $\text{Cl}^-$  profiles of Holes 892A and 892D between about 20 and 100 mbsf (Figs. 45 and 46, respectively). The origin of the reversals is attributed either to advective flow along lithologic or structural elements delineated by the  $\text{Cl}^-$  minima (Fig. 45), or from in-situ dilution (i.e., from dissociation of gas hydrate within specific lithologic horizons). In Hole 892A, the intensities of the dilution minima increase with depth to that at 68 mbsf, the depth of the sample nearest the BSR (73 mbsf). A low in  $\text{Cl}^-$  concentration at the BSR depth is also observed in Hole 892D. The  $\text{Na}^+$ ,  $\text{Ca}^{2+}$ ,  $\text{Mg}^{2+}$ , and other depth profiles show similar concentration reversals. The rather smooth depth profiles of  $\text{Na}^+$ ,  $\text{Ca}^{2+}$ , and  $\text{Mg}^{2+}$ , normalized to  $\text{Cl}^-$ , from 20 to 68 mbsf (Fig. 47), and the fact that the components are diluted equivalent to  $\text{Cl}^-$  at the 30- and 56-mbsf  $\text{Cl}^-$  minima, support the interpretation of dilution by  $\text{H}_2\text{O}$ , most likely through gas-hydrate dissociation. No prominent lithologic or structural boundaries have been observed at 30 mbsf, the depth of the shallowest  $\text{Cl}^-$  minimum. This  $\text{Cl}^-$  minimum is present in both Holes 892A and 892D (Figs. 45–46). The strongest  $\text{Cl}^-$  minimum in Hole 892A, which is observed as a low (but not a minimum value) in Hole 892D, occurs at 68 mbsf, the boundary between lithostratigraphic Subunits IA and IB, where a highly fractured, carbonate-cemented sandstone occurs. At this depth, organic and inorganic carbon contents show a strong minimum and maximum, respectively, and positive peaks in thermogenic gases occur (see “Organic Geochemistry” section, this chapter). The chemistry of this most intense  $\text{Cl}^-$  minimum suggests a complex origin. The existence of the  $\text{Na}/\text{Cl}$  maximum and of the  $\text{Ca}/\text{Cl}$  and

$\text{Mg}/\text{Cl}$  minima at 68 mbsf (Fig. 47) indicates that dilution by gas-hydrate dissociation is not the only process controlling the chemistry of this low- $\text{Cl}^-$  fluid. Mixing with another fluid and/or diagenetic reactions such as carbonate precipitation must also be involved.

Two additional, smaller  $\text{Cl}^-$ -minimum horizons occur below the BSR, at about 87 and 107 mbsf in Hole 892A. The two horizons fall within the calculated  $\text{CH}_4\text{-H}_2\text{O}$  gas-hydrate stability field, based on the measured background linear temperature gradient of  $51^\circ\text{C}/\text{km}$  (see “WSTP and ADARA Temperature Measurements” section, this chapter).

The three strongest  $\text{Cl}^-$  minima in Hole 892A (Fig. 45) correspond to seawater  $\text{Cl}^-$  dilutions of 9%, 11%, and 15% at 30, 56, and 68 mbsf, respectively. The core sections at each of these three  $\text{Cl}^-$  minima are associated with “soupy” layers (see “Lithostratigraphy” section, this chapter). These three depth intervals in Hole 892A and the 30-mbsf  $\text{Cl}^-$ -minimum interval in Hole 892D were resampled. Core samples were squeezed within, above, and below the “soupy” layers associated with the three uppermost  $\text{Cl}^-$  minima. As yet, only the samples surrounding the  $\text{Cl}^-$  minimum at 56 mbsf in Hole 892A and the  $\text{Cl}^-$  minimum at 30 mbsf in Hole 892D have been analyzed for  $\text{Cl}^-$  concentrations. These data indicate that the thickness of these  $\text{Cl}^-$  minima is about 1 m. The limited vertical extent of the low- $\text{Cl}^-$  spikes implies a dissociation of heterogeneously distributed gas hydrate and/or focused flow of warm fluid. The narrow width of the inferred flow zones ( $\sim 1$  m) implies that fluid flow must have begun very recently, no more than 16–32 yr ago, assuming diffusion coefficients of  $1 \times 10^{-5}$  and  $5 \times 10^{-6} \text{ cm}^2/\text{s}$ , respectively. Flow of warm fluid might cause local dissociation of gas hydrate.

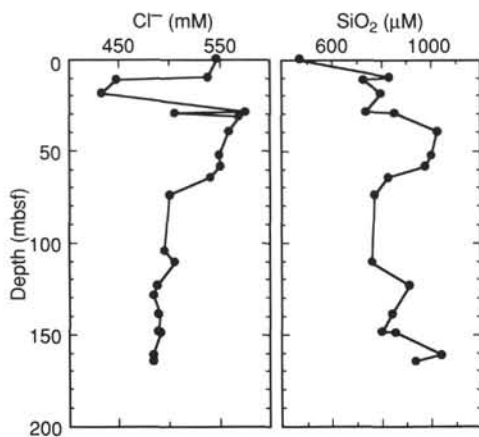


Figure 46. Concentration vs. depth profiles of chloride and silica, Hole 892D.

The extrapolation of the line connecting the  $\text{Cl}^-$  maxima in the  $\text{Cl}^-$  depth profile of Hole 892A approximately intersects the 130 mbsf  $\text{Cl}^-$  minimum and projects to a  $\text{Cl}^-$  concentration of 574 mM at the seafloor (Fig. 45, dotted line B in chlorinity profile). This projected seawater value is equivalent to the  $\text{Cl}^-$  concentration of glacial bottom water. The measured present bottom-water chlorinity at this site is 545 mM. In the chlorinity profile in Figure 45, dashed line A connects the  $\text{Cl}^-$  minimum at 130 mbsf with the modern seafloor  $\text{Cl}^-$  concentration of 545 mM. Line A lies between the  $\text{Cl}^-$ -maxima points that may approximate the residual saline fluids from in-situ formation of gas hydrate, or alternatively may approximate a  $\text{Cl}^-$ -diffusion profile of the last Pleistocene glacial maximum, not yet overprinted during the present interglacial.

In summary, the  $\text{Cl}^-$ -minima horizons above the BSR (73 mbsf) could be interpreted to represent either dilution spikes caused by dissociation of local concentrations of gas hydrate (probably within the "soupy" layers), or by lateral flow of a low- $\text{Cl}^-$  fluid. The low- $\text{Cl}^-$  anomalies deeper than ~100 mbsf, however, can only be reasonably attributed to advective flow from a deeper seated source.

Curiously, the low- $\text{Cl}^-$  fluid recovered at 68 mbsf near the BSR (at 73 mbsf) is remarkably similar to the fault zone fluid discussed below, with the exception of silica. This similarity suggests that the strong  $\text{Cl}^-$  minimum at this depth reflects the mixing of fluids: a low  $\text{Cl}^-$  "warm" fluid advecting from greater depth, with an in-situ dilute fluid from gas-hydrate dissociation.

#### Fluid Chemistry Within a Fault Zone

The set of chemical profiles before and after normalization to the  $\text{Cl}^-$  concentrations (Figs. 45–47) indicates that the fluid between 107 and 135 mbsf is low in  $\text{Cl}^-$  as well as being depleted in  $\text{K}^+$  and  $\text{Mg}^{2+}$  and enriched in  $\text{Na}^+$  and  $\text{Ca}^{2+}$ . The fluid is also characterized by high silica and ammonia as well as by low alkalinity. Except for the high ammonia, which reflects organic matter decomposition, these chemical characteristics are typical of deep-seated fluids in subduction zones. The depletions in  $\text{K}^+$  and  $\text{Mg}^{2+}$  reflect transformation and recrystallization of clay minerals; the  $\text{Na}^+$  enrichment relative to  $\text{Cl}^-$  (Fig. 47) is a result of its expulsion from exchange sites by ammonia and the dissolution of plagioclase. The enrichment in  $\text{Ca}^{2+}$  is controlled by reactions with plagioclase, amphibole, and pyroxene. The  $\text{Mg}/\text{Cl}$  molar ratios profile (Fig. 47) exhibits a minimum at 130 mbsf;  $\text{Mg}^{2+}$  is depleted relative to  $\text{Cl}^-$ , most likely through carbonate precipitation. Although the  $\text{Mg}/\text{Ca}$  molar ratios remain constant throughout the depth interval of the fault zone (Fig. 47), this constant ratio does not necessarily imply that dolomite is the only precipitating carbonate, because  $\text{Mg}^{2+}$  is involved in both carbonate and silicate reactions. In view of this fluid chemistry, observation of widespread

carbonate precipitation at the seafloor, at the Central Oregon accretionary complex, is not surprising. The  $\delta^{13}\text{C}$  value of this carbonate should be considerably heavier than of carbonate formed from methane oxidation. Both types of carbonates should coexist where the fault intersects the seafloor.

## PHYSICAL PROPERTIES

### Introduction

Sediment physical properties were measured on cores recovered from Holes 892A, 892D, and 892E. Measurements for Site 892 include index properties, electrical resistivity, acoustic velocity, undrained shear strength, and thermal conductivity. The methods used for these measurements are described in the "Explanatory Notes" chapter (this volume). The multisensor track (MST) was run on all cores for magnetic susceptibility (see "Paleomagnetism" section, this chapter). The MST  $P$ -wave and gamma-ray attenuation porosity evaluator (GRAPE) data were too scattered for interpretation because of large voids and cracks in the whole cores of Hole 892A. These data are not discussed and their use is not recommended. The GRAPE data for Holes 892D and 892E are of good quality because of improved core recovery in these holes, and these data are reported here. However,  $P$ -wave velocity on the MST for Holes 892D and 892E could not be measured because of the scattering of acoustic energy.

Physical properties trends generally reflect the boundaries of the lithostratigraphic subunits (see "Lithostratigraphy" section, this chapter), but they also show distinct discontinuities at discrete depth intervals that may indicate positions of faults (density/porosity changes induced by shearing) or compositional changes. Five major discontinuities are described. The physical properties data are internally consistent and suggest an underconsolidated sediment column in the upper 20 m, a normal to slightly overconsolidated interval from 20 to 68 mbsf, and a slightly overconsolidated section below 68 mbsf.

### Index Properties

Above 9 mbsf, where gas hydrate was observed in the core (see "Organic Geochemistry" section, this chapter), bulk density is low, porosity is high, and both show little change with depth. A discontinuity (#1, Fig. 48) occurs in the index properties between 14 and 20 mbsf, where bulk density increases and porosity decreases below the discontinuity. With the exception of the upper 14 mbsf, within lithostratigraphic Subunit IA (0–67.75 mbsf), bulk density increases and porosity and water content decrease with depth (Fig. 48 and Table 14), suggesting that the dominant process in this interval is gravitational compaction. Grain density, normally a parameter with only small variation and generally no depth trend, decreases with depth in Subunit IA to approximately 47 mbsf, and then increases to the base of the subunit (Fig. 49).

A second discontinuity (#2, Fig. 48) is coincident with the Subunit IA/IB boundary (67.75 mbsf). Index properties do not vary consistently with depth within Subunit IB, but exhibit three discontinuities. Within Subunit IB, the discontinuities are not similar in character to those in Subunit IA (discontinuities #1 and #2) in which consistent trends of index properties with depth occur above and below the discontinuity. Rather, the Subunit IB discontinuities are characterized by large variations in bulk density ( $>0.3 \text{ Mg/m}^3$ ) and porosity (10%) over small depth intervals ( $<2 \text{ m}$ ). These changes occur at 104 mbsf (#3), 144 mbsf (#4), and 164 mbsf (#5) and are most likely the result of shear consolidation, in which localized zones have experienced high strain that has acted to locally dewater the sediment. Because of the low recovery at this site, it is difficult to assess the true extent of these localized zones within Subunit IB. It may be that they are pervasive throughout the subunit.

The MST GRAPE data show a significant amount of scatter, but GRAPE maxima generally replicate well with the discrete laboratory

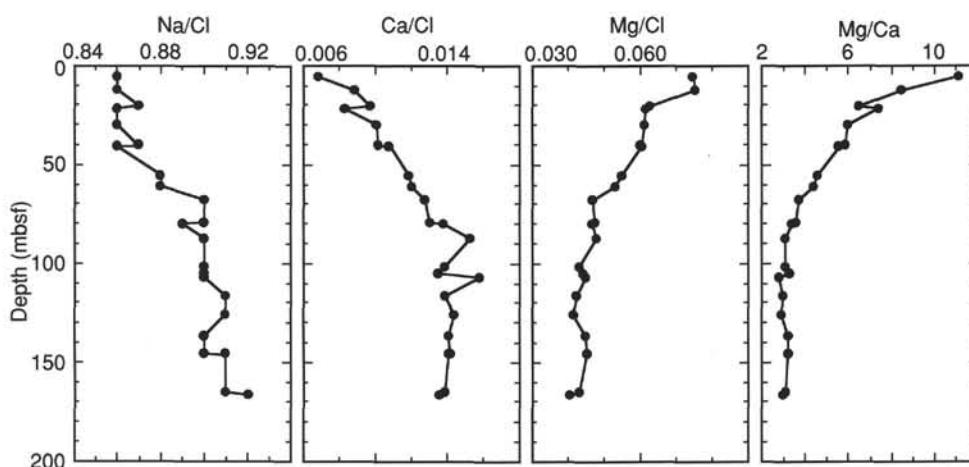


Figure 47. Depth profiles of Na/Cl, Ca/Cl, Mg/Cl, and Mg/Ca molar ratios of pore fluids, Hole 892A.

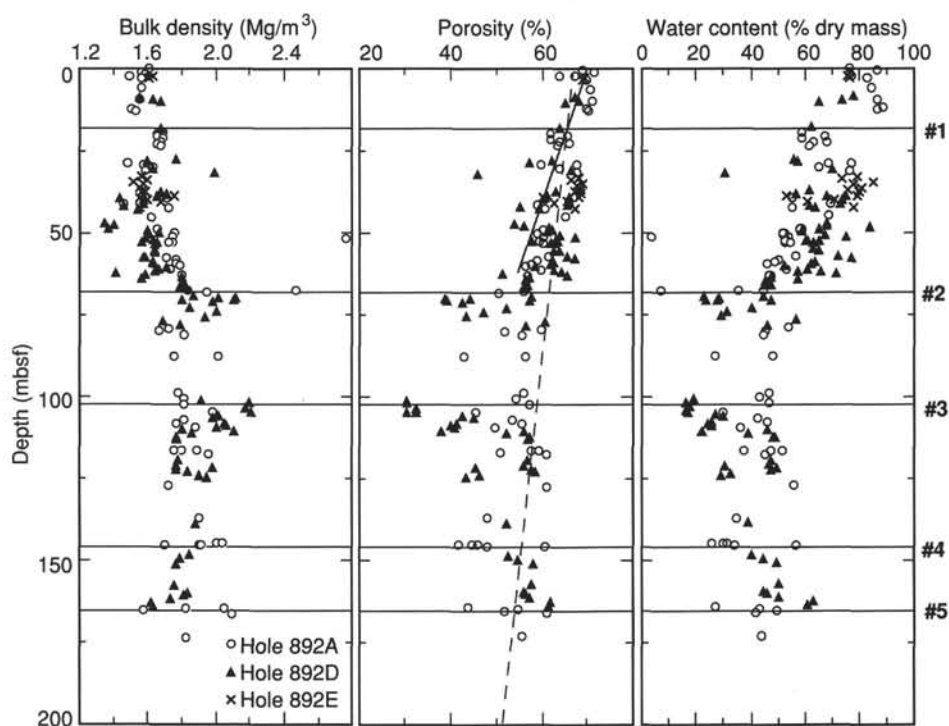


Figure 48. Index properties (bulk density, porosity, and water content) vs. depth with interpreted discontinuities shown as horizontal lines (open circles = Hole 892A, triangles = Hole 892D, and crosses = Hole 892E). Discontinuity #1 is the boundary between sediment that contains observed hydrate and sediment where there was no observed hydrate; Discontinuity #2 is at the boundary between lithostratigraphic Subunits IA and IB. Brückmann's (1989) normally consolidated porosity-depth function (dashed line) and an exponential regression curve (porosity =  $70.6^{(-0.0018 \times \text{depth})}$ ;  $R = 0.5$ ) for Subunit IA (solid line) are also plotted in the porosity profile.

measurements (Fig. 50). The GRAPE data tend to shift the average density to low values because the measurement does not exclude low-density drill slurry, which is pervasive within the XCB cores.

In comparison to normally consolidated porosity-depth functions for silty clay (Brückmann, 1989), Site 892 shows two general regions of stress history, below the section (<19 mbsf) disturbed by gas sublimation. Between 19 and 67.8 mbsf, porosity is generally close to or slightly below the prediction for normally consolidated silty clay, suggesting normal to slight overconsolidation. In Subunit IB, below 67.75 mbsf, the porosity is consistently lower than the prediction curve for normal consolidation, suggesting a generally overconsolidated section.

## Electrical Resistivity

Resistivity was measured in core samples collected in Holes 892A and 892D (Table 15). The measurement interval varied with the amount and quality of recovered sediment. Electrical resistivity is reported here in its nondimensional form as the ratio of saturated-sediment resistivity to the calculated pore-fluid resistivity, known as the formation factor (see "Explanatory Notes" chapter, this volume). At Site 892, Archie coefficients were determined by assuming a fixed value for the cementation coefficient ( $m$ ) of  $-1.76$  (Wang et al., 1976) and fitting an exponential curve to the data (Fig. 51). The resulting tortuosity coeffi-

Table 14. Summary of index property data, Holes 892A, 892D, and 892E.

| Core, section, interval (cm) | Depth (mbsf) | Bulk density (Mg/m <sup>3</sup> ) | Porosity (%) | Water content (%) |            | Grain density (Mg/m <sup>3</sup> ) | Dry-bulk density (Mg/m <sup>3</sup> ) | Core, section, interval (cm) | Depth (mbsf) | Bulk density (Mg/m <sup>3</sup> ) | Porosity (%) | Water content (%) |            | Grain density (Mg/m <sup>3</sup> ) | Dry-bulk density (Mg/m <sup>3</sup> ) |
|------------------------------|--------------|-----------------------------------|--------------|-------------------|------------|------------------------------------|---------------------------------------|------------------------------|--------------|-----------------------------------|--------------|-------------------|------------|------------------------------------|---------------------------------------|
|                              |              |                                   |              | Dry mass          | Total mass |                                    |                                       |                              |              |                                   |              | Dry mass          | Total mass |                                    |                                       |
| 146-892A-                    |              |                                   |              |                   |            |                                    |                                       | 146-892D-                    |              |                                   |              |                   |            |                                    |                                       |
| 1X-1, 40                     | 0.40         | 1.61                              | 69.25        | 76.69             | 43.35      | 2.70                               | 0.91                                  | 5X-3, 10                     | 40.10        | 1.57                              | 66.11        | 73.75             | 42.39      | 2.48                               | 0.91                                  |
| 1X-1, 110                    | 1.10         | 1.56                              | 71.66        | 86.38             | 46.29      | 2.67                               | 0.84                                  | 5X-3, 130                    | 41.30        | 1.57                              | 65.70        | 73.01             | 42.15      | 2.42                               | 0.91                                  |
| 1X-2, 55                     | 2.05         | 1.58                              | 67.55        | 76.38             | 43.25      | 2.66                               | 0.89                                  | 5X-4, 43                     | 41.93        | 1.46                              | 55.10        | 61.40             | 38.00      | 2.53                               | 0.91                                  |
| 1X-2, 85                     | 2.35         | 1.49                              | 63.97        | 76.92             | 43.42      | 2.74                               | 0.84                                  | 5X-4, 113                    | 42.63        | 1.54                              | 59.30        | 63.70             | 38.86      | 2.51                               | 0.94                                  |
| 1X-3, 30                     | 3.30         | 1.56                              | 70.10        | 83.06             | 45.32      | 2.70                               | 0.85                                  | 6X-1, 81                     | 47.31        | 1.35                              | 53.85        | 67.70             | 40.32      | 2.57                               | 0.80                                  |
| 1X-5, 5                      | 6.05         | 1.56                              | 70.89        | 84.58             | 45.77      | 2.72                               | 0.85                                  | 6X-2, 60                     | 48.60        | 1.37                              | 61.58        | 83.79             | 45.53      | 2.52                               | 0.74                                  |
| 2X-1, 15                     | 9.65         | 1.55                              | 71.25        | 86.82             | 46.42      | 2.71                               | 0.83                                  | 6X-2, 115                    | 49.15        | 1.60                              | 62.45        | 65.29             | 39.45      | 2.46                               | 0.97                                  |
| 2X-2, 130                    | 12.30        | 1.51                              | 69.94        | 88.39             | 46.86      | 2.70                               | 0.80                                  | 6X-3, 32                     | 49.57        | 1.66                              | 61.09        | 59.03             | 37.07      | 2.52                               | 1.04                                  |
| 2X-3, 35                     | 12.85        | 1.53                              | 70.16        | 86.70             | 46.38      | 2.70                               | 0.82                                  | 6X-3, 128                    | 50.53        | 1.61                              | 64.01        | 67.23             | 40.15      | 2.47                               | 0.96                                  |
| 3X-1, 55                     | 19.55        | 1.69                              | 61.72        | 58.58             | 36.90      | 2.61                               | 1.06                                  | 6X-4, 50                     | 51.25        | 1.58                              | 67.26        | 75.21             | 42.87      | 2.48                               | 0.90                                  |
| 3X-1, 133                    | 20.33        | 1.65                              |              |                   |            |                                    |                                       | 6X-4, 135                    | 52.10        | 1.63                              | 63.78        | 65.21             | 39.42      | 2.52                               | 0.99                                  |
| 3X-2, 15                     | 20.65        | 1.65                              | 65.57        | 67.23             | 40.15      | 2.66                               | 0.98                                  | 6X-5, 20                     | 52.45        | 1.56                              | 57.87        | 59.98             | 37.44      | 2.54                               | 0.97                                  |
| 3X-2, 100                    | 21.50        | 1.69                              | 61.87        | 58.75             | 36.97      | 2.68                               | 1.06                                  | 6X-5, 35                     | 52.60        | 1.65                              | 61.77        | 60.74             | 37.74      | 2.58                               | 1.03                                  |
| 3X-3, 33                     | 22.33        | 1.68                              | 64.21        | 62.84             | 38.54      | 2.63                               | 1.03                                  | 6X-5, 75                     | 53.00        | 1.64                              | 62.88        | 63.09             | 38.64      | 2.53                               | 1.01                                  |
| 3X-3, 80                     | 22.80        | 1.65                              | 66.19        | 68.12             | 40.47      | 2.65                               | 0.98                                  | 7X-1, 120                    | 55.20        | 1.64                              | 62.72        | 62.85             | 38.55      | 2.48                               | 1.01                                  |
| 3X-CC, 5                     | 23.55        | 1.68                              | 63.46        | 61.58             | 38.07      | 2.61                               | 1.04                                  | 7X-2, 20                     | 55.70        | 1.64                              | 64.14        | 65.50             | 39.53      | 2.56                               | 0.99                                  |
| 4X-1, 45                     | 28.95        | 1.48                              | 60.03        | 69.10             | 40.81      | 2.65                               | 0.88                                  | 7X-3, 30                     | 57.06        | 1.58                              | 65.48        | 72.16             | 41.86      | 2.52                               | 0.92                                  |
| 4X-1, 70                     | 29.20        | 1.57                              | 67.93        | 77.58             | 43.64      | 2.57                               | 0.88                                  | 7X-3, 80                     | 57.56        | 1.57                              | 67.55        | 77.07             | 43.47      | 2.54                               | 0.89                                  |
| 4X-2, 35                     | 30.35        | 1.63                              | 63.83        | 65.52             | 39.54      | 2.50                               | 0.98                                  | 7X-4, 30                     | 58.56        | 1.63                              | 62.82        | 63.90             | 38.94      | 2.46                               | 0.99                                  |
| 4X-CC, 2                     | 31.52        | 1.58                              | 68.01        | 76.76             | 43.38      | 2.58                               | 0.90                                  | 7X-4, 110                    | 59.36        | 1.63                              | 62.10        | 62.42             | 38.38      | 2.48                               | 1.00                                  |
| 6X-1, 56                     | 39.56        | 1.71                              | 60.58        | 55.60             | 35.69      | 2.65                               | 1.10                                  | 7X-5, 30                     | 60.06        | 1.71                              | 58.59        | 52.64             | 34.44      | 2.60                               | 1.12                                  |
| 6X-2, 70                     | 41.20        | 1.46                              | 59.16        | 69.53             | 40.96      | 2.51                               | 0.86                                  | 7X-5, 110                    | 60.86        | 1.66                              | 62.54        | 61.04             | 37.86      | 2.58                               | 1.03                                  |
| 6X-3, 45                     | 42.45        | 1.72                              | 60.47        | 55.02             | 35.45      | 2.68                               | 1.11                                  | 7X-6, 25                     | 61.28        | 1.64                              | 64.46        | 65.92             | 39.68      | 2.56                               | 0.99                                  |
| 6X-5, 15                     | 45.15        | 1.62                              | 65.32        | 68.76             | 40.70      | 2.47                               | 0.96                                  | 8X-1, 48                     | 62.18        | 1.41                              | 51.18        | 57.52             | 36.47      | 2.57                               | 0.90                                  |
| 7X-1, 60                     | 49.10        | 1.65                              | 60.34        | 58.29             | 36.78      | 2.58                               | 1.04                                  | 8X-1, 115                    | 62.85        | 1.58                              | 65.52        | 71.71             | 41.71      | 2.52                               | 0.92                                  |
| 7X-2, 32                     | 50.32        | 1.75                              | 59.02        | 51.62             | 34.01      | 2.66                               | 1.15                                  | 8X-2, 25                     | 63.25        | 1.80                              | 57.29        | 47.40             | 32.12      | 2.65                               | 1.22                                  |
| 7X-2, 125                    | 51.25        | 1.74                              | 60.33        | 53.76             | 34.92      | 2.68                               | 1.13                                  | 8X-2, 87                     | 63.87        | 1.56                              | 56.22        | 57.39             | 36.42      | 2.68                               | 0.99                                  |
| 7X-3, 10                     | 51.60        | 2.76                              | 9.78         | 3.67              | 3.54       | 2.78                               | 2.67                                  | 8X-3, 50                     | 65.00        | 1.81                              | 56.28        | 45.61             | 31.28      | 2.69                               | 1.24                                  |
| 7X-3, 120                    | 52.70        | 1.74                              | 59.52        | 52.76             | 34.50      | 2.72                               | 1.14                                  | 8X-3, 148                    | 65.98        | 1.79                              | 57.04        | 47.12             | 31.99      | 2.62                               | 1.22                                  |
| 7X-4, 18                     | 53.18        | 1.72                              | 60.20        | 54.40             | 35.19      | 2.62                               | 1.12                                  | 8X-4, 10                     | 66.25        | 1.82                              | 56.28        | 45.20             | 31.09      | 2.67                               | 1.25                                  |
| 7X-6, 140                    | 57.40        | 1.71                              | 61.44        | 57.03             | 36.28      | 2.65                               | 1.09                                  | 9X-1, 16                     | 69.46        | 1.87                              | 57.62        | 44.94             | 30.97      | 2.72                               | 1.29                                  |
| 8X-1, 21                     | 58.21        | 1.77                              | 59.05        | 50.56             | 33.54      | 2.70                               | 1.18                                  | 9X-1, 60                     | 69.90        | 2.12                              | 38.93        | 22.59             | 18.40      | 2.65                               | 1.73                                  |
| 8X-1, 132                    | 59.32        | 1.77                              | 57.78        | 48.93             | 32.81      | 2.71                               | 1.19                                  | 9X-1, 90                     | 70.20        | 2.02                              | 44.18        | 28.11             | 21.92      | 2.69                               | 1.58                                  |
| 8X-2, 40                     | 59.90        | 1.79                              | 56.28        | 46.18             | 31.55      | 2.70                               | 1.23                                  | 9X-1, 125                    | 70.55        | 2.11                              | 39.30        | 23.08             | 18.73      | 2.71                               | 1.71                                  |
| 8X-3, 20                     | 61.20        | 1.73                              | 59.74        | 53.34             | 34.75      | 2.68                               | 1.13                                  | 9X-1, 132                    | 70.62        | 1.80                              | 57.17        | 47.09             | 31.97      | 2.69                               | 1.22                                  |
| 8X-4, 40                     | 62.90        | 1.80                              | 56.96        | 46.96             | 31.92      | 2.71                               | 1.22                                  | 9X-2, 15                     | 70.95        | 1.98                              | 42.73        | 27.62             | 21.62      | 2.57                               | 1.55                                  |
| 9X-1, 22                     | 67.72        | 2.47                              | 16.50        | 7.17              | 6.69       | 2.71                               | 2.30                                  | 9X-3, 85                     | 72.46        | 1.84                              | 52.21        | 40.09             | 28.58      | 2.67                               | 1.31                                  |
| 9X-1, 40                     | 67.90        | 1.84                              | 56.24        | 44.41             | 30.72      | 2.72                               | 1.28                                  | 9X-4, 25                     | 72.84        | 2.00                              | 47.30        | 31.18             | 23.74      | 2.72                               | 1.53                                  |
| 9X-1, 55                     | 68.05        | 1.95                              | 50.64        | 35.31             | 26.07      | 2.76                               | 1.44                                  | 9X-5, 25                     | 73.77        | 1.94                              | 43.56        | 29.16             | 22.55      | 2.65                               | 1.50                                  |
| 11X-1, 120                   | 79.20        | 1.72                              | 59.75        | 53.80             | 34.94      | 2.61                               | 1.12                                  | 9X-6, 15                     | 75.00        | 1.69                              | 60.65        | 56.85             | 36.20      | 2.55                               | 1.08                                  |
| 11X-2, 52                    | 80.02        | 1.67                              | 51.93        | 45.43             | 31.20      | 2.60                               | 1.15                                  | 9X-CC, 5                     | 75.38        | 1.79                              | 56.22        | 46.10             | 31.52      | 2.61                               | 1.23                                  |
| 11X-3, 15                    | 81.15        | 1.81                              | 55.81        | 44.93             | 30.97      | 2.64                               | 1.25                                  | 10X-2, 20                    | 100.95       | 2.20                              | 30.27        | 16.02             | 13.79      | 2.68                               | 1.90                                  |
| 12X-1, 14                    | 87.64        | 2.02                              | 43.18        | 27.33             | 21.44      | 2.72                               | 1.59                                  | 10X-1, 96                    | 100.96       | 1.91                              | 30.51        | 19.08             | 16.01      | 2.67                               | 1.61                                  |
| 12X-1, 28                    | 87.78        | 1.75                              | 56.44        | 48.13             | 32.45      | 2.65                               | 1.18                                  | 10X-3, 15                    | 102.40       | 2.17                              | 32.39        | 17.60             | 14.95      | 2.66                               | 1.85                                  |
| 13X-2, 40                    | 98.90        | 1.78                              | 56.08        | 46.55             | 31.73      | 2.57                               | 1.21                                  | 10X-3, 130                   | 103.55       | 2.21                              | 30.53        | 16.08             | 13.84      | 2.66                               | 1.91                                  |
| 13X-3, 50                    | 100.50       | 1.81                              | 54.24        | 43.18             | 30.12      | 2.58                               | 1.27                                  | 10X-4, 35                    | 104.10       | 2.21                              | 32.46        | 17.28             | 14.72      | 2.71                               | 1.88                                  |
| 13X-4, 75                    | 102.25       | 1.81                              | 57.20        | 46.68             | 31.79      | 2.57                               | 1.23                                  | 10X-4, 120                   | 104.95       | 2.02                              | 42.52        | 26.86             | 21.15      | 2.66                               | 1.59                                  |
| 13X-6, 25                    | 104.75       | 1.98                              | 45.49        | 30.11             | 23.12      | 2.67                               | 1.52                                  | 10X-5, 10                    | 105.35       | 1.98                              | 44.89        | 29.54             | 22.78      | 2.63                               | 1.53                                  |
| 13X-7, 75                    | 106.75       | 1.81                              | 53.69        | 42.74             | 29.91      | 2.60                               | 1.27                                  | 10X-6, 35                    | 106.68       | 2.05                              | 41.35        | 25.39             | 20.22      | 2.65                               | 1.64                                  |
| 13X-8, 50                    | 108.00       | 1.77                              | 55.67        | 46.31             | 31.62      | 2.58                               | 1.21                                  | 10X-6, 120                   | 107.53       | 2.06                              | 40.19        | 24.41             | 19.60      | 2.61                               | 1.65                                  |
| 13X-CC, 40109.40             | 1.88         | 49.74                             | 36.38        | 26.64             | 2.62       | 1.38                               |                                       | 10X-7, 20                    | 108.03       | 2.00                              | 40.78        | 25.72             | 20.44      | 2.63                               | 1.59                                  |
| 15X-1, 50                    | 116.50       | 1.76                              | 59.29        | 51.47             | 33.94      | 2.62                               | 1.16                                  | 10X-8, 15                    | 109.48       | 2.10                              | 37.82        | 22.13             | 18.10      | 2.63                               | 1.72                                  |
| 15X-1, 55                    | 116.55       | 1.80                              | 57.61        | 47.47             | 32.15      | 2.61                               | 1.22                                  | 11X-1, 65                    | 110.15       | 1.80                              | 56.09        | 45.83             | 31.39      | 2.57                               | 1.23                                  |
| 15X-1, 65                    | 116.65       | 1.89                              | 51.12        | 37.31             | 27.14      | 2.66                               | 1.38                                  | 11X-2, 15                    | 111.25       | 1.86                              | 52.10        | 39.22             | 28.14      | 2.63                               | 1.34                                  |
| 15X-CC, 20117.70             | 1.96         | 61.02                             | 45.54        | 31.25             | 2.64       | 1.35                               |                                       | 11X-2, 135                   | 112.35       | 1.76                              | 57.11        | 48.73             | 32.72      | 2.58                               | 1.18                                  |
| 16X-CC, 24127.24             | 1.72         | 60.92                             | 55.80        | 35.77             | 2.55       | 1.10                               |                                       | 11X-3, 18                    | 112.68       | 1.76                              | 56.98        | 48.33             | 32.54      | 2.59                               | 1.19                                  |
| 17X-2, 55                    | 137.05       | 1.90                              | 48.24        | 34.37             | 25.55      | 2.60                               | 1.41                                  | 12X-1, 41                    | 119.41       | 1.78                              | 56.84        | 47.62             | 32.22      | 2.49                               | 1.20                                  |
| 18X-1, 20                    | 144.70       | 2.01                              | 45.90        | 29.79             | 22.93      | 2.68                               | 1.55                                  | 12X-2, 45                    | 120.95       | 1.77                              | 55.97        | 46.74             | 31.81      | 2.58                               | 1.21                                  |
| 18X-1, 25                    | 144.75       | 2.04                              | 41.69        | 25.81             | 20.49      | 2.69                               | 1.62                                  | 12X-2, 85                    | 121.35       | 1.98                              | 45.64        | 30.09             | 23.10      | 2.67                               | 1.53                                  |
| 18X-1, 46                    | 144.96       | 1.9                               | 44.69        | 31.05             | 23.67      | 2.52                               | 1.45                                  | 12X-3, 20                    | 122.20       | 1.76                              | 57.53        | 49.29             | 32.97      | 2.60                               | 1.18                                  |
| 18X-1, 85                    | 145.35       | 1.91                              | 48.07        | 33.79             | 25.23      | 2.55                               | 1.43                                  | 12X-3, 80                    | 122.80       | 1.83                              | 58.40        | 47.29             | 32.07      | 2.62                               | 1.24                                  |
| 18X-1, 96                    | 145.46       | 1.7                               | 60.87        | 56.52             | 36.07      | 2.53                               | 1.09                                  | 12X-4, 20                    | 123.70       | 1.90                              | 46.20        | 32.31             | 24.39      | 2.60                               | 1.44                                  |
| 20X-1, 95                    | 164.45       | 2.05                              | 43.63        | 27.18             | 21.35      | 2.73                               | 1.61                                  | 12X-4, 100                   | 124.50       | 1.95                              | 43.54        | 29.01             | 22.46      | 2.57                               | 1.51                                  |
| 20X-1, 120                   | 164.70       | 1.82                              | 54.73        | 43.44             | 30.25      | 2.61                               | 1.27                                  | 14X-1, 35                    | 138.35       | 1.88                              | 52.13        | 38.73             | 27.88      | 2.66                               | 1.35                                  |
| 20X-2, 40                    | 165.40       | 1.57                              | 51.65        | 49.41             | 33.03      | 2.15                               | 1.05                                  | 15X-1, 70                    | 148.20       | 1.84                              | 52.62        | 40.52             | 28.80      | 2.60                               | 1.31                                  |
| 20X-2, 125                   | 166.25       | 2.09                              | 61.09        | 41.74             | 29.42      | 3.24                               | 1.47                                  | 15X-2, 40                    | 149.40       | 1.79                              | 54.78        | 44.70             | 30.86      | 2.53                               | 1.23                                  |
| 21X-1, 33                    | 173.33       | 1.82                              | 55.51        | 44.18             | 30.61      | 2.67                               | 1.27                                  | 15X-3, 20                    | 150.70       | 1.77                              | 58.07        | 49.56             | 33.10      | 2.59                               | 1.18                                  |
| 146-892D-                    |              |                                   |              |                   |            |                                    |                                       | 146-892E-                    |              |                                   |              |                   |            |                                    |                                       |
| 2X-1, 10                     | 8.60         | 1.55                              | 67.22        | 78.24             | 43.84      | 2.70                               | 0.87                                  | 1X-2, 105                    | 1.31         | 1.63                              | 69.65        | 76.02             | 43.14      | 2.65                               | 0.93                                  |
| 2X-1, 115                    | 9.65         | 1.63                              | 68.17        | 73.30             | 42.24      | 2.65                               | 0.94                                  | 1X-3, 10                     | 1.86         | 1.61                              | 69.17        | 76.59             | 43.32      | 2.69                               | 0.91                                  |
| 2X-2, 15                     | 10.15        | 1.67                              | 65.21        | 64.76             | 39.26      | 2.70                               | 1.02                                  | 3H-1, 15                     | 33.15        | 1.56                              | 68.          |                   |            |                                    |                                       |

Table 14 (continued).

| Core, section, interval (cm) | Depth (mbsf) | Bulk density (Mg/m <sup>3</sup> ) | Porosity (%) | Water content (%) |            | Grain density (Mg/m <sup>3</sup> ) | Dry-bulk density (Mg/m <sup>3</sup> ) |
|------------------------------|--------------|-----------------------------------|--------------|-------------------|------------|------------------------------------|---------------------------------------|
|                              |              |                                   |              | Dry mass          | Total mass |                                    |                                       |
| 3H-3, 45                     | 35.62        | 1.55                              | 68.74        | 80.89             | 44.66      | 2.46                               | 0.86                                  |
| 3H-3, 140                    | 36.57        | 1.58                              | 67.18        | 75.64             | 43.01      | 2.50                               | 0.90                                  |
| 3H-4, 30                     | 36.95        | 1.56                              | 68.64        | 79.97             | 44.38      | 2.45                               | 0.87                                  |
| 3H-4, 135                    | 38.00        | 1.75                              | 60.29        | 53.44             | 34.78      | 2.66                               | 1.14                                  |
| 3H-5, 20                     | 38.32        | 1.55                              | 68.12        | 79.47             | 44.23      | 2.56                               | 0.87                                  |
| 3H-5, 120                    | 39.32        | 1.60                              | 65.71        | 70.98             | 41.46      | 2.61                               | 0.93                                  |
| 3H-6, 30                     | 39.92        | 1.67                              | 62.59        | 60.81             | 37.77      | 2.54                               | 1.04                                  |
| 3H-CC, 35                    | 40.7         | 1.55                              | 67.26        | 77.88             | 43.73      | 2.45                               | 0.87                                  |

cient,  $\alpha$ , is 2.18. The correlation coefficient for this regression is 0.87. Relatively large discrepancies were observed in the shallow samples (from above 29.2 mbsf), which show low formation factors and high porosities (Fig. 51). This disparity suggests lower cementation or lower tortuosity of the sediments within this shallow depth interval.

The formation factor increases with depth in the upper 67.75 mbsf (Subunit IA) and is more scattered in Subunit IB (Fig. 52A). High values of formation factor at 144 mbsf correspond to low-porosity, darker colored sediments, which correspond in turn to possible strain-hardened zones, as suggested by the index properties results.

Derived porosity values were calculated using the Archie equation (Archie, 1942) (Table 15). A comparison of the discrete direct measurements of porosity with the resistivity-derived porosity shows modest correlation ( $r = 0.49$ ), except for the upper 29.2 mbsf (Fig. 52B).

### Acoustic Velocity

Because of the extensive fractures in the recovered samples at Site 892, only a few measurements of acoustic velocity were possible (Table 16). The velocity data were corrected to in-situ temperature.

### Undrained Shear Strength

Measurements of undrained shear strength ( $S_u$ ) were made using a pocket penetrometer at Site 892 (see "Explanatory Notes" chapter,

this volume). For Hole 892A, shear strength values (Table 17 and Fig. 53) range from 25 kPa to values greater than the limit of the instrument (>221 kPa). In Subunit IA, 14 measurements were made. The strength generally increases with depth within Subunit IA. No general trend correlates with depth in Subunit IB. However, large variations in strength occur at three of the index property discontinuities (#3, #4, and #5; Fig. 53). At discontinuity #3, shear strength varies from 73 to 132 kPa (106–108 mbsf). At discontinuity #4 (144 mbsf), strength values range from 74 kPa to greater than 250 kPa; and at discontinuity #5 (164–166 mbsf), strength varies from 68 to 162 kPa. These large ranges suggest that these intervals are shear consolidated in localized zones that have undergone strain hardening.

The ratio of undrained shear strength to effective overburden stress ( $S_u/P_o'$ ) illustrates a general decrease with depth (Fig. 53), although the data are highly variable in Subunit IA.

### Thermal Conductivity

Thermal conductivity was measured on sediment samples using the needle-probe method in the full-space mode (see "Explanatory Notes" chapter, this volume). Measurements were usually taken at four points per core. Values range from 0.78 to 1.38 W/(m · K) (Table 18), with a mean of 1.04 W/(m · K) and a standard deviation of 0.10 W/(m · K). Thermal conductivity slightly increases with depth (Fig. 54), with large variations occurring at 99–104 mbsf (index property discontinuity #3; Fig. 48) and at 144 mbsf (index property discontinuity #4, Fig. 48).

## WSTP AND ADARA TEMPERATURE MEASUREMENTS

### Introduction

The primary purpose of the temperature measurements at Site 892 was to detect and analyze possible thermal effects associated with pore-fluid flow along a fault zone that was known from submersible studies (Linke et al., in press) to be associated with chemosynthetic bioherm development in the region of fault outcrop (see "Background and Objectives" section, this chapter). Similar to Sites 889 and 890, another specific objective of the temperature measurements at Site

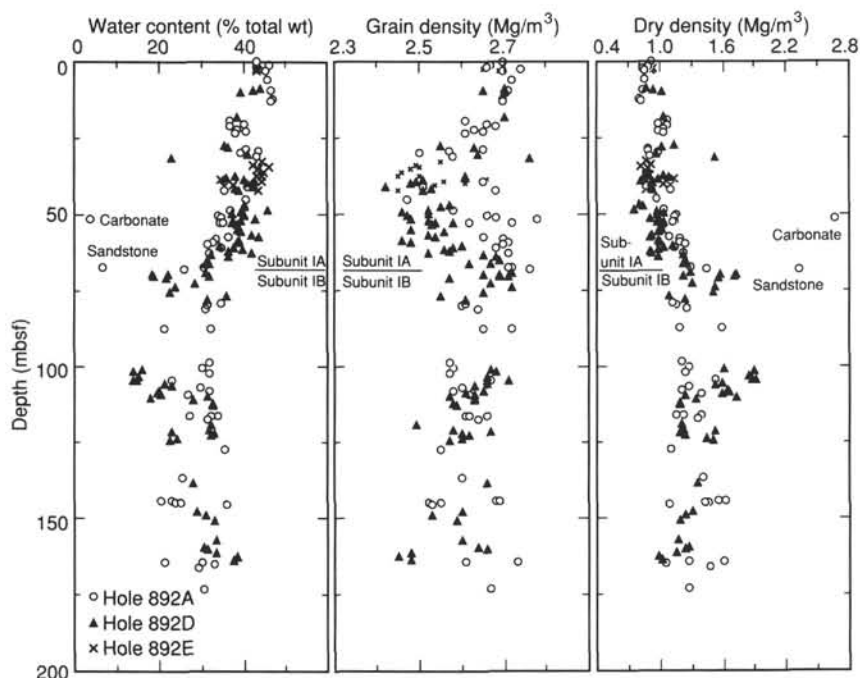


Figure 49. Water content, grain density, and dry density vs. depth for Site 892. Symbols as in Figure 48.

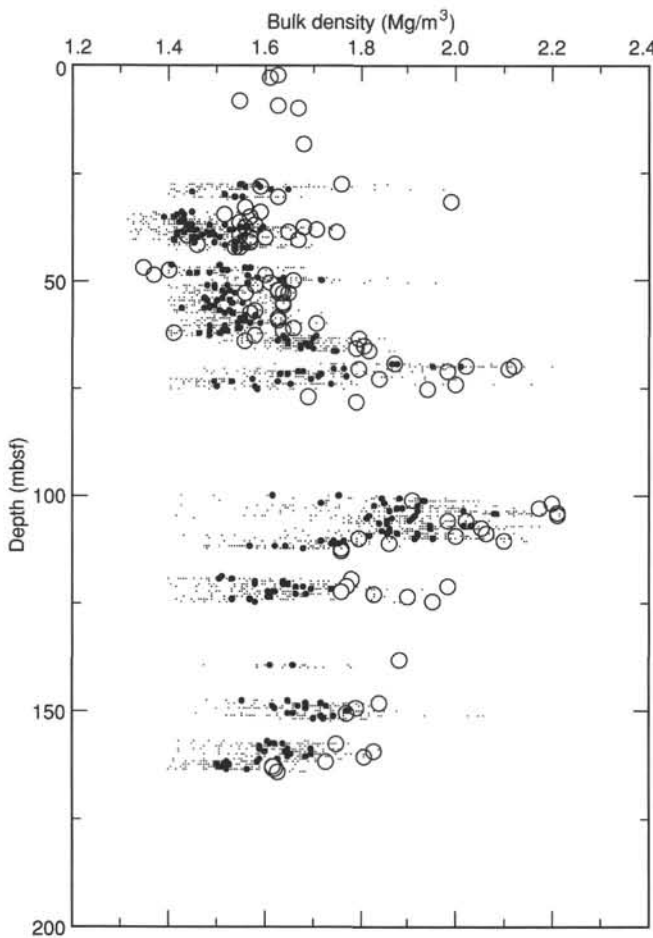


Figure 50. Bulk density vs. depth for Hole 892D. Dots = GRAPE measurements, filled circles = GRAPE values averaged over a 0.5-m depth interval, and open circles = discrete index properties measurements.

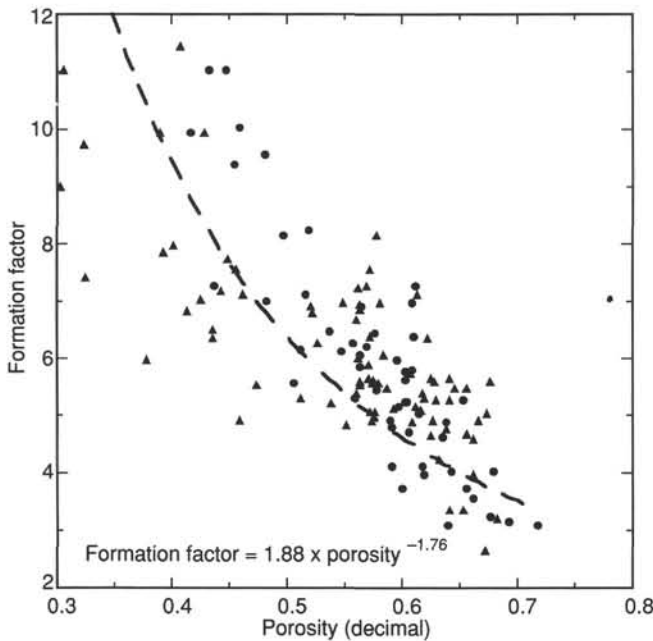


Figure 51. Formation factor vs. measured porosity for Site 892. The curve fit shown is of the form proposed by Archie (1942). Regression parameters are given in the text.

892 was to estimate the temperature at the seismic BSR. The BSR is currently interpreted to mark the base of a hydrate layer. Site 892 presented a further opportunity to calibrate the relationship of the BSR to the stability fields of natural hydrates (Sloan, 1990; Hyndman et al., 1992). An interesting feature at this site was the observation by Moore et al. (in press) of an apparent shallowing of the BSR across the fault-zone outcrop region (see “Background and Objectives” section, this chapter). This observation was used by Moore et al. (1991) to suggest that significantly higher temperature gradients, associated with active warm fluid flow, occur in the local region of the fault zone. Based on these data, the temperature gradient was estimated to lie in the region of 65°–70°C/km in the region of Site 892 (Moore et al., in press).

Because of the firm nature of the sediments, in-situ sediment temperatures were predominantly measured with the WSTP (see “Explanatory Notes” chapter, this volume). The WSTP was deployed at Holes 892A, 892D, and 892E, and a single successful ADARA measurement was obtained in Hole 892E. All the attempted measurements are summarized in Table 19.

### WSTP Temperature Measurements in Hole 892A

Of the 10 WSTP measurements attempted at Hole 892A, only the five measurements between 19 and 97 mbsf are of generally good quality. Problems with poor penetration and hole conditions resulted in dubious quality for the five measurements below 97 mbsf. Measurements taken at 106.5, 125.5, and 144.5 mbsf were rejected.

The tool was first deployed at 19 mbsf in Hole 892A in the version that includes the pore-water sampler (see “Explanatory Notes” chapter, this volume). The penetration record shows a slight excursion to lower temperatures in the profile at approximately 2700 s (Fig. 55), which was probably caused by cooling associated with an earlier than expected opening of the water-sampling valve (the valve should have opened 10 min after penetration). When the early part of the penetra-

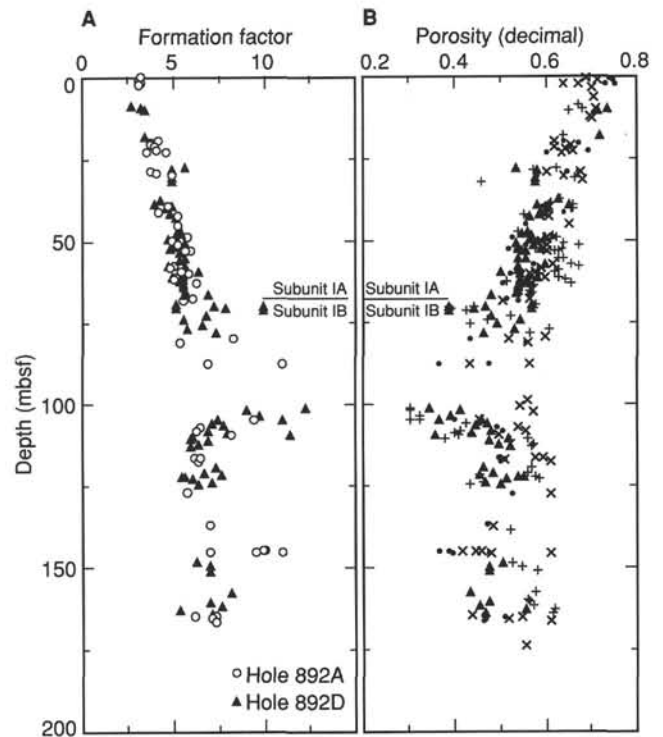


Figure 52. A. Formation factor vs. depth for Site 892 (open circles = Hole 892A, and triangles = Hole 892D). B. Measured porosity (x's = Hole 892A, and +s = Hole 892D) and porosity derived from formation factor vs. depth for Site 892 (dots = Hole 892A, and triangles = Hole 892D).

Table 15. Resistivity, formation factor, and derived porosity, Holes 892A and 892D.

| Core, section, interval (cm) | Depth (mbsf) | Voltage (mV) | Sample resistivity ( $\Omega$ V) | Formation factor | Derived porosity (%) | Core, section, interval (cm) | Depth (mbsf) | Voltage (mV) | Sample resistivity ( $\Omega$ V) | Formation factor | Derived porosity (%) |
|------------------------------|--------------|--------------|----------------------------------|------------------|----------------------|------------------------------|--------------|--------------|----------------------------------|------------------|----------------------|
| 146-892A-                    |              |              |                                  |                  |                      | 146-892D-(cont.)             |              |              |                                  |                  |                      |
| 1X-1, 40                     | 0.40         | 15.80        | 0.701                            | 3.173            | 80.79                | 6X-1, 81                     | 47.31        | 25.30        | 1.12                             | 5.21             | 56                   |
| 1X-1, 110                    | 1.10         | 15.50        | 0.688                            | 3.113            | 81.67                | 6X-1, 107                    | 47.57        | 26.20        | 1.16                             | 5.40             | 55                   |
| 1X-2, 55                     | 2.05         | 16.10        | 0.715                            | 3.234            | 79.92                | 6X-2, 60                     | 48.60        | 24.90        | 1.11                             | 5.11             | 57                   |
| 1X-2, 85                     | 2.35         | 15.40        | 0.684                            | 3.093            | 81.97                | 6X-2, 115                    | 49.15        | 22.70        | 1.01                             | 4.66             | 60                   |
| 3X-1, 55                     | 19.55        | 20.36        | 0.904                            | 4.122            | 69.63                | 6X-3, 32                     | 49.82        | 25.40        | 1.13                             | 5.16             | 56                   |
| 3X-1, 133                    | 20.33        | 18.60        | 0.826                            | 3.765            | 73.31                | 6X-3, 128                    | 50.78        | 27.80        | 1.23                             | 5.65             | 54                   |
| 3X-2, 15                     | 20.65        | 18.50        | 0.821                            | 3.745            | 73.53                | 6X-4, 50                     | 51.50        | 25.00        | 1.11                             | 5.03             | 57                   |
| 3X-2, 100                    | 21.50        | 19.70        | 0.875                            | 3.988            | 70.95                | 6X-4, 135                    | 52.35        | 23.70        | 1.05                             | 4.77             | 59                   |
| 3X-3, 33                     | 22.33        | 19.90        | 0.884                            | 4.028            | 70.55                | 6X-5, 20                     | 52.70        | 27.40        | 1.22                             | 5.57             | 54                   |
| 3X-3, 80                     | 22.80        | 17.70        | 0.786                            | 3.583            | 75.40                | 6X-5, 35                     | 52.85        | 26.60        | 1.18                             | 5.41             | 55                   |
| 3X-CC, 5                     | 23.20        | 22.80        | 1.012                            | 4.615            | 65.30                | 6X-5, 75                     | 53.25        | 25.90        | 1.15                             | 5.26             | 56                   |
| 4X-1, 45                     | 28.95        | 18.57        | 0.824                            | 3.759            | 73.37                | 7X-1, 120                    | 55.20        | 27.50        | 1.22                             | 5.60             | 54                   |
| 4X-1, 70                     | 29.20        | 19.90        | 0.884                            | 4.028            | 70.55                | 7X-2, 20                     | 55.70        | 25.70        | 1.14                             | 5.27             | 56                   |
| 4X-2, 35                     | 30.35        | 24.20        | 1.074                            | 4.899            | 63.12                | 7X-3, 30                     | 57.30        | 22.40        | 0.99                             | 4.68             | 60                   |
| 6X-1, 56                     | 39.56        | 22.70        | 1.008                            | 4.722            | 64.45                | 7X-3, 80                     | 57.80        | 26.80        | 1.19                             | 5.60             | 54                   |
| 6X-2, 70                     | 41.20        | 19.90        | 0.884                            | 4.115            | 69.69                | 7X-4, 30                     | 58.80        | 27.40        | 1.22                             | 5.61             | 54                   |
| 6X-3, 45                     | 42.45        | 25.60        | 1.137                            | 5.233            | 60.80                | 7X-4, 110                    | 59.60        | 31.10        | 1.38                             | 6.37             | 50                   |
| 6X-5, 15                     | 45.15        | 25.90        | 1.150                            | 5.264            | 60.59                | 7X-5, 30                     | 60.30        | 26.30        | 1.17                             | 5.48             | 54                   |
| 7X-1, 60                     | 49.10        | 28.10        | 1.248                            | 5.778            | 57.47                | 7X-5, 110                    | 61.10        | 23.60        | 1.05                             | 4.92             | 58                   |
| 7X-2, 32                     | 50.32        | 24.50        | 1.088                            | 4.911            | 63.03                | 7X-6, 25                     | 61.75        | 26.20        | 1.16                             | 5.47             | 55                   |
| 7X-2, 125                    | 51.25        | 26.20        | 1.163                            | 5.252            | 60.67                | 8X-1, 48                     | 62.18        | 25.60        | 1.14                             | 5.30             | 55                   |
| 7X-3, 120                    | 52.70        | 29.80        | 1.323                            | 5.973            | 56.40                | 8X-1, 115                    | 62.85        | 26.50        | 1.18                             | 5.49             | 54                   |
| 7X-4, 18                     | 53.18        | 28.10        | 1.248                            | 5.633            | 58.31                | 8X-2, 25                     | 63.45        | 27.30        | 1.21                             | 5.57             | 54                   |
| 7X-6, 140                    | 57.40        | 25.10        | 1.114                            | 5.031            | 62.17                | 8X-2, 87                     | 64.07        | 27.20        | 1.21                             | 5.55             | 54                   |
| 8X-1, 21                     | 58.21        | 23.60        | 1.048                            | 4.796            | 63.89                | 8X-3, 50                     | 65.20        | 27.00        | 1.20                             | 5.61             | 54                   |
| 8X-1, 132                    | 59.32        | 26.50        | 1.177                            | 5.459            | 59.35                | 8X-3, 148                    | 66.18        | 27.30        | 1.21                             | 5.65             | 54                   |
| 8X-2, 40                     | 59.90        | 28.70        | 1.274                            | 5.867            | 56.97                | 8X-4, 10                     | 66.30        | 33.80        | 1.50                             | 6.86             | 48                   |
| 8X-3, 20                     | 61.20        | 25.20        | 1.119                            | 5.161            | 61.28                | 9X-1, 16                     | 69.46        | 25.00        | 1.11                             | 5.06             | 57                   |
| 8X-3, 55                     | 61.55        | 24.70        | 1.097                            | 5.059            | 61.98                | 9X-1, 60                     | 69.90        | 49.20        | 2.18                             | 9.96             | 39                   |
| 8X-4, 40                     | 62.90        | 30.40        | 1.350                            | 6.226            | 55.08                | 9X-1, 90                     | 70.20        | 35.56        | 1.58                             | 7.20             | 47                   |
| 9X-1, 40                     | 67.90        | 29.40        | 1.305                            | 6.080            | 55.83                | 9X-1, 125                    | 70.55        | 38.90        | 1.73                             | 7.88             | 44                   |
| 9X-1, 55                     | 68.05        | 26.90        | 1.194                            | 5.563            | 58.72                | 9X-1, 132                    | 70.62        | 25.04        | 1.11                             | 5.07             | 57                   |
| 11X-2, 52                    | 80.02        | 39.80        | 1.767                            | 8.231            | 47.00                | 9X-2, 15                     | 70.95        | 48.89        | 2.17                             | 9.94             | 39                   |
| 11X-3, 15                    | 81.15        | 25.80        | 1.145                            | 5.295            | 60.39                | 9X-3, 85                     | 73.15        | 33.50        | 1.49                             | 6.81             | 48                   |
| 12X-1, 14                    | 87.64        | 53.70        | 2.384                            | 11.02            | 39.82                | 9X-4, 25                     | 74.05        | 27.20        | 1.21                             | 5.53             | 54                   |
| 12X-1, 28                    | 87.78        | 33.70        | 1.496                            | 6.916            | 51.89                | 9X-5, 25                     | 75.55        | 32.10        | 1.43                             | 6.52             | 49                   |
| 13X-6, 25                    | 104.75       | 48.00        | 2.131                            | 9.375            | 43.65                | 9X-6, 15                     | 76.95        | 28.30        | 1.26                             | 5.75             | 53                   |
| 13X-7, 75                    | 106.75       | 33.20        | 1.474                            | 6.485            | 53.82                | 9X-7, 5                      | 78.35        | 35.70        | 1.59                             | 7.26             | 46                   |
| 13X-8, 50                    | 108.00       | 32.10        | 1.425                            | 6.270            | 54.86                | 10X-1, 96                    | 100.96       | 61.00        | 2.71                             | 12.23            | 35                   |
| 13X-CC, 40                   | 109.40       | 41.80        | 1.856                            | 8.164            | 47.22                | 10X-2, 20                    | 101.70       | 45.00        | 2.00                             | 9.00             | 41                   |
| 15X-1, 55                    | 116.55       | 32.70        | 1.452                            | 6.439            | 54.04                | 10X-3, 15                    | 103.15       | 48.57        | 2.16                             | 9.74             | 39                   |
| 15X-1, 65                    | 116.65       | 31.20        | 1.385                            | 6.143            | 55.50                | 10X-3, 130                   | 104.30       | 55.00        | 2.44                             | 11.03            | 37                   |
| 15X-CC, 20                   | 117.70       | 32.40        | 1.438                            | 6.379            | 54.33                | 10X-4, 35                    | 104.85       | 37.40        | 1.66                             | 7.42             | 46                   |
| 16X-2, 24                    | 127.24       | 30.20        | 1.341                            | 5.792            | 57.39                | 10X-4, 120                   | 105.70       | 35.50        | 1.58                             | 7.05             | 47                   |
| 17X-2, 55                    | 137.05       | 34.80        | 1.545                            | 7.017            | 51.46                | 10X-5, 10                    | 106.10       | 39.00        | 1.73                             | 7.74             | 45                   |
| 18X-1, 20                    | 144.70       | 49.00        | 2.175                            | 10.036           | 41.99                | 10X-6, 35                    | 107.85       | 34.50        | 1.53                             | 6.85             | 48                   |
| 18X-1, 25                    | 144.75       | 48.50        | 2.153                            | 9.934            | 42.24                | 10X-6, 120                   | 108.70       | 40.20        | 1.79                             | 7.98             | 44                   |
| 18X-1, 46                    | 144.96       | 53.80        | 2.389                            | 11.019           | 39.82                | 10X-7, 20                    | 109.20       | 57.60        | 2.56                             | 11.43            | 36                   |
| 18X-1, 85                    | 145.35       | 46.70        | 2.073                            | 9.565            | 43.16                | 11X-1, 65                    | 110.15       | 29.80        | 1.32                             | 6.01             | 52                   |
| 18X-1, 96                    | 145.46       | 34.00        | 1.510                            | 6.964            | 51.69                | 10X-8, 15                    | 110.65       | 30.10        | 1.34                             | 5.97             | 52                   |
| 20X-1, 95                    | 164.45       | 35.80        | 1.589                            | 7.276            | 50.41                | 11X-2, 25                    | 111.25       | 34.30        | 1.52                             | 6.92             | 48                   |
| 20X-1, 120                   | 164.70       | 30.10        | 1.336                            | 6.117            | 55.64                | 11X-2, 135                   | 112.35       | 31.70        | 1.41                             | 6.39             | 50                   |
| 20X-2, 40                    | 165.40       | 35.00        | 1.554                            | 7.113            | 51.07                | 11X-3, 18                    | 112.68       | 29.22        | 1.30                             | 5.89             | 52                   |
| 20X-2, 125                   | 166.25       | 35.80        | 1.589                            | 7.276            | 50.41                | 12X-1, 41                    | 119.41       | 34.98        | 1.55                             | 7.28             | 46                   |
| 146-892D-                    |              |              |                                  |                  |                      | 12X-2, 45                    | 120.95       | 32.00        | 1.42                             | 6.69             | 49                   |
| 2X-1, 10                     | 8.60         | 13.30        | 0.59                             | 2.660            | 82                   | 12X-2, 85                    | 121.35       | 36.20        | 1.61                             | 7.57             | 45                   |
| 2X-1, 115                    | 9.65         | 16.10        | 0.72                             | 3.220            | 74                   | 12X-3, 15                    | 122.15       | 25.80        | 1.15                             | 5.39             | 55                   |
| 2X-2, 15                     | 10.15        | 16.80        | 0.75                             | 3.370            | 72                   | 12X-3, 20                    | 122.20       | 26.90        | 1.19                             | 5.62             | 54                   |
| 3X-1, 10                     | 18.10        | 16.80        | 0.75                             | 3.370            | 72                   | 12X-3, 80                    | 122.80       | 29.20        | 1.30                             | 6.06             | 51                   |
| 4X-1, 40                     | 27.90        | 27.30        | 1.21                             | 5.670            | 53                   | 12X-4, 20                    | 123.70       | 34.40        | 1.53                             | 7.13             | 47                   |
| 4X-1, 80                     | 28.30        | 23.80        | 1.06                             | 4.910            | 58                   | 12X-4, 100                   | 124.50       | 30.60        | 1.36                             | 6.35             | 50                   |
| 4X-3, 35                     | 30.85        | 23.80        | 1.06                             | 4.920            | 58                   | 15X-1, 70                    | 148.20       | 30.00        | 1.33                             | 6.29             | 50                   |
| 4X-3, 140                    | 31.90        | 23.80        | 1.06                             | 4.920            | 58                   | 15X-2, 40                    | 149.40       | 33.40        | 1.48                             | 6.97             | 47                   |
| 5X-1, 50                     | 37.50        | 20.50        | 0.91                             | 4.250            | 63                   | 15X-3, 20                    | 150.70       | 33.50        | 1.49                             | 6.98             | 47                   |
| 5X-2, 32                     | 38.82        | 19.00        | 0.84                             | 3.990            | 65                   | 16X-1, 48                    | 157.48       | 39.50        | 1.75                             | 8.15             | 43                   |
| 5X-2, 82                     | 39.32        | 23.35        | 1.04                             | 4.900            | 58                   | 16X-3, 20                    | 160.20       | 33.40        | 1.48                             | 6.96             | 48                   |
| 5X-3, 10                     | 40.10        | 23.20        | 1.03                             | 4.610            | 60                   | 16X-4, 4                     | 161.54       | 36.90        | 1.64                             | 7.57             | 45                   |
| 5X-4, 43                     | 41.93        | 23.05        | 1.02                             | 4.830            | 58                   | 16X-4, 120                   | 162.70       | 25.80        | 1.15                             | 5.30             | 56                   |
| 5X-4, 113                    | 42.63        | 24.50        | 1.09                             | 5.14             | 57                   | 16X-5, 90                    | 163.90       | 34.50        | 1.53                             | 7.14             | 47                   |

tion record is fitted (2430–2690 s), an estimated decay temperature of  $7.0^\circ \pm 0.1^\circ\text{C}$  is obtained (Fig. 55).

Three good-quality temperature measurements of  $8.03^\circ \pm 0.05^\circ\text{C}$ ,  $11.1^\circ \pm 0.05^\circ\text{C}$ , and  $13.0^\circ \pm 0.1^\circ\text{C}$  were subsequently obtained at 39, 67.5, and 87.5 mbsf, respectively (Figs. 56–58). The measurement at 67.5 mbsf was taken with the WSTP in the temperature-only configuration. The measurements at 39 and 87.5 mbsf were obtained with the WSTP in the water-sampler and temperature configuration. The WSTP

deployment at 87.5 mbsf contained an anomaly in the penetration record at 2600 s (approximately 10 min) after penetration. The anomaly was similar to the one that occurred during the deployment at 19 mbsf and is also consistent with a disturbance relating to the opening of the water valve. At 19 mbsf, the fluids show relatively little seawater contamination and, at 87.5 mbsf, only slight contamination (see “Inorganic Geochemistry” section, this chapter). We suggest that cooler formation fluid and/or some borehole fluid may have been drawn into

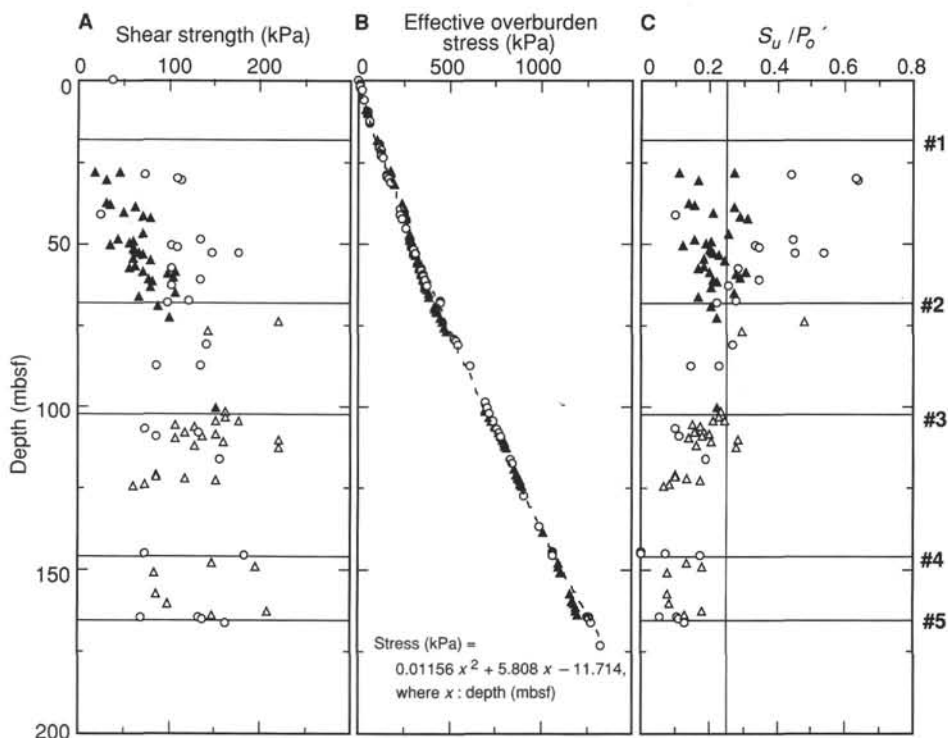


Figure 53. A. Undrained shear strength vs. depth for Site 892 (open circles = pocket penetrometer measurements, Hole 892A; open triangles = pocket penetrometer measurements, Hole 892D; and solid triangles = vane-shear measurements, Hole 892D). B. Effective overburden stress vs. depth. C.  $S_u/P_o'$  vs. depth. Two measurements at 144.7 and 145.35 mbsf in Hole 892A are not included in this figure because the strengths were greater than the maximum limit of the measurement instrument (>221 kPa). The five interpreted index properties discontinuities are shown as horizontal lines.

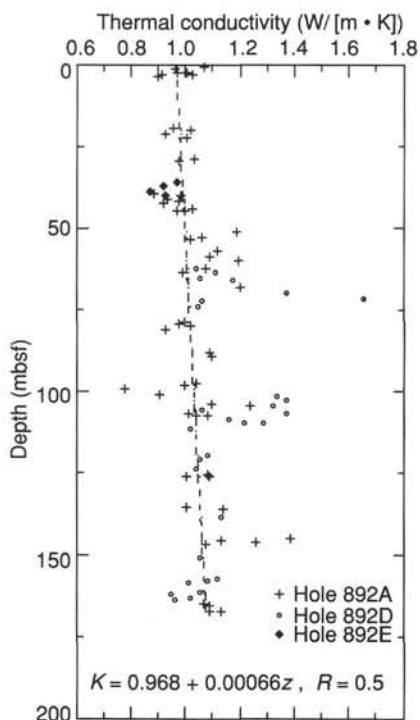


Figure 54. Thermal conductivity vs. depth for Site 892.

the thermally disturbed and warmed region near the probe when the valve opened. Only the early part of the record at 87.5 mbsf was included in the theoretical fit to the data.

The WSTP was deployed at 97 mbsf in the version that includes the pore-water sampler (Fig. 59). The penetration record shows a normal decay curve that indicates an equilibrium temperature of  $11.0^\circ \pm 0.05^\circ\text{C}$ . Some fill was, however, reported in the hole at the time of deployment, and the water sample obtained during this deployment is contaminated with borehole water (see “Inorganic Geochemistry” section, this chapter). The penetration record also shows a relatively small temperature spike on penetration and a small amount of drift toward the end of the record (an increase of  $<0.05^\circ\text{C}$ ). Thus, although the general form of this penetration record is relatively good, the possibility exists that the probe was partially emplaced in the formation through the cool borehole fill. This record is, consequently, considered to be of only moderate reliability.

The five penetration records below 97 mbsf (using the WSTP in its temperature-only configuration) are generally of poor quality. Frequent disturbances of the tool are probably related to poor pene-

Table 16. Acoustic compressional-wave velocity measurements, Hole 892A.

| Core, section, interval (cm) | Depth (mbsf) | Lithology  | Velocity (m/s) |
|------------------------------|--------------|------------|----------------|
| 146-892A-1X-1, 40            | 0.40         | Silty clay | 1507           |
| 9X-1, 20                     | 67.70        | Sandstone  | 3460           |
| 18X-1, 25                    | 144.75       | Silty clay | 1468           |

Table 17. Undrained shear strength measurements, Holes 892A and 892D.

| Core, section, interval (cm) | Depth (mbsf) | Undrained shear strength |            | Test type           | Core, section, interval (cm) | Depth (mbsf) | Undrained shear strength |            | Test type           |
|------------------------------|--------------|--------------------------|------------|---------------------|------------------------------|--------------|--------------------------|------------|---------------------|
|                              |              | (kPa)                    | $S_u/P_o'$ |                     |                              |              | (kPa)                    | $S_u/P_o'$ |                     |
| 146-892A-                    |              |                          |            |                     | 146-892D-(cont.)             |              |                          |            |                     |
| 1X-1, 40                     | 0.40         | 36.77                    | 15.85      | Pocket penetrometer | 6X-4, 134                    | 52.34        | 63.09                    | 0.20       | Shear vane          |
| 4X-2, 60                     | 30.60        | 112.78                   | 0.64       | Pocket penetrometer | 6X-5, 35                     | 52.85        | 66.48                    | 0.21       | Shear vane          |
| 4X-1, 40                     | 28.90        | 73.55                    | 0.44       | Pocket penetrometer | 6X-5, 73                     | 53.23        | 71.86                    | 0.23       | Shear vane          |
| 4X-2, 20                     | 30.20        | 110.32                   | 0.63       | Pocket penetrometer | 7X-1, 90                     | 54.90        | 60.26                    | 0.21       | Shear vane          |
| 6X-2, 70                     | 41.20        | 24.52                    | 0.10       | Pocket penetrometer | 7X-1, 120                    | 55.20        | 80.62                    | 0.29       | Shear vane          |
| 7X-1, 60                     | 49.10        | 134.84                   | 0.45       | Pocket penetrometer | 7X-3, 28                     | 57.28        | 62.75                    | 0.21       | Shear vane          |
| 7X-2, 32                     | 50.32        | 102.97                   | 0.33       | Pocket penetrometer | 7X-3, 80                     | 57.80        | 57.09                    | 0.19       | Shear vane          |
| 7X-2, 125                    | 51.25        | 110.32                   | 0.35       | Pocket penetrometer | 7X-4, 25                     | 58.75        | 70.74                    | 0.23       | Shear vane          |
| 7X-3, 120                    | 52.70        | 147.10                   | 0.45       | Pocket penetrometer | 7X-4, 110                    | 59.60        | 99.27                    | 0.32       | Shear vane          |
| 7X-4, 18                     | 53.18        | 176.52                   | 0.54       | Pocket penetrometer | 7X-5, 30                     | 60.30        | 104.93                   | 0.33       | Shear vane          |
| 7X-6, 140                    | 57.40        | 102.97                   | 0.29       | Pocket penetrometer | 7X-5, 110                    | 61.10        | 77.15                    | 0.24       | Shear vane          |
| 8X-3, 22                     | 61.22        | 134.84                   | 0.35       | Pocket penetrometer | 7X-6, 25                     | 61.75        | 82.30                    | 0.26       | Shear vane          |
| 8X-4, 40                     | 62.90        | 102.97                   | 0.26       | Pocket penetrometer | 8X-2, 25                     | 63.45        | 78.70                    | 0.21       | Shear vane          |
| 9X-1, 40                     | 67.90        | 122.58                   | 0.28       | Pocket penetrometer | 8X-3, 50                     | 65.20        | 106.90                   | 0.27       | Shear vane          |
| 9X-1, 55                     | 68.05        | 98.07                    | 0.22       | Pocket penetrometer | 8X-3, 148                    | 66.18        | 67.38                    | 0.17       | Shear vane          |
| 11X-3, 15                    | 81.15        | 142.20                   | 0.27       | Pocket penetrometer | 7X-4, 10                     | 58.60        | 106.90                   | 0.35       | Shear vane          |
| 12X-1, 14                    | 87.64        | 85.81                    | 0.15       | Pocket penetrometer | 9X-1, 25                     | 69.55        | 87.44                    | 0.21       | Shear vane          |
| 12X-1, 28                    | 87.78        | 134.84                   | 0.23       | Pocket penetrometer | 9X-3, 85                     | 73.15        | 100.81                   | 0.22       | Shear vane          |
| 13X-7, 75                    | 106.75       | 73.55                    | 0.10       | Pocket penetrometer | 9X-6, 25                     | 77.05        | 142.20                   | 0.30       | Pocket penetrometer |
| 13X-8, 50                    | 108.00       | 132.39                   | 0.18       | Pocket penetrometer | 9X-4, 15                     | 73.95        | 220.65                   | 0.48       | Pocket penetrometer |
| 13X-CC, 40                   | 109.40       | 85.81                    | 0.11       | Pocket penetrometer | 10X-1, 45                    | 100.45       | 151.70                   | 0.22       | Shear vane          |
| 15X-1, 64                    | 116.64       | 156.91                   | 0.19       | Pocket penetrometer | 10X-2, 20                    | 101.70       | 161.81                   | 0.23       | Pocket penetrometer |
| 18X-1, 20                    | 144.70       | >221.00                  | 0.21       | Pocket penetrometer | 10X-3, 15                    | 103.15       | 161.81                   | 0.23       | Pocket penetrometer |
| 18X-1, 46                    | 144.96       | 73.55                    | 0.07       | Pocket penetrometer | 10X-3, 130                   | 104.30       | 176.52                   | 0.25       | Pocket penetrometer |
| 18X-1, 85                    | 145.35       | >221.00                  | 0.21       | Pocket penetrometer | 10X-4, 35                    | 104.85       | 152.00                   | 0.21       | Pocket penetrometer |
| 18X-1, 96                    | 145.46       | 183.87                   | 0.17       | Pocket penetrometer | 10X-4, 120                   | 105.70       | 107.87                   | 0.15       | Pocket penetrometer |
| 20X-1, 95                    | 164.45       | 68.65                    | 0.05       | Pocket penetrometer | 10X-5, 10                    | 106.10       | 127.49                   | 0.17       | Pocket penetrometer |
| 20X-1, 120                   | 164.70       | 132.39                   | 0.11       | Pocket penetrometer | 10X-6, 35                    | 107.85       | 117.68                   | 0.16       | Pocket penetrometer |
| 20X-2, 40                    | 165.40       | 137.29                   | 0.11       | Pocket penetrometer | 10X-6, 120                   | 108.70       | 152.00                   | 0.20       | Pocket penetrometer |
| 20X-2, 125                   | 166.25       | 161.81                   | 0.13       | Pocket penetrometer | 10X-7, 20                    | 109.20       | 137.29                   | 0.18       | Pocket penetrometer |
| 146-892D                     |              |                          |            |                     | 10X-8, 15                    | 110.65       | 220.65                   | 0.28       | Pocket penetrometer |
| 4X-1, 50                     | 28.00        | 46.06                    | 0.27       | Shear vane          | 11X-1, 65                    | 110.15       | 107.87                   | 0.14       | Pocket penetrometer |
| 4X-1, 80                     | 28.30        | 18.88                    | 0.11       | Shear vane          | 11X-2, 25                    | 111.25       | 159.36                   | 0.20       | Pocket penetrometer |
| 4X-3, 35                     | 30.85        | 30.76                    | 0.17       | Shear vane          | 11X-2, 135                   | 112.35       | 127.49                   | 0.16       | Pocket penetrometer |
| 5X-1, 50                     | 37.50        | 30.76                    | 0.14       | Shear vane          | 11X-3, 18                    | 112.68       | 220.65                   | 0.28       | Pocket penetrometer |
| 5X-1, 118                    | 38.18        | 35.76                    | 0.16       | Shear vane          | 12X-2, 45                    | 120.95       | 85.81                    | 0.11       | Pocket penetrometer |
| 5X-2, 32                     | 38.82        | 63.52                    | 0.27       | Shear vane          | 12X-2, 85                    | 121.35       | 85.81                    | 0.11       | Pocket penetrometer |
| 5X-3, 70                     | 40.70        | 51.20                    | 0.21       | Shear vane          | 12X-3, 20                    | 122.20       | 117.68                   | 0.15       | Pocket penetrometer |
| 5X-4, 42                     | 41.92        | 71.86                    | 0.29       | Shear vane          | 12X-3, 80                    | 122.80       | 152.00                   | 0.19       | Pocket penetrometer |
| 5X-4, 112                    | 42.62        | 78.93                    | 0.31       | Shear vane          | 12X-4, 20                    | 123.70       | 73.55                    | 0.09       | Pocket penetrometer |
| 6X-1, 81                     | 47.31        | 71.57                    | 0.26       | Shear vane          | 12X-4, 100                   | 124.50       | 61.29                    | 0.07       | Pocket penetrometer |
| 6X-2, 60                     | 48.60        | 44.41                    | 0.15       | Shear vane          | 15X-1, 70                    | 148.20       | 147.10                   | 0.13       | Pocket penetrometer |
| 6X-2, 131                    | 49.31        | 59.97                    | 0.21       | Shear vane          | 15X-2, 40                    | 149.40       | 196.13                   | 0.18       | Pocket penetrometer |
| 6X-3, 32                     | 49.82        | 55.45                    | 0.19       | Shear vane          | 15X-3, 20                    | 150.70       | 83.36                    | 0.07       | Pocket penetrometer |
| 6X-3, 128                    | 50.78        | 36.21                    | 0.12       | Shear vane          | 16X-1, 48                    | 157.48       | 85.81                    | 0.07       | Pocket penetrometer |
| 6X-4, 50                     | 51.50        | 61.67                    | 0.20       | Shear vane          | 16X-3, 20                    | 160.20       | 98.07                    | 0.08       | Pocket penetrometer |
|                              |              |                          |            |                     | 16X-5, 90                    | 163.90       | 147.10                   | 0.12       | Pocket penetrometer |
|                              |              |                          |            |                     | 16X-4, 120                   | 162.70       | 208.39                   | 0.18       | Pocket penetrometer |
|                              |              |                          |            |                     | 16X-4, 20                    | 161.70       | >221.00                  | 0.19       | Pocket penetrometer |

tration of the formation because of the presence of fill in the borehole (with the exception of the deployment at 135 mbsf). The measurements at 106.5, 125.5, and 135 mbsf show considerable disturbances of the tool and were rejected (Fig. 60). The temperature record at 116 mbsf also indicates major disturbances of the tool in the early part of the record. The final part of the record appears, however, to show a reasonable decay profile and small temperature spike on tool extraction (Fig. 61). Analysis of this decay profile indicates an equilibrium temperature of  $12.3^\circ \pm 0.1^\circ\text{C}$ . The formation temperature derived from this record is considered to be only of moderate to dubious quality and reliability because of the disturbances of the tool and the presence of 1–2 m of fill in the hole at the time of tool deployment.

The final WSTP tool deployment at 144.5 mbsf was into 2 or more m of fill, and thus is strongly suspect. A moderate amount of tool disturbance occurred during this measurement (Fig. 62), but a fit to a reasonable decay profile in the central part of the record (between approximately 1830 and 2220 s) gives an equilibrium temperature of  $7.8^\circ \pm 0.05^\circ\text{C}$ . Although the fitted regions of the record appear to present a reasonable decay profile, the presence of large quantities of fill mean that this record is of highly dubious quality; thus, this record was also rejected.

### WSTP Temperature Measurements in Hole 892D

Five WSTP measurements were attempted in Hole 892D at 54, 77, 109.5, 128.5, and 147.5 mbsf (using the temperature-only configuration). Because of poor penetration and subsequent drift in the temperature record, the measurements at 54 and 128.5 mbsf were rejected (Fig. 63). The measurements at 77 and 109.5 mbsf have good-quality, normal temperature decay profiles, for which analysis gives equilibrium temperatures of  $9.8^\circ \pm 0.1^\circ\text{C}$  and  $11.5^\circ \pm 0.2^\circ\text{C}$ , respectively (Figs. 64–65). The WSTP deployment at 147.5 also has a good-quality, normal penetration record, for which analysis gives an equilibrium temperature of  $13.7^\circ \pm 0.1^\circ\text{C}$  (Fig. 66).

### WSTP Temperature Measurements in Hole 892E

Three WSTP measurements were attempted in Hole 892E at 30 (water sampler and temperature configuration), 52, and 62 mbsf (latter two in temperature-only configuration). The penetration record at 30 mbsf shows a normal decay curve that indicates an equilibrium temperature of  $7.5^\circ \pm 0.1^\circ\text{C}$  (Fig. 67). The deployment at 52 mbsf had a noisy temperature record and, although the general form of the

Table 18. Thermal conductivity data, Site 892.

| Depth (mbsf) | Thermal conductivity (W/(m · K)) | Depth (mbsf) | Thermal conductivity (W/(m · K)) |
|--------------|----------------------------------|--------------|----------------------------------|
| 146-892A:    |                                  |              |                                  |
| 0.57         | 1.07                             | 126.13       | 1.01                             |
| 0.90         | 0.96                             | 135.48       | 1.00                             |
| 2.11         | 0.97                             | 136.17       | 1.14                             |
| 2.51         | 1.01                             | 144.80       | 1.39                             |
| 2.81         | 0.91                             | 145.30       | 1.13                             |
| 3.17         | 1.02                             | 146.20       | 1.26                             |
| 3.37         | 0.90                             | 146.67       | 1.08                             |
| 19.20        | 0.96                             | 164.69       | 1.07                             |
| 19.90        | 1.02                             | 165.50       | 1.09                             |
| 20.89        | 0.93                             | 166.80       | 1.13                             |
| 22.51        | 1.01                             | 167.24       | 1.09                             |
| 28.84        | 1.03                             | 146-892B:    |                                  |
| 29.20        | 0.98                             | 62.20        | 1.10                             |
| 39.15        | 0.89                             | 63.50        | 1.22                             |
| 39.70        | 0.98                             | 65.00        | 1.13                             |
| 41.00        | 0.94                             | 65.50        | 1.31                             |
| 41.40        | 0.98                             | 69.80        | 1.63                             |
| 42.20        | 0.92                             | 71.30        | 2.08                             |
| 43.70        | 1.03                             | 72.11        | 1.14                             |
| 44.30        | 0.97                             | 74.02        | 1.11                             |
| 44.70        | 1.00                             | 101.15       | 1.58                             |
| 51.00        | 1.19                             | 102.65       | 1.63                             |
| 52.50        | 1.06                             | 104.15       | 1.54                             |
| 53.52        | 1.02                             | 105.65       | 1.14                             |
| 56.82        | 1.12                             | 106.73       | 1.63                             |
| 58.70        | 1.09                             | 108.23       | 1.29                             |
| 59.85        | 1.20                             | 109.73       | 1.38                             |
| 62.20        | 1.07                             | 109.80       | 1.49                             |
| 63.20        | 0.99                             | 111.65       | 1.06                             |
| 67.92        | 1.20                             | 119.30       | 1.16                             |
| 78.50        | 1.00                             | 120.90       | 1.13                             |
| 78.90        | 0.98                             | 123.80       | 1.10                             |
| 79.94        | 1.02                             | 138.20       | 1.24                             |
| 80.80        | 0.93                             | 150.80       | 1.13                             |
| 87.90        | 1.09                             | 157.20       | 1.23                             |
| 89.22        | 1.10                             | 157.40       | 1.17                             |
| 97.44        | 1.04                             | 158.28       | 1.05                             |
| 97.74        | 1.00                             | 161.43       | 1.13                             |
| 99.28        | 0.78                             | 161.83       | 0.96                             |
| 100.79       | 0.90                             | 162.93       | 1.07                             |
| 103.65       | 1.10                             | 163.33       | 0.98                             |
| 104.40       | 1.24                             | 146-892E:    |                                  |
| 106.85       | 1.01                             | 35.77        | 0.99                             |
| 107.00       | 1.08                             | 37.06        | 0.91                             |
| 107.10       | 1.04                             | 38.62        | 0.82                             |
| 125.65       | 1.08                             | 40.06        | 0.92                             |
| 125.74       | 1.09                             |              |                                  |

decay curve looks reasonable, the decay profile could not be fitted (Fig. 68). Overall, the penetration record suggests a formation temperature of approximately  $8.8^\circ \pm 0.2^\circ\text{C}$ . This estimate is of moderate to doubtful quality.

The measurement at 62 mbsf is of generally good quality. Disturbance of the tool during the latter part of the penetration period, however, meant that only the early part of the record could be used to estimate the formation temperature. The decay curve indicates an equilibrium temperature of  $9.3^\circ \pm 0.1^\circ\text{C}$  (Fig. 69).

#### ADARA Temperature Measurements in Hole 892E

Two ADARA deployments were made in Hole 892E at 42.5 and  $49.0 \pm 3$  mbsf. The ADARA tool was not held in the sediment during the deployment at 42.5 mbsf, and no temperature determination could be made. The penetration record at 46 mbsf was of good quality, but the large temperature spike meant that the equilibrium temperature of  $6.25^\circ\text{C}$  could not be estimated with an accuracy greater than  $\pm 0.5^\circ\text{C}$  (Fig. 70). It was also not possible to determine accurately the depth to the tool deployment because the core barrel did not fully penetrate the formation, the core liner subsequently split, and part of the recovered core was lost. At least 4.3 m of core was recovered, so the minimum depth to deployment probably lies between 46.8 and 52.0 mbsf. As a result of these problems, the reliability of the depth and temperature estimates is relatively low.

#### Temperature Profile with Depth and Heat-Flow Estimates

The near-bottom seawater temperature was measured during each of the WSTP deployments while the probe was held for 10 min at about 20 m above seafloor inside the drill string. The measurements indicate a bottom seawater temperature of  $5.5^\circ \pm 0.1^\circ\text{C}$ . For consistency with the intercalibration procedure conducted for the ADARA and WSTP instruments at Site 888, a constant correction of  $-1.3^\circ\text{C}$  was applied to all the WSTP-measured temperatures at Holes 892A, 892D, and 892E. Similarly, a correction of  $0.3^\circ\text{C}$  was added to the ADARA measurement at Hole 892E. The corrected temperature data are summarized in Table 20, and the accepted and dubious data are plotted as a function of depth in Figure 71.

A first major observation is that the temperature at Site 892 tends to increase linearly with depth, which is consistent with a principally conductive mode of heat transfer. Using a linear regression through all the points, excluding the bottom-water temperature and the measurements at 62.0, 67.5, 87.5, 97.0, and 116.0 mbsf (Fig. 71), the mean geothermal gradient is  $51^\circ \pm 2^\circ\text{C}/\text{km}$ . Based on a thermal conductivity of  $1.04 \pm 0.1$  W/(m · K) (see Fig. 54), this gradient corresponds to a heat flow of  $53 \pm 3$  mW/m<sup>2</sup>. A second major observation is that one can see two excursions from this linear trend to warmer temperatures at 67.5 and 87.5 mbsf. The excess temperatures are  $1.6^\circ$  and  $2.5^\circ\text{C}$ , respectively. The close spacing of the temperature determinations enables us to constrain the total vertical thicknesses of the warmed regions around these two measurements to be less than 15–20 m (Fig. 71). The narrow distribution of these warm regions indicate a limited spatial diffusion, which implies recent emplacement. The temperature spikes could have been generated by transient fluid flow along two localized zones. These warm temperatures correspond to those predicted 30–40 m below on the linear temperature profile.

#### Temperature and Hydrates

The depth to the base of the hydrate layer can be predicted from the in-situ temperature distribution, using experimentally derived pressure-temperature stability curves for hydrates. Previously, the pure water–pure methane curve was proposed to best describe the correlation of depth to the BSR with the in-situ temperature (Fig. 81, “WSTP and ADARA Temperature Measurements” section, “Sites 889 and 890” chapter, this volume; Hyndman et al., 1992). In the region close to Site 892, the BSR becomes shallower across a fault zone that Site 892 was designed to intersect (see “Background and Objectives” section, this chapter). The shallowing of the BSR suggests that warm fluid migrating up the fault zone is locally increasing temperature, which results in moving the base of the hydrate stability field nearer to the surface. Holes 892A, 892D, and 892E are situated on the edge of the region in which the BSR shallows.

Using the constant thermal gradient of  $51^\circ\text{C}/\text{km}$ , it is predicted that the base of the pure water–methane hydrate stability field should lie at  $120 \pm 4$  mbsf (Fig. 72). Instead, the BSR depth at Site 892 is at approximately 73 mbsf, with free gas apparently present below this depth (see “Downhole Logging” section, this chapter). The predicted temperature corresponding to the base of the stability field at 73 mbsf is  $10.4^\circ\text{C}$ , which is  $1.9^\circ\text{C}$  higher than the temperature obtained from the linear gradient fitted to the measurements. This  $1.9^\circ\text{C}$  difference is similar to the discrepancy between the predicted and measured temperatures at the BSR at Site 889 (see “Sites 889 and 890” chapter, this volume). The situation is complicated by the upper of the two warmer temperature excursions at 68 mbsf found in Hole 892A, which should push the base of the hydrate stability field even higher, if the temperature on the best-fit line at 73 mbsf defined the limit of hydrate stability. The sonic log and VSP used to determine the depth of the BSR were run in Hole 892C, 100 m southeast of Hole 892A. The conduit carrying the warm water that gives the excursion at 68 mbsf in Hole 892A probably intersects Hole 892C at a different depth

**Table 19. Summary of WSTP and ADARA temperature measurements, Holes 892A, 892D, and 892E.**

| Summary of WSTP temperature measurements                          |              |                                 |                                 |                               |                             |          |
|-------------------------------------------------------------------|--------------|---------------------------------|---------------------------------|-------------------------------|-----------------------------|----------|
| Core no.                                                          | Depth (mbsf) | Temperature above mud line (°C) | Temperature in sediment (°C)    | Comments                      | Status                      |          |
| 146-892A-                                                         |              |                                 |                                 |                               |                             |          |
| 3X                                                                | 19.0*        | 5.60 ± 0.05                     | 7.00 ± 0.10                     | Good data.                    | Accepted                    |          |
| 6X                                                                | 39.0*        | 5.55 ± 0.05                     | 8.03 ± 0.05                     | Good data.                    | Accepted                    |          |
| 9X                                                                | 67.5         | 5.60 ± 0.10                     | 11.10 ± 0.05                    | Good data.                    | Accepted                    |          |
| 12X                                                               | 87.5*        | 5.40 ± 0.10                     | 13.00 ± 0.10                    | Good data.                    | Accepted                    |          |
| 13X                                                               | 97.0*        | 5.60 ± 0.10                     | 11.00 ± 0.05                    | Some fill reported.           | Dubious                     |          |
| 14X                                                               | 106.5        | 5.50 ± 0.10                     | ?                               | 1–2 m fill.                   | Rejected                    |          |
| 15X                                                               | 116.0        | 5.50 ± 0.10                     | 12.30 ± 0.10                    | 1–2 m fill, temperature only. | Dubious                     |          |
| 16X                                                               | 125.5        | 5.50 ± 0.10                     | ?                               | 1–2 m fill, temperature only. | Rejected                    |          |
| 17X                                                               | 13.5         | 5.60 ± 0.10                     | 13.60 ± 0.10                    | No fill, probe movements.     | Rejected                    |          |
| 18X                                                               | 144.5        | 5.50–6.70                       | 7.80 ± 0.05                     | 2-m fill.                     | Rejected                    |          |
| 146-892D-                                                         |              |                                 |                                 |                               |                             |          |
| 7X                                                                | 54.0         | 5.20 ± 0.10                     | ?                               | High drift.                   | Rejected                    |          |
| 9X                                                                | 77.0         | 5.30 ± 0.10                     | 9.80 ± 0.10                     | Good data.                    | Accepted                    |          |
| 11X                                                               | 109.5        | 5.50 ± 0.10                     | 11.50 ± 0.20                    | Good data.                    | Accepted                    |          |
| 13X                                                               | 128.5        | 5.50 ± 0.10                     | ?                               | 3-m fill.                     | Rejected                    |          |
| 15X                                                               | 147.5        | 5.50 ± 0.10                     | 13.70 ± 0.10                    | Good data.                    | Accepted                    |          |
| 146-892E-                                                         |              |                                 |                                 |                               |                             |          |
| 3H                                                                | 30.0*        | 5.50 ± 0.10                     | 7.50 ± 0.10                     | Good data.                    | Accepted                    |          |
| Following 4H                                                      | 52.0         | 5.70 ± 0.20                     | 8.80 ± 0.20                     | Noisy record.                 | Accepted                    |          |
| Following drilling                                                | 62.0         | 5.50 ± 0.10                     | 9.30 ± 0.10                     | Good data.                    | Accepted                    |          |
| Summary of APC tool temperature measurements (ADARA measurements) |              |                                 |                                 |                               |                             |          |
| Core                                                              | Depth (mbsf) | Probe no.                       | Temperature above mud line (°C) | Temperature in sediment (°C)  | Comments                    | Status   |
| 146-892E-                                                         |              |                                 |                                 |                               |                             |          |
| 3H                                                                | 42.50        | 12                              |                                 |                               | Probe not held in sediment. |          |
| 4H                                                                | 49.0 ± 3.0   | 10                              | 4.1 ± 0.2                       | 6.0 to 6.5                    | Good data.                  | Accepted |

Notes: Measurements with an asterisk (\*) were taken with Probe 105 (with water sampler); other WSTP measurements were taken with Probe 108 (without water sampler).

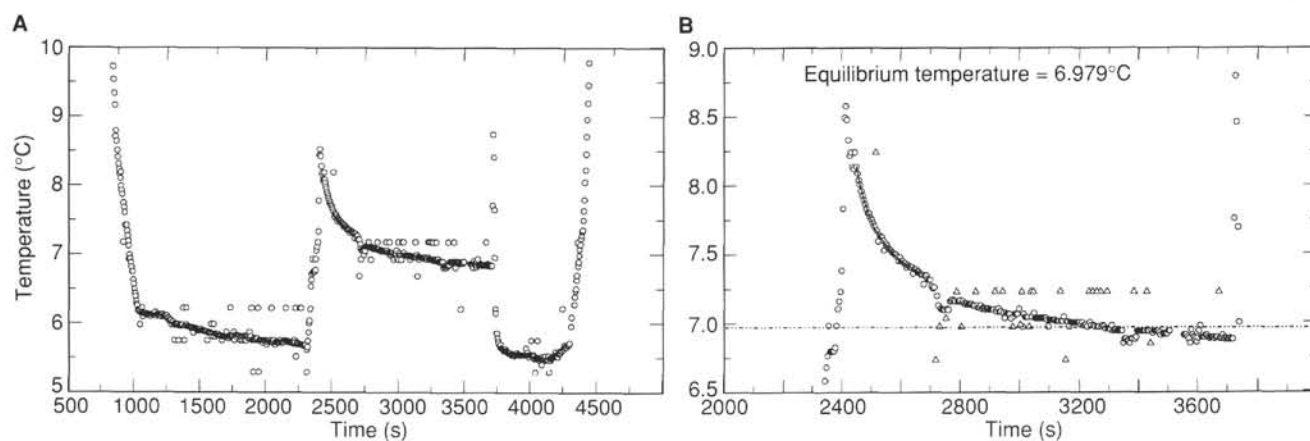


Figure 55. Temperature record in near-bottom seawater and sediment from WSTP deployment in Hole 892A at 19 mbsf (Core 146-892A-3X). **A.** Entire run. **B.** Close-up of record in sediment. The solid line is the regression curve used to estimate the equilibrium temperature (shown by the dashed line). Triangles are points not used for regression calculation.

if it cuts it at all. These small features will have little effect on the overall depth of the BSR as imaged in the seismic reflection section. The general presence of free gas, indicated by the sonic log below 72 mbsf in Hole 892C, and the thermal data show that the experimentally derived curve for pure water–methane hydrates does not apply to the natural gas-hydrate system at the site.

## PACKER EXPERIMENTS

### Introduction

Packer experiments were conducted in Hole 892B to determine bulk permeability and average formation pressure. The packer was

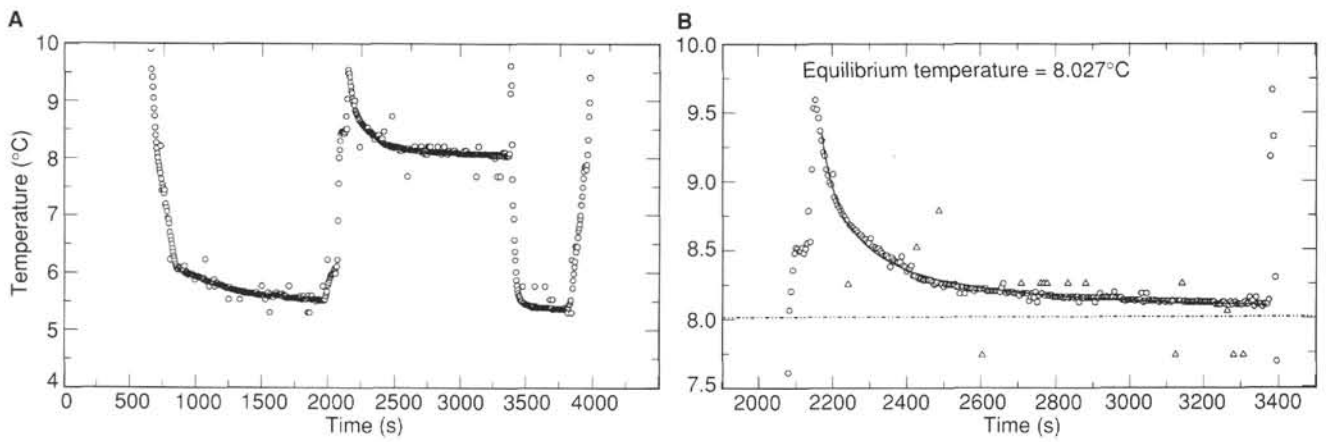


Figure 56. Record from WSTP deployment in Hole 892A at 39 mbsf (Core 146-892A-6X). **A.** Entire run. **B.** Close-up of record in sediment. Conventions as in Figure 55.

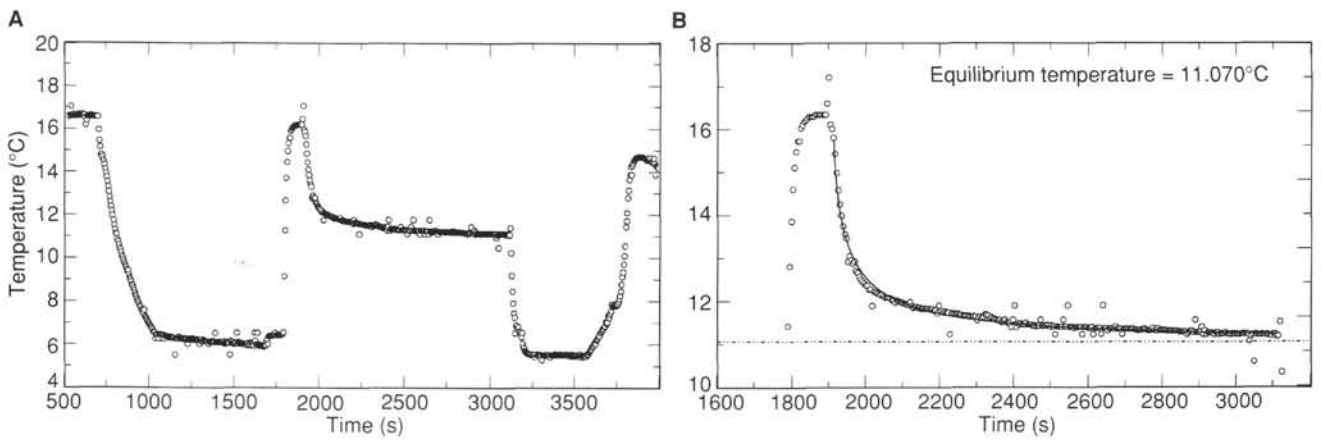


Figure 57. Record from WSTP deployment in Hole 892A at 67.5 mbsf (Core 146-892A-9X). **A.** Entire run. **B.** Close-up of record in sediment. Conventions as in Figure 55.

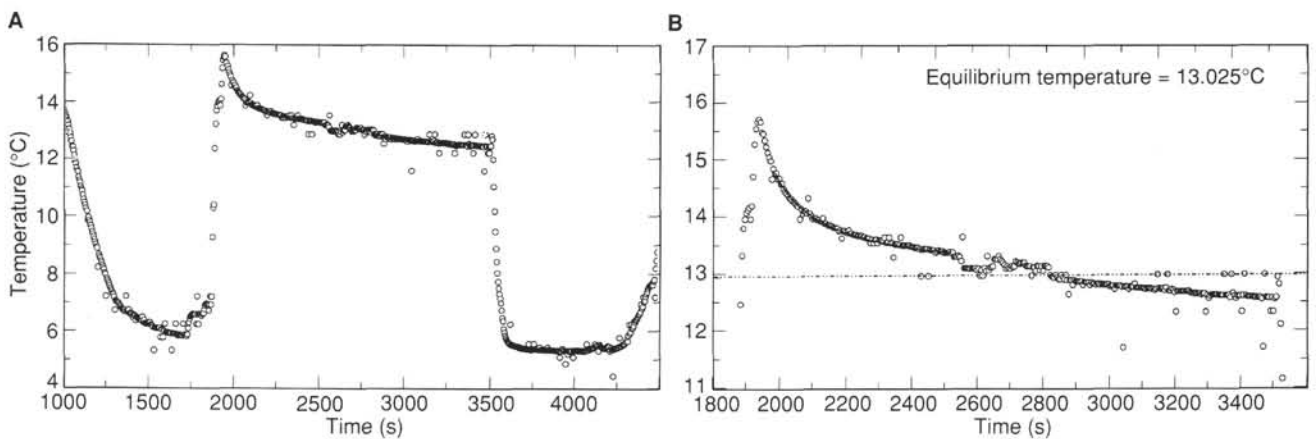


Figure 58. Record from WSTP deployment in Hole 892A at 87.5 mbsf (Core 146-892A-12X). **A.** Entire run. **B.** Close-up of record in sediment. Conventions as in Figure 55.

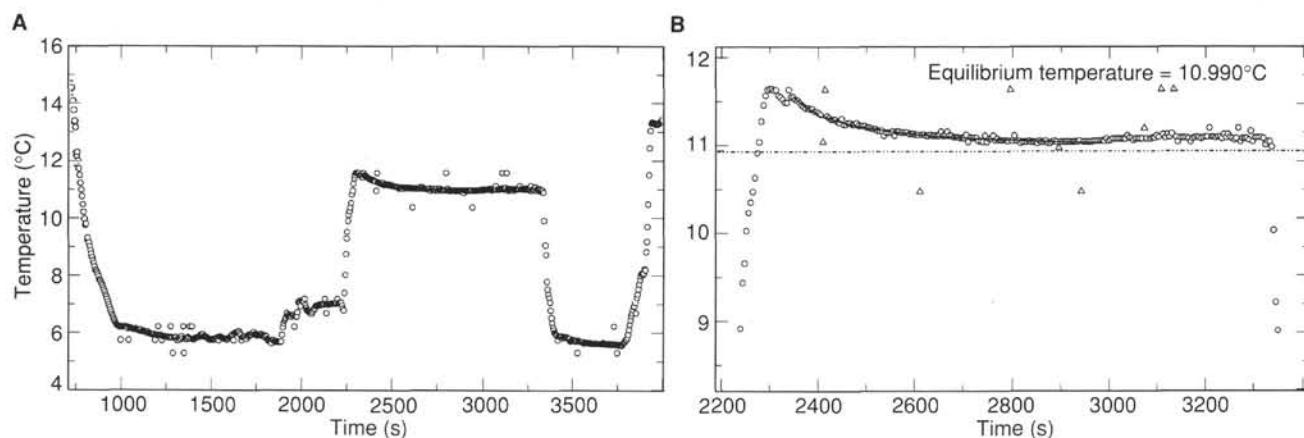


Figure 59. Temperature record from WSTP deployment in Hole 892A at 97.0 mbsf (Core 146-892A-13X). **A.** Entire run. **B.** Close-up of record in sediment. Conventions and symbols as in Figure 55.

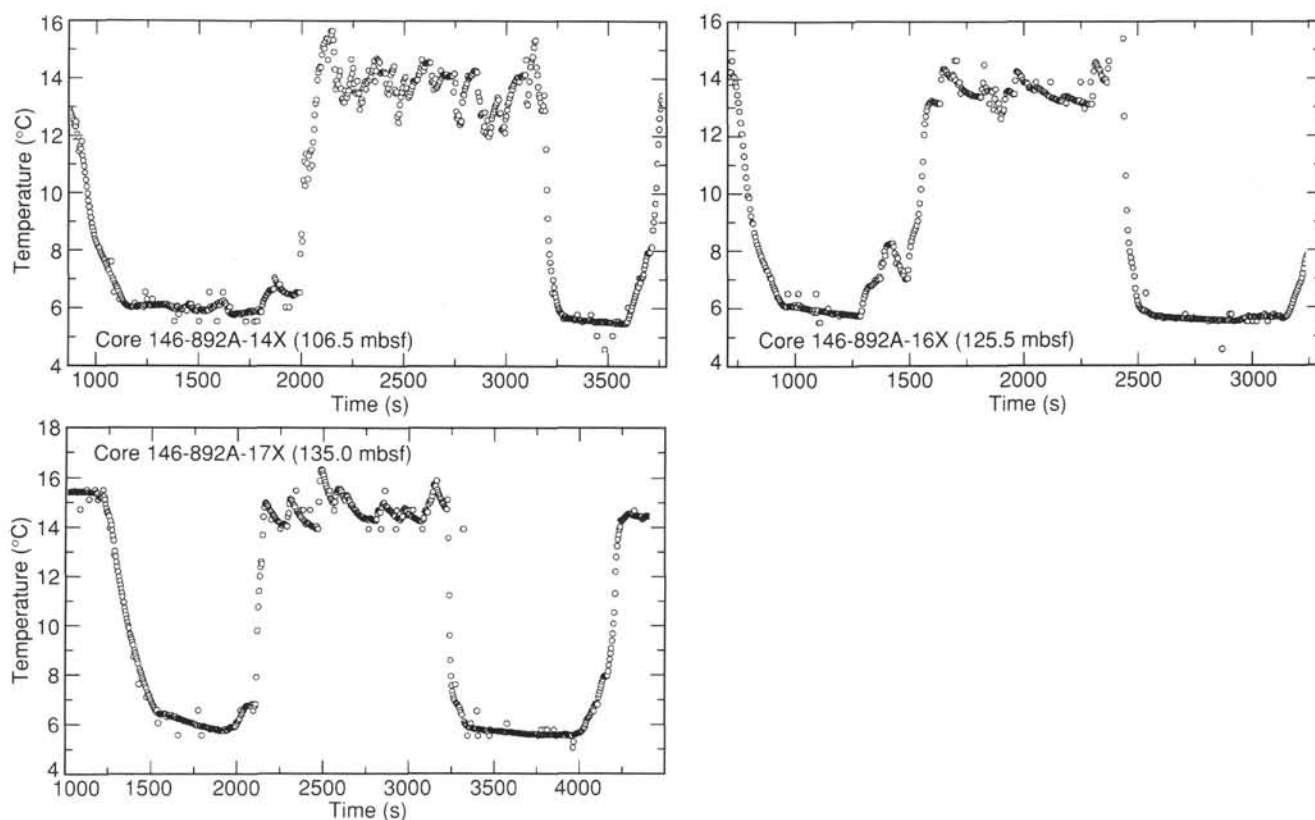


Figure 60. Temperature records from unsuccessful WSTP deployments in Hole 892A at 106.5 mbsf (Core 146-892A-14X), 125.5 mbsf (Core 146-892A-16X), and 135.0 mbsf (Core 146-892A-17X).

set at 64.5 mbsf within the 11 $\frac{3}{4}$ -in. cemented casing to test the permeability of the interval between the base of the cemented hole at 105.5 mbsf and the base of the borehole at 178.5 mbsf. Although 41 m of fill had accumulated in the bottom of the borehole, we assumed that the fill material does not act as a permeability barrier.

Downhole pressures were recorded with a mechanical Kuster gauge and an electronic "ERPG-300" gauge made by Geophysical Research Corporation (GRC). During testing, a pressure transducer at the rig floor provided real-time indication of downhole events. Pumping rates and total volumes pumped were also measured at the rig floor.

### First Packer Deployment

After the first go-devil landed, the packer was inflated to about 1500 psi (10.3 MPa) and four slug tests were conducted, including the slug test that occurs following inflation (Fig. 73). The uphole pressure gauge indicated rapid decay of the pressure pulses; therefore, it was decided to run constant-rate injection tests. The first two tests were run at 10 and 20 strokes per minute (spm); each stroke nominally delivers 5 gal. ( $1.9 \times 10^{-2} \text{ m}^3$ ). Results from the uphole pressure gauge indicated pressure decreases following an initial peak. These pressure

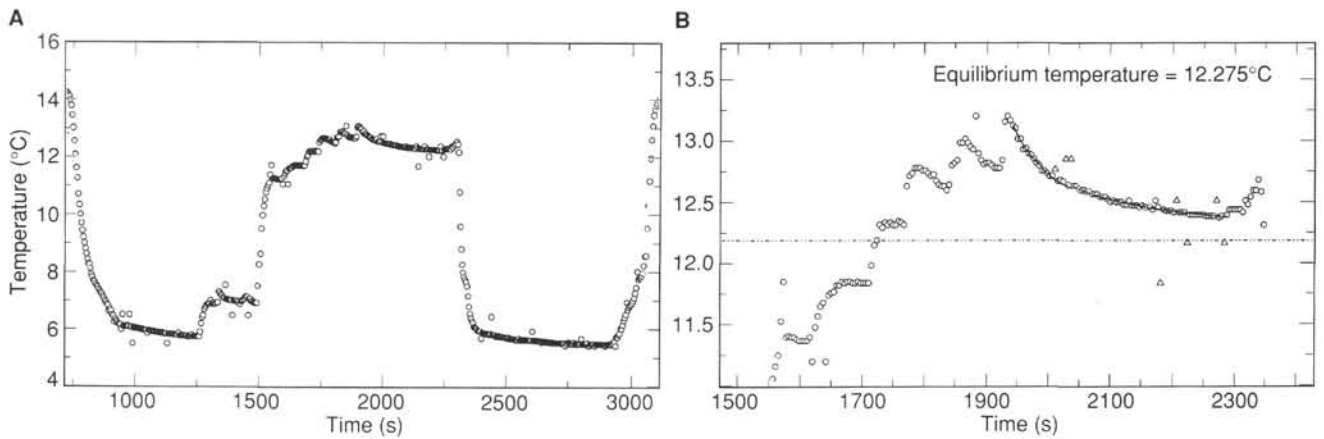


Figure 61. Temperature record from WSTP deployment in Hole 892A at 116 mbsf (Core 146-892A-15X). **A.** Temperature record for entire run. **B.** Close-up of temperature record in sediment. Conventions and symbols as in Figure 55.

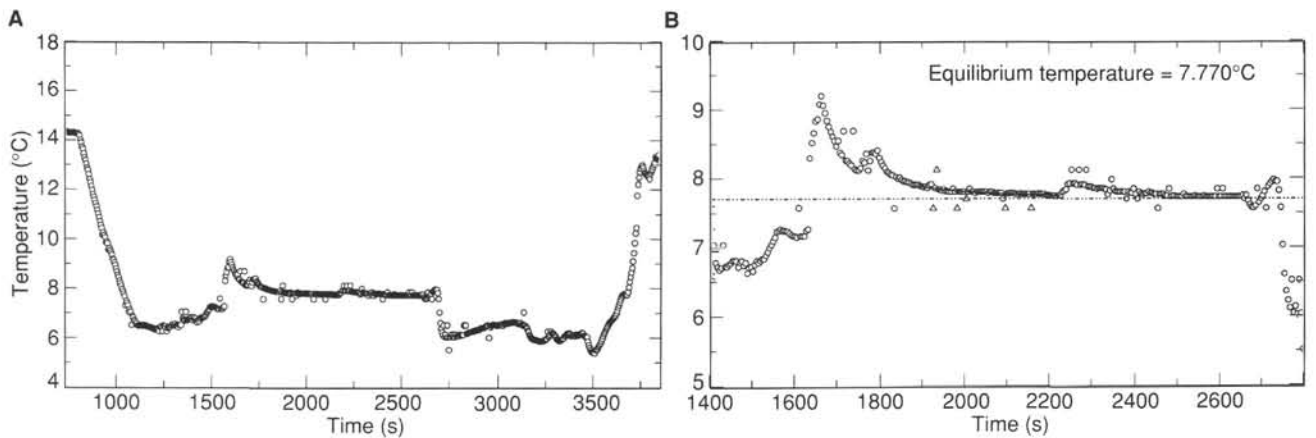


Figure 62. Temperature record from WSTP deployment in Hole 892A at 144.5 mbsf (Core 146-892A-18X). **A.** Temperature record for entire run. **B.** Close-up of temperature record in sediment. Conventions and symbols as in Figure 55.

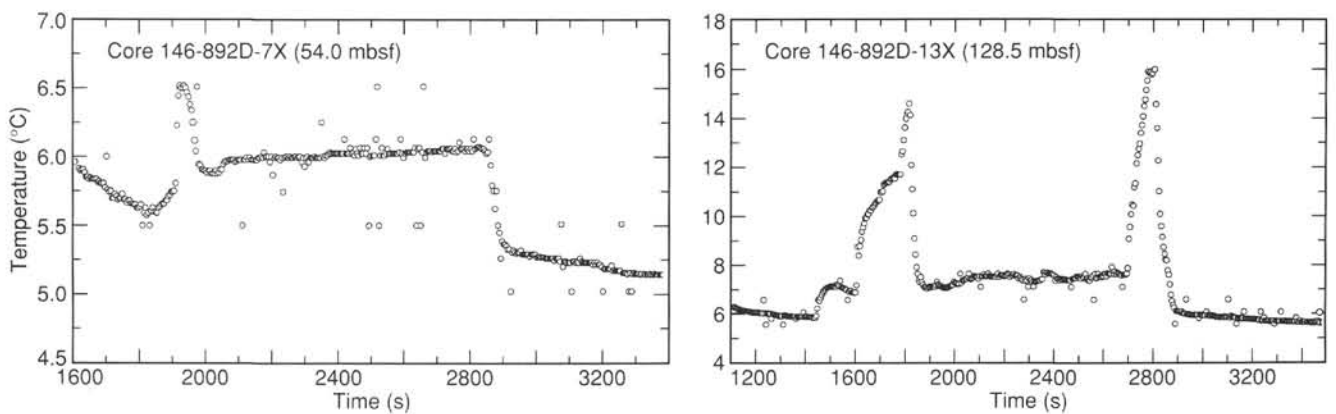


Figure 63. Temperature records from unsuccessful WSTP deployments in Hole 892D at 54 mbsf (Core 146-892D-7X) and 128.5 mbsf (Core 145-892D-13X).

records deviate from the ideal injection test in which pressure increases continuously with time. This effect may represent an incomplete seal of the casing or an increase of permeability within the tested section because of the applied pressure. As the camera at the seafloor showed no evidence of fluid escape through or around the reentry cone while the packer was seated, we decided to run the third injection test at a

lower pumping rate. Pressure data from the third constant-rate injection test, conducted at 8 spm ( $2.5 \times 10^{-3} \text{ m}^3/\text{s}$ ), showed a more ideal pattern.

After these tests, the go-devil was retrieved to ensure that the pressure recorders were operating correctly. The downhole pressure record collected with the GRC recorder during the test (Fig. 73) indicated much slower decay than that suggested by the uphole recorder.

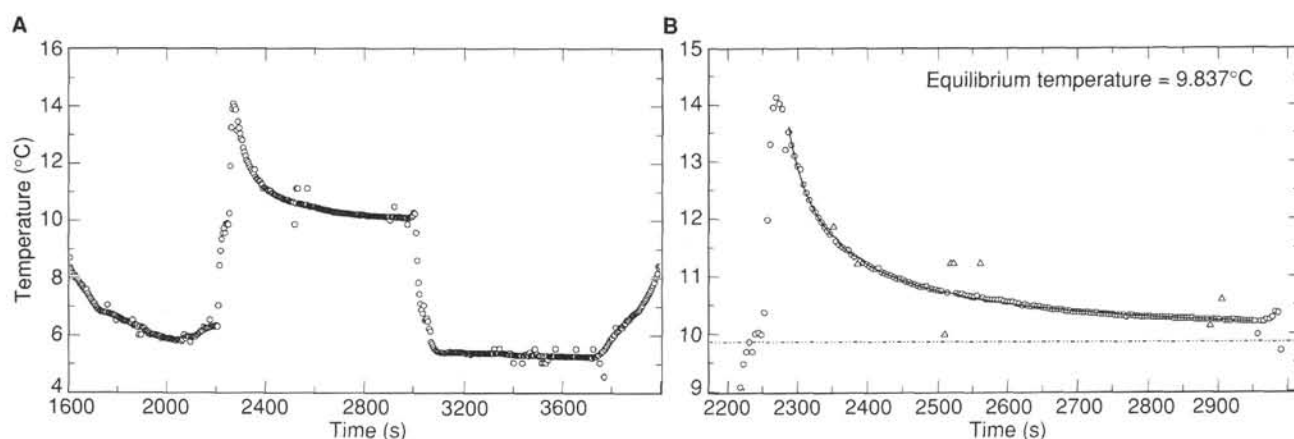


Figure 64. Temperature record from WSTP deployment in Hole 892D at 77 mbsf (Core 146-892D-9X). **A.** Entire run. **B.** Close-up of record in sediment. Conventions and symbols as in Figure 55.

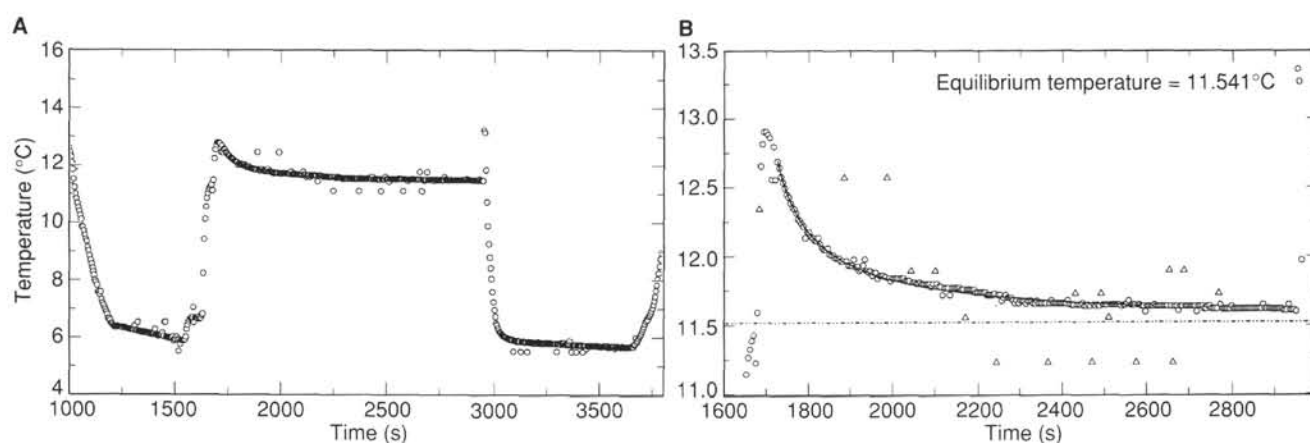


Figure 65. Temperature record from WSTP deployment in Hole 892D at 109.5 mbsf (Core 146-892D-11X). **A.** Entire run. **B.** Close-up of record in sediment. Conventions and symbols as in Figure 55.

## Second and Third Packer Deployments

A second go-devil was deployed with one Kuster and one GRC pressure recorder, but the packer failed to seat. The go-devil was retrieved for a third go-devil deployment. The packer was successfully set at the same depth as in the first deployment. The pressure pulse following packer inflation was allowed to decay for 1 hr, longer than for the first deployment; following the decay period, a constant-rate injection test was run at 5 spm ( $1.6 \times 10^{-3} \text{ m}^3/\text{s}$ ) for 30 min and was subsequently shut-in for 2 hr. The uphole pressure record from the injection test shows a slight pressure decay following the initial peak, even though this test was run at a lower rate than the 8-spm test during the first deployment that showed a continuous pressure rise during testing. A malfunction of the GRC recorder and lack of resolution of the Kuster record precluded analysis of these data.

## Observations

The pressure history during the constant-rate injection tests is problematic; pressure decreases follow initial peaks during the 10- and 20-spm injection tests, and peak pressure from the 20-spm test is only slightly higher than that from the 10-spm test. These results are consistent with an increase in permeability resulting from the applied pressure. Assuming an average bulk density of  $1.7 \text{ Mg/m}^3$  from logs (see "Downhole Logging" section, this chapter) and a water density

of  $1.035 \text{ Mg/m}^3$ , the difference between lithostatic and hydrostatic pressures at 105 mbsf is estimated to be 0.6 MPa. This difference was approached but not exceeded during injection testing.

Qualitative assessment of the pressure decay curves suggests an equilibrium pore pressure above hydrostatic pressure. The equilibrium pressure during the packer experiments does not represent the normal formation pressure because the hole was perturbed by drilling and was open to the seafloor for  $12\frac{3}{4}$  hr preceding the packer experiment. A borehole seal (CORK) was installed in Hole 892B following the packer experiment and should provide a record of pressure recovery and an accurate measurement of the in-situ pore pressure.

## DOWNHOLE LOGGING

### Log Reliability

At Site 892, hole instability caused many enlarged-diameter intervals (Fig. 74) that affected logging in two ways: the accuracy of some logs was degraded, and fill may have contributed to the bridge formation that limited logging to the interval above 139 mbsf. Density tool measurements in Hole 892C showed several excursions to low values because of the inability of the tool's caliper to maintain contact with the borehole wall; these spikes are confined almost entirely to the interval from 89 to 108 mbsf (Fig. 75). The large and rapidly varying hole diameter may also have affected the quality of the neutron-porosity measurements, which will be corrected post-cruise. Simi-

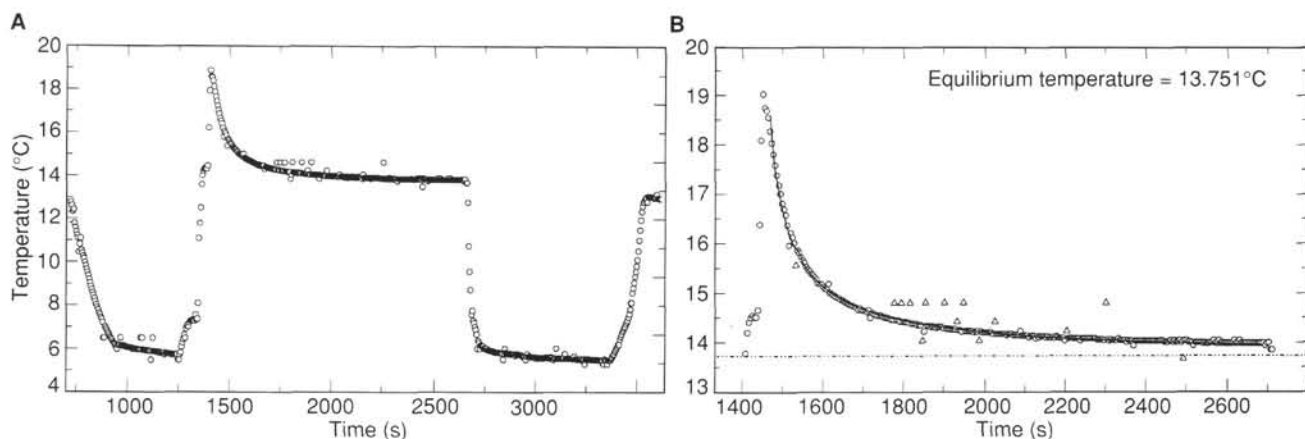


Figure 66. Temperature record from WSTP deployment in Hole 892D at 147.5 mbsf (Core 146-892D-15X). **A.** Entire run. **B.** Close-up of record in sediment. Conventions and symbols as in Figure 55.

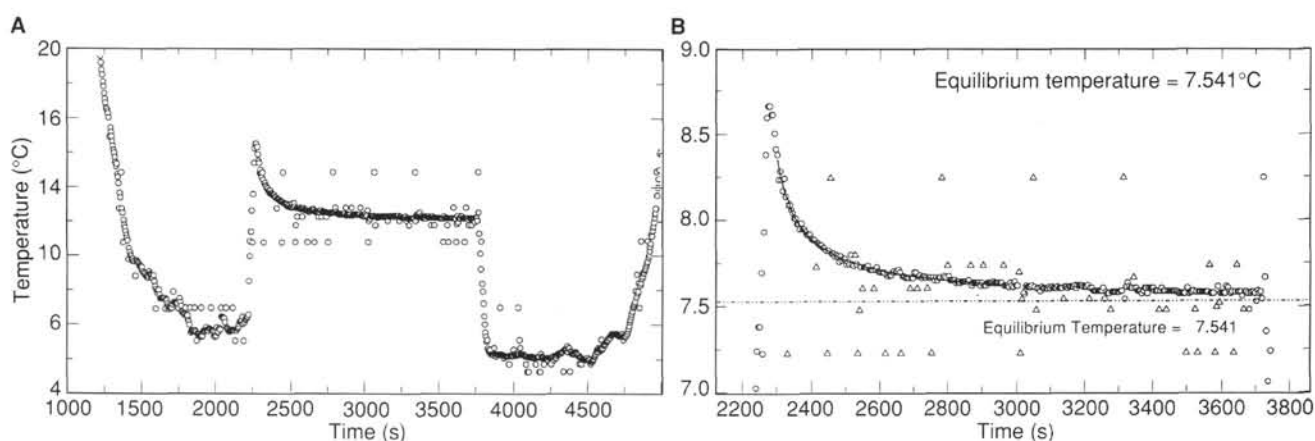


Figure 67. Temperature record from WSTP deployment in Hole 892E at 30 mbsf (Core 146-892E-3H). **A.** Entire run. **B.** Close-up of record in sediment. Conventions and symbols as in Figure 55.

larly, gamma-ray counts and resistivity may be slightly underestimated because of the large hole diameter.

Raw sonic velocities were generally reliable above 60 mbsf but inaccurate below that depth (Fig. 76). For the interval from 87 to 120 mbsf, short- and long-spaced sonic values are consistent, indicating a velocity of 1.4 km/s. Examination of the original traveltimes from which these logs are calculated indicates, however, that two of the four traveltimes curves exhibit delays resulting from cycle skipping. After removal of these cycle skips, the reprocessed sonic velocities (see "Explanatory Notes" chapter, this volume) indicate a velocity of 1.5 km/s (Fig. 76), or water velocity. The cause of this low velocity is discussed later in this section.

The resistivity measurements are expressed as formation resistivities rather than as formation factors, because the latter requires estimation of both drilling-induced temperature variations and the effect of the salinity of the interstitial fluid.

Measured hole deviations were  $1^{\circ}$ – $2^{\circ}$  to the north in Hole 892C. Hole deviation adds inherent inaccuracy to any structural measurements taken on the cores, or from FMS data, and may be a cause of hole ellipticity, although the orientation of maximum ellipticity at this hole is generally east-west, apparently not controlled by the deviation direction.

Gamma-ray measurements are attenuated in the portion of the hole logged through the pipe, which is above 49 mbsf for the lithoporosity

run and 35 mbsf for the seismic stratigraphy run. No correction for pipe attenuation was attempted on board ship.

### Correlation of Logs to Lithologic Units

Throughout the logged interval, the small-scale variations in gamma-ray values are positively correlated with neutron variations in resistivity and negatively correlated with neutron porosity (Fig. 75). This relationship implies that the silty clays and clayey silts are less porous than the sandier beds, because K, Th, and U are normally more abundant in clay minerals than in sands. If so, this pattern is opposite that generally observed in porous, terrigenous sediments (e.g., see "Downhole Logging" section, "Site 888" chapter, this volume), where uncompacted clay minerals increase the porosity because of their near-random orientation of platy particles. The pattern at Site 892 is, however, similar to that normally observed at much greater burial depths, where compaction reorients clay minerals to a subhorizontal orientation that causes high intergrain contact and consequently low porosity. Presumably, the silty clays at Site 892 were initially more porous than the sands but have experienced greater compaction.

The logs of Hole 892C show some gradual variations reflecting lithologic change. Gamma-ray values gradually decrease from about 70 to 100 mbsf and increase from 100 to 130 mbsf, suggesting a down-hole increase and then a decrease in sand content (a fining-upward

**Table 20. Summary of corrected sediment temperatures.**

| Core no.           | Depth (mbsf) | Summary of WTSP measurements  |                       |
|--------------------|--------------|-------------------------------|-----------------------|
|                    |              | Corrected temperature (°C)    | Status                |
| <b>146-892A-</b>   |              |                               |                       |
| 3X                 | 19.0*        | 5.70 ± 0.10                   | Accepted              |
| 6X                 | 39.0*        | 6.73 ± 0.05                   | Accepted              |
| 9X                 | 67.5         | 9.80 ± 0.05                   | Accepted              |
| 12X                | 87.5*        | 11.70 ± 0.10                  | Accepted              |
| 13X                | 97.0*        | 9.70 ± 0.50                   | Dubious               |
| 14X                | 106.5        |                               | Rejected              |
| 15X                | 116.0        | 11.00 ± 0.10                  | Dubious               |
| 16X                | 125.5        |                               | Rejected              |
| 17X                | 135.0        | 12.30 ± 0.10                  | Rejected              |
| 18X                | 144.5        | 6.50 ± 0.05                   | Rejected              |
| <b>146-892D-</b>   |              |                               |                       |
| 7X                 | 54.0         |                               | Rejected              |
| 9X                 | 77.0         | 8.50 ± 0.10                   | Accepted              |
| 11X                | 109.5        | 10.20 ± 0.20                  | Accepted              |
| 13X                | 128.5        |                               | Rejected              |
| 15X                | 147.5        | 12.40 ± 0.10                  | Accepted              |
| <b>146-892E-</b>   |              |                               |                       |
| 3H                 | 30.0*        | 6.20 ± 0.10                   | Accepted              |
| Following 4H       | 52.0         | 7.50 ± 0.20                   | Accepted              |
| Following drilling | 62.0         | 8.00 ± 0.10                   | Accepted              |
|                    |              | Summary of ADARA measurements |                       |
| Core no.           | Depth (mbsf) | Corrected temperature (°C)    | Status                |
| <b>146-892E-</b>   |              |                               |                       |
| 3H                 | 42.5**       |                               |                       |
| 4H                 | 49.0 ± 3.0†  | 6.30–6.80                     | Accepted (high error) |

Notes: Measurements with an asterisk (\*) were taken with Probe 105 (with water sampler); other WTSP measurements were taken with Probe 108 (without water sampler). Measurement with a double asterisk (\*\*) was taken with Probe 12. Measurement with a dagger (†) was taken with Probe 10.

pattern overlying a coarsening-upward sequence). Over the same depth intervals, the neutron porosity exhibits a gradual decrease and then an increase, respectively. This log response is consistent with the enrichment in sand observed in the 100–110 mbsf interval (see “Lithostratigraphy” section, this chapter).

The overall trends in lithology are punctuated by several intervals less than 10 m thick with distinct log characteristics. From 61 to 68 mbsf in Hole 892C, density and resistivity are high and neutron porosity and hole diameter are low (Figs. 74–75). Velocities are also high in this interval but the upper and lower depth limits of this local maximum are obscured by cycle skipping (Fig. 76). Gamma-ray values are high from 61 to 64 mbsf. Cores 146-892A-8X and -9X and Cores 146-892D-7X and -8X indicate that this interval in Hole 892C consists of a clayey siltstone with a downward transition to a cemented and veined sandstone (see “Lithostratigraphy” section, this chapter). The clayey siltstone has a weak structural fabric. Compared to the clay-rich bed, the sandstone exhibits decreased gamma-ray values and continued high resistivity, consistent with its lithology and cementation. Thus, the overall log response could be interpreted as resulting simply from a clay-rich siltstone overlying a cemented sandstone. However, the veined sandstone interval coincides with a negative chloride anomaly, a high in ethane composition, a break in the slope of the porosity and density curves from core measurements, and a spike in the temperature curve (see “Inorganic Geochemistry,” “Organic Geochemistry,” “Physical Properties,” and “WTSP and ADARA Temperature Meas-

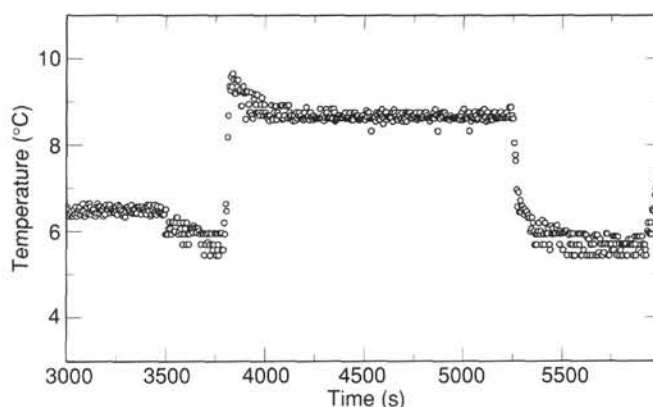


Figure 68. Temperature record from WTSP deployment in Hole 892E at 52 mbsf (following Core 146-892E-4H).

urements” sections, respectively, this chapter). Thus, the log response could also indicate a strain-hardened fault zone.

From 82.5 to 90 mbsf, the logs show two intervals of high gamma-ray values, two highs in bulk density, and arguably a corresponding set of lows in neutron porosity. Only a single resistivity high is shown over this interval, possibly because this tool has lower vertical resolution than the other tools. Log responses for this interval appear to indicate two dense clay-rich intervals. A minor negative peak in chloride and a temperature spike suggest active fluid flow through this zone (see “Inorganic Geochemistry” and “WTSP and ADARA Temperature Measurements” sections, this chapter). However, the lack of a peak in higher order hydrocarbons at this level argues against flow (see “Organic Geochemistry” section, this chapter).

### Velocity, Density, and Porosity Patterns

Neutron porosities at Site 892 decrease slightly downhole, from an average of about 55% at 50–60 mbsf to 50% at 105–123 mbsf (Fig. 75). These neutron porosities are substantially lower than the porosities of 68% and 64%, respectively, that are expected for typical terrigenous sediments at these sub-bottom depths (Hamilton, 1976). Similarly, observed densities average about 1.7 Mg/m<sup>3</sup> (excluding unreliably low density values in the interval 89–108 mbsf), much more than the 1.59–1.66 Mg/m<sup>3</sup> values typical of these sub-bottom depths (Hamilton, 1976). Neutron porosities at Site 892 are, however, generally similar to those measured at reference Sites 888 (see “Downhole Logging” section, “Site 888” chapter, this volume) and 174 (von Huene et al., 1973). Superimposed on the broad trends of neutron porosity and density vs. depth is a substantial small-scale variation that correlates with the gamma-ray values and therefore reflects lithologic variations.

Hyndman and Spence (1992) proposed a model for the origin of gas hydrates and associated BSRs. Based on seismic modeling of the BSR at the Vancouver accretionary prism, they made several specific predictions concerning the log responses to be encountered at BSR sites such as Site 892. The BSR is a strong negative-polarity seismic reflector; therefore, a sharp decrease in impedance is expected at the BSR. Hyndman and Spence (1992) attributed the impedance change entirely to a contrast between fluid-filled pores below the BSR and hydrate-containing pores above the BSR. They followed other investigators in assuming that the BSR is the base of the methane-hydrate stability field, and they suggested that the hydrates crystallize because of fluid advection in the 10- to 30-m-thick interval overlying the BSR. An alternative model for BSR formation is that the impedance contrast is primarily the result of the presence of free gas immediately below the BSR (Minshull and White, 1989; Miller et al., 1991), rather than high-velocity hydrates. Even 2%–4% free gas is sufficient to lower

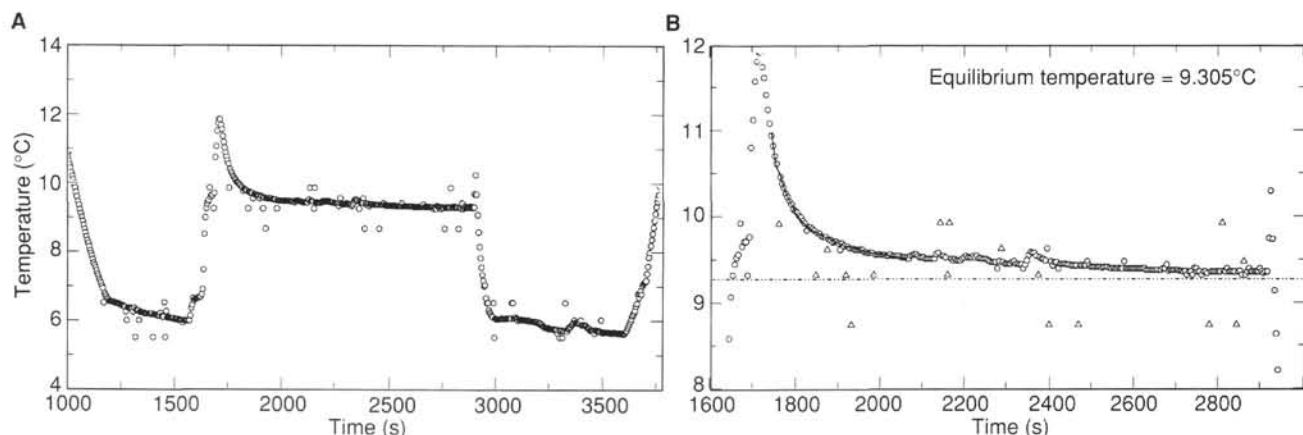


Figure 69. Temperature record from WSTP deployment in Hole 892E at 62 mbsf (following drilling). **A.** Entire run. **B.** Close-up of temperature record in sediment. Conventions and symbols as shown in Figure 55.

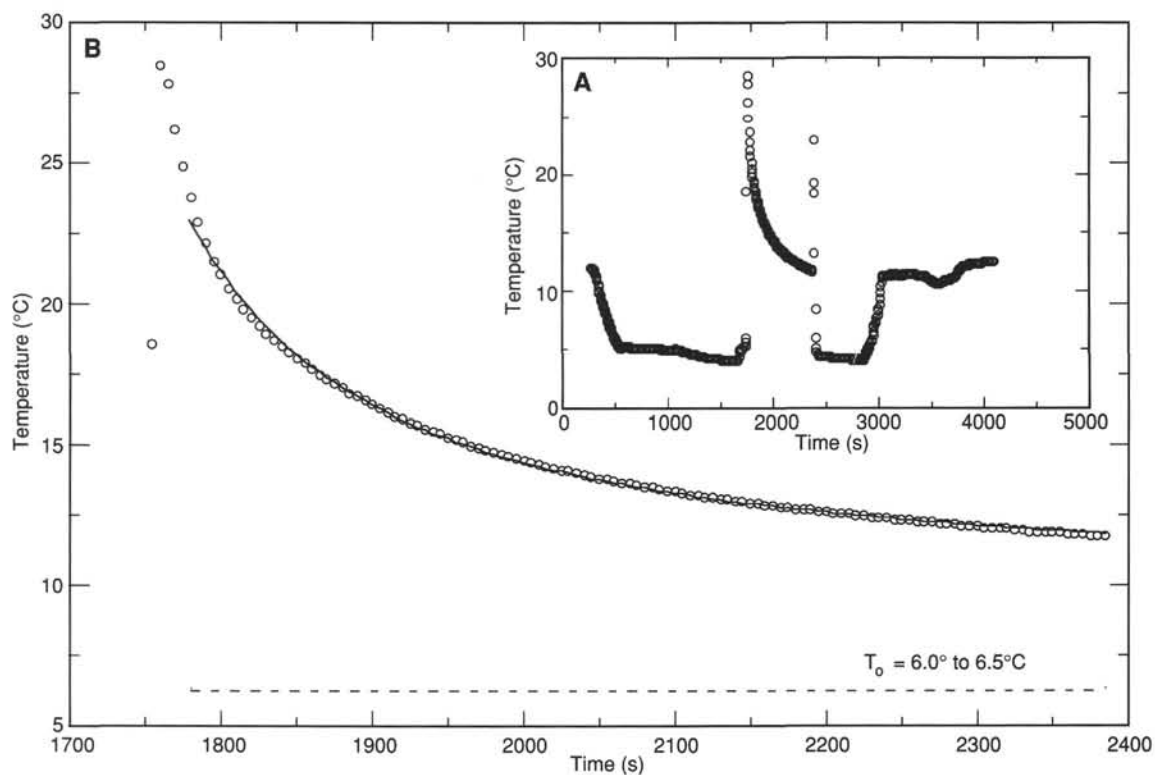


Figure 70. Temperature record from ADARA deployment in Hole 892E at approximately  $49 \pm 3$  mbsf (Core 146-892E-4H). **A.** Temperature record for entire run (inset). **B.** Close-up of temperature record in sediment. The solid line is the regression curve used to estimate the equilibrium temperature (shown by the dashed line).

the compressional-wave velocity of an unconsolidated sediment to less than that of water (Domenico, 1976).

Log responses can be used to detect occurrences of hydrates (e.g., Mathews and von Huene, 1985). In massive methane hydrates, velocity and resistivity are high, and density and gamma-ray response are low. Whalley (1980) calculated that the compressional-wave velocity in pure methane hydrates is about 3.8 km/s and the density is  $0.91 \text{ Mg/m}^3$ . For sediments in which the pores contain a mixture of hydrate and pore water, however, the relationships between hydrate proportion and velocity and resistivity are neither theoretically nor empirically known.

Detection of hydrate can be based on the identification of zones that have anomalously high velocity, in comparison with the velocity

of other sediments with the same porosity. At Site 892, however, only a short interval of the sonic log yields velocities that are indicative of formation velocities. Within this interval (35–72 mbsf), observed velocity variations (Fig. 76) correlate well with the character of the porosity-sensitive logs (Fig. 75); no indications of anomalously high velocities were detected. We saw no evidence for massive methane hydrates as were encountered in the Site 570 logs (Mathews and von Huene, 1985), but we cannot exclude a few percent of methane hydrate.

Hydrate can also be identified based on discrepant responses among the porosity-sensitive logs: velocity and resistivity are increased by hydrate, whereas density and neutron porosity are slightly decreased. Based on this criterion, we can unambiguously identify the high-resistivity zones at 61–67 and 83–89 mbsf not as hydrates but as

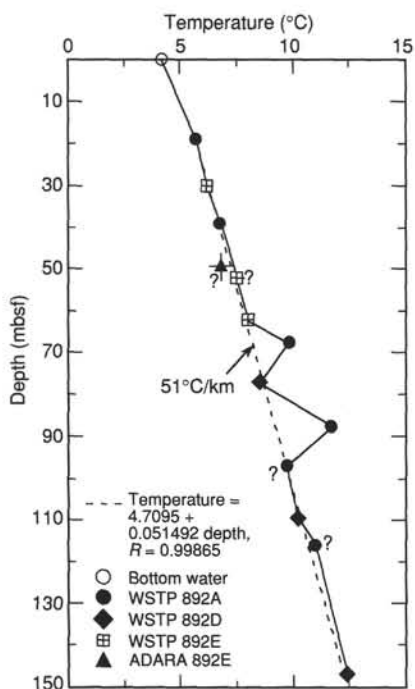


Figure 71. Bottom-seawater and sediment temperatures vs. depth at Site 892. The linear least-squares regression line (dashed) was calculated for all the points excluding the bottom-water temperature and the measurements at 49, 67.5, 87.5, and 97 mbsf. Dubious temperature measurements are denoted with question marks. Unless marked, the error bars for individual measurements are contained within the points.

“hard streaks”: high-density, low-porosity intervals that may be lithologically or diagenetically controlled. Furthermore, we can see from the gamma-ray log that the lower hard streak is actually two adjacent clay-rich beds, separated by a thin low-clay, higher-porosity interval (Figs. 75–76). The upper hard streak is clay rich only in its top half; the lower half may be cemented sandstone; these results agree with the core descriptions (see “Lithostratigraphy” section, this chapter).

In contrast to the absence of log-based evidence for hydrates topping the BSR, the velocity log provides strong indirect evidence for the existence of free gas near and beneath the BSR. The consistent pattern of 1.5-km/s velocities below 72 mbsf indicates that direct compressional waves travelling within the borehole fluid are faster than any waves travelling along the borehole wall. Therefore, the formation velocities must be less than or about equal to 1.5 km/s, although the velocities of water-saturated rocks with 50% porosity are expected to be about 1.75 km/s (Hyndman et al., 1993). Water velocities can be obtained even where formation velocities are normal, if an excessively large hole size causes formation-refracted waves to arrive after the direct water waves. We can, however, exclude this possibility because velocities of 1.5 km/s were observed even in intervals with a caliper-log reading of <38 cm (15 in.) (Fig. 74).

Free gas in the formation appears to be the only viable mechanism for obtaining formation velocities slower than the measured 1.5 km/s fluid velocity. The implications of velocities measured by both logging and a VSP for the presence of free gas are discussed below.

### Vertical Seismic Profile

The zero-offset VSP at Site 892 was shot as a detailed checkshot survey using a 300-in.<sup>3</sup> air gun and a 400-in.<sup>3</sup> water gun fired alternately. Gun and receiver geometries are shown in the “Explanatory Notes” chapter (this volume). Both guns were fired at 2000 psi. The WST data were recorded by Schlumberger as well as on a Sun

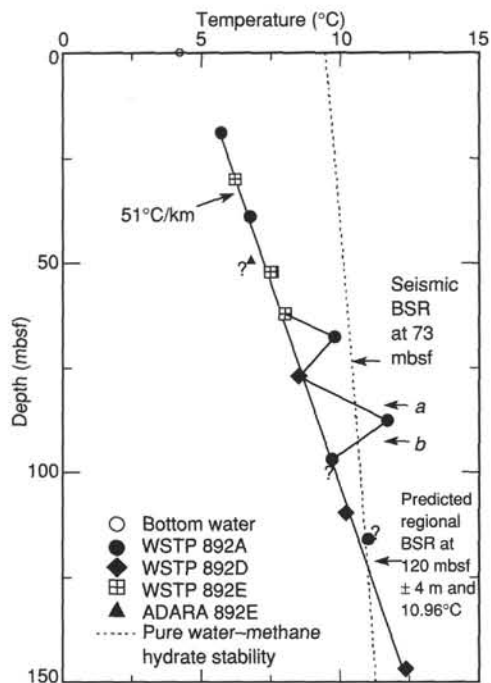


Figure 72. Diagram showing the linear temperature profile plotted vs. the hydrate stability field obtained from laboratory data for pure water and methane (after Hyndman et al., 1992). The predicted depth to the base of the hydrate and the seismic BSR depth are noted. Points *a* and *b* denote depths near which the nonlinear portions of the temperature profile intersect the hydrate stability curve.

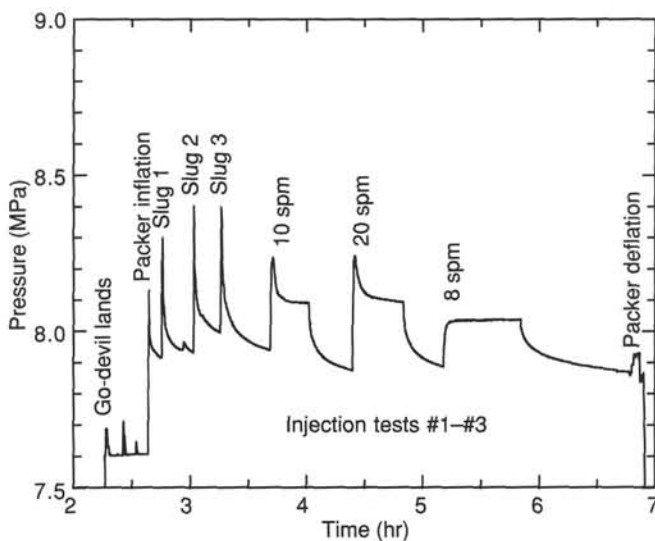


Figure 73. Downhole pressure-time record from the GRC recorder during the first deployment in Hole 892B, with the packer set in casing at 64.5 mbsf.

workstation. In addition, far-field source signatures were recorded on the Sun workstation for both guns throughout the experiment at a depth about 150 m below the guns. Eight receiver stations were run, beginning at 91.5 mbsf and stepping uphole at 5-m intervals to 56.5 mbsf. The large hole size prevented clamping of the WST in the interval from 91.5 to 125 mbsf; however, sonic log velocities were obtained in this interval. Time-depth and velocity data presented here (Fig. 77) are based on air-gun data only; water-gun data have not been analyzed yet.

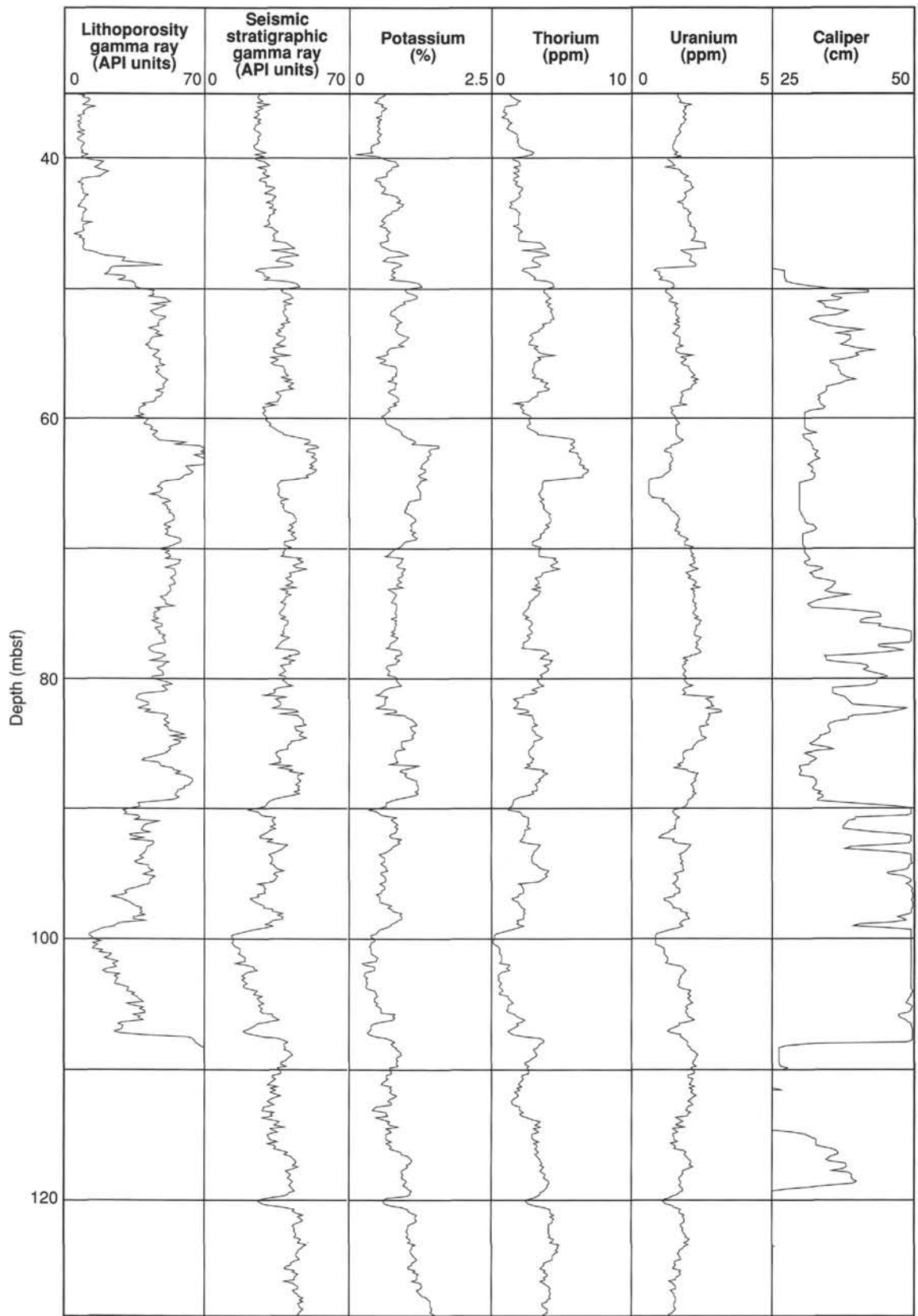


Figure 74. Spectral gamma-ray and caliper logs for Site 892, including the total gamma-ray logs for the lithoporosity logging run and the seismic stratigraphic logging run as well as potassium, thorium, and uranium.

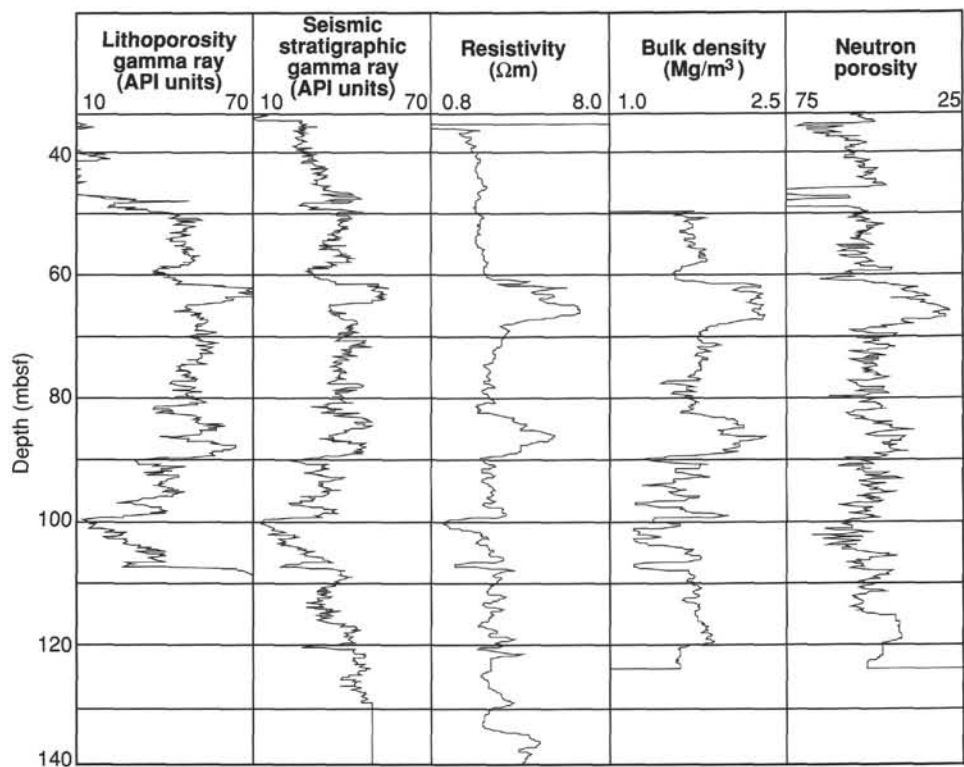


Figure 75. Gamma-ray and porosity-sensitive logs for Site 892. Total gamma-ray logs are shown for the lithoporosity and seismic stratigraphic logging runs. Porosity-sensitive logs are resistivity, bulk density, and neutron porosity. Note the character match between the gamma-ray and porosity-sensitive logs, which implies that porosity variations are caused mainly by changes in clay-mineral abundance.

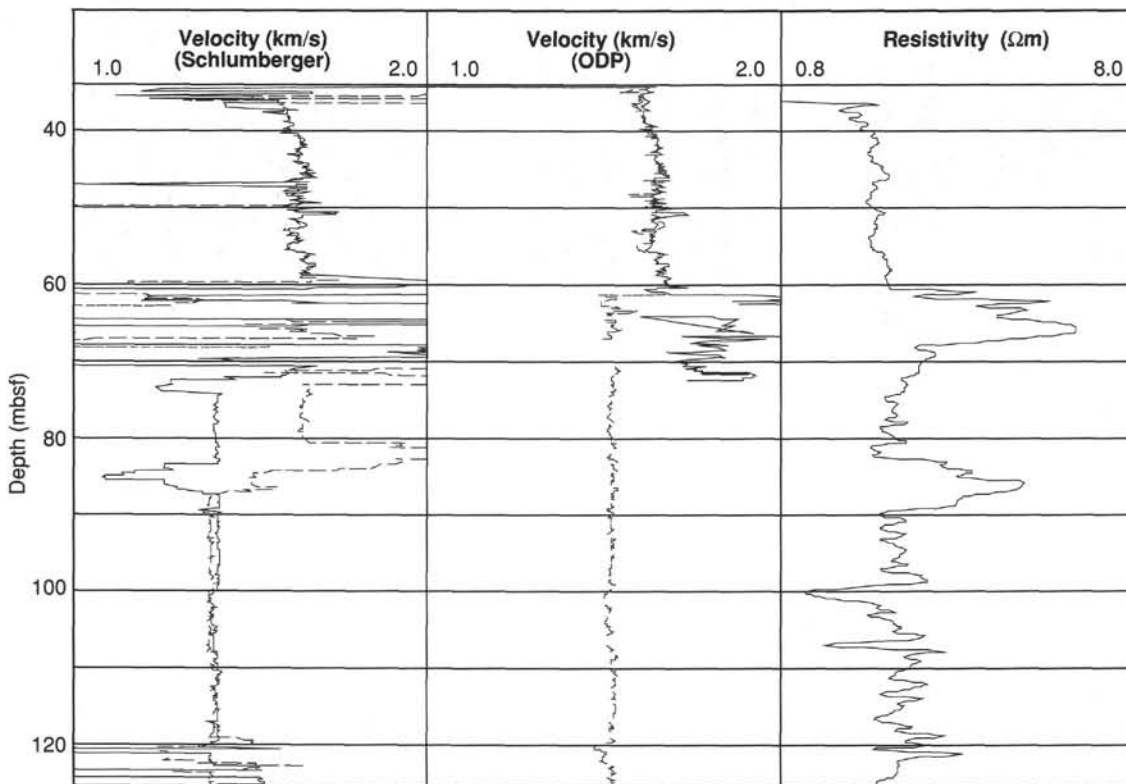


Figure 76. Velocity (Schlumberger processed and ODP reprocessed) and resistivity logs for Site 892.

The VSP provides an unambiguous time-depth relationship from the first-break time of the direct compressional-wave arrival at each receiver depth (Fig. 77). The slope of the time-depth curve provides the average velocity over any specified interval.

Integration of the sonic log yields a time-depth curve with respect to the shallowest log value, but the sonic log provides no information on the traveltimes between the seafloor and the first sonic log measurement at 39.9 mbsf. Therefore, the sonic time-depth curve was shifted to sub-bottom time by using the shallowest VSP datum to constrain the velocity of the unlogged interval (Fig. 77). The VSP-constrained integrated sonic log is used to extend the VSP-based time-depth curve.

The BSR occurs in the multi-channel seismic (MCS) data at 990.6 ms two-way traveltime (TWT) below sea surface at Shotpoint 1097 on MCS line OR-9 (Fig. 3). Based on the VSP time-depth relationship, this traveltime corresponds to 73 mbsf ( $\pm 3$  m) (Fig. 77).

For Site 892, unlike other sites logged during Leg 146, we did not calculate a synthetic seismogram for time-depth conversion. Use of the sonic velocity log for this purpose would be misleading, because the log velocities of 1.5 km/s below 72 mbsf probably are overestimates of formation velocities. Furthermore, velocities are poorly determined in the interval 61–72 mbsf, where some measurements indicate water velocity but others give faster velocities that may be representative of the formation. A synthetic seismogram, if calculated, would simply show a single dominant negative-polarity reflector (the BSR) at either 61 or 72 mbsf, depending on our assumed velocities within that interval.

The VSP-based interval velocities beneath the BSR (73–91.5 mbsf) are 1.4 km/s, significantly slower than water. Such low velocities indicate free gas (e.g., Serra, 1984). Sonic-based velocities equal water velocity (1.5 km/s) throughout this interval and to the base of the logged section at 125 mbsf, which supports the inference that free gas is present to at least 52 m below the BSR. The VSP-based velocities increase above the BSR to approximately 1.59 km/s for the interval from 56.5 to 66.5 mbsf, but they are not well constrained (as discussed below). Sonic velocities in this interval average 1.65 km/s. Neither VSP-based velocities nor sonic log velocities support the interpretation of massive hydrate above the BSR.

The depth to the top of the free gas zone in Hole 892C and the relationship of this depth to the other holes at this site are ambiguous. Geochemical evidence for gas abundance as a function of depth varies substantially from Hole 892A to Hole 892D (see "Organic Geochemistry" section, this chapter). Presumably, the BSR defines the base of the hydrate stability field and therefore the top of the free gas zone; however, the traveltime to the BSR changes abruptly along seismic line OR-9 (Fig. 3) and each seismic trace is averaging across a Fresnel-zone radius that is wider than the hole spacing at this site. Sonic velocities place the top of the free gas zone at Hole 892C in the interval 61–72 mbsf, slightly above the estimate from the surface seismic of 73 mbsf at Hole 892A, but they cannot define it more accurately. We have three VSP stations above the BSR: at 56.5, 61.5, and 66.5 mbsf. If the depth and traveltime of the middle station at 61.5 mbsf are accurate, much of the interval from 61.5 to 66.5 mbsf is also within the low-velocity zone, suggesting that the free gas may extend as high as 61.5 mbsf. Additional work is necessary to refine the upper limit of free gas at Hole 892C, and this location may vary laterally even within the scale of the adjacent holes.

### Core, Log, and Seismic Integration

The time-depth curve from the VSP provides a powerful tool for locating features of the cores and logs on a seismic time section (see Fig. 3 in "Seismic Stratigraphic" section, this chapter). Because Site 892 is shallow, the seismic data have been substantially enlarged; thus, detailed interpretations at this scale must be undertaken with care, lest they exceed the resolution of the data.

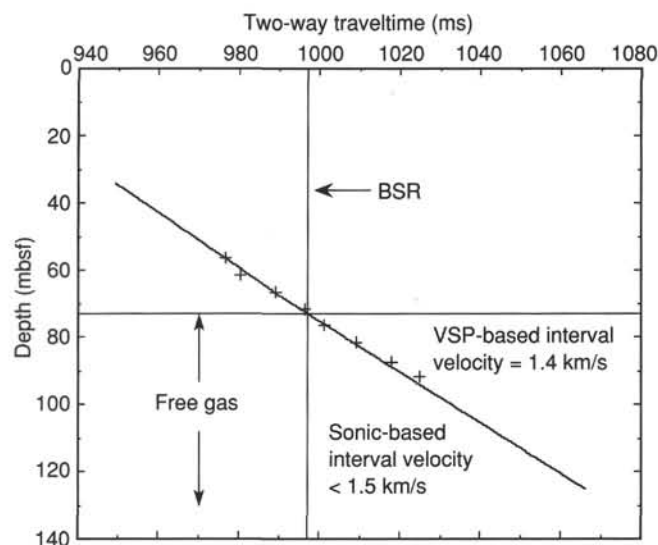


Figure 77. Time-depth relationship for Hole 892C. Diagonal line = integrated sonic log, and crosses = VSP time-depth points are shown by crosses. Based on this time-depth relationship, the BSR, which occurs at 997 ms below the sea surface, is at 73 mbsf. Estimated time to the seafloor is 910 ms, which corresponds to 675.3 mbsf; water depth from drill-pipe measurement from sea level is 674.5 mbsf.

The most prominent features of the seismic data from around Site 892 are the BSR reflector and a fault that forms a prominent reflector and exhibits surface displacement. The BSR cannot be traced through the fault zone, showing a lack of lateral continuity for about 100 m. This break in the BSR could result from shallowing of the base of the hydrate stability field because of warm fluids advecting along the fault.

A strong reflector dipping landward from the fault scarp is interpreted as the downward continuation of the fault. This reflection lies at 1044 ms beneath Hole 892A; based on the time-depth curve from Hole 892C, the depth of this reflector is about 107–113 mbsf, which corresponds to a scaly fabric zone at about 106 mbsf in Hole 892A and a gouge zone between 100 and 110 mbsf in Hole 892D (see "Structural Geology" section, this chapter). Thus, the dip of this reflector, and presumably the average dip of the fault, is 14°. The logs over the 100–110 mbsf interval in Hole 892C show low gamma-ray values, low resistivity, low bulk density, and a local high in porosity. The lowest spikes in resistivity and porosity may be explained by a sand layer observed in the cores, but most of the 100–110 mbsf interval is sheared clayey siltstone with distributed pieces of cataclastized carbonate (see "Lithostratigraphy" section, this chapter). Enhanced carbonate content of this section may have decreased the gamma-ray values. The increase in porosity and decrease in density and resistivity of this fault zone contrast with the response of faults observed between 61 and 68 mbsf in Hole 892C and at 375 mbsf in Hole 891C. The latter two faults are interpreted as strain-hardened mudstones. Perhaps the fault zone at 100 to 110 mbsf at Site 892 has higher porosity and lower density because the distributed and cataclastized carbonate cementation allowed it to become more dilatant.

### Formation MicroScanner Data

The Formation MicroScanner (FMS) made one pass at 550 m/hr from 123 to 47 mbsf. The hole diameter is good from 49 to 89.5 mbsf, but below 89.5 mbsf the caliper measurement is approximately 33 to 39 cm and slightly elliptical. We have excellent images from the upper portion of the logged hole, where all four pads make good contact and features are distinct. In general, the data from 52 to 121 mbsf show the best-quality FMS images from this leg.

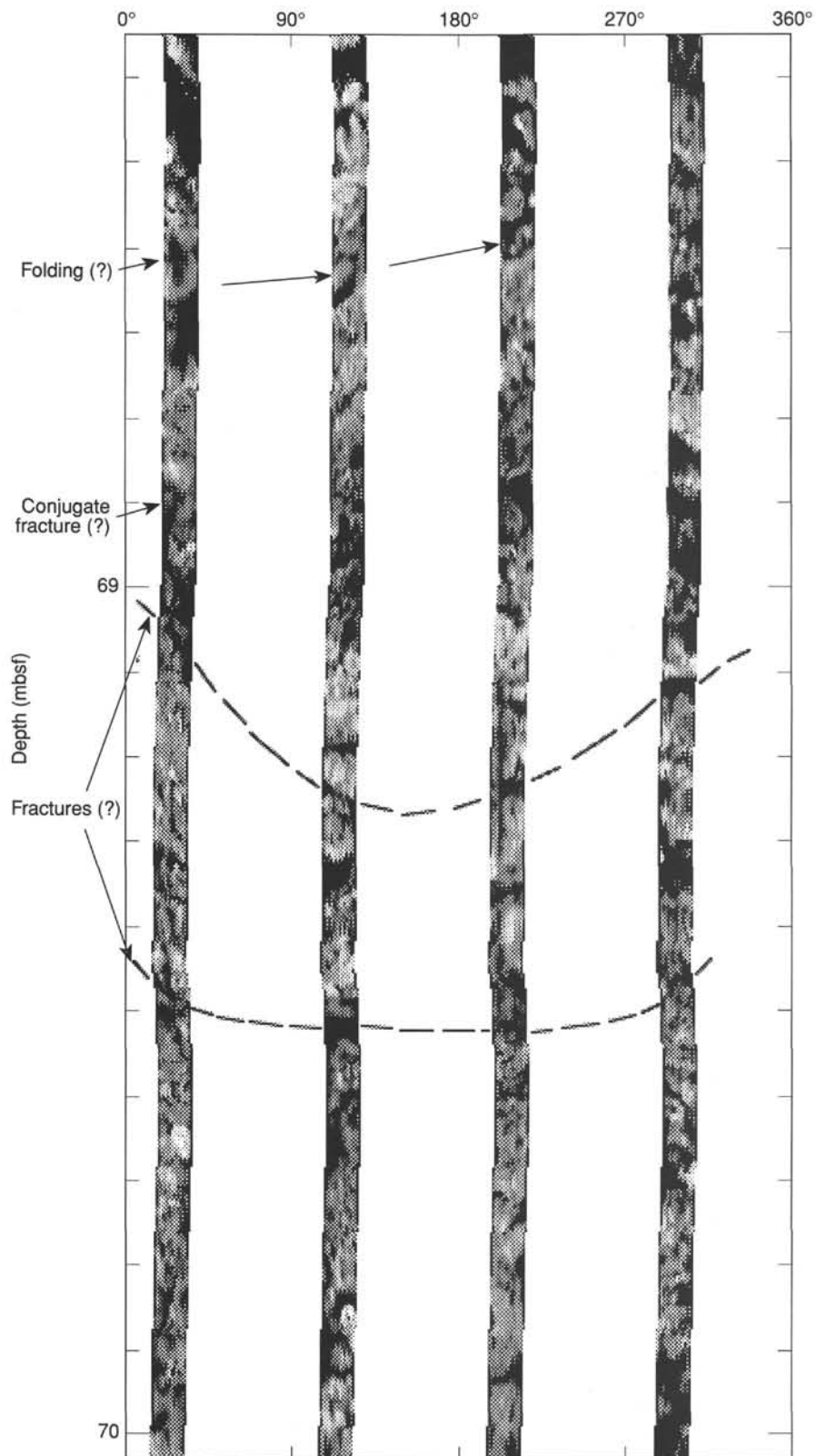


Figure 78. FMS image from one of the two high-conductivity layers in the logged hole. Fractures here are numerous, have widely varying dips, and are imaged across all four pads.

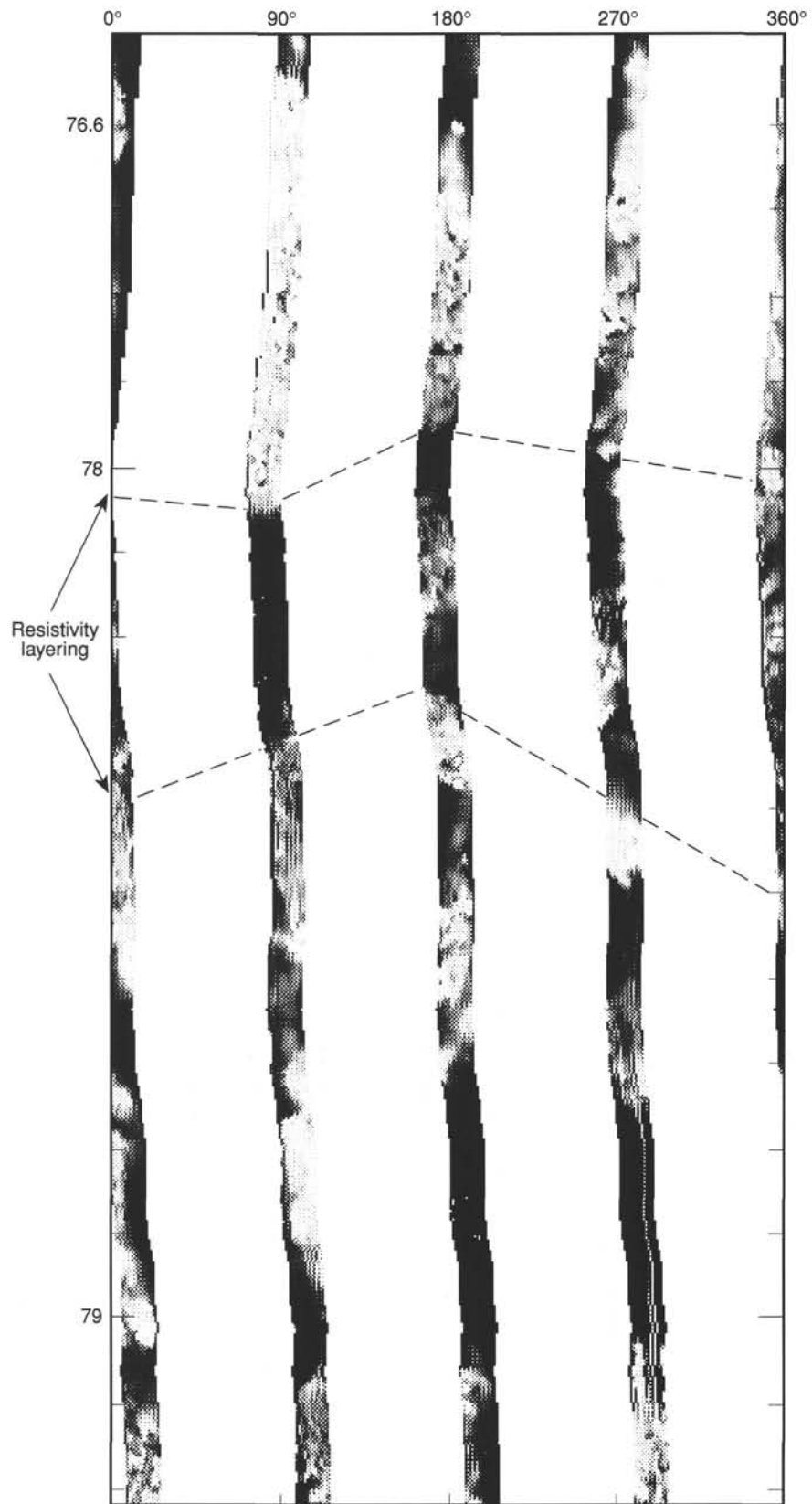


Figure 79. FMS image exhibiting shallow sedimentary layering. Although the layering is broken up and fragmented, it is nearly subhorizontal in this interval.

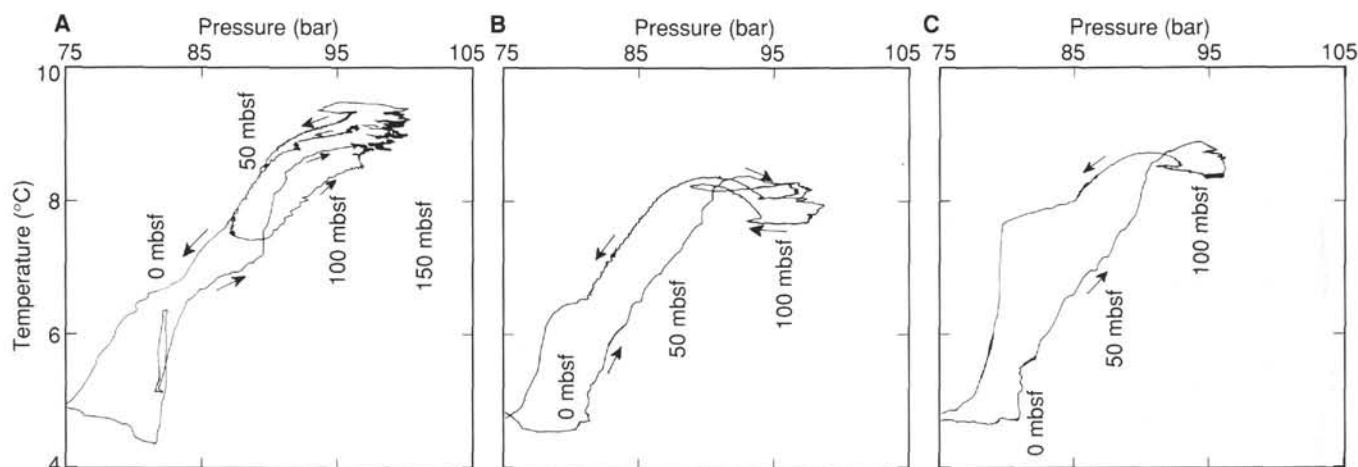


Figure 80. Temperature logs as a function of depth, from (A) seismic stratigraphic, (B) lithoporosity, and (C) FMS logging runs. Temperature data are recorded as a function of pressure, not depth, but the linear transformation between the two is shown.

Beginning at 52 mbsf and continuing downward throughout the hole, the images reveal broken or fractured, angular fragments. Nodular high-resistivity features (carbonate concretions?) are numerous from the top of the logged hole to approximately 64 mbsf and also between 104 and 121 mbsf. As in the standard resistivity log, a resistivity increase appears in the images from 64.4 to 67 mbsf. This high-resistivity interval, corresponding to the possible fault zone discussed above, shows fracture patterns similar to the frontal thrust zone of Hole 891C.

A high-conductivity layer, characterized by subhorizontal to moderately dipping fractures (Fig. 78), begins at 67.5 mbsf. This interval continues to 71.2 mbsf, and the fractures exhibit eastward dips ranging from 7° to 37°. Subhorizontal layering exists throughout the images, but it is most apparent from 71.2 mbsf to the bottom of the FMS log. Resistive and conductive layering is the predominant feature of these lower intervals (Fig. 79).

Another high-conductivity interval, which closely resembles the conductive zone at 67.5–71.2 mbsf, occurs between 79.7 and 86.4 mbsf. Below this interval, the images abruptly change to more resistive. A similar transition also occurs on the logs from 81.5 to 87.5 mbsf, but the abrupt and perfectly horizontal nature of the change on the FMS suggests that it may be an artifact. The caliper measured is 40 cm at 89.5 to about 91 mbsf and the data here are clearly degraded.

### Temperature

The LDGO temperature tool was run at the bottom of the seismic stratigraphic, lithoporosity, and FMS tool strings. Results are illustrated in Figure 80. The ADARA and WSTP measurements at this site indicate a thermal gradient of about 51°C/km and a bottom-water temperature of 4.3°C (see “ADARA and WSTP Temperature Measurements” section, this chapter). Temperature logging measurements of bottom-water temperature range from 4.2° to 4.6°C for different logging runs (Fig. 80), in general agreement with the ADARA measurements. For our maximum logging depths of 125–140 mbsf, ADARA and WSTP measurements predict equilibrium temperatures of 11.2°–12.0°C. Because the hole temperatures were reduced by circulation immediately before logging, it is difficult to infer an equilibrium thermal profile from these logging runs. Our recorded maximum temperatures of 8°–9°C are minimum estimates of the equilibrium temperature, therefore.

The temperature tool was run primarily to detect any fluid flow that may be present. The upcoming temperature logs are higher in temperature than the downgoing logs, because of thermal lags resulting from

a mud-clogged end-sub. The downgoing logs are probably minimally affected by mud clogging. The downgoing log for the seismic stratigraphic run exhibits low temperatures down to the 64.8-mbsf base of pipe (Fig. 80), because the cold pipe retards establishment of equilibrium borehole-fluid temperatures. For this logging run, temperatures below pipe have undergone much larger rebound. In the lithoporosity and FMS logging runs, maximum temperatures are seen 10–20 m above the bottom of the logging run. The greater exposure of the deeper part of the hole to cold fluids probably retarded thermal rebound. Apparently, the temperature logs are so dominated by circulation effects that any thermal effects of fluid flow are indistinguishable.

### SUMMARY AND CONCLUSIONS

Site 892 (prospectus Site OM-7) lies at a depth of 674 mbsl just west of the crest of the second ridge within the accretionary wedge that forms the Oregon lower continental slope (Fig. 1). The site was positioned to intersect both the BSR and a hydrologically active, landward-dipping fault at shallow sub-bottom depths (73 and 107–113 mbsf, respectively). Site 892 was drilled to delineate the hydrogeology and fluid chemistry of a portion of the accretionary wedge older than that sampled at Site 891, to assess the importance of a fault zone as an active aquifer, to determine the history of venting along this fault and its effect on the temperature regime, to analyze the structures developed around active and relict fault zones, and to investigate the effect of focused fluid advection on the development of gas hydrates and the BSR.

Coring reached a depth of 176.5 mbsf at Hole 892A (Fig. 81), and both the gas hydrate zone and the seismically imaged fault zone were sampled. Hole 892B was drilled to a depth of 178.5 mbsf; a packer test was conducted in this hole and a borehole seal (CORK) was deployed subsequently to provide long-term observation of the temperature-depth profile, fluid chemistry, and hydrogeologic conditions associated with the fault zone as these come to post-drilling equilibrium in the hole. Hole 892C was logged to a depth of 139 mbsf with the seismic stratigraphic, lithodensity, and FMS tools, and a VSP was run in the hole. Holes 892D (0–166.5 mbsf) and 892E (0–62 mbsf) provided additional cores and temperature determinations in selected intervals to those collected at Hole 892A.

Site 892 is characterized structurally by pervasive stratal disruption, which starts at less than 38 mbsf and overlies an interval of shear fabrics indicative of a major thrust zone from about 100 to 147 mbsf and possibly below 165 mbsf. Holes 892A and 892D, though broadly similar, exhibit significant differences in recovered structural features, indicating lateral heterogeneity on a scale of 20 m.

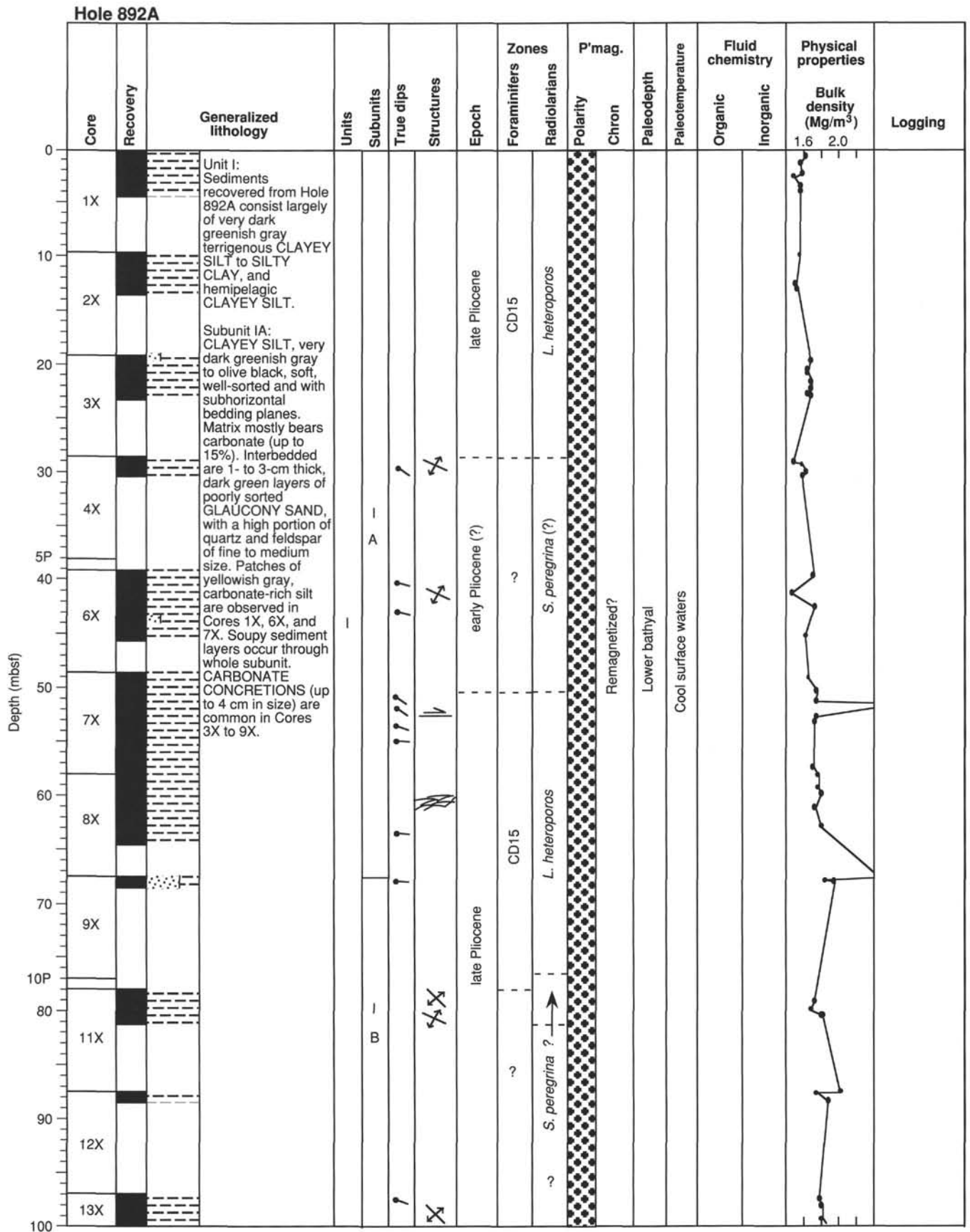


Figure 81. Master charts, Site 892.

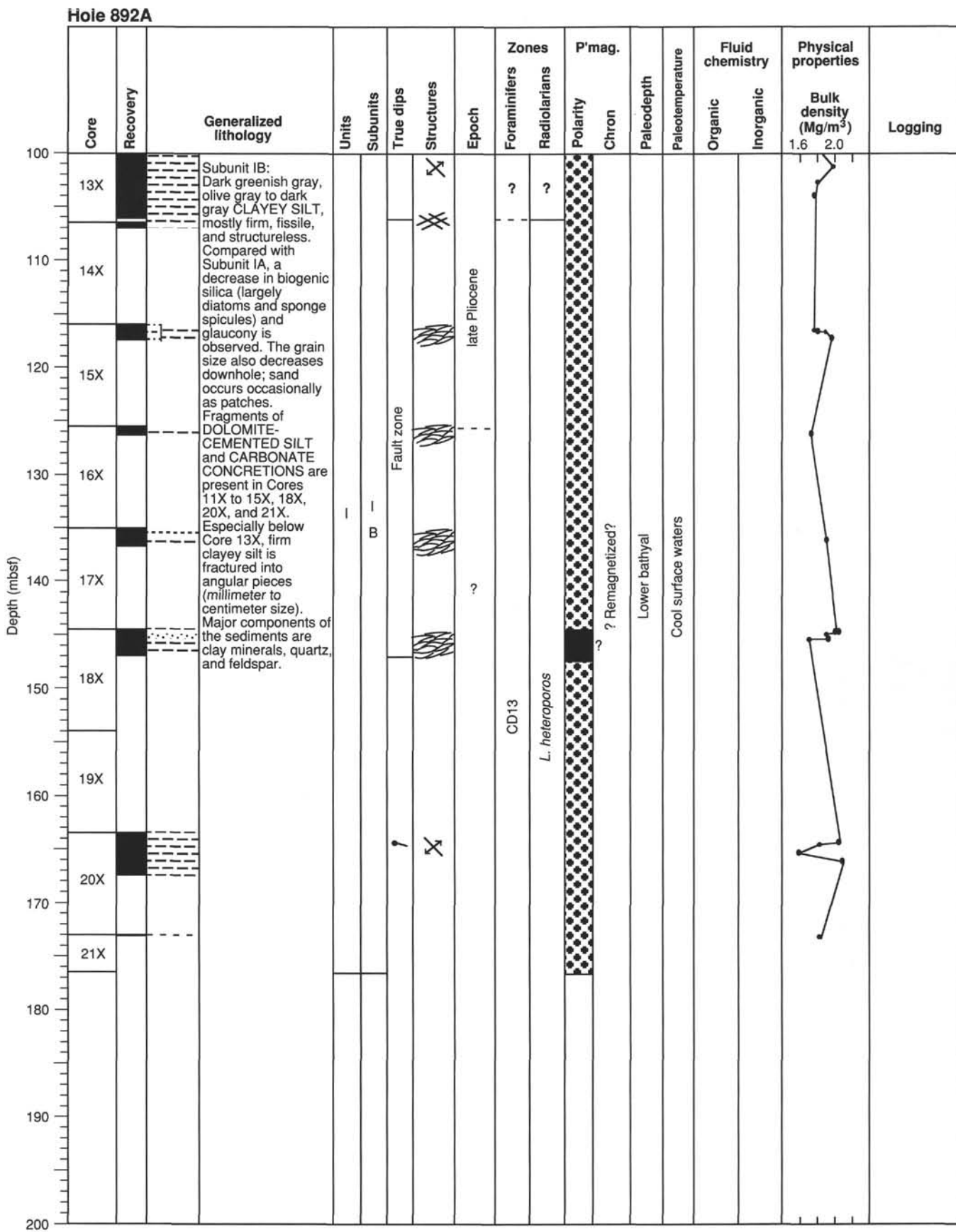


Figure 81 (continued).

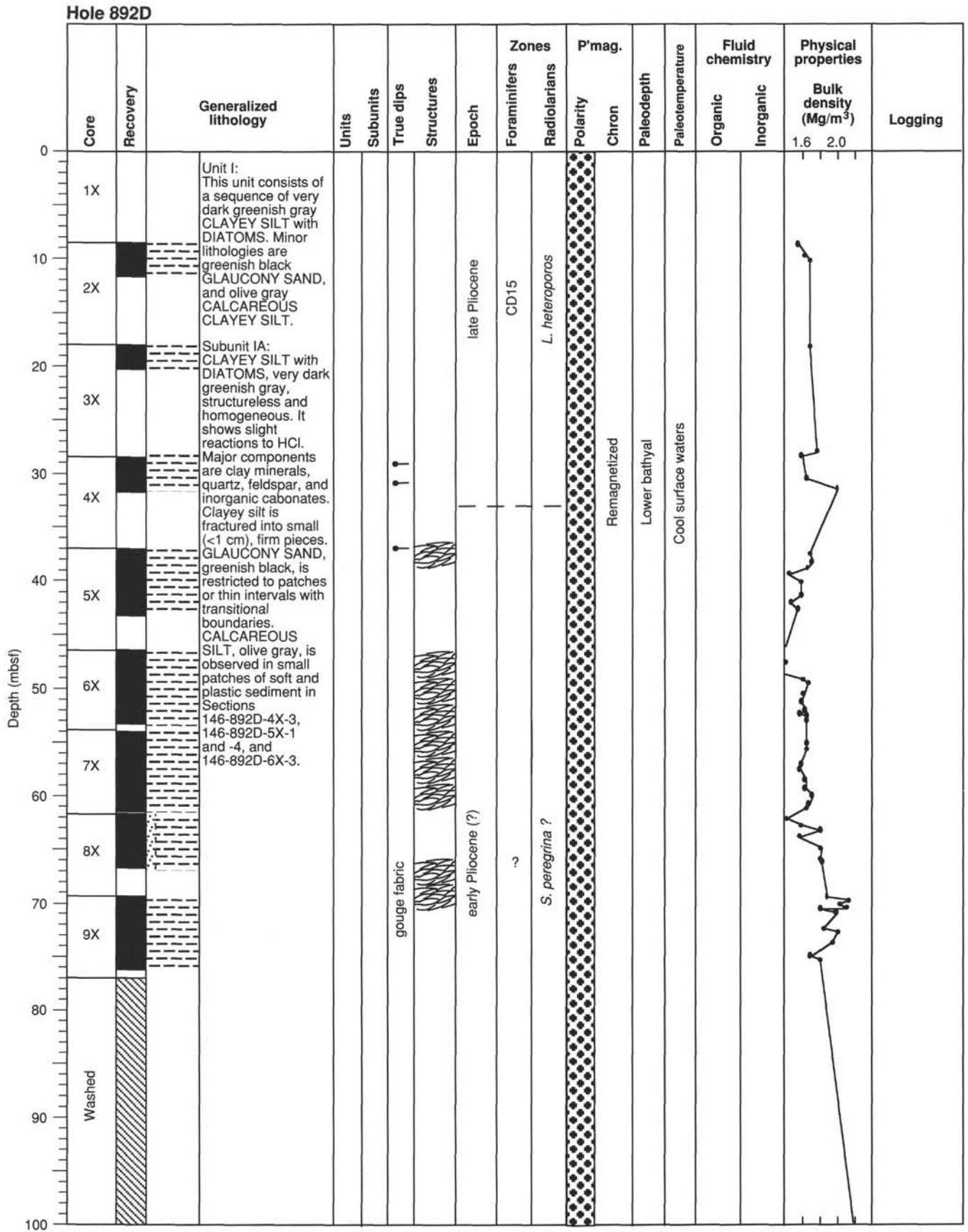


Figure 81 (continued).

Hole 892D

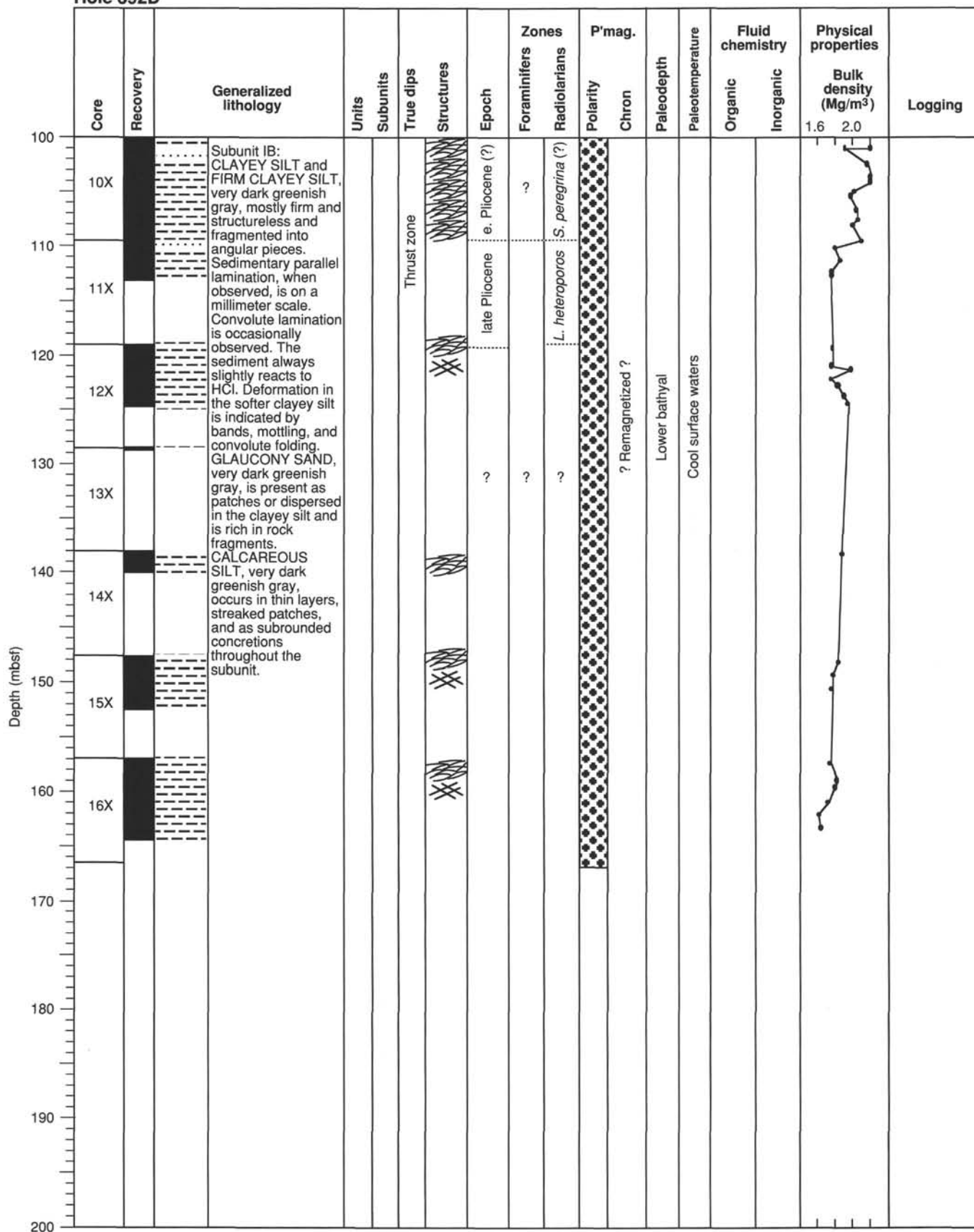


Figure 81 (continued).

Hole 892A can be divided into three domains on the basis of structures observed in the cores (Fig. 30). These domains are reflected in the biostratigraphy, and at least partially in the distribution of physical properties, geochemistry, and records from the downhole logs. Structural Domain I (0–52 mbsf) consists of moderately dipping (<35°) beds of silt and fine sand and fractured intervals in silt sequences. Although the fabric characteristic of a fault zone was not recognized at the boundary between Domains I and II (52 mbsf), its existence is inferred by an abrupt reduction in dip of bedding to 10°–20° in the underlying domain. Fractured intervals, scaly fabric, and veins increase downhole in Domain II to culminate in a strongly developed fault-zone fabric in Domain III (106–175 mbsf). In Hole 892D, the Domain I/II boundary was not recognized; this interval exhibits pervasive stratal disruption from 38 to 77 mbsf. Although all sediments from Domain III are fractured, the interval between 116 and 147 mbsf in Hole 892A exhibits a pervasively sheared, consolidated mélange fabric. It is suggested that the open fractures at about 106 mbsf may indicate the position of the modern, active fault zone, close to the depth of the seismically imaged fault (chosen as the first negative phase of the dipping reflector interpreted as the fault; Fig. 2). In Hole 892D, the thrust zone from 100 to 166 mbsf exhibits mélange, scaly fabric, and apparent cataclastic gouge zones. The reflection could be produced by the locally higher porosity in the 10-m interval beneath 100 mbsf shown by the resistivity, density, and neutron logs. This increased porosity may be produced by fracturing.

Radiolarian-based biostratigraphy confirms the positions of the fault zones inferred from the structural data. Two stratigraphic inversions are apparent in Hole 892A. The uppermost of these inversions occurs between 45 and 50 mbsf, where lower Pliocene deposits (*S. peregrina* Zone) overlie upper Pliocene sediments (*L. heteroporos* Zone). Deeper in the section (107–117 mbsf in Hole 892A and 76–110 mbsf in Hole 892D), lower Pliocene sediments overlie upper Pliocene deposits from the base of the *L. heteroporos* Zone. These two stratigraphic reversals fall close to the structural Domain I/II and II/III boundaries, respectively. In addition, the biostratigraphy defines a hiatus at 23–30 mbsf (32–43 mbsf; Hole 892D) and possibly another near 67 mbsf (not observed in Hole 892D). Foraminifers suggest deposition under cool to temperate surface-water conditions in a lower bathyal environment.

The sediments at Site 892 consist predominantly of terrigenous silty clay and clayey silts with sporadic sand layers. Because the lithology is relatively uniform, a single lithostratigraphic unit was defined, although it is divided into two subunits.

Subunit IA (Hole 892A, 0–67.75 mbsf; Hole 892D, 0–69.3 mbsf; Hole 692E, 0–52.0 mbsf) is richer in sand than the deeper section of the hole. Most of the sand layers consist of authigenic glaucony pellets (see “Lithostratigraphy” section, “Sites 889/890” chapter, this volume). Grain size decreases downward through the subunit, whereas the proportion of biogenic silica increases near its base. Subunit IB (Hole 892A, 67.75–176.5 mbsf; Hole 892D, 69.3–166.5 mbsf) contains fewer sand layers, less glaucony and biogenic silica, and an irregular distribution of grain sizes. Most distinctively, however, Subunit IB exhibits the fracturing and stratal disruption described previously for structural Domains II and III. The top of the subunit is defined by open fractures that may indicate an active fault.

The sediments at Site 892 appear to be Pliocene abyssal plain deposits, similar to the lowermost sediments recovered at DSDP Site 174 in Cascadia Basin. Coeval sections at both locations are characterized by interlayered hemipelagic sediments and silt-sized turbidite intervals.

As expected in a section cut by faults, the physical properties at Site 892 are characterized more by discontinuities in their respective depth distributions than by a normal response to compaction. Abrupt dislocations in bulk density and porosity occur at 17, 68, 116, 144, and 164 mbsf (Fig. 48). Distinct structural features are recognizable at 68 (open fractures), 116, and 144 mbsf (top and bottom, respectively, of major fault zone and stratal disruption in structural Domain III). In addition,

the discontinuity in physical properties at 17 mbsf is clearly a function of the gas hydrates observed between 2 and 19 mbsf, the sublimation of which disrupted the near-surface sediment. As a result, these deposits exhibit an abnormally low density (<1.6 Mg/m<sup>3</sup>; porosity > 67%). Beneath the zone of visible hydrates, the porosity declines normally to about 55% at 67.75 mbsf (the top of lithostratigraphic Subunit IB and the position of the BSR), and then becomes highly variable (42%–62%) to the base of the hole, with little evidence for further general consolidation. Rather, compaction appears to be localized about the faulted intervals, where strain hardening has occurred. These same intervals are juxtaposed with porous, fractured zones that, at 68 and 116 mbsf, apparently serve as active flow conduits for hydrocarbon-bearing fluids.

Active flow at Site 892 is indicated by geochemical anomalies in the pore waters, by a packer test that measured superhydrostatic fluid pressures, by two local increases in temperature above an otherwise linear increase of temperature with depth, and perhaps by the unusual occurrence of gas hydrates and elevated levels of hydrogen sulfide in near-surface sediments.

Bacterial methanogenesis occurs at much shallower depths (possibly within the upper 2 mbsf) at Site 892 than at all previous sites. Although biogenic methane probably persists to the base of the hole, it is mixed with significant amounts of higher hydrocarbon gases below 68 mbsf. These hydrocarbons (ethane through hexane) are thermogenic and must be derived from deeper within the prism, as the maturity of the local kerogen is insufficient to produce them. The gases also include ethene, an olefin that is unstable over geologically significant time periods. Its presence implies rapid transport of thermogenic gas to Site 892, probably by advection of petroliferous pore waters, although gas migration might occur independently. The distribution of higher hydrocarbons (Figs. 39–40) suggests incursion of fluids at 68, 107, and 125 mbsf.

Gas hydrates occur as macroscopic crystals, pellets, and aggregations distributed in the upper 19 m of sediment and probably as disseminated deposits to the depth of the BSR (67.75 mbsf). The disseminated hydrates have a patchy distribution as indicated by the variable dilution of Cl<sup>-</sup> (Fig. 45). Temperature measurements in the cores where observable hydrate occurred (<19 mbsf) indicate that less than 10% of the pore space is filled with hydrate. Although methane hydrate predominates in the cores, the occurrence of higher hydrocarbons and high concentrations of H<sub>2</sub>S suggests that hydrates of these species may occur as well.

High concentrations (up to 10,000 ppmv) of H<sub>2</sub>S in near-surface sediments and the persistence of H<sub>2</sub>S to 60 mbsf (Fig. 38) indicate either that hydrogen sulfide is formed bacterially by sulfate reduction and its usual removal as monosulfides and/or pyrite is inhibited or that H<sub>2</sub>S is allochthonous to these near-surface sediments and has a hydrothermal source. The close association of H<sub>2</sub>S with the gas-hydrate zone suggests that free sulfide may be stored as clathrate in situ, and that it evolves as gas only upon core retrieval. If this is the case, then the occurrence of H<sub>2</sub>S is only an indirect indicator of fluid flow (as are the hydrates, depending upon the mechanism assumed for their formation) because the sulfide is probably derived from seawater by microbial sulfate reduction. Alternatively, the sulfide might be generated at higher temperatures and pressures within the wedge and be advected to the near-surface sediments. The absence of sulfides associated with the thermogenic gas sampled at this site and the low concentrations of thermogenic gas in the near-surface sediments, however, make this hypothesis less likely.

The geophysical logs in Hole 892C (located 20 m southeast of Hole 892A) are sensitive if somewhat inconsistent indicators of fault zones inferred from the cores. Between 61 and 68 mbsf and between 83 and 90 mbsf (Fig. 75), records of high density, high velocity, and high resistivity in the logs apparently define fault zones that are strain hardened. These intervals show temperature and ethane anomalies, and the upper interval exhibits a pronounced discontinuity in density/porosity. By contrast, a fault zone inferred to occur at 106 mbsf (ethane anomaly,

fracturing in core) is represented by low values of resistivity and bulk density and by high values of neutron porosity in the logs.

Logging unequivocally indicates that the BSR is caused by the presence of free gas below 72 mbsf. Because there is no indication of massive hydrates in the cores or in the logs (high velocity and resistivity, low density and gamma-ray response; Mathews and von Huene, 1985), we infer, with confirmation from the  $\text{Cl}^-$  dilution, that the gas hydrates below 17 mbsf are disseminated and patchily distributed. Although no obvious evidence (such as anomalously high velocity relative to porosity) is present for such disseminated hydrates in the logs, the data cannot exclude a few percent gas hydrate in the interval 35–72 mbsf (the logs were not run above 35 mbsf). The velocity log, however, provides an obvious explanation for the position of the BSR: below 72 mbsf sonic velocity drops uniformly to 1.5 km/s (Fig. 76), which is the velocity of borehole fluid. Water velocities are expected where the velocity in the formation is less than 1.5 km/s or where the water-filled borehole provides the fastest travel path if the hole is severely oversized. As the caliper indicates that the hole is not uniformly oversized, the low sonic velocities are attributed to the presence of free gas in the formation below the BSR. The low velocities are confirmed by the VSP, from which velocities of 1.4 km/s or less were determined for depths below the BSR.

A sensitive indicator of advective flow is temperature change. Moore et al. (in press) suggest that warm fluids rising along the fault zone should produce a local thermal gradient of about twice the inferred regional value. Well-constrained in-situ measurements of temperature at Site 892 yield results that indicate fluid flow at two depths in Hole 892A. Most of the data define a linear temperature gradient of  $51^\circ\text{C}/\text{km}$ , which indicates dominantly conductive heat transfer (Fig. 71) and predicts a surface heat flow of about  $53 \text{ mW}/\text{m}^2$ . (Contrast this value with the surface heat-flow values of  $142 \text{ mW}/\text{m}^2$  measured 2.4 km southwest of Site 892 and  $84 \text{ mW}/\text{m}^2$  measured 4 km southwest of the site [Wang et al., 1989]). Measurements at two anomalous points (67.5 and 87.5 mbsf) gave temperatures that lie  $1.6^\circ$  and  $2.5^\circ\text{C}$ , respectively, above the linear regression line of the overall gradient. These points are attributed to local advection of warm fluids (between 67.5 and 87.5 mbsf) along fault zones detected by the logs. The limited vertical extent of the anomalies, however, indicates small spatial diffusion of the temperature signal and requires very recent fluid flow.

The temperature distribution constrains the hydrate stability field at Site 892 (Fig. 72). The linear temperature gradient of  $51^\circ\text{C}/\text{km}$  places the predicted base of the pure methane–pure water stability field at  $120 \text{ mbsf} \pm 4 \text{ m}$ . The BSR, commonly interpreted to indicate the base of the hydrate zone, is situated at 73 mbsf. The disparity of  $1.9^\circ\text{C}$  between the temperature derived from the measured gradient and the predicted temperature at the BSR suggests that the experimentally derived phase boundary for pure methane–pure water is not directly applicable to the gas hydrate system on this margin. The theoretical distribution of hydrate stability is complicated further by the temperature anomalies noted in Hole 892A. These temperature excursions would make gas hydrate unstable below 120 mbsf, between 83 and 93 mbsf, and perhaps near 68.5, and imply two or more layers of hydrate stability. This pattern conflicts with the interpretation of the sonic log that indicates the presence of free gas (which cannot exist within the hydrate stability field) at all depths below 72 mbsf. The disparity between the theoretical position of the gas hydrate stability field and the apparent position of the base of that field observed at Site 892 is similar to the dislocation noted at Site 889. Resolution of this problem must await determination of the gas composition of the hydrates and may require experimental determination of appropriate gas hydrate–seawater stability fields.

The drill-string packer experiment confirmed that the fluid in the formation at Hole 892B is overpressured. Although the results of the packer experiment await analysis to determine permeability, preliminary observation suggests that the formation pressure is 0.25–0.30 MPa above hydrostatic pressure (Fig. 73). Because the hole was open

for  $12\frac{3}{4}$  hr before the test was run, the apparent formation pressure does not represent an equilibrium condition. A post-cruise record of pressure (and temperature) recovery at Hole 892B will come from the borehole seal (CORK) deployed in this hole.

## REFERENCES\*

- Archie, G.E., 1942. The electrical resistivity log as an aid in determining some reservoir characteristics. *Trans. Am. Inst. Min. Metall. Pet. Eng.*, 146:54–62.
- Bouma, A.H., 1962. *Sedimentology of Some Flysch Deposits: A Graphic Approach to Facies Interpretation*. Amsterdam (Elsevier).
- Brooks, J.M., Cox, H.B., Bryant, W.R., Kennicutt, M.C., II, Mann, R.G., and McDonald, T.J., 1989. Association of gas hydrates and oil seepage in the Gulf of Mexico. *Org. Geochem.*, 10:221–234.
- Brückmann, W., 1989. Typische Kompaktionsmuster mariner Sedimente und ihre Modifikation in einem rezenten Akkretionskeil (Barbados Ridge). *Beitr. Geol. Inst. Univ. Tübingen, Rh. A.*, 5:1–135.
- Carson, B., Holmes, M.L., Umstätt, K., Strasser, J.C., and Johnson, H.P., 1991. Fluid expulsion from the Cascadia accretionary prism: evidence from porosity distribution, direct measurements, and GLORIA imagery. *Trans. R. Soc. London A*, 335:331–340.
- Cowan, D.S., 1985. The origin of some common types of melange in the western Cordillera of North America. In Nasu, N., et al. (Eds.), *Formation of Active Ocean Margins*: Tokyo (Terra Publ.), 257–272.
- Domenico, S.N., 1976. Effect of brine-gas mixture on velocity in an unconsolidated sand reservoir. *Geophysics*, 41:882–894.
- Hamilton, E.L., 1976. Variations of density and porosity with depth in deep-sea sediments. *J. Sediment. Petrol.*, 46:280–300.
- Hitchon, B., 1974. Occurrence of natural gas hydrates in sedimentary basins. In Kaplan, I.R. (Ed.), *Natural Gases in Marine Sediments*: New York (Plenum), 195–226.
- Hyndman, R.D., Foucher, J.P., Yamano, M., Fisher, A., Berner, U., Brückmann, W., Byrne, T., Chabernaud, T., Firth, J.V., Gamo, T., Gieskes, J.M., Hill, I.A., Karig, D.E., Kastner, M., Kato, Y., Lallemand, S., Lau, R., Maltman, A.J., Moore, G.F., Moran, K., Olafsson, G., Owens, W.H., Pickering, K.T., Siena, F., Taira, A., Taylor, E., Underwood, M.B., Wilkinson, C., and Zhang, J., 1992. Deep sea bottom-simulating-reflectors: calibration of the base of the hydrate stability field as used for heat flow estimates. *Earth Planet. Sci. Lett.*, 109:289–302.
- Hyndman, R.D., Moore, G.F., and Moran, K., 1993. Velocity, porosity, and pore-fluid loss from the Nankai subduction zone accretionary prism. In Hill, I.A., Taira, A., Firth, J.V., et al., *Proc. ODP, Sci. Results*, 131: College Station, TX (Ocean Drilling Program), 211–220.
- Hyndman, R.D., and Spence, G.D., 1992. A seismic study of methane hydrate marine bottom simulating reflectors. *J. Geophys. Res.*, 97:6683–6698.
- Kulm, L.D., Suess, E., Moore, J.C., Carson, B., Lewis, B.T., Ritger, S.D., Kadko, D.C., Thornburg, T.M., Embley, R.W., Rugh, W.D., Massoth, G.J., Langseth, M.G., Cochrane, G.R., and Scamman, R.L., 1986. Oregon subduction zone: venting, fauna, and carbonates. *Science*, 231:561–566.
- Kulm, L.D., von Huene, R., et al., 1973. *Init. Repts. DSDP*, 18: Washington (U.S. Govt. Printing Office).
- Linke, P., Suess, E., Torres, M., Martens, V., Rugh, W.D., Ziebis, W., and Kulm, V., in press. Determination of fluid flow from subduction zone vents. *Deep Sea Res. Part A*.
- Lundberg, N., and Moore, J.C., 1986. Macroscopic structural features in Deep Sea Drilling Project cores from forearc regions. In Moore, J.C. (Ed.), *Structural Fabrics Preserved in Deep Sea Drilling Project Cores from Forearcs*. Mem.—Geol. Soc. Am., 166:13–44.
- MacKay, M.E., Moore, G.F., Cochrane, G.R., Moore, J.C., and Kulm, L.D., 1992. Landward vergence and oblique structural trends in the Oregon Margin accretionary prism: implications and effect on fluid flow. *Earth Planet. Sci. Lett.*, 109:477–491.
- Mathews, M.A., and von Huene, R., 1985. Site 570 methane hydrate zone. In von Huene R., Aubouin, J., et al., *Init. Repts. DSDP*, 84: Washington (U.S. Govt. Printing Office), 773–790.
- Miller, J.J., Lee, M.W., and von Huene, R., 1991. A quantitative analysis of gas hydrate phase boundary reflection (BSR), offshore Peru. *AAPG Bull.*, 75:910–924.

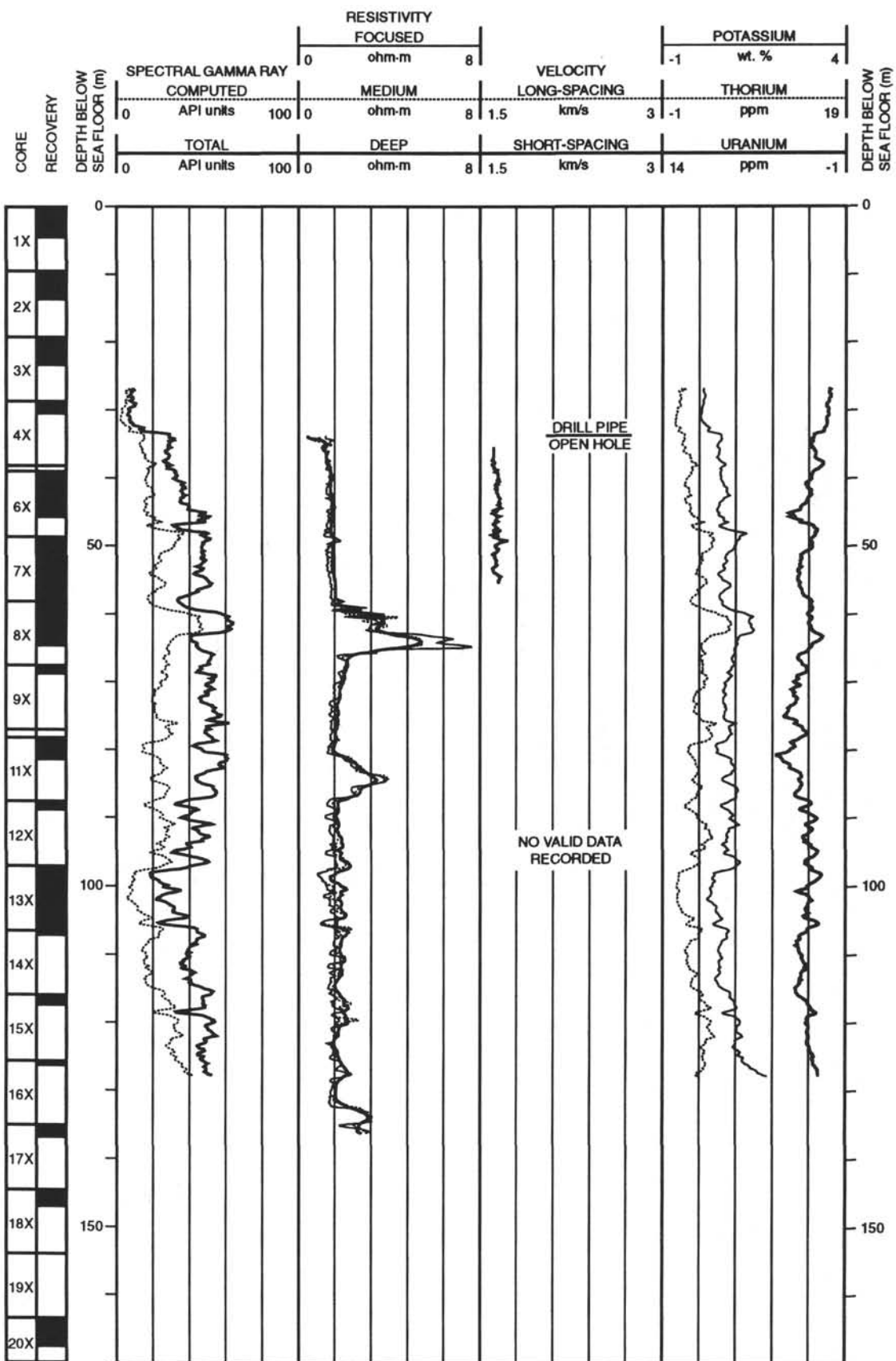
\* Abbreviations for names of organizations and publication titles in ODP reference lists follow the style given in *Chemical Abstracts Service Source Index* (published by American Chemical Society).

- Minshull, T., and White, R., 1989. Sediment compaction and fluid migration in the Makran accretionary prism. *J. Geophys. Res.*, 94:7387-7402.
- Moore, J.C., Brown, K.M., Horath, F., Cochrane, G., MacKay, M., and Moore, G.F., 1991. Plumbing in accretionary prisms: effects of permeability variations. *Philos. Trans. R. Soc. London*, 335:275-288.
- Moore, J.C., Jeanbourquin, P., and Sample, J., in press. Thrusting, fluid flow, and chemosynthetic bioherm development: Oregon accretionary prism. *Geol. Soc. Am. Bull.*
- Nigrini, C.A., and Caulet, J.P., 1992. Late Neogene radiolarian assemblages characteristic of Indo-Pacific areas of upwelling. *Micropaleontology*, 38:139-164.
- Odin, G.S., 1985. Significance of green particles (glaucony, berthierine, chlorite) in arenites. In Zuffa, G.G. (Ed.), *Provenance of Arenites*: Berlin (Reidel), 279-307.
- Ritger, S., Carson, B., and Suess, E., 1987. Methane-derived authigenic carbonates formed by subduction-induced pore water expulsion along the Oregon/Washington margin. *Geol. Soc. Am. Bull.*, 48:147-156.
- Serra, O., 1984. *Fundamentals of Well Log Interpretation* (Vol. 1): *The Acquisition of Logging Data*: Amsterdam (Elsevier).
- Sloan, E.D., 1990. *Clathrate Hydrates of Natural Gases*: New York (Marcel Dekker).
- von Huene, R., and Kulm, L.D., 1973. Tectonic Summary of Leg 18. In Kulm, L.D., von Huene, R., et al., *Init. Repts. DSDP*: Washington (U.S. Govt. Printing Office), 961-976.
- von Huene, R., Piper, D.J.W., and Duncan, J., 1973. Measurements of porosity in sediments of the lower continental margin, deep-sea fans, the Aleutian Trench, and Alaskan Abyssal plain. In Kulm, L.D., von Huene, R., et al., *Init. Repts. DSDP*, 18: Washington (U.S. Govt. Printing Office), 889-895.
- Wang, C.-Y., Shi, Y., Kulm, L.D., and Langseth, M.B., 1989. Thermal constraints on fluid expulsion rate in accretionary prism: a study of the Oregon-Washington Margin. *Eos*, 70:1333.
- Wang, M.C., Nacci, V.A., and Markert, C.D., 1976. Electrical resistivity method for marine sediment consolidation study. *Proc. 8th Ann. Offshore Technol. Conf.*, Houston, TX, Pap. 2623.
- Whalley, E., 1980. Speed of longitudinal sound in clathrate hydrates. *J. Geophys. Res.*, 85:2539-2542.

Ms 146IR-010

**NOTE: For all sites drilled, core-description forms ("barrel sheets") and core photographs can be found in Section 6, beginning on page 429. Forms containing smear-slide data can be found in Section 7, beginning on page 591.**

Hole 892C: Resistivity-Velocity-Natural Gamma Ray Log Summary



Hole 892C: Density-Porosity-Natural Gamma Ray Log Summary

